



**Πανεπιστήμιο
Κύπρου**

DEPARTMENT OF CHEMISTRY

**TIME-RESOLVED STEP-SCAN FTIR STUDIES OF HEME-
BASED OXYGEN SENSOR PROTEINS**

ANDREA PAVLOU

**“A Dissertation Submitted to the University of Cyprus in Partial Fulfillment of the
Requirements for the Degree of Doctor of Philosophy”**

NOVEMBER 2014

Andrea Pavlou

Declaration of Originality

The present doctoral dissertation was submitted in partial fulfillment of the requirements for the degree of Doctor of Philosophy of the University of Cyprus. It is a product of original work of my own, unless otherwise mentioned through references, notes, or any other statements.

Exceptions: Protein samples have been provided by the research groups of Prof. Shigetoshi Aono at the Okazaki Institute of Integrative Biosciences, National Institutes for Natural Sciences, Okazaki Japan, Associate Prof. Marketa Martinkova at Charles University, Prague Czech Republic and Prof. Teizo Kitagawa at the Okazaki Institute of Integrative Biosciences, National Institutes for Natural Sciences, Okazaki Japan.

Full Name:

Signature:

Περίληψη

Η ανακάλυψη και ο χαρακτηρισμός νέων αιμοπρωτεϊνών αισθητήρων κατά την τελευταία δεκαετία έχει προκαλέσει το ενδιαφέρον για την κατανόηση του ρυθμιζόμενου από μια προσθετική ομάδα αίμης μηχανισμού αναγνώρισης και διάκρισης των διατομικών αέριων μορίων O₂, NO και CO, που δρουν ως μόρια σηματοδότησης για πολλές βιολογικές διεργασίες. Στην παρούσα διδακτορική διατριβή, έχουμε χρησιμοποιήσει τη φασματοσκοπία FTIR και χρονικής ανάλυσης step-scan (TRS²) – FTIR, για τη διερεύνηση της δυναμικής και των δομικών αλλαγών που επιφέρονται στην πρωτεΐνη κατά τη φωτοδιάσπαση και επαναδέσμευση του αέριου υποκαταστάτη (CO), οι οποίες αποτελούν πληροφορίες “κλειδιά” για την κατανόηση του μηχανισμού ενδομοριακής μεταγωγής σήματος τριών αιμοπρωτεϊνών αισθητήρων οξυγόνου (HemAT-Bs, YddV και EcDOS).

Η HemAT-Bs είναι μια αιμοπρωτεΐνη αισθητήρας οξυγόνου η οποία ελέγχει το σύστημα αεροτακτικής σηματοδότησης του βακτηρίου *B.subtilis*. ενεργοποιώντας την κίνηση του οργανισμού προς μια περιοχή υψηλή σε περιεκτικότητα οξυγόνου (O₂). Έχουμε μελετήσει τα σύμπλοκα “αγρίου τύπου” HemAT-CO τόσο της άθικτης μορφής της πρωτεΐνης, όσο και της απομονωμένης περιοχής ανίχνευσης, καθώς επίσης και των μεταλλαγμένων Y70F, Y133F, L92A και T95A πρωτεϊνών. Τα φάσματα FTIR του συμπλόκου HemAT-CO εμφανίζουν δύο δονήσεις του δεσμευμένου στην αίμη CO στους 1967 cm⁻¹ και 1928 cm⁻¹. Οι μεταβολές των συγκεκριμένων διαμορφώσεων κατά τη μετάλλαξη των καταλοίπων Tyr70 και Leu92 της μακρινής περιοχής της αίμης, καθώς και του καταλοίπου Tyr133 της εγγύς περιοχής αποκαλύπτουν το ρόλο του κάθε καταλοίπου στον καθορισμό της δομής του συμπλόκου Fe²⁺-CO. Η παρατήρηση της κινητικής εξέλιξης της επαναδέσμευσης του CO στο Fe²⁺ της αίμης ($t_d = 8 \mu s - ms$) με φασματοσκοπία TRS²-FTIR δείχνει διφασική κινητική τόσο για την άθικτη μορφή της HemAT-Bs, όσο και για την απομονωμένη περιοχή ανίχνευσης. Τα TRS²-FTIR πειράματα έχουν επίσης επιτρέψει την παρατήρηση των δομικών αλλαγών και της διατάραξης στις προπιονικές ομάδες της αίμης κατά τη φωτοδιάσπαση του υποκαταστάτη (CO). Προτείνουμε σημαντική αλλαγή προσανατολισμού για τις B- και G- έλικες κατά τη δέσμευση του CO. Επιπλέον, η ανίχνευση δευτερευόντων θέσεων δέσμευσης του υποκαταστάτη στα TRS²-FTIR φάσματα ($t_d = 300 ns$) της αγρίου τύπου πρωτεΐνης και της μετάλλαξης L92A υποδηλώνει το ρόλο του καταλοίπου Leu92 ως πύλη στη διαδρομή του φωτοδιασπώμενου CO από/προς το κέντρο της αίμης.

Η YddV είναι μια αιμοπρωτεΐνη αισθητήρας οξυγόνου του βακτηρίου *E.coli*, που ανήκει στην οικογένεια πρωτεϊνών-αισθητήρων GCS (globin-coupled sensors). Η λειτουργία

του ενζύμου αυτού είναι να ρυθμίζει τη σύνθεση του c-di-GMP μέσω δραστηκότητας διγουανυλικής κυκλάσης (DGC), με σκοπό τη δημιουργία βιοφίλμ. Η YddV αναγνωρίζει το O₂ και το CO και τα διακρίνει έναντι άλλων αέριων διατομικών μορίων όπως το NO. Έχουμε πραγματοποιήσει πειράματα με φασματοσκοπία TRS²-FTIR τόσο στην αγρίου τύπου μορφή της πρωτεΐνης, όσον και στις σημαντικές για την αναγνώριση του O₂ και τη σταθερότητα του Fe²⁺-O₂ συμπλόκου μεταλλάξεις L65M, L65T, Y43A, Y43F και Y43W, για να καθορίσουμε τις δομικές αλλαγές στην περιοχή του ενεργού κέντρου της αίμης κατά τη φωτοδιάσπαση του CO. Οι συγκεκριμένες μεταλλάξεις έχουν σχεδιαστεί έτσι ώστε να διαταράσσουν το ηλεκτροστατικό πεδίο κοντά στον δεσμευμένο στην αίμη υποκαταστάτη (CO), και επίσης για να επιτρέψουν τη μελέτη του “διαδρόμου” επικοινωνίας μεταξύ των καταλοίπων της μακρινής περιοχής με την ομάδα αίμης. Τα TRS²-FTIR φάσματα διαφοράς έχουν υποδείξει ότι οι προπιονικές ομάδες της αίμης βρίσκονται τόσο στην πρωτονιομένη, όσο και στην αποπρωτονιομένη μορφή. Επιπλέον, η κινητική εξέλιξη των δονήσεων των προπιονικών ομάδων και του αμιδίου I συμπίπτει χρονικά με το ρυθμό επαναδέσμευσης του CO, προτείνοντας έτσι ότι υπάρχει σύζευξη μεταξύ της δέσμευσης του υποκαταστάτη με α) το περιβάλλον των προπιονικών ομάδων της αίμης και β) την αποδιέγερση της πρωτεΐνης. Η κινητική επαναδέσμευσης του CO στις μεταλλάξεις L65M, L65T και Y43W, υποδηλώνει ότι τα κατάλοιπα Leu65 κ Tyr43 ελέγχουν σημαντικά τη δυναμική του υποκαταστάτη. Οι επιπτώσεις των αποτελεσμάτων αυτών, όσον αφορά το ρόλο των προπιονικών ομάδων της αίμης και των θετικά - φορτισμένων ή δοτών πρωτονίων καταλοίπων της μακρινής περιοχής του ενεργού κέντρου στη σταθεροποίηση των δεσμευμένων στην αίμη αέριων υποκαταστατών περιγράφονται στην μελέτη.

Η πρωτεΐνη *EcDOS* (*E. coli* Direct Oxygen Sensor), παρουσιάζει δραστηκότητα φωσφοδιεστεράσης (PDE), καταλύοντας τη μετατροπή του c-di-GMP σε linear di-GMP μέσω ενεργοποίησης με την ανίχνευση διατομικών αέριων μορίων. Στα φάσματα FTIR του συμπλόκου *EcDOS*H-CO αγρίου τύπου, έχουν παρατηρηθεί δύο δονήσεις του δεσμευμένου στην αίμη CO στους 1970 cm⁻¹ και 1923 cm⁻¹, οι οποίες αποδίδονται στις “ανοιχτή” και “κλειστή” διαμόρφωση του συμπλόκου αντίστοιχα. Οι δύο διαμορφώσεις διαταράσσονται σημαντικά κατά τις μεταλλάξεις των καταλοίπων της μακρινής περιοχής Arg97 και Phe113, υποδηλώνοντας έτσι ότι η Arg97 αλληλεπιδρά άμεσα με το δεσμευμένο στην αίμη CO μέσω δεσμών υδρογόνου, ενώ η Phe113 ελέγχει σημαντικά το δίκτυο δεσμών υδρογόνου κοντά στο δεσμευμένο στην αίμη CO. Τα TRS²- FTIR φάσματα διαφοράς της αγρίου τύπου *EcDOS*H κατά τη φωτοδιάσπαση του CO στα $t_d = 6 \mu s$, έχουν υποδείξει 55% παραγωγή φωτοπροϊόντος, με το υπόλοιπο 45% του CO να υπόκειται σε άμεση επανασύνδεση

(geminate recombination). Μελετώντας την κινητική εξέλιξη της επαναδέσμευσης του CO στο σίδηρο της αίμης ($t_d = \mu\text{s} - \text{ms}$) παρατηρούμε διαφασική κινητική. Μετά τη φωτοδιάσπαση του CO εμφανίζεται μια γρήγορη φάση ($k_1 = 7267 \text{ s}^{-1}$), ενώ στη συνέχεια δομικές αλλαγές στο ενεργό κέντρο της αίμης καθορίζουν την επαναδέσμευση του CO σε πιο αργό ρυθμό ($k_2 = 186 \text{ s}^{-1}$). Τα TRS²-FTIR φάσματα του συμπλόκου της M95A με το CO υποδηλώνουν μια ανταγωνιστική διαδικασία επαναδέσμευσης μεταξύ του καταλοίπου Met95 και του CO. Η αποδέσμευση του CO οδηγεί σε δομική αναδιοργάνωση του ενεργού κέντρου της αίμης η οποία προωθεί τη γρήγορη δέσμευση του εσωτερικού υποκαταστάτη (Met95). Τέλος, περιγράφεται η επίδραση των μεταλλάξεων R97A, R97I, F113T, N84V, Y126F, W53F και E93I στην κινητική επαναδέσμευσης του CO και στις ταυτόχρονες δυναμικές δομικές μεταβολές της πρωτεΐνης.

Abstract

The discovery and characterization of new heme-based sensor proteins during the past decade has invigorated the interest in understanding the mechanism of heme-mediated recognition and discrimination of the diatomic gaseous ligands O₂, NO and CO that act as signaling molecules for many biological processes. We have employed FTIR and time-resolved step-scan (TRS²) – FTIR spectroscopy to investigate the protein structural changes induced by ligand (CO) photodissociation and rebinding that are crucial for understanding the intramolecular signal transduction mechanism of three heme-based oxygen sensor proteins; HemAT-*Bs*, YddV and *EcDOS*.

HemAT-*Bs* is a heme-based O₂ sensor protein that acts as a signal transducer for aerotaxis in *Bacillus subtilis*, controlling the organism's movement towards increasing O₂ gradients. We have studied the full length and truncated sensor domain HemAT-CO adducts as well as the Y70F, L92A, T95A and Y133F mutants. The FTIR spectra of wild type HemAT-CO have revealed two conformations of the heme-bound CO at 1967 cm⁻¹ and 1928 cm⁻¹ that are attributed to an “open” and a “closed” conformation, respectively. The perturbation of the $\nu(\text{CO})$ conformations upon mutation of the distal residues Tyr70, Leu92 and the proximal residue Tyr133 reveal the distinct roles of these residues in determining the structure of the heme Fe²⁺-CO complex. Monitoring the rebinding of CO to the heme-Fe²⁺ by TRS² – FTIR spectroscopy ($t_d = 8 \mu\text{s} - \text{ms}$) has revealed biphasic kinetics for both the full length and truncated sensor domain HemAT-*Bs*. These experiments have also allowed us to monitor conformational changes and the perturbation of the heme propionates upon ligand (CO) photodissociation. We propose substantial structural reorientation for B- and G- helices upon CO binding. Moreover, the detection of secondary docking sites in the time-resolved step-scan FTIR experiments ($t_d = 300 \text{ ns}$) of the wild type full length protein and the L92A mutant suggest that Leu92 operates as a conformational gate in the migration pathway of photodissociated CO.

YddV is a heme-bound globin-coupled oxygen sensor protein, found in *E.coli* that regulates the synthesis of second messenger c-di-GMP through diguanylate cyclase activity ultimately leading to biofilm formation. YddV recognizes O₂ and CO and discriminates against other gases such as NO. Time-resolved step-scan FTIR studies of wild type and on the important in the oxygen recognition and stability of the heme Fe(II)-O₂ distal L65T, L65M, Y43W, Y43F and Y43A mutants were performed to determine the site-specific protein dynamics following CO photodissociation. These mutations were designed to perturb the

electrostatic field near the iron bound gaseous ligand (CO), and also to allow us to investigate the communication pathway between the distal residues of the protein with the heme. The TRS²-FTIR spectra show that the heme propionates are in the protonated and deprotonated state. Moreover, the rate of decay of the heme propionates and amide I vibrations are on a time-scale coincident with the rate of rebinding of CO suggesting that there is a coupling between ligation dynamics in the distal heme environment and a) the environment sensed by the heme propionates and b) the protein backbone relaxation. The fast recombination rates in L65M, L65T and Y43W implies significant role of L65 and Y43 in controlling the ligand dynamics. The implications of these results with respect to the role of the heme propionates and the positively charged or proton donating residues in the distal pocket which are crucial for stabilizing the bound gaseous ligands are discussed.

EcDOS (*E.coli* Direct Oxygen Sensor) is a heme- regulated phosphodiesterase (PDE) protein that catalyzes the degradation of 2nd messenger c- di-GMP to linear di-GMP via gas sensing, ultimately altering the bacterium's state from sessile to motile. The FTIR spectra of the wild type protein denote the presence of a "closed" and an "open" conformation of the *EcDOS*-CO complex at 1923 and 1970 cm⁻¹, respectively. The two conformations are largely perturbed upon mutation of distal residues Arg97 and Phe113 suggesting that Arg97 directly interacts through hydrogen bonding with the heme-bound CO, while Phe113 largely controls the hydrogen bonding network near the heme-bound CO. The TRS²- FTIR difference spectra of wild type *EcDOS* upon CO photodissociation at $t_d = 6 \mu\text{s}$ have demonstrated a 55% photoproduct yield, suggesting 45% CO geminate recombination. Monitoring the kinetic evolution of CO-rebinding on the microsecond-millisecond timescale has revealed biphasic kinetics. Upon CO dissociation, we have observed a fast phase ($k_1 = 7267 \text{ s}^{-1}$), while structural reorientation of the heme active site allows rebinding of CO at a slower rate ($k_2 = 186 \text{ s}^{-1}$). The TRS²-FTIR experiments on the CO adduct of the M95A mutant indicate a "binding and replacement" competitive rebinding process between Met95 and CO; dissociation of CO leads to structural reorganization of the heme active site that promotes fast binding of the endogenous ligand (Met95). The effect of the R97A, R97I, F113T, N84V, Y126F, W53F and E93I mutations on the kinetics of CO rebinding and concurrent protein conformational dynamics are discussed.

ACKNOWLEDGEMENTS

The completion of this doctoral thesis wouldn't have been possible without the support of a number of people who made their scientific skills, ideas and above all moral encouragement available to me during the course of my PhD studies.

First and foremost, I would like to thank my supervisor, Assistant Prof. Eftychia Pinakoulaki, whose scientific support and guidance made my thesis work possible. She has been keenly interested in my work and has always been available to advise me. Her encouragement to work independently in the lab has certainly helped me form a stronger character as a young scientist.

I would like to thank Associate Professor Niovi Santama, Associate Professor Marketa Martinkova, Associate Professor Ioannis Paschalidis and Assistant Professor Sophia C. Hayes for accepting the invitation to be members of my examination committee.

I am grateful to our scientific collaborators Prof. Shigetoshi Aono at the Okazaki Institute of Integrative Biosciences, National Institutes for Natural Sciences, Okazaki Japan, Associate Prof. Marketa Martinkova at Charles University, Prague Czech Republic, Prof. Teizo Kitagawa at the Okazaki Institute of Integrative Biosciences, National Institutes for Natural Sciences, Okazaki Japan and their research groups for providing me with the protein samples. Without their contribution, the completion of this doctoral thesis would have been impossible.

I would also like to thank the Cyprus Research Promotion Foundation and the European Structural Funds for financial support (Grant IIIΕ/ΠΙΕΝΕΚ/0609/41) and the University of Cyprus for providing the research facilities.

I want to thank past and present members of the BBC lab, as we liked to call it, Andria Palari and Andreas Loullis for making my time spent in the lab a very pleasant experience. Although the immense amount of beer and take-out food shared with Andreas while pulling all-nighters in the lab have permanently damaged my health, I will always remember these times with a smile. I would also like to thank him for eventually not killing us that night while driving from Los Angeles to San Diego. I will reminisce the ACS conference in San Diego with great joy.

The -3 floor of the Pure and Applied Sciences building of the University of Cyprus has been my "house" for the past 5 years, so I consider it imperative to thank my neighbors and friends, Maria Riala, Charalambos Ioannou, Maria Manoli, Maria Charalambous, Eleni Kyprianidou, Eleni Moushi, Eleni Andreou, Andreas Kourtellaris, Natalia Rizeq, Eleni

Tseriotou and Sofia Alexandrou for the legendary “tsiknopempti” parties, long conversations in the cold and great hazelnut coffee. It has been a pleasure guys.

Finally, special recognition goes out to my family, for their financial support, encouragement and patience during my pursuit of this doctorate degree. To my amazing parents, thank you for believing in me in times of distress and disappointment, and for encouraging me in all of my pursuits. To my husband Alexis, your unremitting patience and support made this long academic journey possible.

Andrea Pavlou

Table of Contents	Page
DECLARATION OF ORIGINALITY	i
ΠΕΡΙΛΗΨΗ	ii
ABSTRACT	v
ACKNOWLEDGEMENTS	vii
TABLE OF CONTENTS	ix
INDEX OF FIGURES	xii
INDEX OF TABLES	xx
INDEX OF ABBREVIATIONS	xxi
CHAPTER 1 : Introduction	1
1.1 Introduction	2
1.2 Objective and Originality of Doctoral Thesis	4
CHAPTER 2 : Heme-based Sensor Proteins: Structure and function	5
2.1 Background on bacterial heme-based sensor proteins	6
2.1.1 Heme-based proteins as sensors for physiological gas molecules	6
2.1.2 O ₂ , NO and CO recognition and discrimination by heme-based gas sensors	7
2.1.3 Heme-based oxygen sensor proteins	9
2.2 Structure and function of heme-based aerotactic transducer HemAT- <i>Bs</i>	11
2.2.1 HemAT: A heme-based oxygen sensor with aerotactic function	11
2.2.2 X-ray crystal structure of the truncated sensor domain of HemAT- <i>Bs</i>	12
2.2.3 Structure and function of the effector domain of HemAT- <i>Bs</i>	14
2.2.4 Spectroscopic studies of heme-based oxygen sensor protein HemAT- <i>Bs</i>	16
2.3 Structure and function of heme-based sensor proteins YddV (or <i>EcDosC</i>) and <i>EcDOS</i> (or <i>EcDosP</i>)	21
2.3.1 Modulation of c-di-GMP metabolism: The <i>yddV-dos</i> bicistronic operon	21
2.3.2 Structure of globin-bound oxygen sensor DGS protein YddV (<i>EcDosC</i>)	23

2.3.3	Spectroscopic studies of globin-bound sensor DGS protein YddV	24
2.3.4	The direct oxygen sensor phosphodiesterase protein <i>EcDOS</i> (<i>EcDosP</i>)	25
2.3.5	X-ray crystal structure of the heme-bound PAS-A sensor domain <i>EcDOSH</i>	26
2.3.6	Spectroscopic studies of Fe(II)-O ₂ and Fe(II)-CO <i>EcDOSH</i>	30
2.3.7	X-ray crystal structure of the catalytic EAL domain of <i>EcDOS</i>	31
CHAPTER 3 : Methodology : FTIR and Time-Resolved Step-Scan FTIR Spectroscopy		42
3.1	Introduction	43
3.2	FTIR Spectroscopy	44
3.2.1	Michelson Interferometer	46
3.1	Time-Resolved Step-Scan FTIR Spectroscopy	50
3.2	Time-Resolved Step-Scan FTIR Spectroscopy Experimental Setup	51
CHAPTER 4 : Materials and Experimental Procedures		54
4.1	Materials	55
4.1.1	Expression and purification of wild type full length and truncated sensor domain forms of HemAT- <i>Bs</i>	55
4.1.2	Design and isolation of full length and truncated sensor domain mutants of HemAT- <i>Bs</i>	55
4.1.3	Expression and purification of wild type heme domain YddV	57
4.1.4	Design and isolation of heme domain mutants of YddV	57
4.1.5	Expression and purification of wild type isolated PAS domain of <i>EcDOS</i>	58
4.1.6	Design and isolation of <i>EcDOS</i> -PAS domain mutants	59
4.1.6	List of chemicals used for the TRS ² - FTIR experiments	59
4.2	Experimental Procedures	60
4.2.1	Time-resolved step-scan FTIR spectroscopy of heme-based sensor proteins	60
CHAPTER 5 : Dynamics of the Signal Transducer Protein HemAT Revealed by Time-resolved Step-scan FTIR Spectroscopy		64
5.1	Introduction	65
5.2	Experimental Procedures	66
5.3	Results	67
5.4	Discussion	79

CHAPTER 6 : Ligand Docking Sites in HemAT-Bs	92
6.1 Introduction	93
6.2 Results and Discussion	94
CHAPTER 7 : Probing the Ligand Recognition and Discrimination Environment of the Globin-coupled Oxygen Sensor Protein YddV (or EcDosC) by FTIR and Time-resolved step-scan FTIR (TRS²-FTIR) Spectroscopy	101
7.1 Introduction	102
7.2 Experimental Procedures	104
7.3 Results and Discussion	105
CHAPTER 8 : Structural Properties and Dynamics of EcDOSH Probed by FTIR and Time-resolved Step-Scan FTIR Spectroscopy	118
8.1 Introduction	119
8.2 Experimental Procedures	121
8.3 Results	122
8.4 Discussion	135
CONCLUSIONS	150
FUTURE WORK	157
APPENDIX	159

Index of Figures	Page
CHAPTER 2 : Heme-based Sensor Proteins: Structure and function	5
Figure 2.1 Schematic representation of the cellular signal transduction system triggered in heme-based gas sensor proteins upon ligand binding.	7
Figure 2.2 X-ray crystal structure of the unliganded sensor domain of HemAT- <i>Bs</i> .	12
Figure 2.3 Superposition of the HemAT- <i>Bs</i> heme active sites of the (A) unliganded and (B) liganded forms of the protein.	13
Figure 2.4 Function of HemAT- <i>Bs</i> as a class IV methyl accepting chemotaxis protein.	14
Figure 2.5 Schematic representation of the proposed two component signaling system in HemAT- <i>Bs</i> .	15
Figure 2.6 Structural representation of the unliganded truncated sensor domain heme active site of HemAT- <i>Bs</i> .	17
Figure 2.7 Structural representation of the position of the proximal residue Tyr133 in the (A) unliganded and (B) CN-bound HemAT- <i>Bs</i> indicating the distance between its side chain and His123.	19
Figure 2.8 Schematic representation of the binding of O ₂ to YddV heme-Fe ²⁺ that initiates intramolecular signal transduction.	23
Figure 2.9 Schematic representation of the catalytic activity of <i>Ec</i> DOS towards the hydrolysis of c-di-GMP to linear -di-GMP (5'pGpG) via phosphodiesterase activity.	26
Figure 2.10 X-ray crystal structures of the (A) Fe(III) and (B) Fe(II) <i>Ec</i> DOS PAS-A domain.	27
Figure 2.11 X-ray crystal structure of the Fe(II)-O ₂ <i>Ec</i> DOS PAS-A domain depicting the two distinct subunits of the dimer.	28
Figure 2.12 Structural representation of the heme active site conformational changes induced to (A) Fe(II) <i>Ec</i> DOS PAS-A signaling domain upon (B) O ₂ binding.	29
Figure 2.13 X-ray crystal structure of the dimeric form of the <i>Ec</i> DOS EAL catalytic domain.	32
Figure 2.14 Illustration of the structural conformations of the flanking PAS-A sensory and EAL catalytic domains in the Fe(II)-O ₂ form of <i>Ec</i> DOS.	33

CHAPTER 3 : Methodology : FTIR and Time-Resolved Step-Scan FTIR Spectroscopy	42
Figure 3.1	Schematic representation of the IR vibrational process. 43
Figure 3.2	Permitted energy levels and transitions in a diatomic molecule that executes simple harmonic motion. 44
Figure 3.3	The fundamental components and the complete path of the radiation beam in a Michelson Interferometer. 47
Figure 3.4	Schematic representation of the phase of the electromagnetic waves from the fixed and translating mirrors of the interferometer at different optical retardation values. 48
Figure 3.5	Schematic representation of the “stepping” process taking place at every data sampling position the interferometer moving mirror is held stationary during a time-resolved step-scan FTIR measurement. 50
Figure 3.6	Schematic representation of a basic time-resolved step-scan FTIR experimental setup. 52
CHAPTER 4 : Materials and Experimental Procedures	54
Figure 4.1	Schematic representation of the unliganded HemAT active site of the truncated sensor domain, along with the proposed mutated residues. 56
Figure 4.2	Proposed heme active site structure of the unliganded Fe(II) YddV based on the structure of the Fe(III)–cyanide complex of HemAT- <i>Bs</i> . 58
Figure 4.3	Schematic representation of the proposed mutated residues of the heme active site of the direct oxygen sensor protein <i>EcDOS</i> in the Fe(II) form with Met95 as the axial ligand. 59
Figure 4.4	Schematic representation of the time-resolved step-scan FTIR experimental setup used for the investigation of heme-based oxygen sensor proteins HemAT- <i>Bs</i> , YddV and <i>EcDOSH</i> . 61

CHAPTER 5 : Dynamics of the Signal Transducer Protein HemAT-<i>Bs</i> Revealed	64
by Time-resolved Step-scan FTIR Spectroscopy	
Figure 5.1	Structural representation of the unliganded truncated sensor domain heme active site of HemAT- <i>Bs</i> . 66
Figure 5.2	FTIR spectra of the HemAT-CO adducts at pH 8. 68
Figure 5.3	Time-resolved step-scan FTIR difference spectra of WT truncated sensor domain HemAT-CO adduct at pD 8, subjected to CO photodissociation at $t_d = 250, 800, \text{ and } 4000 \text{ ns}$. 69
Figure 5.4	(A) Time-resolved step-scan FTIR difference spectra of the wild type truncated sensor domain HemAT-CO adduct at pH 8 from 0.008 to 2.952 ms subsequent to CO photolysis. (B) Plot of the ΔA of the 1967 cm^{-1} mode versus time on a logarithmic scale subsequent to CO photolysis. 70
Figure 5.5	(A) Time-resolved step-scan FTIR difference spectra of the wild type truncated sensor domain HemAT-CO adduct at pD 8 from 0.008 to 3.432 ms subsequent to CO photolysis. (B) Plot of the ΔA of the 1967 cm^{-1} mode versus time on a logarithmic scale subsequent to CO photolysis. 71
Figure 5.6	(A) Time-resolved step-scan FTIR difference spectra of the wild type truncated sensor domain HemAT-CO adduct at pD 8 in the range of $1700\text{-}1500 \text{ cm}^{-1}$ and $t_d = 8 - 3400 \mu\text{s}$. Plot of the ΔA of (B) 1638 cm^{-1} , and (C) 1654 cm^{-1} , protein vibration modes of the truncated sensor domain HemAT-CO adduct at pD 8 versus time on a logarithmic scale subsequent to CO photolysis. 72
Figure 5.7	(A) Time-resolved step-scan FTIR difference spectra of the wild type full length HemAT-CO adduct at pH 8 from 0.008 to 5.432 ms subsequent to CO photolysis. (B) Plot of the ΔA of the 1967 cm^{-1} mode versus time on a logarithmic scale subsequent to CO photolysis. 72
Figure 5.8	(A) Time-resolved step-scan FTIR difference spectra of the wild type full length HemAT-CO adduct at pD 8 from 0.008 to 6.232 ms subsequent to CO photolysis. (B) Plot of the ΔA of the 1967 cm^{-1} mode versus time on a logarithmic scale subsequent to CO photolysis. 73
Figure 5.9	(A) Time-resolved step-scan FTIR difference spectra of the wild type full length HemAT-CO adduct at pD 8 in the range of $1700\text{-}1500 \text{ cm}^{-1}$ and $t_d = 8 - 6232 \mu\text{s}$. Plot of the ΔA of the (B) 1638 cm^{-1} protein vibration mode of the full length HemAT-CO adduct at pD 8 versus time on a logarithmic scale subsequent to CO photolysis. 74

Figure 5.10	Time-resolved step-scan FTIR difference spectra of the wild type full length HemAT-CO adduct at pD 8 in the range of 2000-1850 cm^{-1} / 1750-1560 cm^{-1} and $t_d = 8 - 1104 \mu\text{s}$.	74
Figure 5.11	(A) Time-resolved step-scan FTIR difference spectra of the sensor domain L92A HemAT-CO adduct at pD 8 from 0.008 to 1.794 ms subsequent to CO photolysis. (B) Plot of the ΔA of the 1970 cm^{-1} mode versus time on a logarithmic scale subsequent to CO photolysis.	75
Figure 5.12	(A) Time-resolved step-scan FTIR difference spectra of the sensor domain T95A HemAT-CO adduct at pD 8 from 0.006 to 7.158 ms subsequent to CO photolysis. (B) Plot of the ΔA of the 1965 cm^{-1} mode versus time on a logarithmic scale subsequent to CO photolysis.	76
Figure 5.13	(A) Time-resolved step-scan FTIR difference spectra of the sensor domain Y70F HemAT-CO adduct at pD 8 from 0.008 to 4.712 ms subsequent to CO photolysis. (B) Plot of the ΔA of the 1965 cm^{-1} mode versus time on a logarithmic scale subsequent to CO photolysis..	76
Figure 5.14	(A) Time-resolved step-scan FTIR difference spectra of the sensor domain Y133F HemAT-CO adduct at pD 8 from 0.006 to 4.472 ms subsequent to CO photolysis. (B) Plot of the ΔA of the 1965 cm^{-1} mode versus time on a logarithmic scale subsequent to CO photolysis.	77
Figure 5.15	Time-resolved step-scan FTIR difference spectra of HemAT-CO adducts at pD 8, $t_d = 8$ and 6 μs .	82
Figure 5.16	Schematic representation of the proposed structural reorientation of Tyr70 and its hydrogen bonding interaction with Fe ²⁺ -CO upon CO-binding to the heme-iron.	84
Figure 5.17	Schematic representation of the proposed structural reorientation of Tyr133 and its hydrogen bonding interaction with the N δ H of the trans axial His123 upon CO-binding to the heme-iron.	85
Figure 5.18	Schematic representation of the proposed lateral movement of Leu92 upon CO-binding that blocks water molecules from entering the distal site of the heme pocket.	86
Figure 5.19	Schematic representation of the proposed model describing the conformational motions that take place upon CO binding to HemAT-Bs. homodimer constructed based on the FTIR and time-resolved step-scan FTIR experiments of the current work.	87

CHAPTER 6 : Ligand Docking Sites in HemAT-Bs	92
Figure 6.1	(A) Time-resolved step- scan FTIR difference spectra of the L92A full length HemAT-CO adduct at pD 8 from 0.006 to 600 μ s subsequent to CO photolysis. (B) Plot of the ΔA of the 1970 cm^{-1} mode versus time on a logarithmic scale subsequent to CO photolysis. 94
Figure 6.2	Time-resolved step-scan FTIR difference spectra of the wild type full length HemAT-CO adduct at pD 8 from 300 ns to 6 μ s subsequent to CO photolysis. 95
Figure 6.3	Schematic representation of the photodissociation reaction of wild-type sperm whale MbCO depicting the movement of CO from the bound state A to the primary docking site B, and from there to the secondary docking sites C, and D until it is finally released into the solvent S. 96
Figure 6.4	Plot of the ΔA of the 1967 cm^{-1} mode versus time on a logarithmic scale of the wild type full length HemAT-CO adduct subsequent to CO photolysis during the transient phase $t_d = 1 - 50 \mu$ s. 97
Figure 6.5	Time-resolved step-scan FTIR difference spectra of the L92A full length HemAT-CO adduct at pD 8 from 500 ns to 6 μ s subsequent to CO photolysis. 97
Figure 6.6	Plot of the ΔA of the 1970 cm^{-1} mode versus time on a logarithmic scale of full length L92A HemAT-CO adduct subsequent to CO photolysis during the transient phase $t_d = 1 - 50 \mu$ s.. 98
CHAPTER 7 : Probing the Ligand Recognition and Discrimination Environment of the Globin-coupled Oxygen Sensor Protein YddV (or EcDosC) by FTIR and Time-resolved step-scan FTIR (TRS²-FTIR) Spectroscopy	101
Figure 7.1	Schematic representation of the proposed structure of the CO-bound form of YddV (residues are numbered for YddV), based on the crystal structure of Fe(III)-CN adduct of HemAT-Bs. 105
Figure 7.2	Optical absorption spectra of YddV-heme at pH 8. 106
Figure 7.3	FTIR spectra of the heme domain YddV-CO adducts at (A) pH 8 and (B) pD 8. 108
Figure 7.4	(A) Time-resolved step-scan FTIR difference spectra of the wild type heme domain YddV-CO adduct at pD 8 from 0.006 to 7.398 ms subsequent to CO photolysis. (B) Plot of the ΔA of the 1962 cm^{-1} mode versus time on a logarithmic scale subsequent to CO photolysis. 109

Figure 7.5	(A) Time-resolved step-scan FTIR difference spectra of the wild type heme domain YddV-CO adduct at pD 8 in the range of 1700-1300 cm^{-1} and $t_d = 6 - 7398 \mu\text{s}$. Plot of the ΔA of (B) 1656 cm^{-1} protein vibration mode of the heme domain YddV-CO adduct at pD 8 versus time on a logarithmic scale subsequent to CO photolysis..	109
Figure 7.6	(A) Time-resolved step-scan FTIR difference spectra of the heme domain L65M-CO adduct at pD 8 from 0.006 to 2.238 ms subsequent to CO photolysis. (B) Plot of the ΔA of the 1953 cm^{-1} mode versus time on a logarithmic scale subsequent to CO photolysis.	110
Figure 7.7	(A) Time-resolved step-scan FTIR difference spectra of the heme domain L65T-CO adduct at pD 8 from 0.006 to 1.140 ms subsequent to CO photolysis. (B) Plot of the ΔA of the 1962 cm^{-1} mode versus time on a logarithmic scale subsequent to CO photolysis.	111
Figure 7.8	(A) Time-resolved step-scan FTIR difference spectra of the heme domain Y43A-CO adduct at pD 8 from 0.006 to 9.780 ms subsequent to CO photolysis. (B) Plot of the ΔA of the 1962 cm^{-1} mode versus time on a logarithmic scale subsequent to CO photolysis.	112
Figure 7.9	(A) Time-resolved step-scan FTIR difference spectra of the heme domain Y43F-CO adduct at pD 8 from 0.006 to 3.888 ms subsequent to CO photolysis. (B) Plot of the ΔA of the 1962 cm^{-1} mode versus time on a logarithmic scale subsequent to CO photolysis..	112
Figure 7.10	(A) Time-resolved step-scan FTIR difference spectra of the heme domain Y43W-CO adduct at pD 8 from 0.006 to 4.638 ms subsequent to CO photolysis. (B) Plot of the ΔA of the 1953 cm^{-1} mode versus time on a logarithmic scale subsequent to CO photolysis.	113
CHAPTER 8 : Structural Properties and Dynamics of EcDOSH Probed by FTIR and Time-resolved Step-Scan FTIR Spectroscopy		118
Figure 8.1	Structural representation of the Fe(II) form of the EcDOSH heme active site	119
Figure 8.2	FTIR spectra of the EcDOSH-CO adducts at pD 7.5 and pH 7.5.	123
Figure 8.3	(A) Time-resolved step-scan FTIR difference spectra of the wild type EcDOSH-CO adduct at pH 7.5 from 0.006 to 7.728 ms subsequent to CO photolysis. (B) Plot of the ΔA of the 1970 cm^{-1} mode versus time on a logarithmic scale subsequent to CO photolysis.	125

Figure 8.4	(A) Time-resolved step-scan FTIR difference spectra of the wild type <i>Ee</i> DOSH-CO adduct at pD 7.5 from 0.006 to 11.838 ms subsequent to CO photolysis. (B) Plot of the ΔA of the 1970 cm^{-1} mode versus time on a logarithmic scale subsequent to CO photolysis.	125
Figure 8.5	Time-resolved step-scan FTIR difference spectra of the wild <i>Ee</i> DOSH-CO adduct at pD 7.5 in the range of 1700-1500 cm^{-1} and $t_d = 6, 24, 60, 108, 198, 288, 1000, 3100$ and 1200 μs .	126
Figure 8.6	(A) Time-resolved step-scan FTIR difference spectra of the PAS domain M95A-CO adduct at pD 7.5 from 0.006 to 438 ms subsequent to CO photolysis. (B) Plot of the ΔA of the 1968 cm^{-1} mode versus time on a logarithmic scale subsequent to CO photolysis.	128
Figure 8.7	(A) Time-resolved step-scan FTIR difference spectra of the PAS domain R97A-CO adduct at pD 7.5 from 0.006 to 10.398 ms subsequent to CO photolysis. (B) Plot of the ΔA of the 1972 cm^{-1} mode versus time on a logarithmic scale subsequent to CO photolysis.	129
Figure 8.8	(A) Time-resolved step-scan FTIR difference spectra of the PAS domain R97I-CO adduct at pD 7.5 from 0.006 to 114 ms subsequent to CO photolysis. (B) Plot of the ΔA of the 1972 cm^{-1} mode versus time on a logarithmic scale subsequent to CO photolysis.	129
Figure 8.9	(A) Time-resolved step-scan FTIR difference spectra of the PAS domain F113T-CO adduct at pD 7.5 from 0.006 to 11.748 ms subsequent to CO photolysis. (B) Plot of the ΔA of the 1965 cm^{-1} mode versus time on a logarithmic scale subsequent to CO photolysis.	130
Figure 8.10	(A) Time-resolved step-scan FTIR difference spectra of the PAS domain Y126F-CO adduct at pD 7.5 from 0.006 to 13.278 ms subsequent to CO photolysis. (B) Plot of the ΔA of the 1967 cm^{-1} mode versus time on a logarithmic scale subsequent to CO photolysis.	130
Figure 8.11	(A) Time-resolved step-scan FTIR difference spectra of the PAS domain N84V-CO adduct at pD 7.5 from 0.006 to 6.438 ms subsequent to CO photolysis. (B) Plot of the ΔA of the 1967 cm^{-1} mode versus time on a logarithmic scale subsequent to CO photolysis.	131
Figure 8.12	(A) Time-resolved step-scan FTIR difference spectra of the PAS domain W53F-CO adduct at pD 7.5 from 0.006 to 9.438 ms subsequent to CO photolysis. (B) Plot of the ΔA of the 1967 cm^{-1} mode versus time on a logarithmic scale subsequent to CO photolysis..	132

Figure 8.13	(A) Time-resolved step-scan FTIR difference spectra of the PAS domain W53F-CO adduct at pD 7.5 from 0.006 to 9.438 ms subsequent to CO photolysis. (B) Plot of the ΔA of the 1967 cm^{-1} mode versus time on a logarithmic scale subsequent to CO photolysis.	132
Figure 8.14	TRS2 - FTIR difference spectra subsequent to CO-photodissociation at $t_d = 6\ \mu\text{s}$ and pD 7.5 of <i>Ec</i> DOSH-CO adducts.	134
Figure 8.15	Superposition of chain A and B of Fe(II) <i>Ec</i> DOSH heme active site (grey) over chain A and B Fe(II)-O ₂ <i>Ec</i> DOSH heme active site (blue).	140
Figure 8.16	Schematic representation of the hydrogen bonding network between F113 located on the H _{β} sheet and G94 located on the rigid FG loop through a water molecule and L115, formed in the Fe(II) <i>Ec</i> DOSH (A) and its cleavage upon oxygen binding (B).	144

Index of Tables	Page
CHAPTER 2 : Heme-based Sensor Proteins: Structure and function	5
Table 2.1 Organization of identified heme-based gas sensor proteins based on their structure and function.	9
CHAPTER 5 : Dynamics of the Signal Transducer Protein HemAT Revealed by Time-resolved Step-scan FTIR Spectroscopy	64
Table 5.1 Summary of estimated % photoproduct yield at $t_d = 6 \mu s$, as well as calculated constants and amplitude for each of the CO-rebinding phases for the wild type and mutant HemAT-CO adducts.	78
CHAPTER 7 : Probing the Ligand Recognition and Discrimination Environment of the Globin-coupled Oxygen Sensor Protein YddV (or EcDosC) by FTIR and Time-resolved step-scan FTIR (TRS²-FTIR) Spectroscopy	101
Table 7.1 Summary of the calculated CO rebinding constants as well as % photolysis for the wild type and mutant YddV-CO adducts.	113
CHAPTER 8 : Structural Properties and Dynamics of EcDOSH Probed by FTIR and Time-resolved Step-Scan FTIR Spectroscopy	118
Table 8.1 Summary of estimated % photoproduct yield at $t_d = 6 \mu s$ as well as calculated constants and amplitude for each of the CO-rebinding phases for the wild type and mutant EcDOSH-CO adducts.	133

Index of Abbreviations

AC	Alternate Current Optical Measurements
AfGcHK	Globin-coupled histidine kinase from <i>Anaeromyxobacter</i> sp.
AvGReg	Globin-coupled oxygen-sensor with DGC activity from <i>A. vinelandii</i>
BpeGReg	Globin-coupled oxygen-sensor with DGC activity from <i>B. pertussis</i>
c-AMP	Cyclic Adenosine Monophosphate
GCS	Globin-coupled Sensor
GDDEF domain	Gly-Gly-Asp-Glu-Phe protein effector domain
c-di-GMP	Cyclic Diguanosine Monophosphate
GsGCS	Heme-bound globin-coupled Sensor from <i>G. sulfurreducens</i>
GTP	Guanosine Triphosphate
CT	Charge Transfer
DC	Direct Current Optical Measurements
DGC	Diguanylate Cyclase
EcDOS	<i>E.coli</i> Direct Oxygen Sensor
EcDOSH	Isolated heme PAS sensor domain of <i>EcDOS</i> protein from <i>E.coli</i>
FixL	Heme-bound oxygen-sensor histidine kinase that regulates nitrogen fixation in <i>R. meliloti</i> or <i>B. japonicum</i>
FTIR	Fourier-Transform Infrared Spectroscopy
Hb	Hemoglobin

HemDGC	Globin-coupled oxygen-sensor with DGC activity from <i>D psychrophila</i>
heme-Fe(III)	Protoporphyrin IX-ferric Complex
heme-Fe(II)	Protoporphyrin IX-ferrus Complex
HemAT-Bs	Heme-based Aerotactic Transducer from <i>B.subtilis</i>
HemAT- Hs	Heme-based Aerotactic Transducer from <i>H. salinarum</i>
HemAT-Bh	Heme-based Aerotactic Transducer from <i>B. halodurans</i>
l-di-GMP	Linear Diguanosine Monophosphate (pGpG)
Mb	Myoglobin
MCP	Methyl-accepting Chemotaxis Protein
MCT	Mercury Cadmium Telluride detector
Nd:YAG	Neodymium-Doped Yttrium Aluminium Garnet (Nd:Y ₃ Al ₅ O ₁₂) a crystal used as a lasing medium for solid-state lasers.
PAS domain	Acronym of Per (<i>Drosophila</i> period clock protein)-Arnt (vertebrate aryl hydrocarbon receptor nuclear translocator)-Sim (<i>Drosophila</i> single-minded protein) protein domain
PDE	Phosphodiesterase
RMS	Root Mean Square
RR	Resonance Raman Spectroscopy
sGC	Soluble guanylate cyclase is a key enzyme in the nitric oxide signalling pathway
S_wMb	Sperm whale Myoglobin
TR³	Time-resolved Resonance Raman Spectroscopy
TRS²-FTIR	Time-resolved Step-Scan Fourier-Transform Infrared Spectroscopy

Tsr	Methyl-accepting chemotaxis protein I from <i>E.coli</i>
TTL	Transistor-Transistor-Logic Digital Pulse
UVR	Ultraviolet Resonance Raman Spectroscopy
YddV	Heme-based oxygen sensor diguanylate cyclase from <i>E. coli</i>

Andrea Pavlou



CHAPTER 1

Introduction

Andrea Pavlou

1.1 Introduction

In a great variety of organisms throughout all kingdoms of life, the heme-based-sensor proteins are the key regulators of adaptive responses to fluctuating oxygen (O₂), carbon monoxide (CO), and nitric oxide (NO) levels.¹⁻³ These signal transducers achieve their responses by coupling a regulatory heme-binding domain (sensor domain) to a neighboring transmitter (effector domain). The past decade has witnessed an explosion in the numbers of these modular sensory proteins known, from just two recognized members, FixL and soluble guanylyl cyclase (sGC), to four broad families comprising of more than fifty sensors. The heme-containing sensor domain detects the presence of the gaseous ligand by coordination to the iron atom, and then transmits the conformational changes induced by ligand binding to the effector domain. The transmitters include histidine protein kinases, cyclic nucleotide phosphodiesterases, chemotaxis methyl-carrier protein receptors, and transcription factors of the basic helix-loop helix and helix-turn-helix classes.² Our understanding of how the chemoreceptors detect external molecules and transmit signals to their regulatory proteins is limited. While most enzymes recognize their cognate substrates on the basis of size, shape, and charge, this challenge is made more difficult for heme proteins sensors, because the ligand they must discriminate, O₂, CO, and NO are nearly the same size and shape.

The molecular mechanisms and the origin of the ligand specificity of the signal transduction of the heme-based gas sensors are open questions. To understand the appearance of such specificity, we have focused our attention on the gas-protein interactions of HemAT (Heme-based Aerotactic Transducer) a heme-based O₂ sensor responsible for aerotaxis, as well as globin-coupled diguanylate cyclase YddV and *E.coli* direct oxygen sensor *EcDOS*, which regulate the intracellular amounts of c-di-GMP in some bacteria and archaea. HemAT-*Bs* controls the movement of *B.subtilis* towards increasing O₂ gradients. Sequence analysis revealed a sensor domain with globin arrangement located in the amino (N)-terminus with limited homology to sperm whale myoglobin (*SwMb*), as well as an effector domain located in the carboxyl (C)-terminus with MCP (methyl-accepting chemotaxis protein) structural arrangement, demonstrating 30% homology to the *E.coli* MCP cytoplasmic protein Tsr. Based on its genetic organization HemAT-*Bs* is termed as a globin-coupled methyl-accepting chemotaxis sensor protein. Its globin-coupled sensor domain contains a heme group, allowing HemAT-*Bs* to bind reversibly small diatomic gas molecules such as O₂, CO and NO to

initiate signal transduction. Nonetheless, up until now, no specific facilitation of the protein's aerotaxis function by either CO or O₂ binding has been clearly depicted, presumably due to the fact that unlike other gas sensor proteins no exclusive substrate of the HemAT-*Bs*-regulated reaction has been acknowledged. Hence, the HemAT-*Bs* active / inactive species cannot be unambiguously defined. The other two enzymes of interest, *EcDOS* and *YddV*, are encoded as a stable protein complex by the *yddV-dos* bicistronic operon in *E.coli*. The biosynthetic globin-coupled sensor *YddV*, displaying diguanylate cyclase activity (DGC) and the degradative PAS-containing sensor *EcDOS* displaying phosphodiesterase activity (PDE), regulate the c-di-GMP overproduction in response to environmental signals. Synthesis and degradation of c-di-GMP are triggered by initial signals such as phosphorylation, light illumination and gas binding. In turn, increased or decreased concentrations of c-di-GMP regulate functions such as motility, virulence, biofilm formation etc. Although termed oxygen sensors, *EcDOS* and *YddV* appear to be less selective compared to other heme-based oxygen sensor proteins. Therefore, we consider it imperative to investigate the structure-function properties of these enzymes upon ligand-binding.

To gain insight into the mechanism of ligand recognition and discrimination, its dynamical aspects, and the underlying mechanism of signal transduction we have applied the structure-sensitive FTIR and time-resolved step-scan FTIR spectroscopy on the wild type as well as specific mutations of full length and truncated sensor domain HemAT-*Bs*, *YddV* heme domain and *EcDOS* heme domain, that have been designed to perturb the electrostatic field near the heme-bound gaseous ligand (CO). Time-resolved step-scan FTIR is a form of difference spectroscopy. Hence, the time-resolved spectra contain only the vibrations arising from the intermediates and vibrations from protein groups that participate in the reaction/process and allow for accurate observation of the dynamics of protonation and protein backbone conformation changes throughout the ligand dissociation and rebinding process of the three oxygen sensor proteins. In addition, amino acids that are suspected to participate in the function of the protein can be identified by combination of site-directed mutagenesis with TRS²-FTIR. The experiments of the current doctoral thesis have principally focused on photodissociation studies of the CO-adducts of HemAT-*Bs*, *YddV*-heme and *EcDOS*H and observation of transient species on the ns to ms time-scales, providing valuable information that are essential in elucidating the initial steps of their intramolecular signal transduction mechanism. It is notable to mention that the time-resolved step-scan FTIR measurements in the ns to μ s time-scale have allowed us to identify transient binding sites and internal cavities that may serve as a local storehouse for ligands near the active site, thereby

increasing the effective concentration of the ligand by many times. The identification of internal cavities and their potential fields can serve as the means for determining the discrimination in favor or against ligand binding.

1.2 Objective and Originality of Doctoral Thesis

Taking all the above information into consideration, the research objective of the current doctoral thesis is the investigation of the ligand recognition and discrimination mechanism that triggers a conformational switch for signaling in three gas sensor proteins, heme-based aerotactic transducer HemAT-*Bs*, globin-coupled diguanylate cyclase YddV, and *E.coli* direct oxygen sensor *EcDOS*, with the use of FTIR and time-resolved step-scan (TRS²) - FTIR. In an effort to better comprehend the above-mentioned mechanism, particular attention has been given to the identification of the structural and dynamic properties of the three gas sensor proteins brought upon CO-photodissociation and rebinding. The originality of the current project lies in the use of time-resolved step-scan (TRS²) – FTIR in the ns to ms time-scales to monitor the dynamics of protonation and protein backbone conformation changes induced to heme-based gas sensor proteins upon ligand dissociation/rebinding for the first time. The pronounced sensitivity to structural conformational changes, the high spectral resolution as well as the significant range of time resolved analysis for the time-dependent experiments displayed by the latter spectroscopic method, rendered it a particularly effective technique in such studies, allowing the detection of transient conformational changes even at the level of single protein residue.

1.3 References

1. R. Jain, M. K. Chan, *J. Biol. Inorg. Chem.* **2003**, *8*, 1-11.
2. M. A. Gilles-Gonzalez, G. Gonzalez, *J. Inorg. Biochem.* **2005**, *99*, 1-22.
3. S. Aono, *Dalton Trans.* **2008**, *24*, 3137-3146.
4. J. Changeux, S. J. Edelstein, *Science* **2005**, *308*, 1424 -1428.



CHAPTER 2

Heme-based Sensor Proteins: Structure and function

Andrea Pavlou

2.1 Background on bacterial heme-based sensor proteins

2.1.1 Heme-based proteins as sensors for physiological gas molecules

Sensing and responding to fluctuations in the contiguous environment is fundamental for all living organisms to preserve their existence and growth. In bacteria, the need for maintaining cellular homeostasis so as to preserve the survival of the organism, stirred these microorganisms to develop and perfect an array of biochemical regulatory systems. These systems help cells to sense and respond to their environment by detecting external chemical and physiological stimuli and in turn, trigger the appropriate internal responses such as cell motility, gene expression and / or enzymatic activity.¹ Such vital systems are regulated by a specific group of sensor proteins, termed heme sensor proteins. They are essentially multi-domain proteins responsible for the cellular adaptive responses to environmental changes. The signal transduction is facilitated by the sensing ability of the heme-bound sensor domain, which propagates a utilizable signal to the equivalent effector or signaling domain, responsible for providing an adaptive response.^{2,3,4}

Each heme sensor protein possesses distinct structural and physiological features. However, they all follow certain primary principles concerning ligand sensing and binding to heme iron. According to Gonzalez *et al.*,⁵ for a sensor protein to be effective, it should retain some specific characteristics. Efficient sensor proteins should be able to detect their true signal and adopt a mechanism that would exclude other signals. In addition, they should successfully switch on or off an activity when they come across a true signal, and also be in a position to discriminate against false signals by initiating mechanisms such as poor binding or non-effective switching, that result in inactivity if physiologically necessary.⁴ For heme sensor proteins the above translates to a heme group incorporated into a hydrophobic pocket to remain active. Alterations in the redox state, along with ligand binding, cause structural rearrangements so as for the true signal to be recognized and discriminated from false signals.^{5,6,7} Due to their structure, which consists of more than one functional domains (sensor and effector domains), these conformational changes can be communicated through the protein moiety and cause modulation of activity.

Recent studies have indicated that heme-based sensor proteins demonstrate a novel biological function as sensors for physiological gas molecules such as O₂, NO and CO.⁸ Specifically, it has been observed that by sensing diatomic gases O₂, CO, and NO heme

proteins are able to regulate fundamental physiological functions, including respiration, O₂ transport and storage, vasoregulation, neuronal function, transcriptional control, and heme degradation⁹. These gas molecules can act as signaling molecules for the regulation of biological signal transduction systems, in which the sensor domain senses the gaseous ligand and then regulates the biological process of the effector domain through an intra-molecular signal transduction between the sensor and effector domains (**Figure 2.1**).^{5,10} To do so, heme-based gas sensor proteins utilize a sensor domain-bound heme group to effectively bind O₂, CO and NO; as O₂ and CO cannot bind to the protein directly, the gaseous ligand binds to the heme iron. The heme iron, assisted by the protein environment consists the epicenter of protein activity. Specifically, in heme-based gas sensor proteins, the heme group is typically concealed in a structure formed by the peptide chain of the enzyme. The peptide chain together with certain amino acid residues, transiently open channels for the appropriate gaseous ligand to bind to heme iron and initiate protein activity.¹¹

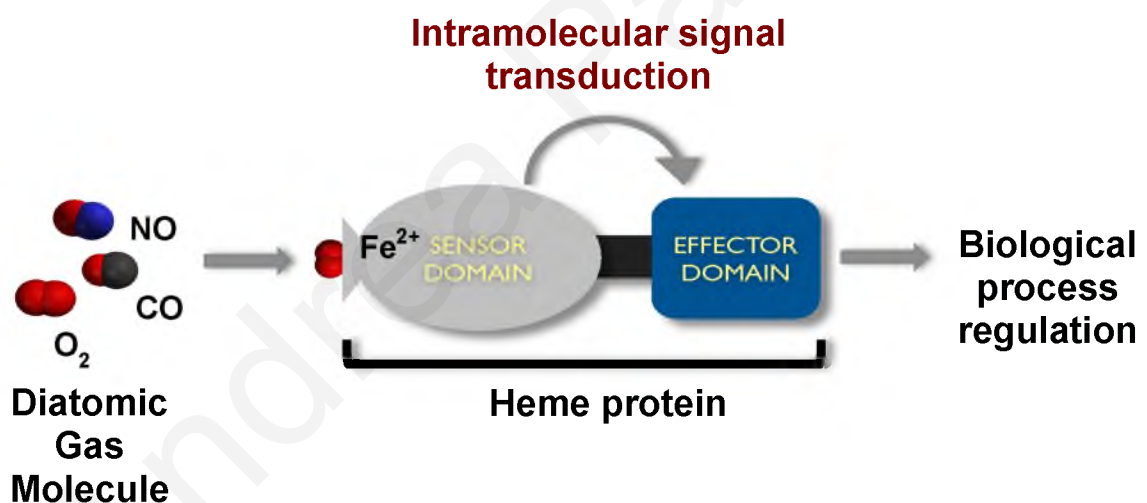


Figure 2.1 Schematic representation of the cellular signal transduction system triggered in heme-based gas sensor proteins upon ligand binding. When diatomic gases bind to the sensor domain, conformational changes are induced in the N-terminus sensor domain. In turn, these changes are transmitted via intramolecular signal transduction to the C-terminus effector domain, allowing the regulation of the appropriate biological process.

2.1.2 O₂, NO and CO recognition and discrimination by heme-based gas sensors

Heme-based gas sensor proteins are categorized into subgroups depending whether

they are activated by O₂, NO or CO. They differ from gas transporting enzymes and catalysts of oxygen-atom and electron transfer reactions, as their effector domains usually have the ability to transmit intracellular signals to non-heme proteins such as protein-histidine kinase, serine-threonine kinase, cyclic-dinucleotide phosphodiesterase, nucleotide cyclase, chemotaxis receptors, and DNA-binding transcription-factors.⁹ The recognition and discrimination between O₂, NO and CO is a difficult task for a heme-based gas sensor protein involving highly developed molecular mechanisms, as these diatomic gas molecules are very similar in size, shape and polarity. Some heme-based gas sensor proteins retain the ability to bind more than one of the diatomic gas molecules. However, as only one of them is actively switching “on” the signal transduction system, the implementation of such molecular mechanisms for gas recognition and discrimination is critical.⁷ In general, binding of O₂, NO and CO to a heme protein is a four step process. It involves the (1) displacement of endogenously bound ligands to create an open or “empty” distal pocket followed by (2) ligand movement into the protein to form an intermediate in which the gas is trapped in the active site near the heme group, (3) bond formation with the iron atom and finally (4) the stabilization of the bound ligand by electrostatic interactions.^{9,12} In the first step, a negative mechanism is created so as to control the affinity of the ligands. During the second step, a transition state is formed where the ligand is weakly non-covalently bound near the active site of the protein. Because as stated earlier diatomic gases are very much alike in size shape and polarity contrary to substrates, the first two steps in ligand binding to heme proteins are not sufficient in discriminating between the three gases at ambient conditions. In the third and fourth step, difference in heme binding affinity is clearer, where selectivity arises at the level of the covalent heme Fe-ligand complexes, since the three gaseous ligands demonstrate significantly different bond strengths and electrostatic properties. O₂, NO and CO interrelate with the heme pocket through distinct interactions with charged side chains or hydrogen bonding networks.¹³ Therefore, it is these hydrogen bonding networks and electrostatic interactions that are unique for each gaseous ligand, eventually exerting significant contribution in their recognition and discrimination. Such interactions ultimately determine the reactivity and functionality of the various heme-based gas sensor proteins.

Four main families of heme-based gas sensor proteins have been identified until now, which have been organized based on structural architecture and ligand binding properties of their sensor domains. More precisely, they have been organized as (a) heme-binding PAS domain, (b) CO-sensitive carbon monoxide oxidation activator, (c) heme NO-binding domain, and (d) globin-coupled sensor proteins.¹³ They are further distinguished based on the function

and resulting activity of their effector domain as (i) sensors with aerotactic function, (ii) sensors with gene-regulating function, and (iii) sensors with c-di-GMP catalytic function.¹⁴ Representatives of each family of heme-based gas sensor proteins are summarized in **Table 2.1**.

Sensor protein	Effector	Prosthetic Group	Function
FixL	O ₂	Heme b	Sensor kinase in FixL/FixJ two component system
HemAT	O ₂	Heme b	Signal transducer for aerotaxis
EcDOS	O ₂	Heme b	Phosphodiesterase activity for c-di-GMP
YddV	O ₂	Heme b	Diguanylate cyclase activity for c-di-GMP
AxPDEA1	O ₂	Heme b	Transcriptional regulator
FNR	O ₂	Fe-S cluster	Transcriptional regulator
sGC	NO	Heme b	Guanylate cyclase
CooA	CO	Heme b	Transcriptional regulator
NPAS2	CO	Heme bCu(i)	Transcriptional regulator

Table 2.1 Organization of identified heme-based gas sensor proteins based on their structure and function. Table constructed with information from Ref 15

2.1.3 Heme-based oxygen sensor proteins

As illustrated in **Table 2.1**, heme proteins that recognize and discriminate O₂, comprise the most distinct and thoroughly investigated group of signal transducers. The oxygen molecule is amid the most prolific gas molecules in the environment, rendering it essential for an abundance of physiological functions with much different properties from those of NO and CO. The levels of molecular oxygen began rising in the Earth's atmosphere roughly two billion years ago. Its increased concentration threatened the homeostasis of anaerobes but at the same time allowed the adaptation to aerobic respiration, which offered better energy conservation.¹⁴ Henceforth, the capability to sense environmental O₂ developed to an important function for many bacteria, both for conserving valuable energy and retaining their homeostasis. For example, hypoxic conditions serve as an external stimulus for certain bacteria to change to a more viable lifestyle. Therefore, they possess the capacity to adjust to changes in O₂ availability by expressing distinctive groups of genes that are transcriptionally controlled by heme-based O₂-sensor proteins.^{2,16,17}

Considering the latter evolutionary facts, heme-based O₂-sensor proteins are indeed physiologically important in living organisms and particularly prokaryotes. Oxygen sensing mechanisms by these enzymes are distinguished into two principal categories. The first mechanism is driven by the thermodynamic properties of O₂, to affect oxygen atom transfer-dependent changes in protein structural architecture and conformation. The second mechanism relies on reversible O₂ binding and the capability to propagate the free energy change related to the formation or breaking of the Fe–O₂ bond to initiate conformational changes of the protein.¹⁸⁻²⁰ It is exactly this ability of diatomic oxygen to form a reversible Fe–O₂ bond that is utilized by heme-based oxygen sensor proteins to detect O₂ and switch between active and inactive forms, that is investigated in the current PhD thesis.

Two of the most well-characterized prokaryotic oxygen sensor enzymes are *EcDOS* from *Escherichia coli*^{21,22} and *HemAT-Bs* from *Bacillus subtilis*.^{23,24} The heme-binding domain of *EcDOS* possesses a PAS (Per-Arnt-Sim) protein fold,²⁵ whereas the sensor domain of *HemAT-Bs* demonstrates globin folding.²⁶ The globin fold is successful at protecting the heme iron from rapid oxidation and at the same time permits reversible O₂ binding, while PAS domains are adept in accepting an array of external input stimuli as well as having the capability of reversibly binding oxygen when the domain is heme-bound.^{12,27,28} In terms of function, *EcDOS* is a phosphodiesterase (PDE) that catalyzes the degradation of c-di-GMP, and *HemAT-Bs* is an aerotactic transducer responsible for cell motility towards more favorable oxygen conditions. Accordingly, the O₂ recognition and discrimination as well as the intramolecular signal transduction mechanisms utilized by each of the two heme-based oxygen sensors should be significantly different from each other and their investigation should serve as a model for understanding the structure-function relationship for both GCS and PAS-bound proteins. Recently, a new heme-based oxygen sensor protein has been identified and named YddV, as per the gene that it is encoded from. The sensor domain of YddV demonstrates globin folding, while its effector domain demonstrates diguanylate cyclase activity towards the synthesis of c-di-GMP.²⁹⁻³¹ Interestingly, although YddV contains a GCS sensor domain with significantly different structural architecture from PAS-bound *EcDOS*, it also utilizes O₂ as an effector molecule for c-diGMP-dependent signal transduction in bacteria. Therefore, it would be of particular importance to observe how the intracellular concentrations of the same molecule (c-di-GMP) can be regulated by two structurally different proteins.

2.2 Structure and function of heme-based aerotactic transducer HemAT-Bs

2.2.1 HemAT : A heme-based oxygen sensor with aerotactic function

Proteins termed aerotactic sensors are responsible for sensing changes in the intracellular amounts of carbon monoxide, nitric oxide or oxygen and initiating an array of intra- and inter-molecular signal transduction processes, that modulate the flagellar rotation motor switch. When the flagellar motor is activated, bacterial swimming behavior is altered. In the context of this doctoral thesis, an aerotactic sensor is designated as a molecular oxygen sensor. For example, the organism can move towards an environment with increased oxygen gradients and demonstrate aerophilicity or it can move away and demonstrate aerophobicity.³²⁻³⁵ Aerotaxis is a crucial biological process for bacteria, as their ability to rapidly sense and respond to fluctuating O₂ levels, allows them to retain their homeostasis. Until now, the only identified representatives of this class of proteins are the heme-based aerotactic transducers, known as HemATs. HemAT (Heme-based Aerotactic Transducer) is a heme-based sensor protein that is responsible for aerotaxis in bacteria. Three homologues of the protein were discovered by Hou *et al.*, thirteen years ago in three different bacteria, *Halobacterium salinarum* (HemAT-*Hs*), *B. subtilis* (HemAT-*Bs*), and *Bacillus halodurans* (HemAT-*Bh*).^{23,36} Although structurally homologous, HemAT-*Bs* and HemAT-*Hs* display counter aerotactic function as the protein demonstrates negative aerotaxis in *H. salinarum* and positive aerotaxis in *B. subtilis*.³⁶ HemAT is the most expressed chemoreceptor in *B. subtilis*, with about 19,000-3900 copies per cell.³⁷

As previously cited, HemAT-*Bs* controls the movement of *B. subtilis* towards increasing O₂ gradients. Sequence analysis revealed a sensor domain with globin arrangement located in the amino (N)-terminus spanning amino acids 1-175 with limited homology (15%) to sperm whale myoglobin (*SwMb*), as well as an effector domain located in the carboxyl (C)-terminus with MCP (methyl-accepting chemotaxis protein) structural arrangement, covering amino acids 198–432 and demonstrating 30% homology to the *E. coli* MCP cytoplasmic protein Tsr.^{23,36} Based on its genetic organization HemAT-*Bs* is termed as a globin-coupled methyl-accepting chemotaxis sensor protein. Its globin-coupled sensor domain contains a heme group, allowing HemAT-*Bs* to bind reversibly small diatomic gas molecules such as O₂, CO and NO to initiate signal transduction, demonstrating however, increased affinity for molecular oxygen.^{24,38} The HemAT homologous protein found in *Halobacterium salinarum*

is the first myoglobin-like protein found in Archaea and it is speculated to be the evolutionary origin of Mb.^{26,36} Therefore, it is projected for HemAT-*Bs* to bind to oxygen in a manner analogous to Mb, causing conformational changes to the N-terminal sensor domain that forward structural information to the C-terminal effector domain.³⁹

2.2.2 X-ray crystal structure of the truncated sensor domain of HemAT-*Bs*

A decade ago, Zhang and Phillips resolved the crystal structures of the truncated sensor domain HemAT-*Bs* in the CN-bound and unliganded forms. They have revealed a homodimeric sensor domain with a classic globin-coupled sensor (GCS) structural motif.^{26,36} The dimer is characterized by an antiparallel four-helical bundle formed by helices G and H as a core, with the rest of the helices closely surrounding the core. Each subunit preserves a classic globin helix arrangement, with the helices named according to classic GCS nomenclature: A, B, C, E, F, G, and H. The truncated sensor domain of HemAT-*Bs* has an extra helix at the N-terminus, named Z helix, and is missing a D helix found in other GCS (**Figure 2.2**). Each of the monomers (subunits I & II) contain a heme group. Circular dichroism confirmed the above structure with results indicating a primarily α -helical motif.

26,36

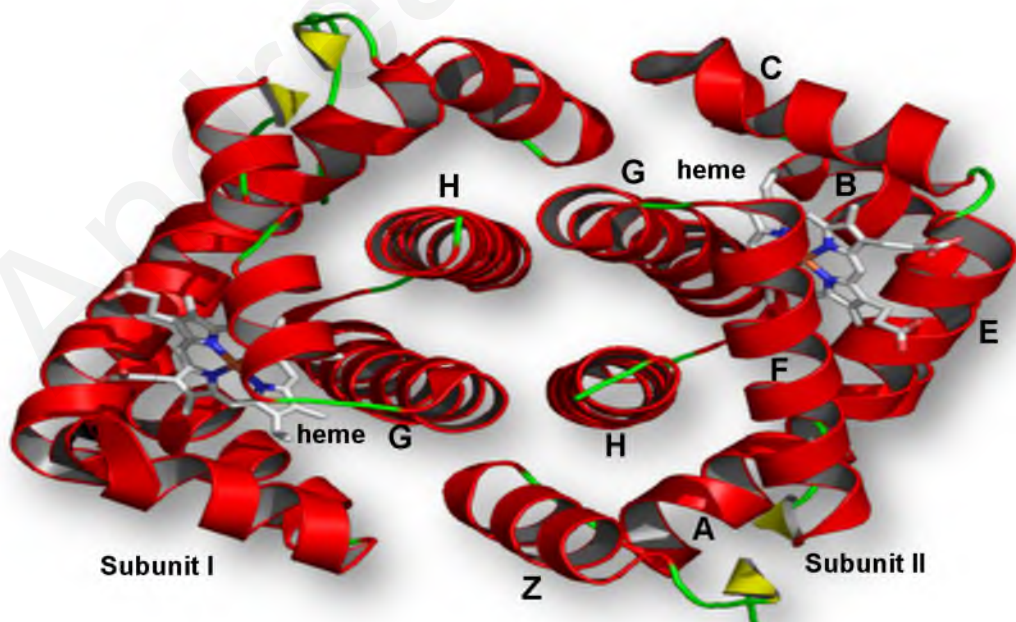


Figure 2.2 X-ray crystal structure of the unliganded sensor domain of HemAT-*Bs*. The homodimer forms a four-helical bundle as a core and each subunit contains a heme group (PDB ID 1OR6).

The two subunits of the liganded form appear to have symmetric structures. It has been observed, however, that asymmetry of the HemAT-*Bs* structure increases when switching from the liganded to the unliganded form.²⁶ Specifically, super-positioning subunit I over subunit II for both the liganded and the unliganded forms, indicates a more asymmetric structure for the unliganded HemAT-*Bs* compared to the liganded form, with the calculated root-mean-square (RMS) for the unliganded form being twice as for the liganded (**Figure 2.3**). Comparing the two subunits of the unliganded form, it is evident that symmetry disruption in HemAT-*Bs* is predominantly caused by a unique conformational change in subunit II involving an outward and upward movement of the distal site residue Tyr70 away from the heme iron atom. This suggests that the two subunits undergo different structural reorganization upon shifting from the liganded to the unliganded form.^{26,36}

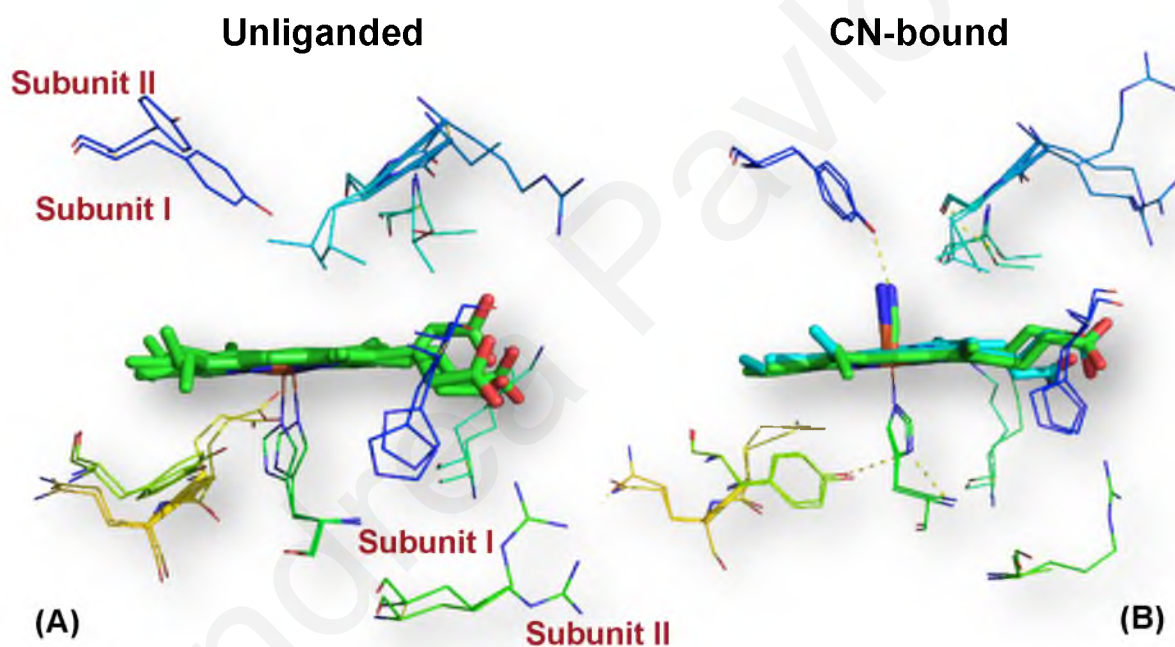


Figure 2.3 Superposition of the HemAT-*Bs* heme active sites of the (A) unliganded and (B) liganded forms of the protein, indicating an asymmetric unliganded form compared to the liganded (PDB IDs 1OR6 & 1OR7).

Asymmetry between subunits in the unliganded form was also evident from the helical movements of each subunit. The H and G helices located in the core of the dimer show slight displacement in subunit II compared to subunit I.^{26,36} Specifically a distinct upward movement was observed for H helix and a downward movement for G helix in subunit II while no movement of either was detected in subunit I. Based on the latter observations, Zhang and Phillips proposed a signal transduction mechanism, where the unliganded form is presumably energetically unfavorable. Upon diffusion of molecular oxygen from the environment into the protein's cytoplasm, O₂ binds to the heme-Fe(II) of one of the subunits

of the homodimer. The binding of O₂ switches the state of the subunit to “energetically favorable” and thus, it experiences distinct conformational changes. These conformational changes in one subunit, however, diminish O₂ affinity of the second subunit, consequently displaying negative cooperativity and allowing for partially liganded HemAT-*Bs* to exist. As the organism travels through the oxygen-rich environment, O₂ concentration increases gradually until it saturates the second subunit. Hence, negative cooperativity could increase the responsiveness of HemAT-*Bs* to a range of oxygen concentrations.²⁶

2.2.3 Structure and function of the effector domain of HemAT-*Bs*

Very little information is known about the effector (signaling) domain of HemAT-*Bs*, and until now it was rendered impossible to resolve its structure. Because of its homology however to the *E.coli* chemoreceptor protein Tsr, HemAT-*Bs* has been categorized as a methyl-accepting chemotaxis protein (MCP).³⁶ It is further classified as a sensory Class IV MCP due to being entirely cytoplasmic, thus lacking any transmembrane helices. Despite the absence of a transmembrane domain, HemAT-*Bs* has been shown to bundle at the cell poles along with other transmembrane chemoreceptors.³⁷ HemAT-*Bs* appears unique when compared to other MCP proteins, as no third domain, a HAMP linker region usually located between the sensor and effector domain, has been definitively identified to date. Therefore, it is possible that the the input signal sensed in the sensor domain is directly propagated to the effector domain (**Figure 2.4**).^{36,40,41}

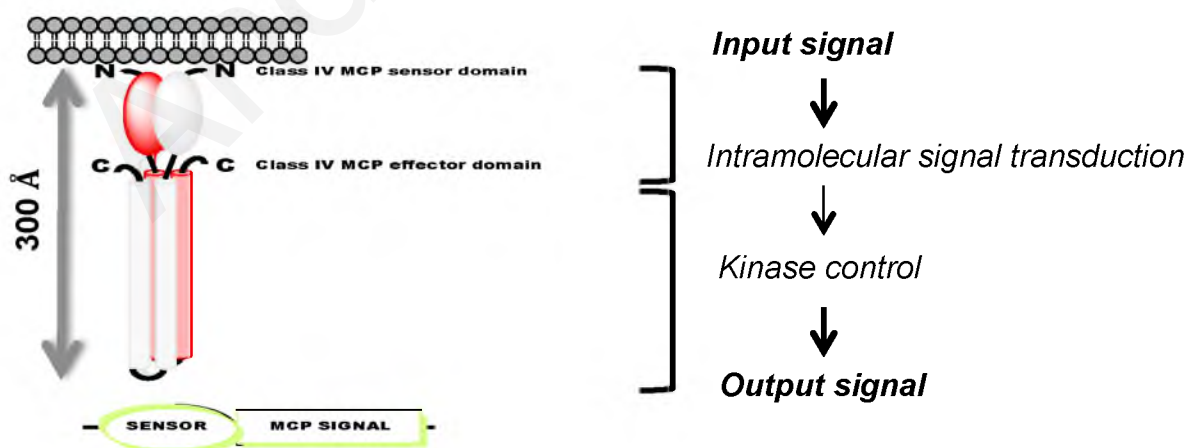


Figure 2.4 Function of HemAT-*Bs* as a class IV methyl accepting chemotaxis protein.

Because of the structural architecture of its effector domain, it is speculated that HemAT-*Bs*

adopts a similar to *E.coli* chemoreceptor proteins, two component signaling system, to propagate the input signal and control the flagellar rotation motor switch. The two component signaling system in *E.coli* chemoreceptor proteins includes two conserved components, a histidine kinase and a response regulator protein.^{40,41} The histidine kinase protein (CheA) is able to autophosphorylate itself by receiving an intra-molecular signal from the sensor domain assisted by CheW protein.⁴²⁻⁴⁴ The resulting phosphate thenceforward can be transported to the response regulator protein (CheY) and to methylesterase CheB, subsequently forming a phosphoaspartate in the regulator protein. The phosphoaspartate will then regulate downstream events in the signaling pathway resulting in modulation of flagellar rotational behaviors by CheZ.⁴⁴⁻⁴⁷ The chemotaxis system in *B.subtilis* is considered to be more complicated, as it lacks CheZ and utilizes two more regulator proteins termed CheD and CheC, which although speculated to function upon the regulation of the CheW-CheA complex, their actual role in the system is still unknown.^{40,41} Nonetheless, based on the latter information, a general chemotaxis signaling transduction model was constructed for HemAT-*Bs* (**Figure 2.5**), where binding of O₂ to the proteins sensor domain, stimulates direct interaction of the chemoreceptor's effector domain with the CheW-CheA histidine autokinase complex, and promotes the formation of phosphorylated CheY, which controls the flagellar rotation motor switch.

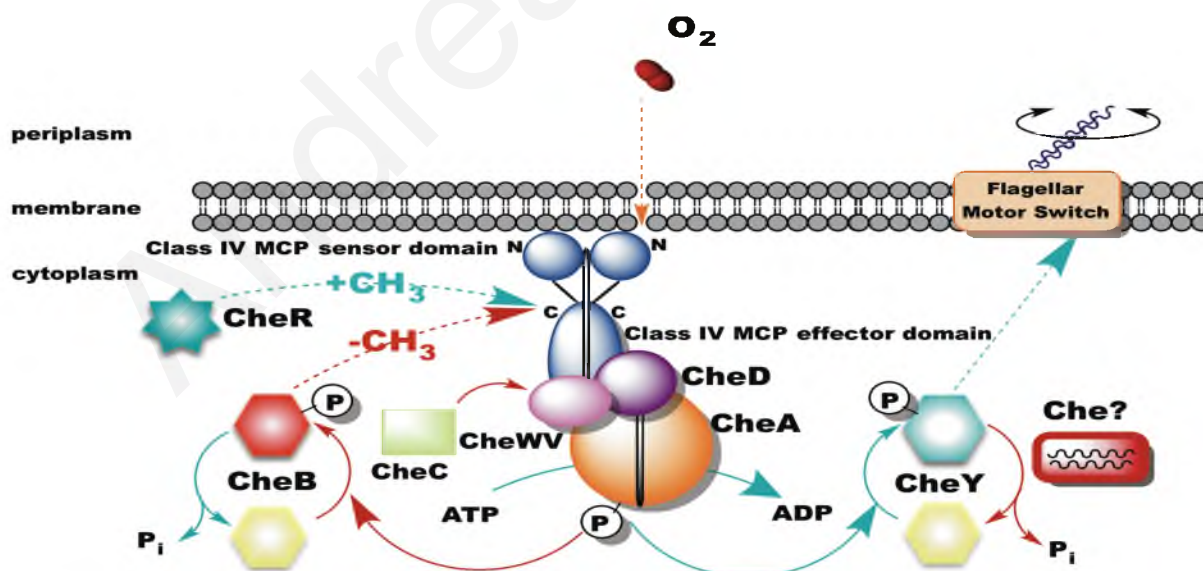


Figure 2.5 Schematic representation of the proposed two component signaling system in HemAT-*Bs* involving an autophosphorylated histidine kinase (CheA) and a response regulator protein (CheW) for the activation of phosphorylated CheY that controls the flagellar rotation motor switch. Adapted from ref 48 with modifications.

2.2.4 Spectroscopic studies of heme-based oxygen sensor protein HemAT-Bs

To understand the regulation mechanism of HemAT-Bs, it was important to elucidate the structural changes the heme active site upon CO, NO and O₂ binding, as well as the interactions of the heme pocket with the heme-bound gaseous ligands. Binding/dissociation of O₂ to the heme-Fe(II) of the sensor domain brings upon such conformational changes in the heme periphery that the external signal is transmitted to the effector domain.⁴⁹⁻⁵⁵ A range of spectroscopic techniques have been employed by certain research groups in order to relate the structural properties of HemAT-Bs with its functionality and explicate the aerotaxis signal transduction mechanism. The first spectroscopic and ligand binding studies, were conducted by Aono *et al.*, on the Fe(II) HemAT-O₂ and -CO complexes.⁵⁴ From their work HemAT-Bs was shown to possess similar spectroscopic and ligand binding properties to those of Mbs and Hbs. The resonance Raman (RR) spectra demonstrated a noticeably lower Fe-O₂ stretching ($\nu_{\text{Fe-His}}$) frequency compared to other oxygen-bound heme proteins, but similar to bacterial Hbs, suggesting that the heme-Fe(II) bound O₂ is involved in a distinct hydrogen bonding network with the distal site residues. In addition, they have observed that upon gas binding a movement of the heme-Fe(II) with the proximal ligand and F helix could trigger signal transduction. It is interesting that both CO and O₂ triggered similar conformational changes to the heme pocket. Nonetheless, up until now, no specific facilitation of the protein's aerotaxis function by either CO or O₂ binding has been clearly depicted, presumably due to the fact that unlike other gas sensor proteins (i.e. YddV and *EcDOS*) no exclusive substrate of the HemAT-Bs-regulated reaction has been acknowledged. Hence, the HemAT-Bs active / inactive species cannot be unambiguously defined.⁵⁶

In the crystal structure of the truncated sensor domain, Tyr70 and Thr95 are the two distal site residues that surround the heme pocket (**Figure 2.6**).^{26,36} Ohta *et al.* revealed with the use of resonance Raman (RR) spectroscopy, three O₂ binding conformations, which have been attributed to different hydrogen bonding interactions between the heme-bound O₂ and residue Thr95. The three binding conformations have been assigned as “closed form” ($\nu_{\text{Fe-O}_2}$ at 554 cm⁻¹), “open α form” ($\nu_{\text{Fe-O}_2}$ at 566 cm⁻¹) and “open β form” ($\nu_{\text{Fe-O}_2}$ at 572 cm⁻¹).⁵⁷ The “closed” conformation was deemed the high oxygen affinity form and the two “open” conformations the low oxygen affinity forms. They suggest that in the open α -form, Thr95 acts as hydrogen bond donor to the heme-bound O₂, thus playing a crucial role in gas recognition and discrimination. In turn, orientation change of Tyr70 from the open form to the closed form, renders the residue essential in intramolecular signal transduction, however,

without forming any hydrogen bonding interactions with the bound ligand to stabilize the complex. The observed structural conformations are consistent with those proposed by Zhang *et al.*, based on the crystal structure of the unliganded truncated sensor domain HemAT-*Bs*.^{26,36} They have designated the low-affinity subunit II with Tyr70 facing the solvent as the “up” conformer and the high-affinity subunit I demonstrating low O₂ dissociation rate with Tyr70 situated in such position to allow interaction with the bound ligand, as the “down” conformer. The two conformers (“up” and “down”) are suggested to be the equivalents of the open and closed forms, respectively. Nonetheless, the functional significance of each of the observed conformations has not been demonstrated thus far.

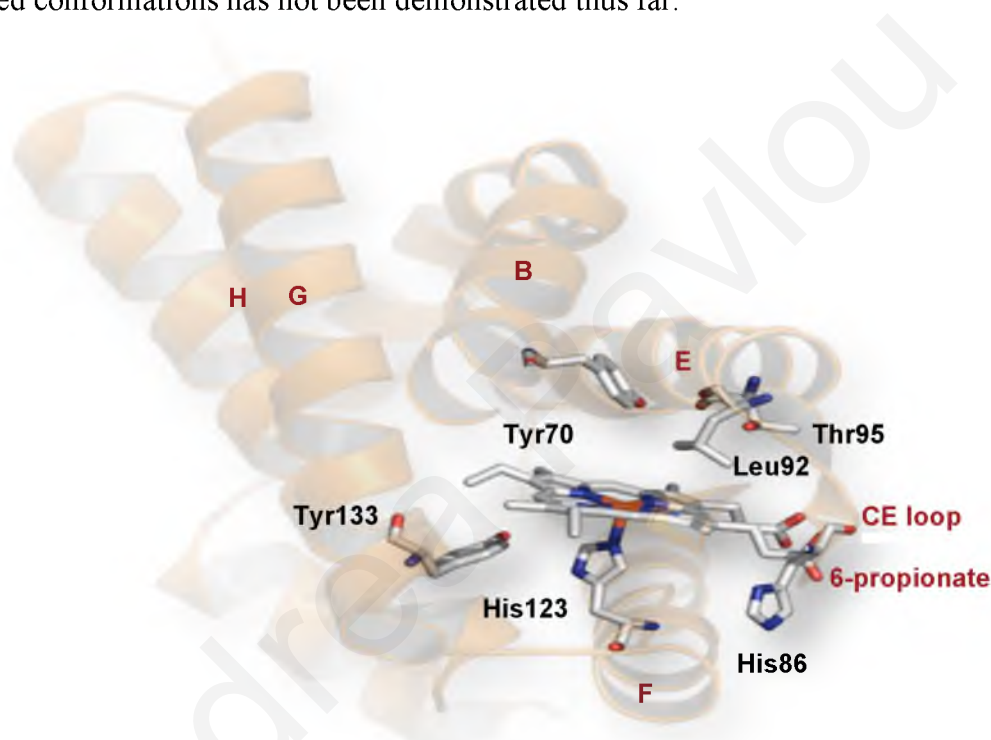


Figure 2.6 Structural representation of the unliganded truncated sensor domain heme active site of HemAT-*Bs* (PDB ID 1OR6)

It is important to mention that the work of Ohta *et al.* suggested no interaction of the heme-bound CO with the distal site of the heme pocket, as the RR spectra of truncated sensor domain HemAT-*Bs* mutants Y70F and T95A were similar to those of the wild type protein.⁵⁷ On the other hand, steady-state FTIR studies by Pinakoulaki *et al.* suggested that although Thr95 does not seem to play an important role in CO binding to HemAT-*Bs*, Tyr70 is in fact critical in controlling the hydrogen bonding interactions of the heme-bound CO with distal site of the protein.⁵⁸ In the static FTIR spectra of the CO-bound wild type truncated sensor domain HemAT-*Bs*, two conformers were detected, a non-hydrogen bonded and a strongly hydrogen bonded to the distal site residues.⁵⁸ However, upon mutation of Tyr70 to Phe, the spectra of the HemAT-CO adduct indicated that the non-hydrogen bonded conformer is

perturbed and shifted and a new moderately hydrogen bonded conformer was observed suggesting that Tyr70 is critical for hydrogen bond formation in the distal heme pocket upon CO-binding. In addition, they have suggested for the first time that another distal site residue might be important for the CO-bound ligand. Specifically, they have proposed that Leu92 is necessary for the initiation of the appropriate structural changes to the distal environment for maintenance of the H-bonded conformation (“closed”).⁵⁸

Yoshimura *et al* characterized further the coordination structure of the heme active site and the formed hydrogen bonding network between the heme-bound ligand, the heme-periphery and the surrounding residues.⁵² Their RR spectroscopy results suggested that formation of a hydrogen bond between proximal residue His86 (**Figure 2.6**) and heme-6-propionate upon O₂ binding triggers a conformational change that permits the formation of a distinct hydrogen bond between Thr95 and the heme-Fe(II) bound O₂. No hydrogen bonding interaction was evident between Thr95 and the heme-bound ligand in the CO- and NO-bound forms, suggesting that the hydrogen bond between Thr95 located on the E-helix and the heme-bound ligand is specific for the O₂-bound form. Although, hydrogen bonding interactions between the heme-bound O₂ were evident in the RR spectra, the distance between heme-Fe(II) and Thr95 as depicted in the X-ray crystal structure of Fe(II) HemAT-*Bs* is more than 3Å and therefore prohibitory for direct hydrogen bonding. Thus, they proposed that upon O₂ binding the distal site of the heme pocket undergoes a structural rearrangement that moves Thr95 to a position optimal for hydrogen bond formation.⁵²

To test the above postulation the RR spectra of the O₂-bound H86A HemAT-*Bs* mutants were investigated. The spectra revealed absence of direct hydrogen bonding between the heme-bound oxygen and Thr95 in the H86A mutant, confirming that the hydrogen bond forming between His86 located on the CE loop and the heme-6-propionate is responsible for inducing a structural rearrangement of the CE loop which is then propagated to the E-helix, ultimately changing the conformation of Thr95 and allowing hydrogen bond formation with the heme-bound O₂.⁵² The latter proposed structural rearrangement was confirmed by El-Mashtoly *et al.*, using UVRR spectroscopy on the full length WT and mutated forms of O₂ -, NO- and CO-bound HemAT-*Bs*. Specifically, they have suggested that the hydrogen bonding interactions between the heme-bound O₂ and Thr95, as well as the hydrogen bonding network between proximal residue His86 and the heme-6-propionate results in propagation of the heme structural rearrangement to the effector domain of the protein. In addition, they have proposed that upon the binding of different ligands (CO, NO, O₂) to the heme, helix G undergoes distinct conformational changes.⁵⁵

Experiments on the dynamics of the truncated sensor domain as well as the full length HemAT-*Bs* adducts had been limited until lately to the time-resolved resonance Raman studies of the HemAT-CO adduct by Yoshimura *et al.*, focusing on the investigation of the role of the proximal heme active site and the Fe-His bond in the signal transduction communication pathway⁴⁹, as well as to the study of CO photodissociation using time resolved optical absorption spectroscopy by Mokdad *et al.*⁵⁰ However, very recently El Mashtoly *et al.*, have provided a detailed site-specific observation of the protein dynamics in the communication pathway from the sensor to the effector domain of HemAT-*Bs* using time-resolved UVRR spectroscopy.⁵³

Based on the crystal structures of the truncated sensor domain HemAT-*Bs*, in the CN-bound form the proximal residue Tyr133 is located at a distance (3.4 Angstrom) (**Figure 2.7(B)**) that allows for hydrogen bonding to the proximal His123. In contrast, in the unliganded form, the distance between Tyr133 and His123 is beyond the optimal for hydrogen bonding (4.6 Angstrom) (**Figure 2.7(A)**).²⁶

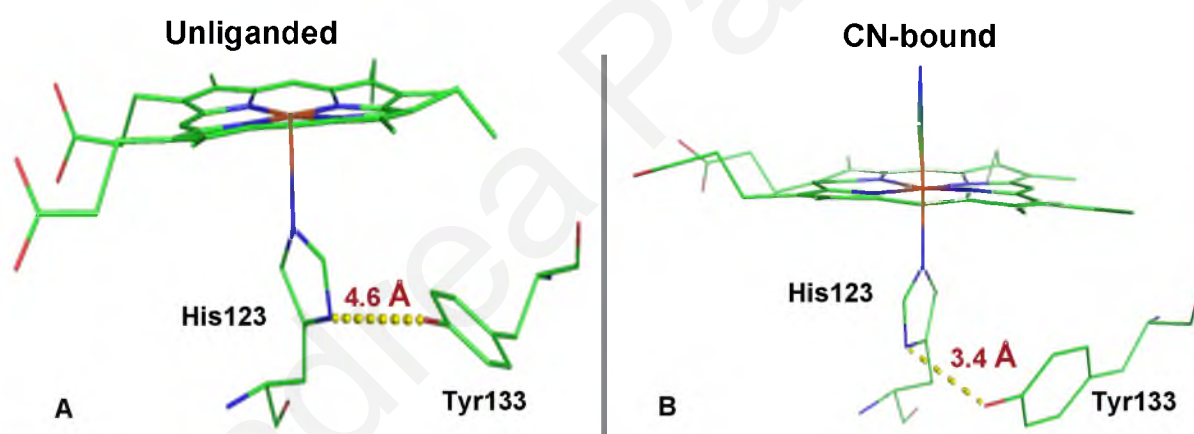


Figure 2.7 Structural representation of the position of the proximal residue Tyr133 in the (A) unliganded and (B) CN-bound HemAT-*Bs* indicating the distance between its side chain and His123.

As these data suggest a possible conformational change in the G-helix located near the H-helix that connects the sensor to the effector domain, Yoshimura *et al.* used TR³ spectroscopy to investigate the effect on the proximal pathway of HemAT-*Bs* upon mutation of the WT CO-bound protein to Y133F.⁴⁹ The time-resolved resonance Raman (TR³) spectra of the WT deoxy HemAT-*Bs* revealed a clear Fe-His stretching band ($\nu_{\text{Fe-His}}$) indicating a 5-coordinate structure. After CO photolysis of the WT HemAT-CO complex, the $\nu_{\text{Fe-His}}$ exhibited a 2 cm⁻¹ downshift, proposed to be caused by an alteration of the hydrogen bond to the proximal axial ligand His123. Although small, observation of similar shifts of the $\nu_{\text{Fe-His}}$ peak upon CO-

photodissociation in Mb, confirms the speculation. It is widely accepted that a hydrogen bond to the proximal His, results in the reinforcing of the Fe-His bond. The $\nu_{\text{Fe-His}}$ frequency shift was not observed in the spectra of the Y133F mutant, indicating the interaction between His123 and Tyr133 through the reversible hydrogen bonding formation upon ligand binding.⁴⁹

As mentioned earlier Tyr133 is located on the G-helix. The G-helices along with the H-helices of the homodimer form the four-helical bundle that connects the sensor domain to the effector domain. Because the G-helix is near the B-helix, it is possible that the conformational changes in the distal site of the heme are communicated to the proximal heme pocket through the hydrogen bond between Tyr133 and His123 that would induce movement of the G-helix, which would ultimately rearrange the G-H helix structural matrix and allow signal transduction from the sensor to the effector domain.^{26,49} The structural rearrangement of the G- and B-helices (**Figure 2.7**) was also observed in the time-resolved UVRR spectra of HemAT-CO by El-Mashtoly *et al.* using the aromatic side chains of proximal Trp132 and distal Tyr70 residues as probes. The observed intensity change of the Trp bands was attributed to the alteration in the environment surrounding Trp132 upon CO binding due to displacement of the G-helix. In addition, absence of two distinct peaks observed in the wild type protein upon its mutation to Y70F, confirmed that Tyr70 located in the distal site of the heme pocket undergoes conformational changes upon ligand binding. As there was no frequency shift of the Tyr bands observed in the of the wild type CO-bound HemAT-Bs but rather just an intensity change, they have suggested that Tyr70 is subjected only to hydrophobicity change upon CO photolysis and no hydrogen bonding alteration exists.⁵³

By observing the dynamic conformational changes induced to the protein matrix upon CO photodissociation by TR-UVRR, Mokdad *et al* suggested that the majority of the photodissociated CO leaves the heme pocket on a $\sim 20 \mu\text{s}$ time scale. In addition, the kinetic optical difference spectrum obtained at $\sim 4 \mu\text{s}$ subsequent to CO-photolysis demonstrated an un-relaxed heme pocket geometry.⁵⁰ On the other hand, El-Mashtoly *et al.* suggested the presence of two phases of conformational changes in a time frame of nanoseconds to microseconds following CO photodissociation. In detail, monitoring the protein dynamics upon CO photolysis, they demonstrated two species attributed to a B- and G-helix displacement at $0.45\mu\text{s}$ and $0.20\mu\text{s}$ (C-intermediate) for the full length and truncated sensor domain HemAT-Bs respectively, and again at $45\mu\text{s}$ for both forms of the protein (D-intermediate).⁵³ Following these observations providing proof of structural changes involving helical movements upon ligand binding, El-Mashtoly *et al.* proposed a potential signal

transduction mechanism for HemAT-*Bs* involving structural changes to the B- and G-helices that eventually trigger an intramolecular signal transduction from the sensor to the effector domain.⁵³

Agreeably, the spectroscopic studies and the X-ray crystal structure of the sensor domain HemaT-*Bs* provide solid evidence that both B- and G-helices play an important role in the formation of a hydrogen bonding network necessary for signal transduction. However, to fully understand the signal transduction mechanism of the heme-based oxygen sensor protein HemAT-*Bs*, it is necessary to further investigate the conformational dynamics of this protein and identify the interaction between the sensor and effector domains.

2.3 Structure and function of heme-based sensor proteins YddV (or *EcDosC*) and *EcDOS* (or *EcDosP*)

2.3.1 Modulation of c-di-GMP metabolism: The *yddV-dos* bicistronic operon

The Gram negative enterobacterium *Escherichia coli*, employs an array of regulatory systems in order to monitor the oxidative and metabolic conditions of the cell, so as to adjust to less optimal aerobic life. Through these regulatory systems *E. coli* modulates the expression of more than 70 operons, and at least six of these distinct genes encode bis-(3'-5')-cyclic dimeric guanosine monophosphate (c-di-GMP) - related proteins. One of these gene sequences is the *yddV-dos* bicistronic operon that controls the intracellular amounts of the signal molecule, 2nd messenger c-di-GMP.⁵⁹ A second messenger regulating operon usually includes a two-enzyme complex which in response to certain stimuli biosynthesizes and degrades the second messenger. Accordingly, the *yddV-dos* bicistronic operon encodes for a stable protein complex consisting of the biosynthetic enzyme YddV, exhibiting diguanylate cyclase (DGC) activity, and the degradative enzyme *EcDOS* exhibiting phosphodiesterase (PDE) activity. The two genes encoding for the specific enzymes are only separated by the stop codon of the *yddV* gene. Although they demonstrate counter function, they are jointly transcribed so as to regulate the c-di-GMP overproduction in response to environmental signals. Specifically, synthesis and degradation of c-di-GMP are triggered by initial signals such as phosphorylation, light illumination and gas binding. In turn, increased or decreased concentrations of c-di-GMP regulate functions such as motility, virulence, biofilm formation etc.⁶⁰⁻⁶⁶

Oxygen appears to be a critical signaling ligand for the regulation of c-di-GMP metabolism by DGCs and PDEs.^{64,65} In *E. coli*, O₂ regulation of c-di-GMP levels is achieved by opposing synthesis and degradation activities that are both O₂-controlled. For example, when oxygen gradients drop below the ambient threshold, binding of O₂ by YddV releases an intracellular signal that triggers c-di-GMP synthesis through diguanylate cyclase activity. Conversely, to control the intracellular amounts of c-di-GMP synthesized and diffused into the cytoplasm, binding of O₂ by *EcDOS* releases an intracellular signal that triggers c-di-GMP hydrolysis to l-di-GMP through phosphodiesterase activity. In fact, the DGC activity of YddV has been found to be lower compared with the PDE activity of *EcDOS*. Thus, the formation of cyclic di-GMP by YddV is suggested to be the rate-determining step in the YddV-*EcDOS* system. The outcome of this complex bacterial signaling system is the fine tuning of *curli fimbriae* production that switches bacterial lifestyle from planktonic to biofilm and vice versa, in response to oxygen availability.⁶⁰ It is of great interest that, unlike other bacteria, *E. coli* allosterically regulates two opposing activities by binding of the same molecule. This characteristic allows the bacterium to rapidly and efficiently interchange between sessile (biofilm) and motile (planktonic) states so as to conserve its homeostasis.^{22, 61-66}

When in biofilm form, the bacteria are implanted in an extracellular polymeric layer cluster. This layer cluster ensures their shielding against environmental strains such as decreased oxygen gradients by switching to anaerobic metabolism in its innermost biofilm layer. Both YddV and *EcDOS* proteins are active in regulating the transcription of the *csgBAC* operon responsible for the formation of curli structural subunits. According to studies by Tagliabue *et al.*,⁶⁰ DGC and PDE activities by YddV and *EcDOS*, respectively, are inhibited in the absence of oxygen, resulting in inhibition of the expression of the *csgBAC* operon. In addition, the recently published physiochemical studies conducted by Kitanishi *et al.*,⁶⁸ suggested that in hypoxic conditions, YddV would adopt an inactive form and cease the c-di-GMP biosynthesis. The latter observations provide solid evidence that curli fiber production leading to bacterial biofilm lifestyle is *yddV-dos* dependent, therefore related to oxygen sensing c-di-GMP modulation by the heme-based oxygen sensor proteins YddV.^{22,30,68}

The exact mechanisms of conversion of gas signals by YddV and *EcDOS* into production and hydrolysis of 2nd messenger c-di-GMP are complex and not yet fully comprehended. Although it is evident that both DGC activity by YddV and PDE activity by *EcDOS* are inhibited in the absence of oxygen, they respond differently to oxygen

concentrations, which translates to different gas recognition and signal transduction mechanisms between the two. Hence, it is necessary to investigate the structures of these proteins in detail so as to gain inside into their individual molecular signal transduction processes.

2.3.2 Structure of globin-bound oxygen sensor DGS protein YddV (*EcDosC*)

YddV is a heme-bound globin-coupled oxygen sensor protein, found in *Escherichia coli* that synthesizes c-di-GMP through diguanylate cyclase activity. Genetic organization studies conducted by Gilles-Gonzalez and colleagues, revealed that the structure of the protein demonstrates a GGDEF domain at the C-terminus and lacks the EAL domain.^{22,65,66} The GGDEF (Gly-Gly-Asp-Glu-Phe) domain consists of a highly conserved, 170 - amino acid sequence, homologous to the adenylyl cyclase catalytic domain. Initial studies by Benziman *et al.* involving the bacterium *G. xylinus* have shown that the GGDEF domain demonstrates diguanylate cyclase activity, resulting in the synthesis and hydrolysis of c-di-GMP from two molecules of GTP through the linear intermediate diguanosine-tetraphosphate (pppGpG).^{59,67,69}

The C-terminus GGDEF domain of YddV is linked to a sensor domain, where external signals are perceived. The N-terminus sensor domain of the YddV protein demonstrates globin folding and controls the DGC activity of the C-terminus GGDEF domain through an intramolecular signal transduction mechanism.^{29,30} The globin domain contains a heme group, where oxygen sensing occurs. Possessing a heme-bound globin domain as the oxygen-sensing site, categorizes YddV as a globin coupled oxygen sensor protein.

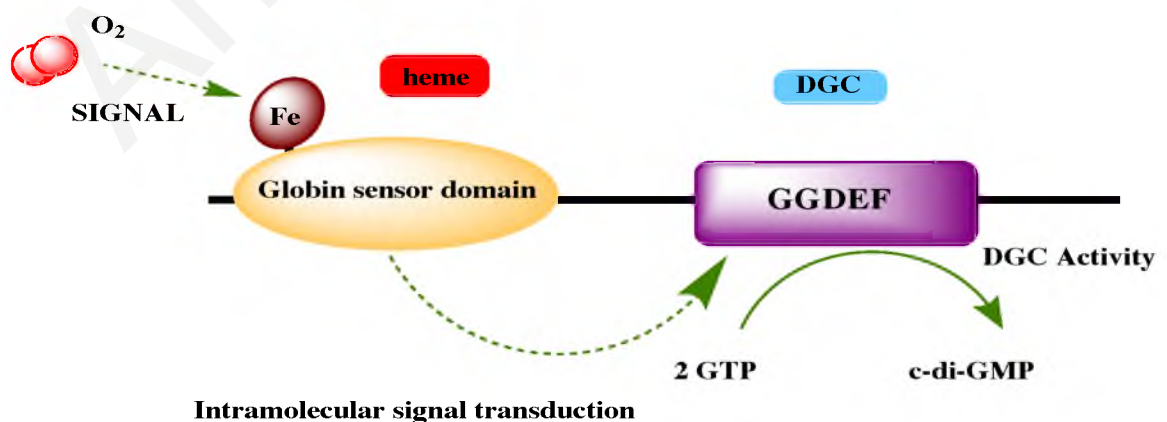


Figure 2.8 Schematic representation of the binding of O₂ to YddV heme-Fe(II) that initiates an intramolecular signal transduction, which increases DGC activity in GGDEF domain, triggering the conversion of 2GTP to c-di-GMP.

In addition, genetic sequencing of the sensor domain of the protein revealed 47% sequence similarity and 18% identity to HemAT-*Bs*, which is a more archaic globin sensor, rather than to mammalian Mb. Consequently, binding of O₂ to the heme-Fe(II) in the sensor domain initiates an intramolecular signal transduction that triggers DGC activity in the GGDEF domain, promoting therefore the catalysis of 2GTP to c-di-GMP, and ultimately leading to biofilm formation (**Figure 2.8**).^{22,30,60,68}

The crystal structure of the YddV protein has not been yet resolved. Shimizu and coworkers relied their proposed structure of the YddV heme active site, on the amino acid sequence alignment of GCS proteins *AvGReg*, *BpeGReg*, HemAT-*Bs* and sperm whale Mb, as well as the structure of the CN-bound HemAT-*Bs* complex. Based on the proposed structure, it has been hypothesized that the heme proximal axial ligand is residue His98 (corresponding HemAT residue His123) (**See Figure 2.6**). In addition, two residues, Tyr43 and Leu65, presumably corresponding to Tyr70 and Leu92 of HemAT-*Bs* respectively, have been suggested to cooperatively preserve a heme periphery that promotes the oxygen sensing function of YddV.^{22,68,70}

2.3.3 Spectroscopic studies of globin-bound sensor DGS protein YddV

Physicochemical and spectroscopic studies were conducted by Shimizu and coworkers on the wild type and mutated forms of YddV, to assess their postulated structure. Specifically, the measured catalytic activity of the wild type Fe(III), Fe(II)–O₂, and Fe(II)–CO complexes defined them as active forms, whereas the Fe(II) and Fe(II)–NO forms appeared inactive. The latter observations suggested a possible a combination of change in the redox state of the heme and ligand binding to cause critical protein conformational changes at the heme-distal side.⁷⁰

In its wild type Fe(III) form, optical absorption spectra indicate that the protein adopts a 5-coordinated high-spin state, denoting a protected heme distal site. This structural property appears to be characteristic of the YddV protein, as other globin-coupled oxygen sensor proteins in the Fe(III) form acquire 6-coordinated high-spin or 6-coordinated low-spin states.⁷⁰ However, when Leu65 was mutated, the optical absorption spectrum of the Fe(III) was changed considerably; mutating the Leu65 residue permits H₂O to enter the heme active site, converting the coordination structure to 6-coordinated high-spin state. Therefore, based on the optical absorption spectra and autooxidation rate constants calculated, Leu65 has been proposed to be playing a critical role in blocking H₂O entry to the heme active site, thus

lowering the autooxidation rate constant of YddV so as to maintain the proper autooxidation rate for adequate oxygen sensing. It is notable to mention that from kinetic studies of CO binding to the heme complex, it has been suggested that Leu65 is not critical for CO binding. The low dissociation rate constants of the L65M and L65T mutants were attributed to the instability of the liganded structure of the protein, due to the lack of interaction between the absent Leu65 residue and the heme-bound CO.⁷⁰

Mutation of Tyr43 to Phe, resulted in significant changes in the Fe-CO and C-O frequencies proposing that Tyr43 interacts with the heme-Fe(II) bound CO molecule. On the other hand, the suggested interaction of the distal oxygen atom of CO with Tyr43 was based on the kinetic analysis and autoxidation rate constants of the Tyr43 mutant proteins.⁶⁸

2.3.4 The direct oxygen sensor phosphodiesterase protein *EcDOS* (*EcDosP*)

EcDOS (*E. coli* Direct Oxygen Sensor) from the bacterium *Escherichia coli* is a heme-regulated phosphodiesterase (PDE) protein that catalyzes the degradation of 2nd messenger c-di-GMP to linear di-GMP (5'-pGpG) via gas sensing, ultimately altering the bacterium's state from sessile to motile (**Figure 2.9**).^{71,72} It is essentially a fusion protein created by the translation of the *yddV-dos* bicistronic operon with functional properties derived from the *dos* gene of the complex. Genetic organization of the enzyme indicated high-sequence homology amongst its N-terminal region and the PAS domain of rhizobial FixL with 25% identity and 60% similarity, as well as 30% identity and 50% similarity amongst its full-length sequence and the *G. xylinus* PDE domain. *EcDOS* is a tetramer composed of 807 amino acid residues, which make up a three-domain sequence; two PAS domains PAS-A and PAS-B located at the N-terminus and a GGDEF-EAL tandem at the C-terminus. The PAS-A domain controls the EAL phosphodiesterase activity towards c-di-GMP, while the adjacent GGDEF domain is inactive (**Figure 2.9**).^{25,73,74} PAS-A domain contains a heme group. The term PAS is derived from the acronyms of "Drosophila period clock protein (PER)", "vertebrate aryl hydrocarbon receptor nuclear translocator (ARNT)", and "Drosophila single-minded protein (SIM)". It is a fundamental structural motif which can be found in a plethora of organisms, from prokaryotes to mammals. In eukaryotic organisms the PAS domain mainly controls the function of voltage-gated ion channels and the transcription factors that modulate the organism's reaction to hypoxic and toxic environments. In bacteria, it acts predominantly as a sensor for light, redox state and gas molecules.⁷⁵

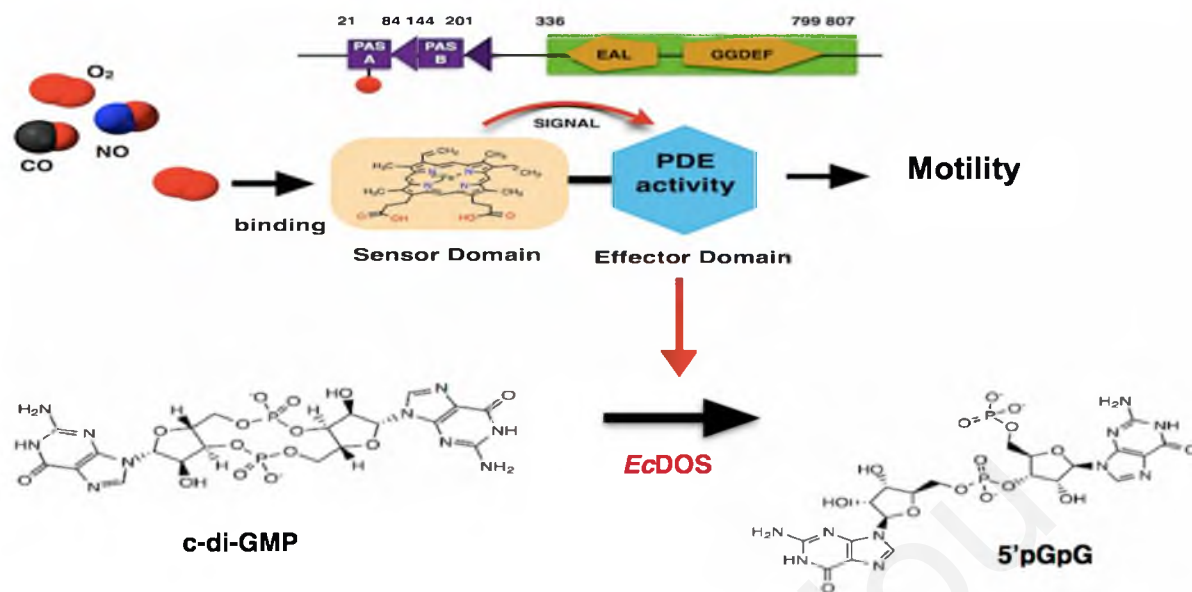


Figure 2.9 Schematic representation of the catalytic activity of EcDOS towards the hydrolysis of *c*-di-GMP to linear-di-GMP (5'pGpG) via phosphodiesterase activity after binding of gaseous molecules such as O₂, CO, and NO to the heme-Fe(II) of its sensor domain. Adapted from Ref 95 & 96

2.3.5 X-ray crystal structure of the heme-bound PAS-A heme domain EcDOS

Two different research groups have reported crystal structures of the heme-containing PAS-A domain of EcDOS in the Fe(III), Fe(II), and Fe(II)-O₂ forms. The PAS-A domain has been defined as a 120 amino acid dimer comprised of two distinct monomers (subunit I and subunit II), each containing a heme group. In addition, they have reported monomer secondary structure with a characteristic PAS folding, comprising of five α -helices and a five-stranded antiparallel β sheet. The heme group is located between the F helix and the G and H β -strands. In the Fe(III) form, the heme-iron retains a water molecule and His77 as the axial ligands in both subunits (**Figure 2.10(A)**).^{25,73,74} Upon redox state change to Fe(II), a redox-dependent ligand interchange is observed where Met95 coordinates to the heme, replacing the water molecule to form a six-coordinate complex. It is interesting to mention that as illustrated in **Figure 2.10(B)**, in the Fe(II) form Met95 is situated on the FG loop. Since Met95 is anchored on heme-Fe(II), the plasticity of the FG loop is restricted, rendering it rigid compared to being disordered in the Fe(III) form of the protein.⁷⁶ The flexibility of the FG loop in the ferric form, does not allow its structural representation (**Figure 2.10(A)**), however upon rigidifying in the ferrous form, its structure is adequately determined (**Figure 2.10(B)**).^{73,74,76}

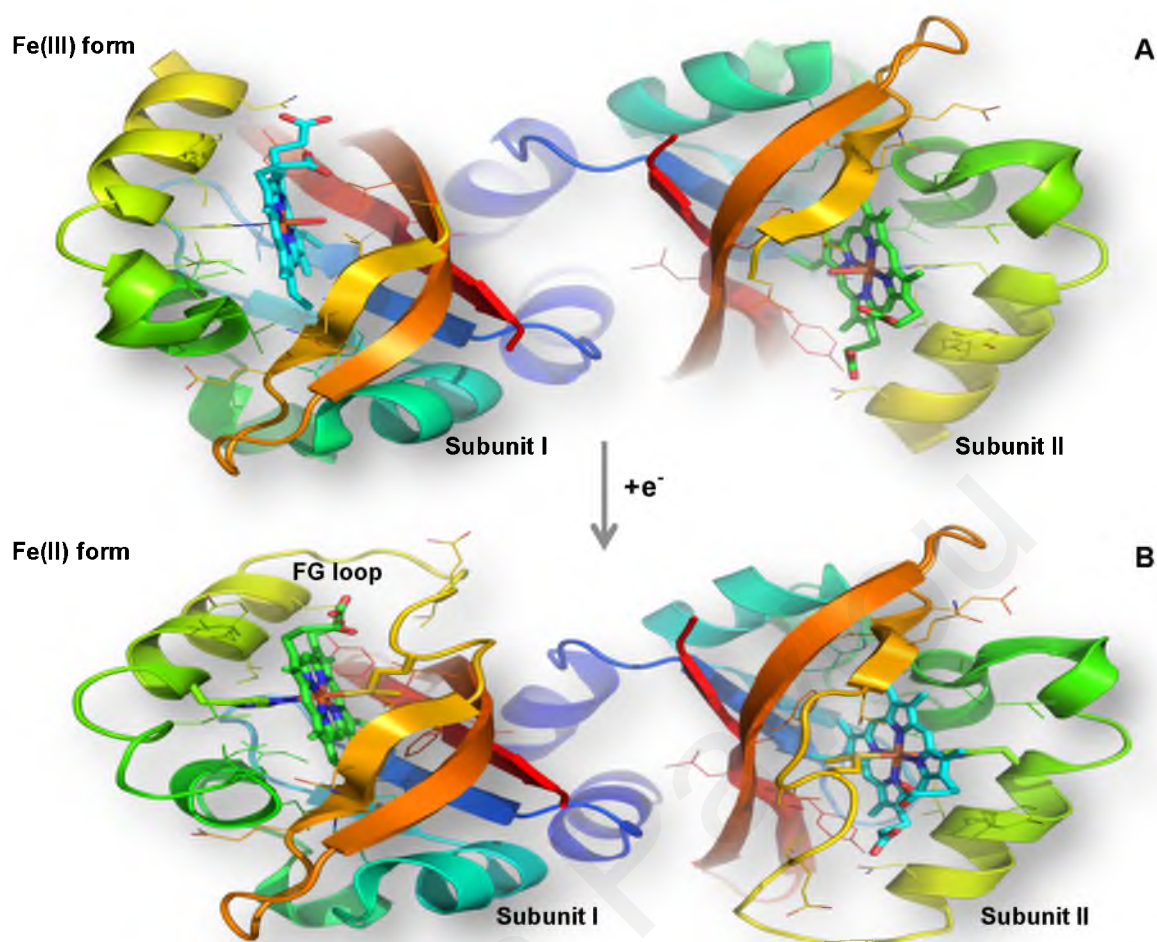


Figure 2.10 X-ray crystal structures of the (A) Fe(III) (PDB ID 1V9Y) and (B) Fe(II) *EcdOS PAS-A* domain (PDB ID 1V9Z).

EcdOS demonstrates dynamic changes in its heme coordination structure, in response to the binding of an external ligand. In the reduced form (Fe(II)) the heme is six-coordinate and does not possess an unoccupied site for an external ligand to bind. However, it still retains the ability to bind small diatomic gas molecules such as O₂, CO, and NO by an interchange between the gaseous ligand and Met95. This unorthodox ligand binding mechanism becomes even more complex as the exogenous gaseous ligand probably causes different conformational changes to each of the dimer subunits upon binding to the heme iron (**Figure 2.11**). Both subunits still possess as a proximal ligand the His77. The X-ray crystal structure of the oxygen-bound *EcdOSH*, clearly depicts the side chain of Met95, changing orientation upon its displacement by oxygen binding, turning away towards the solvent. This displacement of the heme-Fe(II) bound Met95 causes distinct conformational changes to the FG loop ultimately distorting it, and hence cleaving the Fe(II)-Met95 bond.⁷⁷

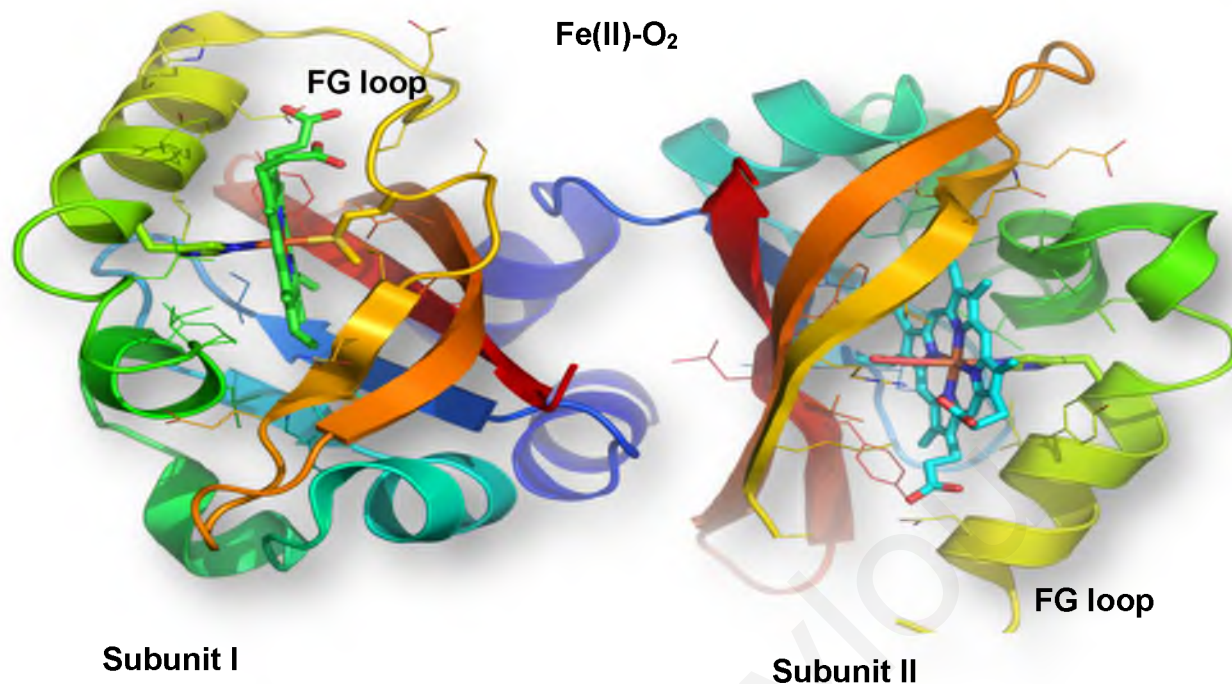


Figure 2.11 X-ray crystal structure of the Fe(II)-O₂ EcDOS PAS-A domain depicting the two distinct subunits of the dimer. Subunit I has a Met95 residue as axial ligand where subunit II is bound to O₂ (PDB ID 1VR6, 1S67).

Like Met95, Arg97 is located in the G_β-strand.⁷⁴ As illustrated in **Figure 2.12(B)**, the crystal structure of EcDOSH-O₂ depicts Arg97 as the residue that directly interacts with the heme-bound O₂. When Met95 coordinates to the heme-Fe(II), the side chain of Arg97 is turned outwards away from the heme active site. Upon O₂ binding, a drastic rotation of the side chain of Arg97 towards the bound oxygen is observed, so as to act as a hydrogen bond donor to the hydrogen bonding network formed with the heme-bound O₂ and the heme-7-propionate that stabilizes the complex. Besides the imperative roles of Arg97 and Met95 in ligand binding resulting in conformational changes observed in the vicinity of the heme binding pocket, structural differences between the Fe(II) and Fe(II)-O₂ complexes concerning other residues located in the surroundings of the heme active site have been detected in the X-ray crystal structure of EcDOSH. Specifically, Tyr80 undergoes a 115° ring rotation while Asn84 forms a hydrogen bonding network with heme 6-propionate. In addition, rotation of the heme-6-propionate group upon O₂ binding which may trigger the formation of the hydrogen bond between Asn84 and Tyr126 through the heme-6-propionate hydrogen-bond network.^{73,74}

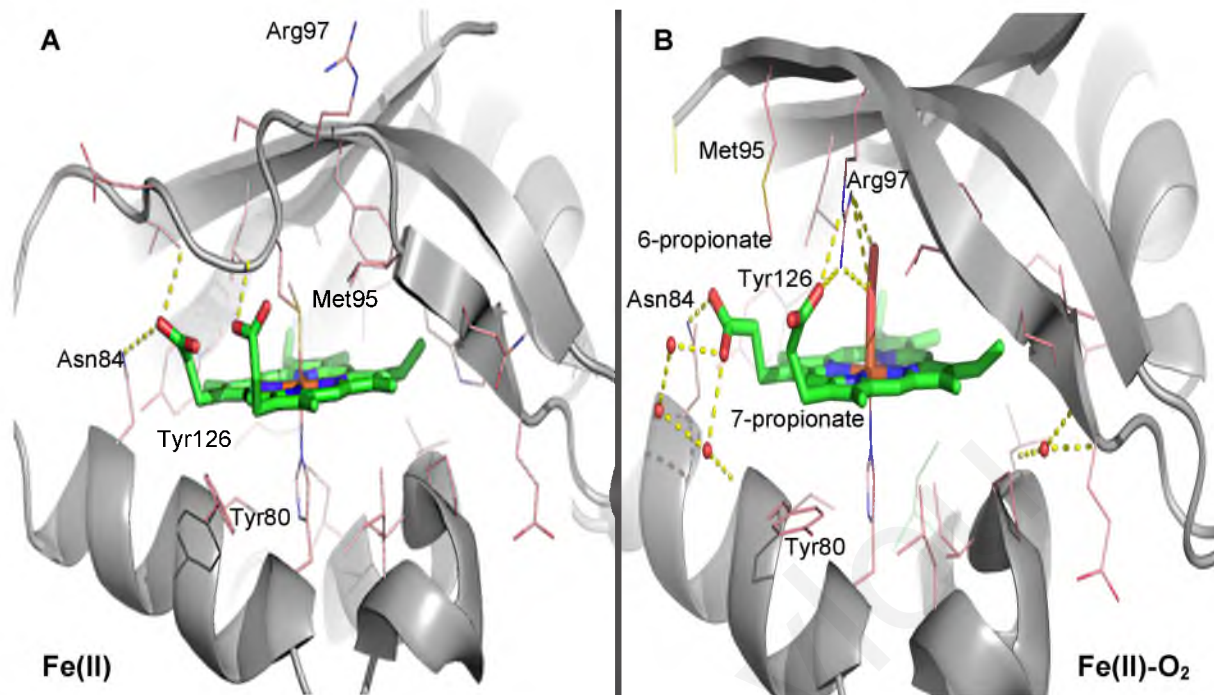


Figure 2.12 Structural representation of the heme active site conformational changes induced to (A) Fe(II) *EcDOS PAS-A* (PDB ID 1VZ9, 1S66) signaling domain upon (B) O₂ binding (PDB ID 1VR6, 1S67).

Interestingly, while *EcDOSH* has as an inherent substrate c-di-GMP, it was initially thought that the native substrate was c-AMP. The behavior of the protein is substantially different towards the catalysis of the two substrates. To elaborate, PDE activity toward c-AMP was observed in the full length *EcDOS* Fe(II), while this activity was practically insignificant in the case of the full length *EcDOS* Fe(III) form. On the contrary, when the substrate is changed to c-di-GMP, the *EcDOS* Fe(III) and Fe(II) forms are both PDE inactive. In addition, while the PDE catalysis of c-di-GMP is increased by the binding of NO or CO to the form of the protein, the PDE catalysis of c-AMP is markedly suppressed by the binding of NO or CO. The PDE activity of the *EcDOS*-O₂ adduct towards catalysis of c-AMP was not possible to measure due to instability of the complex. Conclusively, although *EcDOS* has definitely shown activity of heme redox-regulated catalysis of c-AMP, its native substrate seems to be c-di-GMP, and it has been established that the Fe(II)-O₂, Fe(II)-CO and Fe(II)-NO forms of *EcDOS* are active towards PDE catalysis of c-di-GMP while the Fe(III) and Fe(II) forms are inactive. The latter results supported the initial assumption that *EcDOS* is a gas sensor protein.^{21,73,78,79}

2.3.6 Spectroscopic studies of Fe(II) -O₂ and Fe(II) -CO *Ec*DOSH

Resonance Raman spectra revealed a 6-coordinate, low-spin state for *Ec*DOSH Fe(III) and heme complexes, with the distal site axial ligand Met95 in forming a hydrogen bond with the heme-7-propionate.^{80,81} Upon O₂ binding, Met95 is replaced by O₂, and a hydrogen bonding network forms between heme-7-propionate, the bound O₂, Arg97 and Phe113 rather than Met95. This H-bonding network stabilizes the heme -O₂ complex. Based on the latter RR results, it has been suggested that the role of the electrostatic interactions of Arg97 with the heme-7-propionate, and the steric interactions of Phe113 with the bound O₂ is fundamental in modulating the competitive binding and displacement mechanism between Met95 and O₂ to heme-Fe(II).^{73,74,80-83}

Although *Ec*DOS is termed an oxygen sensor, this enzyme appears to be less selective compared to other heme-based oxygen sensor proteins; its PDE activity displays increase upon binding of other exogenous gas ligands such as CO and NO despite not being the physiological candidates.^{22,84} The resonance Raman spectra of the Fe(II)-CO form of *Ec*DOSH have indicated a nearly linear Fe-C-O geometry with a distinct hydrophobic distal pocket in the heme active site, in contrast to a more bend and hydrophilic distal site for the oxygen – bound *Ec*DOSH. Prior to the determination of the crystal structure of *Ec*DOSH, RR studies with mutations of His77 and Met95 had indicated that they are the heme axial ligands. When His77 was mutated to Ala time-resolved resonance Raman (TR³) spectra revealed the absence of the Fe-His stretching band ($\nu_{\text{Fe-His}}$) at 214 cm⁻¹ in the photodissociated -CO complex, otherwise present in the WT *Ec*DOS protein.^{80,81}

In addition to the axial ligands, several other residues of the heme active site have been identified as potentially playing an important role in modulating the ligand-binding properties and the enzymatic activity of the protein.^{37,82,85-92} Specifically, static UVRR spectra have shown that the environment of residue Trp53 located near the heme-2-vinyl group as well as Tyr55 located near the Glu59-Lys104 conserved salt bridge become more hydrophilic upon CO binding rather than more hydrophobic upon O₂ binding. El-Mashtoly *et al.* confirmed this observation by time-resolved UVRR spectroscopy. They have also observed transient conformational changes in *Ec*DOSH (<0.5 ns) induced by CO photodissociation. The dissociated CO subjected to geminate recombination (~60%), is likely to be trapped and docked in the heme cavity.⁸⁸ Performing kinetic analysis of CO dissociation from the time-resolved UVRR spectra, indicated that Trp53 residue undergoes conformational changes on

the subnanosecond time scale as a result of its interaction with docked CO. Based on the above findings, they have suggested that the heme structural changes are presumably communicated through the interaction of the 2-vinyl-Trp53-Tyr55 cluster with the Glu59-Lys104 conserved salt bridge located on the PAS-A surface, to the PDE domain. Furthermore, static UVRR spectra indicated that when CO binds to heme-Fe(II), Asn84 forms a hydrogen bond with Tyr126, but not in the ligand-free heme complex. These observations suggest that the hydrogen-bonding network formed between the heme-6-propionate and proximal residues Tyr126 and Asp84 is important in transducing the signal from the PAS-A domain to the catalytic EAL domain in *EcDOS*.^{83,90}

These studies provided evidence that heme structural changes in the proximal environment of vinyl and propionate side chains, trigger conformational changes of the protein matrix upon CO-binding. Lechaue *et al.*⁹² have performed ultrafast spectroscopic studies as well as extensive kinetic analysis of ligand binding to *EcDOS*. They argue that the binding of gaseous ligands to the heme is not mediated by the environment of the PAS-A domain, rather the Met95 dynamic parameters are subjective to (a) the presence of the monomer-monomer interface, (b) whether one or two ligands are bound to the dimer and (c) the existence of the EAL catalytic domain; Met95 affinity increases one-fold in the full length protein. They suggest that the positive co-operativity between the two subunits of the *EcDOS* PAS-A dimer induced by Met95 displacement upon O₂ binding, might be the key behind an increased oxygen affinity. In addition, they have observed that a second O₂ can bind to heme-Fe(II) with six times more affinity than the first one, thus decreasing the existence of unliganded and monoliganded species of *EcDOS*. Based on the latter observation, they have proposed that substitution of Met95 by O₂ in subunit II leads to conformational changes in the heme active site that intrinsically decrease Met95 affinity for the heme-Fe(II), simultaneously increasing binding affinity for O₂, in subunit I.⁹² If such cooperative mechanism exists, then it is safe to assume that the organism's sensitivity to perceive and react to changes of the ambient concentrations of O₂ in its natural environment will be enhanced.^{22,92,93}

2.3.7 X-ray crystal structure of the catalytic EAL domain of *EcDOS*

In the previous section the PAS-A sensor domain of *EcDOS* has been described in detail. Despite the insight into the structure and function of the PAS-A domain, the signal transduction mechanism from the sensor domain to the active site of the catalytic domain is still unclear. Until lately no structural information concerning its catalytic PDE domain were

available, and the description of its function relied on genetic organization as well as comparative studies to other proteins known to contain PDE active EAL domains.

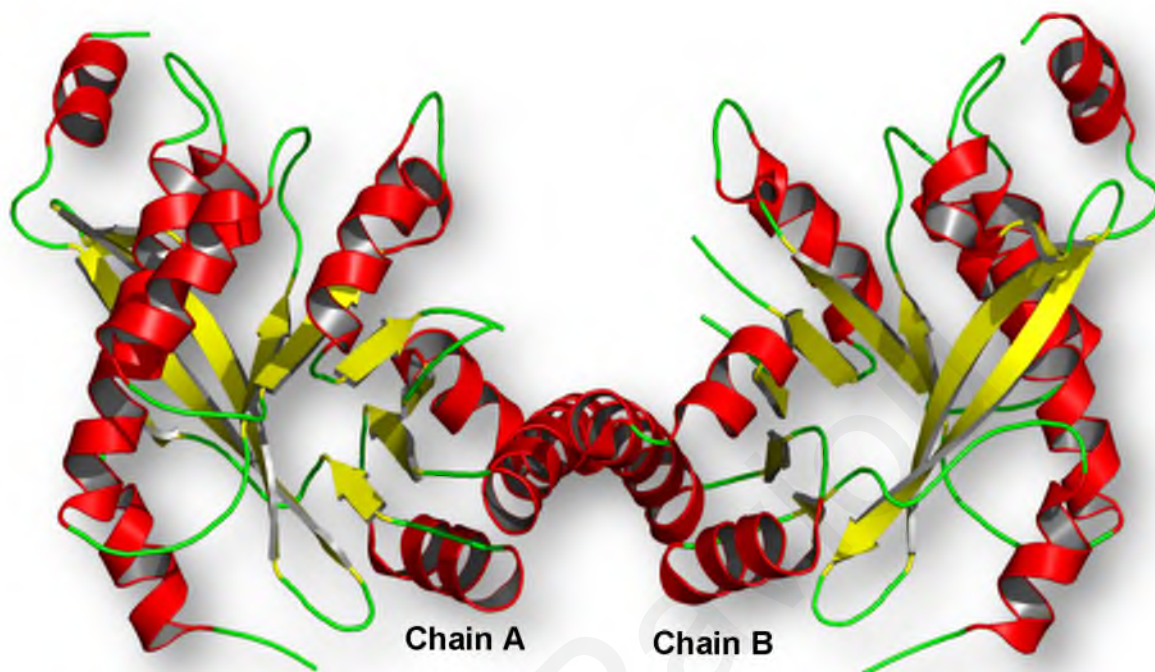


Figure 2.13 X-ray crystal structure of the dimeric form of the *EcDOS* EAL catalytic domain. Each chain demonstrates characteristic triosephosphate isomerase barrel fold (TIM) with one antiparallel β -strand (PDB ID 4HU4).

It has been established by now that the *EcDOS* EAL domain (**Figure 2.13**) regulates c-di-GMP through phosphodiesterase activity. Therefore, it is speculated that the inactive conformation observed in the crystal structure should be of functional significance for the DGC activity mechanism of YddV. Taking all the above structural information into consideration, Tarnawski *et al.*⁹⁴ propose that upon O₂ binding, an intramolecular signal transduction occurs from the PAS-A sensor domain, crosses the dimer “border” and induces a conformational rearrangement of loops L3 and L5 so as for the EAL active site to be capable of binding c-d-GMP and catalyze it to l-di.GMP (**Figure 2.14**).⁹⁴

Conformational changes induced by sensing specific effector molecules are crucial processes for triggering individual regulating activities of sensor proteins. As described in this section, spectroscopic and structural studies of the isolated PAS domain as well as the newly resolved structure of the catalytic EAL domain of *EcDOS* provided detailed information of what and how conformational changes occur in the PAS-A domain upon sensing O₂ and which structural elements of the EAL domain might play a crucial role in intramolecular signal transduction. However, more elaborate studies owed to be achieved on both the *EcDOS*

and the isolated *EcDOSH* so as to clarify how exactly is the signal propagated from PAS-A to EAL domain and why its PDE mediated c-di-GMP hydrolysis to l-di-GMP is O₂- controlled and not CO- or NO- controlled despite the fact that all three *EcDOS* forms (Fe(II)-NO, -CO, -O₂) are active.

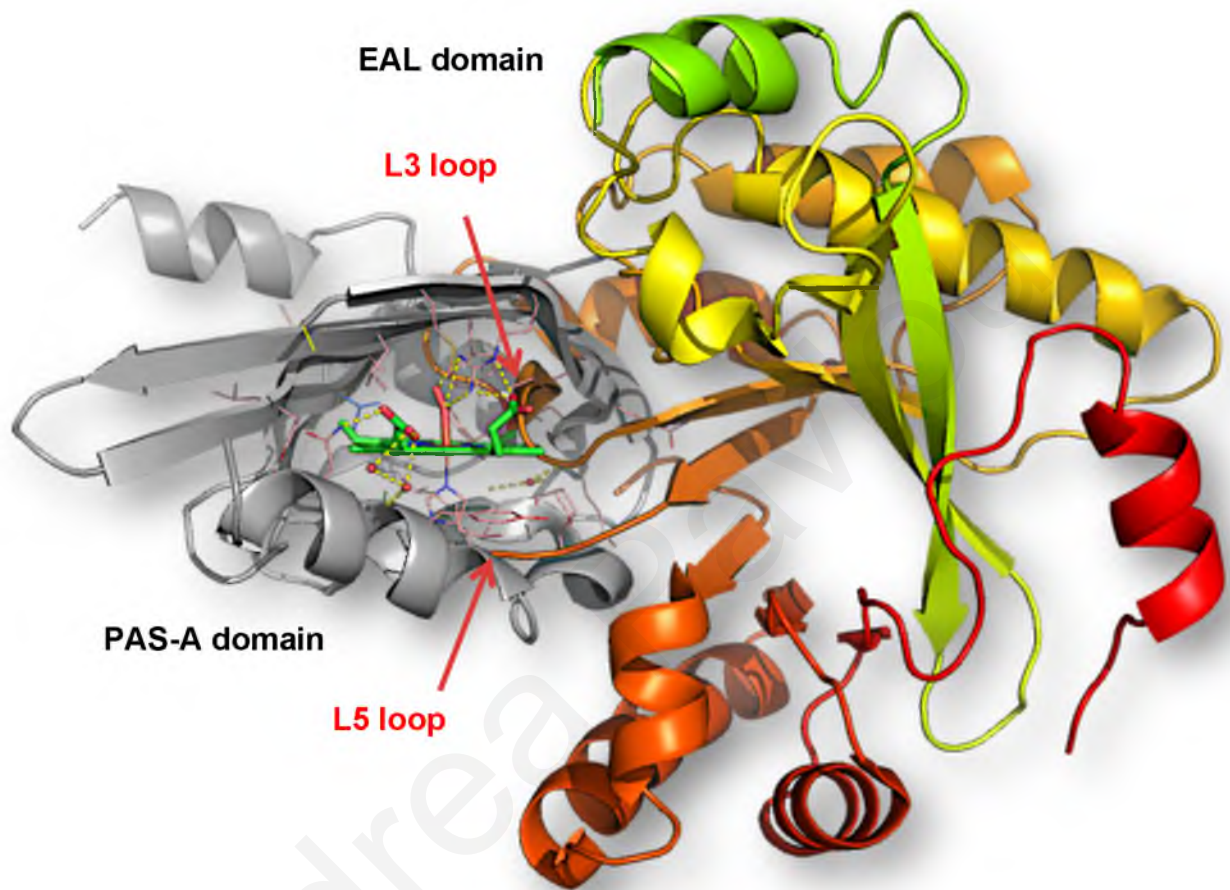


Figure 2.14 Illustration of the structural conformations of the flanking PAS-A sensory and EAL catalytic domains in the -O₂ form of *EcDOS*, demonstrating the position of L3 and L5 loops of the EAL domain that are proposed to be critical in the intramolecular signal transduction from the sensory to the catalytic domain of the protein (PDB IDs 4HU4, 1VR6, 1S67).

2.4 References

1. B. Alberts, A. Johnson, J. Lewis, M. Raff, K. Roberts, P. Walter, *Molecular Biology of the Cell*, Garland Science, New York USA **2002**
2. K. Rodgers *Curr. Opin. Chem. Biol.* **1999**, 3, 158-167.
3. R. Jain, M. K. Chan, *J. Biol. Inorg. Chem.* **2003**, 8, 1-11.
4. T. G. Spiro, A. V. Soldatova, G. Balakrishnan, *Coord. Chem. Rev.* **2013**, 253, 511–527.
5. M.A Gilles-Gonzalez, G. Gonzalez, *J. Inorg. Biochem.* **2005**, 99, 1–22.
6. A. Farhana, V. Saini, A. Kumar, J. R. Lancaster, Jr., A. J. C. Steyn *Antioxid. Redox Signal.* **2012**, 17, 1232–1245.
7. T. G. Spiro, A. A. Jarzecki, *Curr. Opin. Chem. Biol.* **2001**, 5, 715–723.
8. S. Aono, *Antioxid. Redox Signal.* **2011**, 16, 678–686.
9. J. S. Olson, and A. Ghosh, *The Smallest Biomolecules: Diatomics and their Interactions with Heme Proteins: Diatomics and their Interactions with Heme Proteins*, Elsevier, Amsterdam The Netherlands **2008**
10. M. A. Gilles-Gonzalez and G. Gonzalez *J Appl Physiol* **2004**, 96,774–783.
11. W. Zeng, Vibrational dynamics of heme proteins: a study by nuclear resonance vibrational spectroscopy and resonance Raman spectroscopy. *Physics Dissertations* **2010**, Paper 20.
12. J. S. Olson, and G. N. Jr Phillips, *J. Biol. Inorg. Chem.* **1997**, 2, 544–552.

13. V. Daskalakis, C. Varotsis, *Int J Mol Sci.* **2009**, *10*, 4137–4156.
14. F. Germani, L. Moens, S. Dewilde, *Adv Microb Physiol.* **2013**, *63*, 1-47.
15. K. R. Rodgers, *Curr. Opin. Chem. Biol.* **1999**, *3*, 158–167.
16. J. Green, J. C. Crack, A. J. Thomson, N. E. LeBrun, *Curr. Opin. Microbiol.* **2009**, *12*, 145–151.
17. H. M. Girvan, A. W. Munro *J. Biol. Chem.* **2013**, *288*, 13194-13203.
18. M. Kajimura, R. Fukuda, R. M. Bateman, T. Yamamoto, M. Suematsu, *Antioxid Redox Signal.* **2010**, *13*, 157–192.
19. T. A. K. Freitas, S. Hou, E. M. Dioum, J. A. Saito, J. Newhouse, G. Gonzalez, M. A. Gilles-Gonzalez, M. Alam, *Proc Natl Acad Sci U S A.* **2004**, *101*, 6675–6680.
20. H. Szurmant, G. Ordal, *Mol. Biol. Rev.* **2004**, *68*, 301-319.
21. V. M. Delgado-Nixon, G. Gonzalez, M. A. Gilles-Gonzalez, *Biochemistry* **2000**, *39*, 2685–2691.
22. J. R. Tuckerman, G. Gonzalez, E. H. S. Sousa, X. Wan, J. A. Saito, M. Alam, M. A. Gilles Gonzalez, *Biochemistry* **2009**, *48*, 9764–9774.
23. S. Hou, C. Belisle, S. Lam, M. Piatibratov, V. Sivozhelezov, H. Takami, *Extremophiles* **2001**, *5*, 351–354.
24. S. Hou, T. Freitas, R. W. Larsen, M. Piatibratov, V. Sivozhelezov, A. Yamamoto, E. A. Meleshkevitch, M. Zimmer, G. W. Ordal, M. Alam, *Proc. Natl. Acad. Sci. USA* **2001**, *98*, 9353-9358.
25. H. Park, C. Suquet, M. I. Savenkova, J. D. Satterlee, C. Kang, *Acta Cryst.* **2002**, *58*, 1504–1506.

26. W. Zhang, G. N. Jr. Phillips, *Structure* **2003**, *11*, 1097-1110.
27. J.A. Saito, X. Wan, K. S. Lee, S. Hou, M. Alam, *FEBS Lett.* **2008**, *582*, 1840–1846.
28. M. A. Gilles-Gonzalez and G. Gonzalez *J Appl Physiol* **2004**, *96*, 774–783.
29. N. A. Possling, G. Becker, C. Pesavento, N. Tschowri, R. Hengge, *Microbiology* **2009**, *155*, 1318–1331.
30. L. Tagliabue, A. Maciag, D. Antoniani, P. Landini, *FEMS Immunol Med Microbiol.* **2010**, *59*, 477-484
31. S. Aono *Dalton Trans.* **2008**, *24*, 3137-3146.
32. J. B. Stock, G. S. Lukat, A. M. Stock, *Annu Rev of Biophys Biophys Chem* **1991**, *20*, 109–136.
33. D. F. Blair, *Annu Rev Microbiol B*, **1995**, *49*, 489–522.
34. M. Stock, L. Robinson, P. Goudreau, *Annu Rev Biochem.* **2000**, *69*, 183- 215.
35. S. Hou, R. W. Larsen, D. Boudko, C. W. Riley, E. Karatan, M. Zimmer, G. W. Ordal, M. Alam *Nature* **2000**, *403*, 540-544.
36. W. Zhang, J. S. Olson, G. N. Jr. Phillips G.N.Jr.; *Biophys. J.* **2005**, *88*, 2801-2815.
37. S. Ito, Y. Araki, A. Tanaka, J. Igarashi, T. Wada, T. Shimizu, *J. Inorg. Biochem.* **2009**, *103*, 989–996.
38. S. Bischoff, W. Ordal, *Mol Microbiol.* **1992**, *18*, 2715-23.
39. S. Aono, T. Kato, H. Nakajima, T. Ohta, T. Uchida, T. Kitagawa, *J. Biol. Chem.* **2002**, *277*, 13528-13538.

40. K. Wuichet, R. Alexander, I. Zhulin, *Methods Enzymol.* **2007**, *422*, 1–31.
41. T. S. Shimizu, N. Le Novèrn, M. D Levin, A. J. Beavil, B. J. Sutton, D. Bray, *Nat Cell Biol.* **2000**, *2*, 792-796.
42. J. A. Gegner, D.R. Graham, A. F. Roth, F. W. Dahlquist, *Cell.* **1992**, *70*, 975-982.
43. S. Djordjevic, A. M. Stock, *Nat Struct Biol.* **1998**, *5*, 446-450.
44. H. F. Bunn, R. O. Poyton, *Physiol Rev.* **1996**, *76*, 839-885.
45. J. J. Falke, R. B. Bass, S. L. Butler, S. A. Chervitz, M. A. Danielson, *Annu Rev Cell Dev Biol.* **1997**, *13*, 457-512.
46. M. D. Coleman, R. B. Bass, R. S. Mehan, J. J. Falke, *Biochemistry* **2005**, *44*, 7687-95.
47. A. G. Vescovi, M. I. Sciara, M. E. Castelli, *Curr. Opin. Microbiol.* **2010**, *13*, 210–218.
48. J. S. Parkinson, *Cell* **1993**, *73*, 857-871.
49. H. Yoshimura, S. Yoshioka, Y. Mizutani, S Aono, *Biochem. Biophys. Res. Comm.* **2007**, *357*, 1053–1057
50. A. Mokdad, M. Nissen, J. D. Satterlee, R. W. Larsen, *FEBS Lett.* **2007**, *581*, 4512–4518.
51. Y. Yoshida, H. Ishikawa, S. Aono, Y. Mizutani, *Biochim. Biophys. Act.* **2012**, *1824*, 866–872.
52. H. Yoshimura, S. Yoshioka, K. Kobayashi, T. Ohta, T. Uchida, M. Kubo, T. Kitagawa, S. Aono, *Biochemistry* **2006**, *45*, 8301-8307.
53. S. F. El-Mashtoly, M. Kubo, Y. Gu, H. Sawai, S. Nakashima, T. Ogura, S. Aono T.

- Kitagawa, *J. Biol. Chem.* **2012**, *287*, 19973-19984.
54. S. Aono, T. Kato, M. Matsuki, H. Nakajima, T. Ohta, T. Uchida, T. Kitagawa, *J. Biol. Chem.* **2002**, *277*, 13528-13538.
55. S. F. El-Mashtoly, Y. Gu, H. Yoshimura, S. Yoshioka, S. Aono, T. Kitagawa, *J. Biol. Chem.* **2008**, *283*, 6942-6949.
56. M. Martinková, K. Kitanishi, T. Shimizu, *J. Biol. Chem.* **2013**, *288*, 27702-27711.
57. T. Ohta, H. Yoshimura, S. Yoshioka, S. Aono, T. Kitagawa, *J. Am. Chem. Soc.* **2004**, *126*, 15000-15001.
58. E. Pinakoulaki, H. Yoshimura, S. Yoshioka, S. Aono, C. Varotsis, *Biochemistry* **2006**, *45*, 7763-7766.
59. A. J. Schmidt, D. A. Ryjenkov, M. Gomelsky, *J. Bacteriol.* **2005**, *187*, 4774.
60. L. Tagliabue, D. Antoniani, A. Maciag, P. Bocci, N. Raffaelli, P. Landini, *Microbiology*, **2010**, *156*, 2901-2911.
61. J. A Mayfield, C. A Dehner, J. L. DuBois, *Curr. Opin. Chem. Biol.* **2011**, *15*, 260-266.
62. A. D'Argenio, S. I. Miller, *Microbiology*, **2004**, *150*, 2497-2502.
63. U. Jenal, *Curr. Opin. Microbiol.* **2004**, *7*, 185-191.
64. R. Hengge, *Nat. Rev. Microbiol.* **2009**, *7*, 263-273
65. R. Simm, M. Morr, A. Kader, M. Nimtz, U. Römling, *Molec. Microbiol.* **2004**, *53*, 1123-1134

66. D. A. Ryjenkov, M. Tarutina, O. V. Moskvina, M. Gomelsky *J. Bacteriol.* **2005**, *187*, 1792-1801.
67. N. Ausmees, R. Mayer, H. Weinhouse, G. Volman, D. Amikam, M. Benziman, M., *et al.*, *FEMS Microbiol. Lett.* **2001**, *204*, 163-167.
68. K. Kitanishi, K. Kobayashi, Y. Kawamura, I. Ishigami, T. Ogura, K. Nakajima, J. Igarashi, A. Tanaka, T. Shimizu, *Biochemistry* **2010**, *49*, 10381-10393.
69. M. Benziman, P. Ross, D. Amikam, R. Mayer, H. Weinhouse, P. Ohana, D. Michaeli.. *The role of cyclic diguanylic acid in the regulation of bacterial cellulose synthesis*, 519-535. In C. Schuerch (ed.), *Cellulose and wood-chemistry and technology*, John Wiley & Sons Inc., New York USA **1989**.
70. K. Nakajima, K. Kitanishi, K. Kobayashi, N. Kobayashi, J. Igarashi, T. Shimizu, *J. Inorg. Biochem.* **2012**, *108*, 163-170.
71. J. Green, J. C. Crack, A. J. Thomson, N. E. LeBrun, *Curr. Opin Microbiol.* **2009**, *12*, 145-151.
72. T. Schirmer, U. Jenal, *Nat. Rev. Microbiol.* **2009**, *7*, 724-735.
73. H. Kurokawa, D.S Lee, M. Watanabe, I. Sagami, B. Mikami, C.S. Raman, T. Shimizu, *J Biol Chem.* **2004**, *279*, 20186-20193.
74. H. Park, C. Suquet, J. D. Satterlee, C. Kang, *Biochemistry* **2004**, *43*, 2738-2746.
75. B. Hao, C. Isaza, J. Arndt, M. Soltis, M.K Chan, *Biochemistry* **2002**, *41*, 12952-12958.
76. J. Green, M. S. Paget, *Nat. Rev. Microbiol.* **2004**, *2*, 954-966.
77. S. Hirata, T. Matsui, Y. Sasakura, S. Sugiyama, T. Yoshimura, I. Sagami, T. Shimizu, *Eur. J. Biochem.* **2003**, *270*, 4771-4779.
78. T. Yoshimura, I. Sagami, Y. Sasakura, T. Shimizu *J. Biol. Chem.* **2003**, *278*, 53105-

- 53111.
79. Y. Sasakura, S. Hirata, S. Sugiyama, S. Suzuki, S. Taguchi, M. Watanabe, T. Matsui, I. Sagami, Toru Shimizu, *J. Biol. Chem.* **2002**, *277*, 23821-23827.
80. Sato, Y. Sasakura, S. Sugiyama, I. Sagami, T. Shimizu, Y. Mizutani, T. Kitagawa, *J. Biol. Chem.* **2002**, *277*, 32650–32658.
81. T. Tomita, G. Gonzalez, A.L. Chang, M. Ikeda-Saito, M.A. Gilles-Gonzalez, *Biochemistry* **2002**, *41*, 4819–4826.
82. S. F. El-Mashtoly, S. Nakashima, A. Tanaka, T. Shimizu, T. Kitagawa *J. Biol. Chem.* **2008**, *283*, 19000-19010.
83. S. F. El-Mashtoly, T. Kitagawa, *Pure Appl. Chem.* **2008**, *80*, 2667–2678.
84. A. Tanaka, H. Takahashi, T. Shimizu, *J. Biol. Chem.* **2007**, *282*, 21301-21307.
85. A. Tanaka, T. Shimizu, *Biochemistry* **2008**, *47*, 13438–13446.
86. Y. Ishitsuka, Y. Araki, A. Tanaka, J. Igarashi, O. Ito, T. Shimizu, *Biochemistry* **2008**, *47*, 8874–8884.
87. S. F. El-Mashtoly, H. Takahashi, H. Kurokawa, A. Sato, T. Shimizu, T. Kitagawa, *J. Raman Spectrosc.* **2008**, *39*, 1614–1626.
88. S. F. El-Mashtoly, M. Kubo, S. Nakashima, T. Shimizu, T. Kitagawa, *J. Phys. Chem. Lett.* **2011**, *2*, 2212–2217.
89. M. Watanabe, T. Matsui, Y. Sasakura, I. Sagami, T. Shimizu, *Biochem. Biophys. Res. Commun.* **2002**, *299*, 169–172.
90. S. F. El-Mashtoly, H. Takahashi, T. Shimizu, T. Kitagawa, *J. Am. Chem. Soc.* **2007**, *129*, 3556–3563.

91. S. Ito, J. Igarashi, T. Shimizu, J. Inorg. Biochem. **2009**, *103*, 1380–1385.
92. A. Lechauve, L. Bouzhir-Sima, T. Yamashita, M.C. Marden, M.H. Vos, U. Liebl, L. Kiger, *J Biol Chem.* **2009**, *284*, 36146–36159.
93. S. Taguchi, T. Matsui, J. Igarashi, Y. Sasakura, Y. Araki, O. Ito, S. Sugiyama, I. Sagami, T. Shimizu, *J. Biol. Chem.* **2004**, *279*, 3340–3347.
94. M. Tarnawski, T. R. M. Barends, E. Hartmann, I. Schlichting, *Acta Cryst. D* **2013**, *69*, 1045–1053.
95. F. Germani, L. Moens, S. Dewilde, *Adv Microb Physiol* **2013**, *63*, 1–47.
96. T. Shimizu, *Biosensors* **2013**, *3*, 211–237.



CHAPTER 3

Methodology : FTIR and Time-Resolved Step-Scan FTIR Spectroscopy

Andrea Pavlou

3.1 Introduction

Vibrational spectroscopy techniques are defined as the most time effective and accurate tools to obtain information about the molecular conformation, structure and interactions within a system, rather than merely permitting the observation of the presence or absence of certain functional groups. These techniques measure chemical bond – associated vibrational energy levels with high selectivity, resulting in a distinctive spectrum (“fingerprint”) and thus allowing the characterization, structure elucidation and reaction monitoring of a sample. The principal constituents of vibrational spectroscopy techniques are Infrared (IR) and Raman spectroscopy.^{1,2}

Although both techniques implicate the investigation of the interaction of radiation with molecular vibrations, they diverge in the mode in which photon energy is transmitted to the molecule by changing its vibrational state. Specifically, two physical means exist that molecular vibrations can be excited by: a) the absorption of light quanta and b) the inelastic scattering of photons. Raman spectroscopy consists of an event that results from the scattering of monochromatic light by the vibrating molecules. It involves a transient change in polarizability where the electrons distributed around a molecular bond are distorted. The temporary induced dipole then disappears upon bond relaxation and radiation reemission. In contrast, IR spectroscopy measures transitions between molecular vibrational energy levels as a result of the absorption of mid-IR radiation. In the IR absorption process (**Figure 3.1**), direct absorption of photons is attained by polychromatic light irradiation of molecules, that contains photons of energy equivalent to the energy difference between two vibrational energy levels, the n (ground state) and the m (1st excited state) vibrational state.^{3,4}

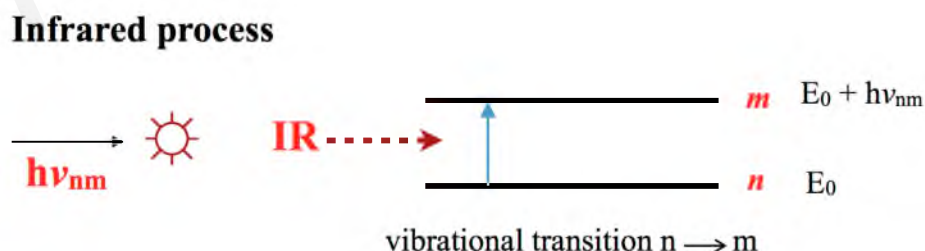


Figure 3.1 Schematic representation of the IR vibrational process.

The selection rule governing the IR absorption process states that the vibration is IR active,

only should there be a change in dipole moment during the vibration. Consequently, if the vibrations of a diatomic molecule include changes in dipole moment, then the molecule interacts with the infrared range of electromagnetic radiation, causing absorption at a particular energy. Depending on the molecule, similar or distinctive vibrational transitions could be probed in IR and Raman spectroscopy. Hence, the two vibrational spectroscopy techniques are usually used in conjunction in order to enable comparison and provide complementary information.^{3,4}

3.2 FTIR spectroscopy

The principle of infrared spectroscopy (**Figure 3.1**) is based on the notion that, for a molecule found on the ground electronic state, transitions between quantized vibrational energy levels occur. The energies of these vibrational transitions and the strength of their interaction with the IR radiation result in spectral observable parameters such as frequency and band intensity of vibrational modes. For example, the energy difference for transitions amid the ground state ($n=0$) and the 1st excited state ($n=1$) of the majority of vibrational modes relates to the energy of radiation in the mid-infrared spectrum (400 to 4000 cm^{-1}).

Two essential elements to the IR absorption process are a) radiation frequency and b) molecular dipole moment. According to the classical electromagnetic theory, the interaction of the radiation frequency is equivalent to the natural frequency of a particular normal mode of vibration. To define this frequency let's assume a simple diatomic molecule A–B as spheres with masses m_A and m_B , adjoined by a mass-less spring denoting the intramolecular interactions between the atoms (**Figure 3.2**).³⁻⁶

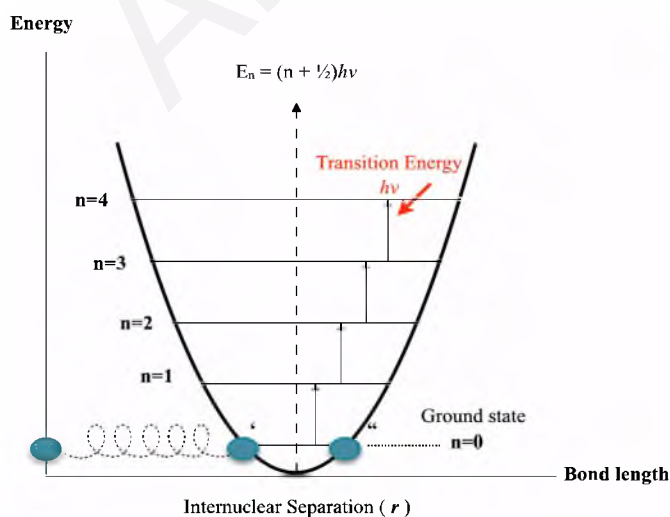


Figure 3.2 Permitted energy levels and transitions in a diatomic molecule that executes simple harmonic motion. For the ground state ($n=0$), $E = \frac{1}{2}hv$. This is called the zero point energy. Adapted from Ref.7 with modifications.

Upon translation of the spheres along the x -axis from the equilibrium position, the potential energy V of the system according to Hooke's law is defined as:

$$V = \frac{1}{2}k \cdot \Delta x^2 \quad (3.1)$$

where the k is the force constant that defines the strength of the bond. The system also carries kinetic energy T due to the oscillation motion which is given by:

$$T = \frac{1}{2}\mu \cdot (\Delta x)^2 \quad (3.2)$$

where μ is the reduced mass equal to:

$$\mu = \frac{m_A \cdot m_B}{m_A + m_B} \quad (3.3)$$

Since energy is conserved, the sum of the first derivatives of V and T must be equal to zero and therefore:

$$\frac{dV}{dt} + \frac{dT}{dt} = \frac{1}{2}\mu \frac{d(\Delta x^2)}{dt} + \frac{1}{2}k \frac{d(\Delta x^2)}{dt} = 0 \quad (3.4)$$

which translates to Newton's equation of motion:

$$\frac{d^2\Delta x}{dt^2} + \frac{k}{\mu}\Delta x = 0 \quad (3.5)$$

Eq. (3.5) corresponds to the differential equation of a harmonic motion and can be solved as:

$$\Delta x = A \cdot \cos(\omega t + \varphi) \quad (3.6)$$

where A , ω and φ denote the amplitude, circular frequency and phase respectively. Relating Eq. (3.6) with (3.5) results to:

$$\frac{d^2\Delta x}{dt^2} + \omega^2\Delta x = 0 \quad (3.7)$$

Comparing Eq. (3.7) with (3.5) generates the frequency of molecular vibration equation:

$$\nu_m = \frac{1}{2\pi} \sqrt{\frac{k}{\mu}} \quad (3.8)$$

In order for the energy to be transferred from the IR photon to the molecule via absorption the molecular vibration must cause a change to the dipole moment of the molecule.

The dipole moment $\mu_{(M)}$ for a molecule (M) is a function of the magnitude of the atomic charges e and their positions r given by the equation:

$$\mu_{(M)} = e \cdot r \quad (3.9)$$

Vibrational transitions for a heteronuclear diatomic molecule (AB) arise if oscillation of the molecule about its equilibrium bond configuration exist. If the frequencies of light and of the vibrating dipole coincide then IR absorption occurs. The dipole moment depends on the internuclear distance r and can be expressed as a Taylor expansion:

$$\mu_{(AB)} = \mu_0 + \left(\frac{\partial\mu}{\partial r}\right)_0 \cdot q + \frac{1}{2!} \left(\frac{\partial^2\mu}{\partial r^2}\right)_0 \cdot q^2 + \dots \quad (3.10)$$

where q is the vibrational coordinate equal to $r - r_e$, r_e being the equilibrium bond length and μ_0 the permanent dipole moment at equilibrium ($q=0$). The relation $(\partial\mu/\partial r)_0$ denotes the change in the dipole moment with distance calculated at the equilibrium internuclear distance.

If equation (3.10) is substituted in equation (3.9), the relation of transition dipole moment (TDM) μ_{nm} is obtained, from which we can evaluate the strength of interaction that causes a transition between two vibrational levels $m \rightarrow n$. For the vibration that corresponds to the transition from the vibrational level m to level n of the electronic ground state to be IR active, $\mu_{nm} \neq 0$. According to Fermi's golden rule, the transition probability between the two vibrational levels is relative to $(\partial\mu/\partial q)^2$ and the intensity of the transition is defined by the Beer-Lambert Law as:

$$I = I_0 \cdot 10^{-\varepsilon(\bar{\nu})c\ell} \quad (3.11)$$

where $\varepsilon(\bar{\nu})$ is the molar extinction coefficient length, ℓ the path length of the cell, and c the molar concentration. The I and I_0 represent the transmitted and incident intensities respectively.^{1,3,5,6}

3.2.1 Michelson Interferometer

The primary component of an FTIR spectrometer is the interferometer and it relies its function on that of the two-beam interferometer originally designed by Michelson in 1891. The purpose of this device is to divide a beam of radiation into two paths and then recombine the two beams after a path difference has been created, henceforth to initiate a condition that

favors the occurrence of interference between the two beams. The variation of intensity of the beam emerging from the interferometer is measured as a function of optical path difference (retardation δ) by a detector.

Specifically, a Michelson interferometer (**Figure 3.3**) comprises of two equally perpendicular mirrors, with one being able to translate horizontally along its axis. When the translating mirror is being moved at a constant velocity, it is known as a continuous-scan interferometer. Rather, when the translating mirror is being held stationary at proportionately distant points for fixed brief intervals, ultimately stepping rapidly between these points, it is referred to as a step-scan interferometer. A 45-degree angled beamsplitter intersects the fixed mirror and the translating mirror, allowing a perfectly parallel beam of external source radiation to be partially reflected to the fixed mirror (at point F) and partially transmitted to the translating mirror (at point T). The beams eventually return to the beamsplitter, interfering and are again partially reflected and partially transmitted. The Fourier transform spectrometer spectral information is ultimately produced by the intensity difference between the beams reaching the detector and returning to the source as a function of retardation.

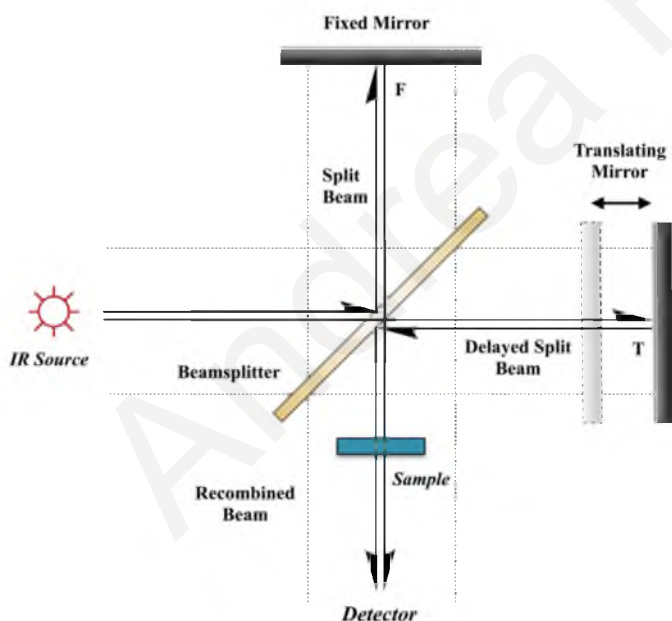


Figure 3.3 The fundamental components and the complete path of the radiation beam in a Michelson Interferometer. Adapted from Ref 5 with modifications.

If we assume a perfectly monochromatic light source, depending on the optical retardation, the source beams can interfere either constructively or destructively. At zero retardation where the distance of the fixed and translating mirrors from the beamsplitter is equal, upon recombination the two beams are completely in phase (**Figure 3.4**). In this case, the beams interfere constructively, with the intensity of the beam reaching the detector defined as the sum of the intensities of the beams and the intensity of the beam returning to

the source equal to zero. Conversely, if the translating mirror is shifted a distance $\frac{1}{4} \lambda$, then the optical retardation is $\delta = \frac{1}{2} \lambda$ and the two beams upon recombination are out of phase. At this instance the beams are said to interfere destructively where no source light reaches the detector.

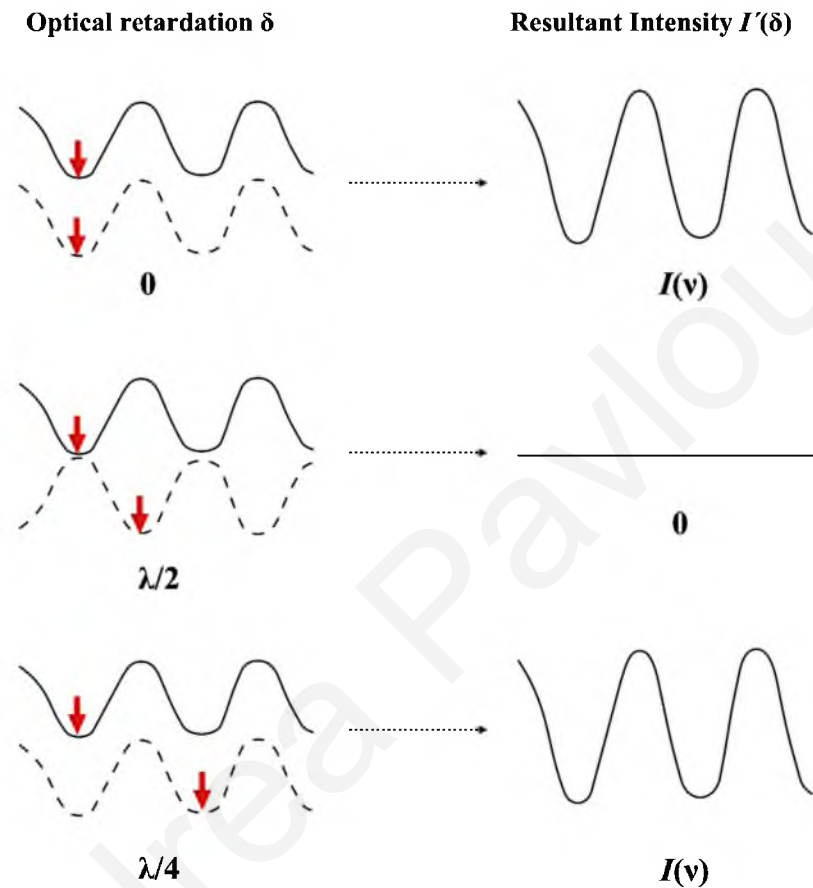


Figure 3.4 Schematic representation of the phase of the electromagnetic waves from the fixed and translating mirrors of the interferometer at different optical retardation values. Adapted from Ref 5.

The intensity of the beam that passes the detector measured as a function of optical retardation δ and the radiation wavelength λ for an ideal system is defined by the mathematical relation:

$$I'(\delta) = 0.5I(\lambda) \left[1 + \cos \frac{2\pi\delta}{\lambda} \right] \quad (3.12)$$

The latter is essentially composed of two components (a) the DC static component equal to $0.5I(\lambda)$ which is of no importance for spectroscopy and (b) the AC variable component equal to $0.5I(\lambda) \cos \left(\frac{2\pi\delta}{\lambda} \right)$. Thus, Eq. (3.12) can be rearranged as an

interferogram $I(\delta)$:

$$I(\delta) = 0.5I(\lambda) \cos\left(\frac{2\pi\delta}{\lambda}\right) \quad (3.13)$$

It is rationally impossible to have an ideal system. Consequently, a number of different factors such as the beamsplitter efficiency and the detector response can affect the magnitude of the signal that reaches the detector. Therefore, Eq. (3.13) is modified as:

$$I(\delta) = B(\lambda) \cos\left(\frac{2\pi\delta}{\lambda}\right) \quad (3.14)$$

where $B(\lambda)$ defines the intensity of the signal in terms of wavelength λ , as it is modified by the instrumental non-ideality. The intensity $I(\delta)$ denotes the cosine Fourier transform of $B(\lambda)$, hence the designation as FTIR spectroscopy.

If the translating mirror is scanned at a constant velocity, it is essential to consider the relation of the interferogram as it is modified with time $S(t)$ rather than retardation $S(\delta)$. The retardation in time t after $\delta=0$ is defined as $\delta = 2vt$. Based on the latter, Eq.(3.14) transforms to:

$$S(t) = B(\lambda) \cos\left(\frac{2\pi}{\lambda} \cdot (2vt)\right) \quad (3.15)$$

When the radiation source is not monochromatic but rather a broadband spectral source, then the interferogram can be represented by the integral:

$$S(\delta) = \int_{-\infty}^{+\infty} B(\lambda) \cos\left(\frac{2\pi\delta}{\lambda}\right) d\lambda \quad (3.16)$$

which represents the half part of a cosine Fourier transform pair, with the other being:

$$B(\lambda) = \int_{-\infty}^{+\infty} S(\delta) \cos\left(\frac{2\pi\delta}{\lambda}\right) d\delta \quad (3.17)$$

and since $S(\delta)$ is an even function, Eq. (3.17) can be rearranged as:

$$B(\lambda) = 2 \int_0^{+\infty} S(\delta) \cos\left(\frac{2\pi\delta}{\lambda}\right) d\delta \quad (3.18)$$

From Eq. (3.18) one could argue that theoretically it is possible to measure the complete 0 to $\infty \text{ cm}^{-1}$ frequency range at infinitely high resolution. However, this argument asserts that the translating mirror of the interferometer moves an infinitely long distance, with retardation δ varying in the range of 0 to $\infty \text{ cm}^{-1}$. In practice, if the first time the two waves

are in phase is at $\delta = (\Delta\lambda)^{-1}$ and if the maximum retardation the interferometer can achieve is Δ_{\max} , then the greatest resolution $\Delta\lambda$ that can be obtained is $\Delta\lambda = (\Delta_{\max})^{-1}$.⁵

3.3 Time-resolved step-scan FTIR spectroscopy

The need for identification and characterization of transient events that take place as fast as the nanosecond time scale led to the development of time-resolved step-scan FTIR spectroscopy. As briefly discussed in Section 3.3, for the implementation of TRS²-FTIR a step-scan interferometer is employed rather than a continuous-scan interferometer. To elaborate, in the step-scan mode, the interferometer moving mirror is being held stationary at the first interferogram data position x_n ; the reaction is initiated, and the time dependence of the intensity change at this interferogram position x_n is measured. Then the interferometer moves “step-wise” to the next interferogram data position x_{n+1} and the reaction is repeated and measured again. The final set of interferograms results from the sum of the total signal measurements at each sampling position the interferometer moving mirror is being held stationary (**Figure 3.5**).

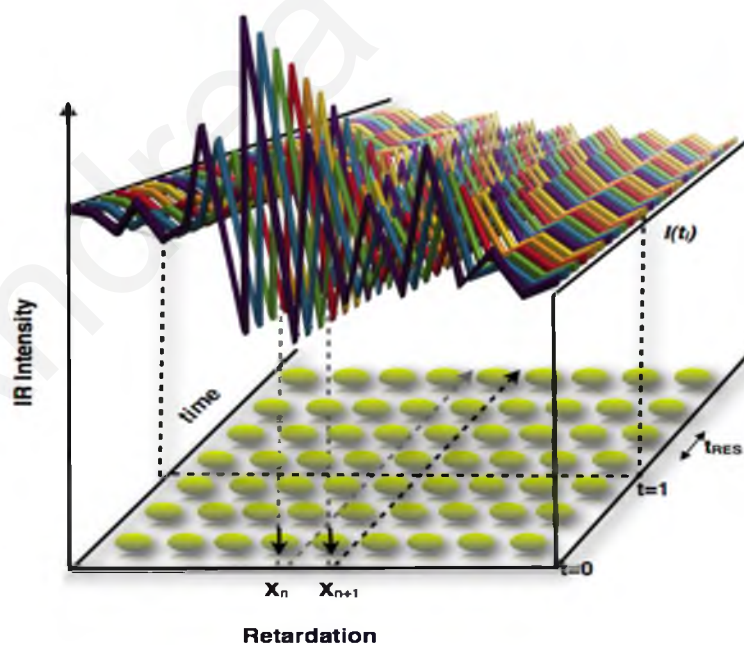


Figure 3.5 Schematic representation of the “stepping” process taking place at every data sampling position the interferometer moving mirror is held stationary during a time-resolved step-scan FTIR measurement. Adapted from Ref 5 with modifications.

The success of this technique relies on the unvaryingly increase of optical path

difference of approximately 1–2 nm, after each equally spaced data position the interferometer translating mirror is held stationary, so as to achieve the best signal-to-noise ratio. The positions at which the translating mirror is briefly held fixed are modulated by a He-Ne laser. The laser serves as the means for monitoring the movement and stability of the mirror at each retardation step. For this reason, TRS²-FTIR is very sensitive to disturbances from the surrounding environment and thus a fundamental condition for achieving the best signal-to-noise ratio is performing a substantial number of measurement repetitions.⁵ A considerable advantage of TRS²-FTIR spectroscopy over other time-resolved IR techniques lies in its time resolution that allows the monitoring of dynamic processes taking place concurrently at scale from nanoseconds to seconds. Its time resolution is ultimately limited only by the response time of the detector and the digitizer. It is notable to mention that the step-scan method is only applicable if the reaction induced by the trigger is fully reversible because the trigger must be repeated many times. Hence, very fast reactions must be repeated at each retardation step of the step-scan interferometer. For non-reversible reactions continuous-flow experiments can be performed.¹⁰

3.4 Time-resolved step-scan FTIR spectroscopy experimental setup

A typical experimental setup that can be used for the time-resolved step-scan FTIR experiments is depicted in **Figure 3.6**. More elaborate information and details of the procedure and data processing specifically used for the investigation of heme-based oxygen sensor proteins are included in Chapter 4. As can be observed, the main component of the setup is the FTIR spectrometer which is equipped with a liquid nitrogen-cooled photovoltaic MCT (Mercury Cadmium Telluride) detector. The photovoltaic HgCdTe detector is a semiconductor that bases its operation on the existence of a *pn* junction between a region where the conductivity is due to electrons and a region where the conductivity is due to holes. When incident light forays the device, voltage is generated and thus signal detection occurs. The required operation of the MCT detector in low temperatures allows for low noise and higher sensitivity, rendering it ideal for the detection of signals with intensity as low as 10⁻⁴ absorbance units.^{7,8} For a complete system, it is necessary to include a laser which will not only trigger the reaction in the sample, but it will also serve as the reference point for the initiation of the cycle within which the measurement takes place. For our experimental procedure we have used the 532 nm pulse from a Nd:YAG laser.¹¹

3. A. Barth, C. Zscherp, *Quart. Rev. Biophys.* **2002**, 35, 369–430.
4. A. Stuart, *Infrared Spectroscopy: Fundamentals and Applications*, Wiley, New York U.S.A **2004**.
5. P. R. Griffiths, J. A. de Haseth, *Fourier Transform Infrared Spectrometry*, 2nd ed. Wiley, New Jersey U.S.A **2007**.
6. J. Brown, A. Carrington, *Rotational Spectroscopy of Diatomic Molecules* Cambridge University Press, New York **2003**.
7. A. Beiser, *Concepts of Modern Physics*, 5th Ed., McGraw-Hill, New York City, New York, USA **1995**.
8. A. Rogalski, *Rep. Prog. Phys.* **2005**, 68, 2267-2336.
9. M. Baker, *HgCdTe Photovoltaic Infrared Detectors*, in *Mercury Cadmium Telluride*, Wiley, Chichester UK **2010**.
10. Z.Y. Zhou, S.G. Sun, *Electrochim. Acta.* **2005**, 50, 5163–5171.
11. K. A. Vincent, *Phil. Trans. R. Soc. A.* **2010**, 368, 3713–3731.



CHAPTER 4

Materials and Experimental Procedures

Andrea Pavlou

4.1 Materials

4.1.1 Expression and purification of wild type full length and truncated sensor domain forms of HemAT

Expression and purification of HemAT-*Bs* has been performed by the group of Prof. Shigetoshi Aono at the Okazaki Institute of Integrative Biosciences, National Institutes for Natural Sciences, Okazaki Japan.

The heme-based oxygen sensor from *Bacillus subtilis*, HemAT-*Bs*, has been expressed and purified according to published procedures (Aono et al. 2002; Pinakoulaki et al. 2006; Yoshimura et al. 2006). Briefly, HemAT-*Bs* has been expressed in *E. coli* BL21(DE3) under the control of the T7 promoter in pET24(+) vector. HemAT-*Bs* was obtained as a C-terminal 6×His-tagged protein. All mutants were prepared using a Quick Change Site-Directed Mutagenesis Kit. The *E. coli* BL21 (DE3) harboring the expression vector of HemAT-*Bs* was grown aerobically at 37°C for 4 hours in TB medium containing 30 µg/mL kanamycin. The expression was induced by adding 1 mM of isopropyl-1-thio-D-galactopyranosid (IPTG), and then the cultivation continued at 22°C for 18 hours. The cells were harvested by centrifugation at 4,000×g and stored at -80°C until use. Purification of HemAT-*Bs* was carried out as follows. The cells were thawed and re-suspended in 50 mM Tris-HCl buffer (pH 8.0) containing 15 mM glycine and 1 M NaCl, and then broken by sonication. The resulting suspension was centrifuged at 28,000 rpm for 20 minutes, and the supernatant was loaded on a Ni-charged Chelating column. After washing the column with 50 mM Tris-HCl buffer (pH 8.0) containing 15 mM glycine and then with 1 M NaCl, and 50 mM Tris-HCl buffer (pH 8.0), the adsorbed proteins were eluted by 50 mM Tris-HCl buffer (pH 8.0) containing 100 mM imidazole. The fractions containing HemAT were combined and loaded on a HiTrap Q HP. The column was washed with 50 mM Tris-HCl buffer (pH 8.0) containing 100 mM NaCl, and then HemAT-*Bs* was eluted by increasing the concentration of NaCl in 50 mM Tris-HCl buffer (pH 8.0).

4.1.2 Design and isolation of full length and sensor domain mutants of HemAT

In addition to samples of the wild type full length and truncated sensor domain forms of HemAT, specific mutated forms of the protein have been designed and isolated so as to

investigate the role of each unique amino acid of the distal and proximal heme active site, in the process of gas recognition and discrimination, as well as in the intramolecular signal transduction mechanism. The mutations targeted residues Gln173, Lys115, Arg125, Arg91, Glu172, Tyr133, Tyr70, Thr95, His86 and Leu92 which were mutated to Q173A, K115A, R125A, R91A, E172A, Y133F, Y70F, T95A, H86A and L92A (**Figure 4.1**).

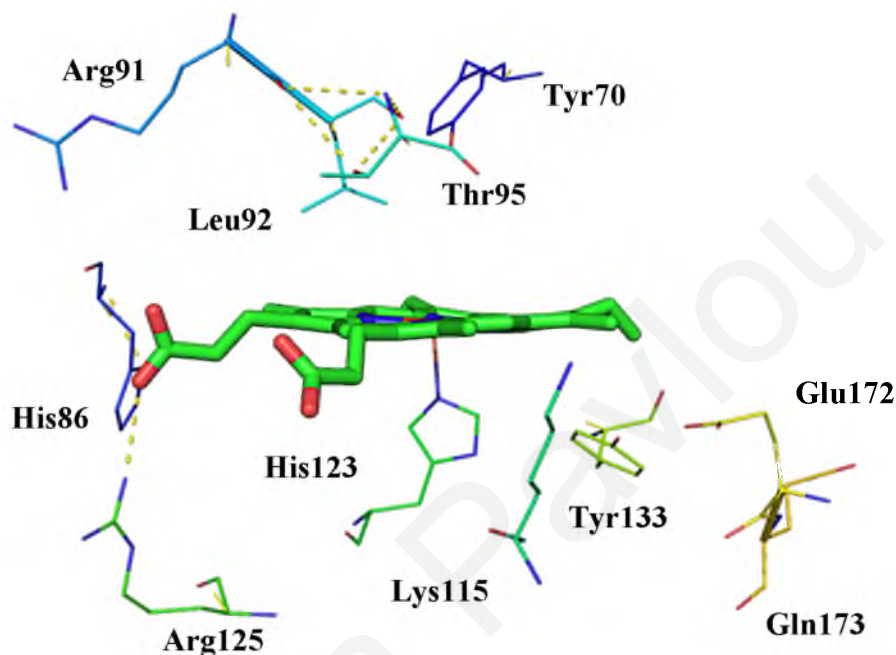


Figure 4.1 Schematic representation of the unliganded HemAT active site of the truncated sensor domain, along with the proposed mutated residues (PDB ID 1OR6).^{1,2,3}

Taking into consideration the structural information desired to be collected from the time-resolved step-scan FTIR experiments, the mutated heme active site amino acids were categorized into two groups. The first group included amino acids Thr95, Tyr70, Leu92 located in the distal site of the heme and Tyr133 located at the proximal site of the heme. These mutations have been designed to perturb the electrostatic field and steric interactions of the heme-bound ligand. The investigation of these mutations aimed in clarifying the residues that directly interact with the gaseous ligand, thereby setting the basis for understanding the ligand recognition and discrimination mechanism. The second group included amino acids Gln173, Lys115, Arg125, Arg91, Glu172 from which we expected to accumulate details on the implication of amino acids located in other sites, such as in cavities acting as storehouses for ligands, in the intramolecular signal transduction process.

4.1.3 Expression and purification of wild type heme domain YddV

Expression and purification of YddV has been performed by the group of Associate Prof. Marketa Martinkova at Charles University, Prague Czech Republic.

The expression and purification procedures for the DGC oxygen sensor protein YddV from the bacterium *Escherichia coli* were performed according to published procedures (Kitanishi et al. 2010; Nakajima et al. 2012). Briefly, *E. coli* BL21(DE3) (Stratagene, Novagen) was transformed with the appropriate plasmid (pET28a(+)/YddV-heme-Histag), plated on LB agar containing kanamycin (50 µg/ml) and incubated at 37 °C overnight. On the following day, a single colony was inoculated in TB medium containing kanamycin and shaken overnight at 250 rpm and 37 °C. The culture medium was then added to fresh TB medium (1:200 dilution) containing kanamycin and the mixture was again shaken at 250 rpm and 37 °C. Once the culture reached an OD600 of 1.2, the medium was cooled to 20 °C and protein expression was induced by the addition of 0.1 mM isopropyl β-D-thiogalactopyranoside and 0.45 mM δ-aminolevulinic acid, followed by further shaking for 24 hr. The *E. coli* cells were harvested by centrifugation for 30 min at 5,000 g and 4 °C, frozen in liquid nitrogen, and stored at -80 °C until protein extraction and purification. Frozen pellet cells were suspended in buffer A [50 mM Tris-HCl pH 8.0, 150 mM NaCl, 20 mM imidazole] containing 1 mM phenylmethanesulfonyl fluoride (PMSF) and lysed with 0.2 mg/ml lysozyme. The crude extract was sonicated and then centrifuged at 25,000g for 1 hr. The resulting supernatant was applied to a His Trap HP column (GE Healthcare, Amersham, U.K.) that had been pre-equilibrated with buffer A containing PMSF. The recombinant proteins were retained due to their (His)₆ tags and then eluted using a linear gradient from 20 to 300 mM imidazole in buffer A. Protein fractions were pooled and dialyzed against a 50 mM pH 8.0 Tris-HCl buffer overnight. Finally the purified proteins were quickly frozen in liquid nitrogen and stored at -80 °C.

4.1.4 Design and isolation of heme domain mutants of YddV

As there is no X-ray crystal structure available to date for the YddV protein, the mutagenesis work has relied on a combination of sequencing work and comparison with the HemAT-CN crystal structure. Through these comparative studies, it has been speculated that amino acids Leu65, and Tyr43 are the two distal site residues that seem to be playing a crucial role in gas recognition and discrimination (**Figure 4.2**) Hence, in addition to samples of the wild type form of YddV, a number of different mutations targeting Tyr43 and Leu65 have

been designed and isolated to investigate whether these residues are indeed of functional importance in the ligand recognition and signal transduction processes. Specifically Leu65 was mutated to L65T, L65M and L65Q, where Tyr43 was mutated to Y43A, Y43W and Y43F.

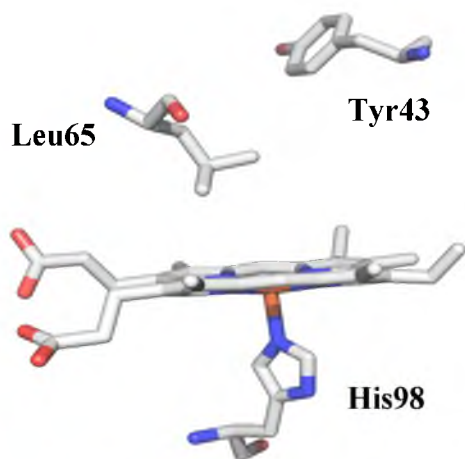


Figure 4.2 Proposed heme active site structure of the unliganded Fe(II) YddV based on the structure of the Fe(III)–cyanide complex of HemAT-Bs (PDB ID 1OR6).^{4,5}

4.1.5 Expression and purification of wild type isolated PAS domain of *EcDOS*

Expression and purification of *EcDOS* has been performed by the group of Prof. Teizo Kitagawa at the Okazaki Institute of Integrative Biosciences, National Institutes for Natural Sciences, Okazaki Japan.

The expression of the direct oxygen sensor protein *EcDOS* in *Escherichia coli* and the purification processes were performed according to previously published procedures (Sasakura et al.; 2002, Atsunari et al.; 2007). Concisely, the wild-type *EcDOS*-PAS protein was over-expressed in *E. coli* BL21 (DE3) with the use of pET28a(+)-*EcDOS*-PAS plasmid that contained an N-terminal His6 tag and thrombin cleavage site. The purification of the protein was carried out on ice at 4 °C. The protein over-expressed *E. coli* cells which were kept frozen at –80 °C were thawed and transferred in 50 mM potassium phosphate buffer, pH 7.5, containing 20 mM imidazole, 150 mM NaCl, 5% (v/v) glycerol, 1 mM PMSF (buffer A), and 0.1 mg/mL lysozyme. Following the sonication and centrifugation of the solution at 100,000 g for 30 min, the supernatant fractions were collected and ran on a nickel–nitrilotriacetic acid–agarose column. *EcDOS*-PAS fractions were eluted with a linear gradient of 20–300 mM imidazole in buffer A. The solution containing *EcDOS*-PAS was suspended in 20 mM Tris–HCl, pH 8.0, with 5% (v/v) glycerol (buffer B). To cleave the His-tag, thrombin protease (Wako Pure Chemicals) (1 unit/mg of protein) was added. Consequently, the sample solution was applied to a Ni-NTA agarose column, and His-tag-free *EcDOS*-PAS eluted in

the flow-through fractions using buffer B. DEAE column chromatography was performed on *EcDOS*-PAS, and eluted with a linear gradient of 0–1 M NaCl in buffer B. Following the dissolution of proteins against buffer B, purified *EcDOS*-PAS was concentrated with an Amicon Ultra filter (Millipore, Billerica, MA, USA).

4.1.6 Design and isolation of *EcDOS*-PAS domain mutants

To comprehend the gas-sensing mechanism of *EcDOS*, it is fundamental to determine the changes brought upon the heme and surrounding amino acids by ligand binding and dissociation. For this reason specific mutated forms of the heme active site residues have been designed and isolated, with amino acids Glu93, Met95, Arg97, Phe113, Trp110, Trp53, Tyr126 and Asn84 as illustrated in **Figure 4.3** mutated to E93I, M95A, R97I, R97A, F113T, W110F, W53F, Y126F and N84V respectively.

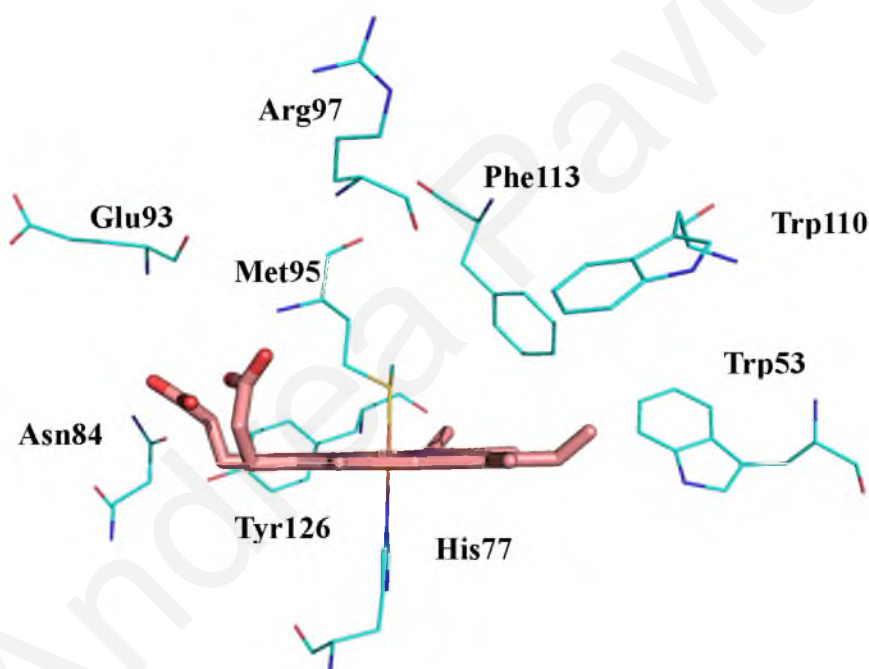


Figure 4.3 Schematic representation of the proposed mutated residues of the heme active site of the direct oxygen sensor protein *EcDOS* in the *Fe(II)* form with Met95 as the axial ligand. (PDB ID 1V9Z, 1S66).^{6,7,8}

4.1.7 List of chemicals used for the TRS² - FTIR experiments

- Sodium hydrosulfite (sodium dithionite) $\geq 82\%$ (RT) – Sigma Aldrich
- Deuterium oxide 99.9 atom % D – Sigma Aldrich
- Trizma® base primary standard and buffer, $\geq 99.9\%$ (titration) – Sigma Aldrich
- CO gas 99.9% – Linde Gas

4.2 Experimental Procedures

4.2.1 Time-resolved step-scan FTIR spectroscopy of heme-based sensor proteins

For the preparation of the HemAT-*Bs*, YddV and *Ec*DOSH-CO adducts, sodium dithionite ($\text{Na}_2\text{S}_2\text{O}_4$) reduced Fe(II) form protein samples were exposed to 1 atm of CO in an anaerobic cell to prepare the carbomonoxy adduct. They were then transferred to a tightly sealed FTIR cell with two CaF_2 windows under anaerobic conditions to avoid oxidation of the sample. The spacer used to define the path length for the full length and truncated sensor domain HemAT-*Bs* as well as for the *Ec*DOS-PAS samples was 6 μm . For the YddV samples the spacer used was 12 μm . CO gas was obtained from Linde. The static FTIR spectra were recorded with 4 cm^{-1} spectral resolution on a Bruker Vertex 70 FTIR spectrometer equipped with a liquid nitrogen cooled mercury cadmium telluride (MCT) detector. The HemAT-*Bs* samples used for the FTIR measurements had an enzyme concentration of $\sim 1\text{mM}$ for the full-length and $\sim 2\text{mM}$ for the truncated sensor domain protein. The samples were placed in 50mM Tris-HCl buffer pH 8 and pD 8. The heme domain YddV samples had an enzyme concentration of $\sim 1\text{mM}$ and were placed in 50mM Tris-HCl buffer pH 8 and pD 8. The *Ec*DOS-PAS samples had an enzyme concentration of $\sim 1.5\text{mM}$ and were placed in 50mM Tris-HCl buffer pH 7.5 and pD 7.5. The pD solutions were prepared in D_2O buffers, and are measured by using a pH meter assuming $\text{pD} = \text{pH}(\text{observed}) + 0.4$.

For the photodissociation TRS²-FTIR spectroscopy experiments, we employed the second harmonic 532 nm pulse (5 ns pulse width) from a Nd:YAG laser to photodissociate the bound ligand from the CO- adducts of HemAT, YddV and *Ec*DOS thus permit the observation of transient species on the nanosecond to millisecond time scale. Specifically as illustrated in **Figure 4.4**, to initiate the reaction the 532 nm pulses from a Continuum Minilite II Nd:YAG laser (5 ns width, 10 Hz) was used as a pump light (2 mJ/pulse) to photolyze the HemAT-CO, *Ec*DOSH and YddV-CO adducts. To achieve better overlap of the laser beam with the IR source beam, a 532nm laser beam expander (Newport Corporation) was used, expanding the laser beam by 2x. The measurements were performed on a Bruker Vertex 80V spectrometer equipped with the step-scan option. A vacuum pump was used to evacuate the interferometer compartment to a final pressure of 3 mbar. The FTIR spectrometer was placed on a Newport VH optical vibration isolator table to ensure that vibrational background noise from environmental sources was avoided. For the time resolved

experiments, a TTL (transistor-transistor logic) pulse provided by a digital delay generator (Quantum Composers, 9524) triggered in sequence the flashlamps, the Q-switch, and the FTIR spectrophotometer. Changes in intensity were recorded with a photovoltaic 20 MHz MCT detector (Kolmar Technologies KV100-1B-7/190 response limit 850 cm^{-1}) with a low-noise preamplifier that provided two outputs (AC and DC); the DC output used to furnish the static interferogram whereas the AC output used to furnish the laser-induced change of the interferogram. The analog signal was then digitized by a 180-kHz, 24-bit, internal analog-to-digital converter (ADC) for measurements in the μs to ms time scale and with a 200-MHz, 12-bit external MI analog-to-digital converter for measurements in the ns to μs time scale. The above process is repeated at every position the interferometer, moving mirror is being held stationary so as to achieve the best signal-to-noise ratio. A broadband interference optical filter (LP- 4200, Spectrogon) with a short wavelength cutoff at $4.2\ \mu\text{m}$ is used to limit the free spectral range from 4.2 to $11.8\ \mu\text{m}$. This leads to a spectral range of 2633 cm^{-1} , which is equal to an undersampling ratio of 6.

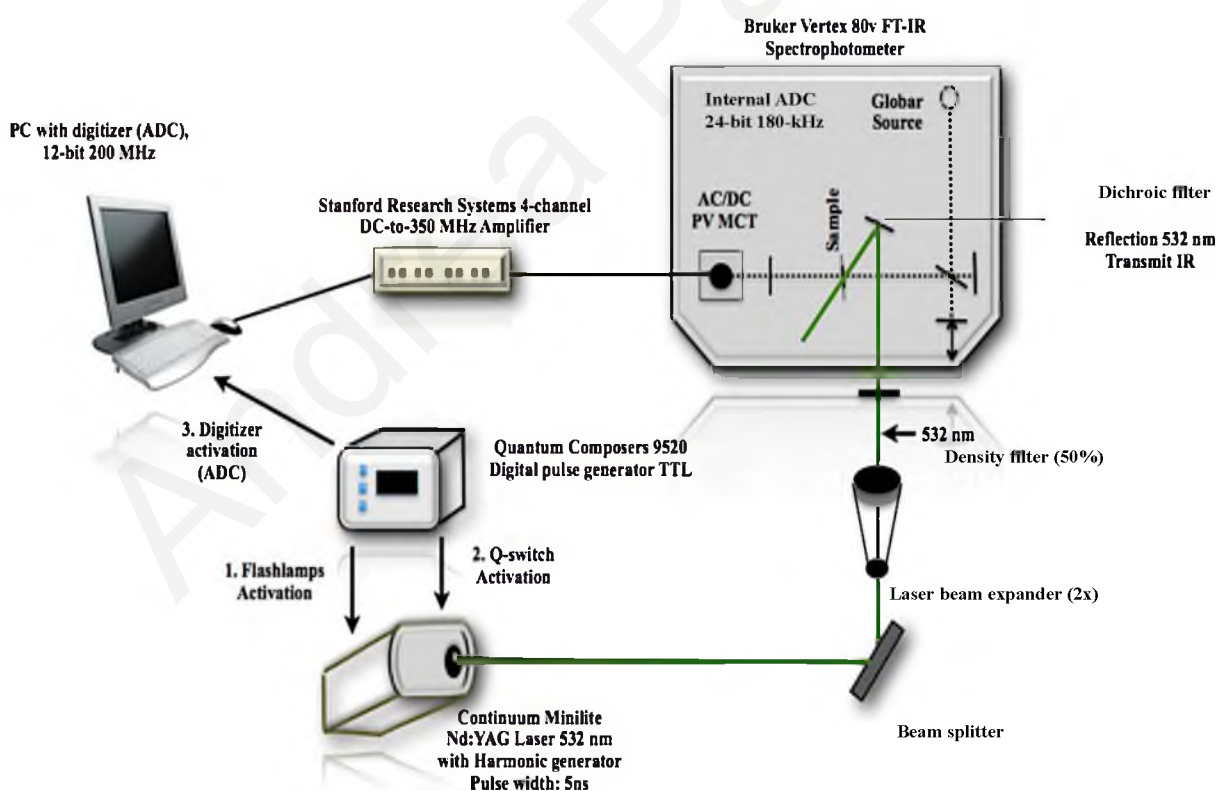


Figure 4.4 Schematic representation of the time-resolved step-scan FTIR experimental setup used for the investigation of heme-based oxygen sensor proteins HemAT-Bs, YddV and EcDOSH. The process of reaction triggering, IR signal pre-amplification and data recording is illustrated.

In the case of $\mu\text{s} \rightarrow \text{ms}$ time scale measurements, single-sided spectra were collected at 4 cm^{-1} spectral resolution, 6 and 8 μs time resolution and 10 coadditions per data point for noise reduction. The total accumulation time for each measurement was 25 min and 15 to 20 measurements were collected and averaged. The Blackman-Harris 3-Term apodization with 32 cm^{-1} phase resolution and the Mertz phase correction algorithm is used. Pre-triggering of the FTIR spectrometer was achieved so as to begin data collection before the firing of the laser thus, allowing for fixed reference points to be collected at each mirror position. For the $\text{ns} \rightarrow \mu\text{s}$ time scale measurements, the AC single-channel spectra as well as their raw data interferograms were collected at 4 cm^{-1} spectral resolution, 200 ns time resolution and 10 coadditions per data point. The Blackman-Harris 3-Term apodization with 32 cm^{-1} phase resolution and the Mertz No Peak Search phase correction algorithm was used. To ensure optimal fill of the dynamic range of the ADC of the transient recorder, an external 4-channel DC-to-350 MHz signal amplifier (Stanford Research Systems) was used to amplify the AC signal 5x. The total accumulation time for each $\text{ns} \rightarrow \mu\text{s}$ measurement was 25 min and 60 to 75 measurements (15 measurements per sample) were collected and processed individually. The DC spectrum for each sample was collected separately without laser excitation. It is notable to mention that usually, phase correction algorithms function properly only if the resulting spectrum has exclusively positive intensities. Therefore, since the DC signal produces a positive spectrum, it was used for calculating the correct phase which was hence utilized to correct the phase of the AC signal.

For both the $\text{ns} \rightarrow \mu\text{s}$ and the $\mu\text{s} \rightarrow \text{ms}$ time scale measurements, the final difference spectra were calculated as:

$$\Delta A = -\log[1 + (I(\text{AC}) / (\text{Gain} \cdot I(\text{DC})))] \quad (4.1)$$

where the *Gain* factor is defined as the ratio of the DC-to-AC channel input range used, multiplied by the AC signal amplification value. Since signal digitization for the $\mu\text{s} \rightarrow \text{ms}$ time scale measurements was done using the internal ADC, where the only possible setting for the input range for both channels is ± 10 Volt and no AC signal amplification was necessary, Eq. (4.1) was modified as :

$$\Delta A = -\log[1 + (I(\text{AC}) / I(\text{DC}))] \quad (4.2)$$

4.3 References

1. S. Aono, T. Kato, *et al. J. Biol. Chem.* **2002**, *277*, 13528-13538.
2. E. Pinakoulaki, H. Yoshimura, V. Daskalakis, *et al. Proc. Natl. Acad. Sci. USA* **2006**, *103*, 14796-14801.
3. H. Yoshimura, S. Yoshioka, K. Kobayashi, *et al. Biochem.* **2006**, *45*, 8301-8307.
4. K. Nakajima, K. Kitanishi, K. Kobayashi, *et al. J. Inorg. Biochem.* **2012**, *108*, 163-170.
5. K. Kitanishi, K. Kobayashi, Y. Kawamura, *et al. Biochem.* **2010**, *49*, 10381-10393.
6. Y. Sasakura, S. Hirata, S. Sugiyama, *et al. J. Biol. Chem.* **2002**, *277*, 23821-23827.
7. A. T. Atsunari, H. Takahashi, T. Shimizu. *J. Biol. Chem.* **2007**, *282*, 21301-21307.
8. H. Park, C. Suquet, J. D. Satterlee, C. Kang, *Biochemistry* **2004**, *43*, 2738-2746.



CHAPTER 5

Dynamics of the Signal Transducer Protein HemAT Revealed by Time-resolved Step-scan FTIR Spectroscopy

Andrea Pavlou

5.1 Introduction

A range of spectroscopic techniques have been employed in order to relate the structural properties of HemAT-*Bs* with its function and elucidate the aerotaxis signal transduction mechanism. Early studies using resonance Raman (RR) spectroscopy have revealed three O₂ bound conformations, which have been attributed to different hydrogen bonding interactions between the heme-bound O₂ and the distal site residues.^{1,2,3} However, the functional significance of each of the three conformations has not been demonstrated thus far. Experiments on the dynamic changes induced to HemAT-*Bs* upon ligand binding have been performed. Time-resolved resonance Raman studies of the HemAT-CO adduct by Yoshimura *et al.* investigating the role of the proximal heme active site in the signal transduction communication pathway suggested hydrogen bond formation between His123 and proximal Tyr133 upon ligand binding, with His123 adopting a distinct orientation for each ligand.⁴ In addition, studies of CO-photodissociation using time resolved optical absorption spectroscopy suggested protein relaxation at a time scale of milliseconds, while also inferring a monophasic CO-rebinding pattern.⁵ Recently, El Mashtoly *et al.*⁶ conducted site-specific time resolved UVRR studies that indicated the existence of at least two intermediate events of conformational changes in a time scale of ns to ms following CO photodissociation, and have proposed a potential intramolecular signal transduction mechanism for HemAT-*Bs* involving significant structural re-arrangement of helices B and G. Although, ample insight has been gained until now into both the ligand specificity and the signal transduction mechanisms of HemAT-*Bs*, important aspects of the above molecular processes still remain to be answered.

In our work, we have employed time-resolved step-scan Fourier transform infrared (TRS²-FTIR) spectroscopy to investigate the protein structural changes induced by CO photodissociation/rebinding that are crucial for understanding the initial events of the intramolecular signal transduction mechanism in HemAT-*Bs*. We have investigated both the wild type and mutated truncated sensor domain as well as full length HemAT-CO adducts. **Figure 5.1** illustrates a schematic representation of the unbound heme active site of HemAT-*Bs*, denoting the amino acids of the proximal and distal site of the heme periphery signified as critical in ligand recognition and discrimination. The TRS²-FTIR spectra revealed significant contribution of distal Tyr70 to the control of the conformational changes that are induced to the protein matrix upon CO photodissociation. In addition, Leu92 has been shown to act as the conformational gate in the migration pathway of photodissociated CO. The kinetic

evolution of CO-rebinding has been determined as biphasic for both the wild type full length and truncated sensor domain forms of HemAT-*Bs*, with however distinct differences between the two forms in the process of protein structural relaxation.

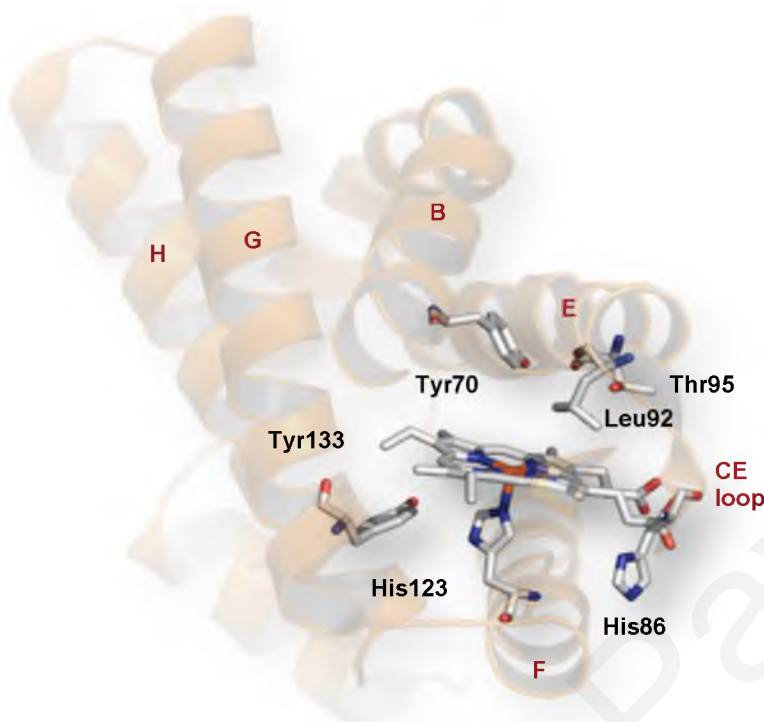


Figure 5.1 Structural representation of the unliganded truncated sensor domain heme active site of HemAT-*Bs* (PDB ID 1OR6).

5.2 Experimental Procedures

HemAT from *B.subtilis* was expressed and purified according to previously published procedures.^{3,7,8} The samples used for the FTIR measurements had an enzyme concentration of ~1.0 mM for the full length and ~2 mM for the truncated sensor domain HemAT in 50 mM Tris for pH 8 and pD 8 after buffer exchange. The pD solutions prepared in D₂O buffers were measured by using a pH meter and assuming pD = pH (observed) + 0.4. Dithionite reduced Fe(II) form pretein samples were exposed to 1 atm of CO in an anaerobic cell to prepare the carbonmonoxy adduct and transferred to a tightly sealed FTIR cell with two CaF₂ windows, under anaerobic conditions (path length (l)= 6μm). CO gas was obtained from Linde. The static FTIR spectra were recorded with 4 cm⁻¹ spectral resolution on a Bruker Vertex 70 FTIR spectrometer equipped with a liquid nitrogen cooled mercury cadmium telluride (MCT) detector.

For the time-resolved step-scan FTIR measurements, the 532 nm pulses from a Continuum Minilite II Nd:YAG laser (5 ns width, 10 Hz) were used as a pump light (8 mJ/pulse) to photolyze the YddV- CO adducts. These measurements were performed on a

Bruker Vertex 80 V spectrometer equipped with the step-scan option. A vacuum pump was used to evacuate the interferometer compartment to a final pressure of 3.2 mbar. The FTIR spectrometer was placed on a Newport VH optical vibration isolation table to ensure that vibrational background noise from environmental sources was avoided. For the time-resolved experiments, a TTL (transistor transistor logic) pulse provided by a digital delay pulse generator (Quantum Composers, 9524) triggered in order the flashlamps, the Q-switch, and the FTIR spectrometer. Pre-triggering the FTIR spectrometer to begin data collection before the laser fires allowed fixed reference points to be collected at each mirror position, which were used as the reference spectrum in the calculation of the difference spectra. Changes in intensity were recorded with a photovoltaic MCT detector (Kolmar Technologies KV100-1B-7/190, response limit 850 cm^{-1}) and digitized with a 180-kHz, 24-bit, analog-to-digital converter (ADC) for measurements in the μs to ms time scale and with a 200-MHz, 12-bit external MI analog-to-digital converter for measurements in the ns to μs time scale. A broadband interference optical filter (LP-4200, Spectrogon) with a short wavelength cutoff at $4.2\text{ }\mu\text{m}$ was used to limit the free spectral range from 4.2 to $11.8\text{ }\mu\text{m}$. This led to a spectral range of 2633 cm^{-1} , which was equal to an undersampling ratio of 6.

In the case of $\mu\text{s} \rightarrow \text{ms}$ time scale measurements, single-sided spectra were collected at 4 cm^{-1} spectral resolution, 6 and $8\text{ }\mu\text{s}$ time resolution and 10 coadditions per data point for noise reduction. The total accumulation time for each measurement was 25 min and 15 to 20 measurements were collected and averaged. The Blackman-Harris 3-Term apodization with 32 cm^{-1} phase resolution and the Mertz phase correction algorithm is used. Pre-triggering of the FTIR spectrometer was achieved so as to begin data collection before the firing of the laser thus, allowing for fixed reference points to be collected at each mirror position. For the ns $\rightarrow \mu\text{s}$ time scale measurements, the AC single-channel spectra as well as their raw data interferograms were collected at 4 cm^{-1} spectral resolution, 200 ns time resolution and 10 coadditions per data point. The Blackman-Harris 3-Term apodization with 32 cm^{-1} phase resolution and the Mertz No Peak Search phase correction algorithm was used. Difference spectra were calculated as $\Delta A = -\log(I_S / I_R)$. Optical absorption spectra were also recorded with a Shimadzu UV1700 UV-visible spectrometer before and after the FTIR measurements to ensure the formation and stability of the CO adducts.

5.2 Results

Figure 5.2 shows the FTIR spectra of the HemAT-CO adducts. In agreement with

previous studies the two C-O stretching modes observed at 1967 cm^{-1} and 1928 cm^{-1} are attributed to the “open” and “closed” conformations respectively, and are similar for the sensor domain (**trace A**) and full length (**trace B**) HemAT-CO adducts.⁸ In the “open” conformer (1967 cm^{-1} mode) the heme-bound CO exhibits weak interactions with the distal site residues, while in the “closed” conformer strong H-bonded interactions between the heme-bound CO and the distal heme active site are observed.^{9,10} The FTIR spectra of the L92A (**trace C**), Y133F (**trace D**), Y70F (**trace E**) and T95A (**trace F**) HemAT-CO adducts are similar to those previously reported.⁸ Briefly, the “closed” conformer is absent in the L92A and Y133F mutants, while the most significant differences are observed upon the Y70F mutation. Specifically the “closed” conformer upshifts at 1943 cm^{-1} indicating moderate hydrogen bonding interactions of the heme-bound CO with the distal residues. Hence, Y70 directly interacts with CO, in the HemAT-CO adduct.

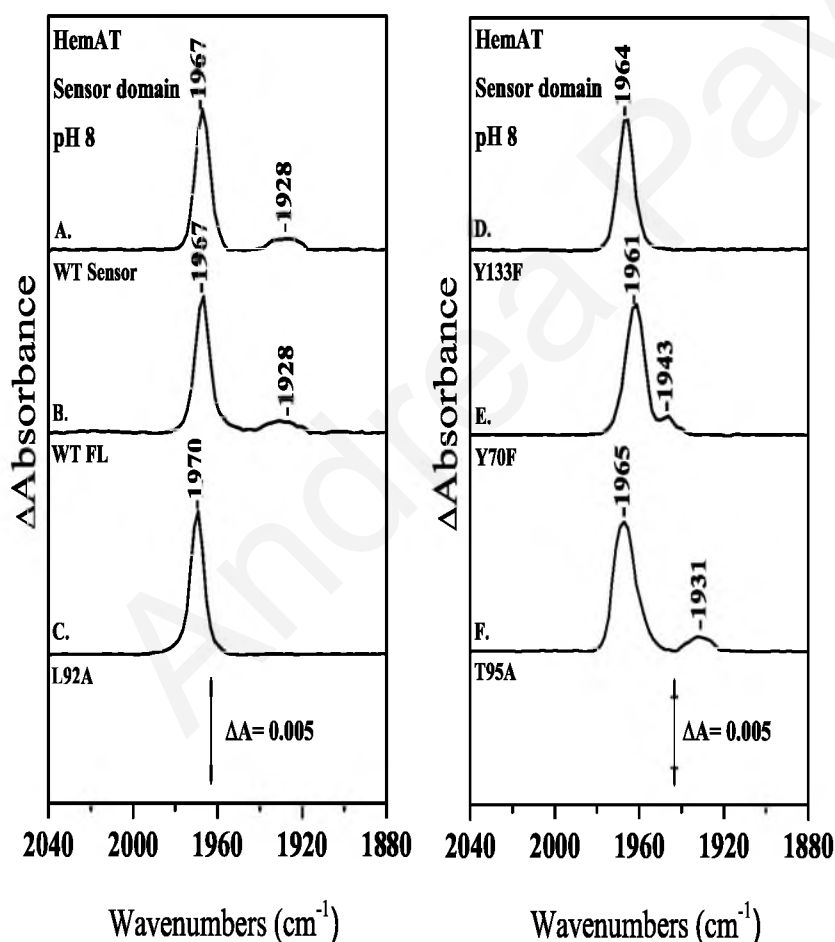


Figure 5.2 FTIR spectra of the HemAT-CO adducts at pH 8 of WT truncated Sensor domain (**trace A**), WT Full length (**trace B**), and of the truncated Sensor domain mutants, L92A (**trace C**), Y133F (**trace D**), Y70F (**trace E**), and T95A (**trace F**). The pathlength was $6\ \mu\text{m}$ and the spectral resolution was 4 cm^{-1} .

To understand the functional mechanism of the heme-based oxygen sensor protein HemAT, it is necessary to study the dynamic changes induced by ligand binding. Time-resolved step-scan FTIR spectroscopy has been proven to be a valuable tool, as it can be used to monitor the kinetic evolution of ligand rebinding after its photodissociation on timescales

of ns-ms. In addition, it allows the observation of structural changes during the ligand dissociation / rebinding processes even down to the level of individual residues.¹¹

We have initially performed time-resolved step-scan FTIR experiments with time resolution $t_d = 250$ ns (**Figure 5.3**). The time-resolved step-scan FTIR difference spectra of the Fe(II) form, wild type truncated sensor domain HemAT-CO at pD 8 subsequent to CO photolysis have revealed a negative peak at 1967 cm^{-1} resulting from the photolyzed heme Fe-CO complex, indicating that the HemAT-CO adduct is photolabile. From the latter spectra, we have identified protein vibrations in the $1700\text{-}1600\text{ cm}^{-1}$ frequency range. Specifically we have observed a positive peak at 1677 cm^{-1} which we attribute to $\nu(\text{C}=\text{O})$ of the protonated heme propionates that are perturbed upon CO photolysis. Conversely, we attribute the large peak-trough at $1654(-)/1638(+)\text{ cm}^{-1}$ to amide I - α -helix. In addition, by monitoring the kinetic evolution of CO-rebinding to heme-Fe(II), we have concluded that no geminate recombination occurs and that CO rebinding starts after $t_d = 4\text{ }\mu\text{s}$. Hence, since no significant transient protein events have been observed in the spectra of the wild type truncated sensor domain HemAT-*Bs*-CO in the nanosecond time scale, we have performed time-resolved step-scan FTIR experiments in the microsecond-to-millisecond timescale to further investigate the dynamic changes induced to the protein upon CO dissociation/rebinding.

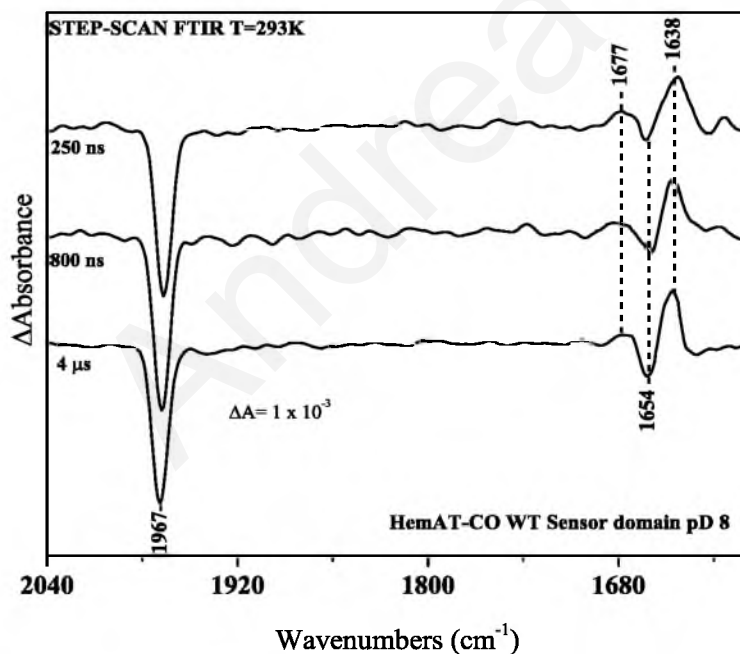


Figure 5.3 Time-resolved step-scan FTIR difference spectra of WT truncated sensor domain HemAT-CO adduct at pD 8, subjected to CO photodissociation at $t_d = 250, 800, \text{ and } 4000$ ns.

We have investigated the photodissociation of CO from the HemAT-CO adducts of the wild type full length and the wild type truncated sensor domain forms of the protein at pH 8 and pD 8 with time resolution $t_d = 8\text{ }\mu\text{s}$, which have allowed us to monitor the kinetics for ligand rebinding on the μs -ms timescale. In **Figure 5.4 (A)**, we present the time-resolved

step-scan FTIR difference spectra ($t_d = 8 \mu\text{s} - 3.4 \text{ ms}$) of the Fe(II) form, wild type truncated sensor domain HemAT-CO adduct at pH 8 subsequent to CO photolysis by a 532 nm 5 ns laser pulse. The above experimental conditions have allowed for the 1967 cm^{-1} and 1925 cm^{-1} peaks to be well resolved. The negative peaks at 1967 cm^{-1} and 1925 cm^{-1} arise from the photolyzed heme Fe-CO complex, indicating that both conformers are photolabile. In the transient difference spectra ($t_d = 8 - 40 \mu\text{s}$) after laser photolysis, we have observed a rapidly decreasing intensity for the 1967 cm^{-1} mode, indicating a fast CO rebinding phase with a small amplitude ($\sim 18\%$). The transient fast phase is followed by a slow phase ($t_d = 56 \mu\text{s} - 2.9 \text{ ms}$) of a much larger amplitude ($\sim 82\%$) persisting until the process of CO rebinding to heme Fe is completed. The distinct biphasic CO rebinding time course for the wild-type protein possibly indicates the existence of two different components within the homodimer.

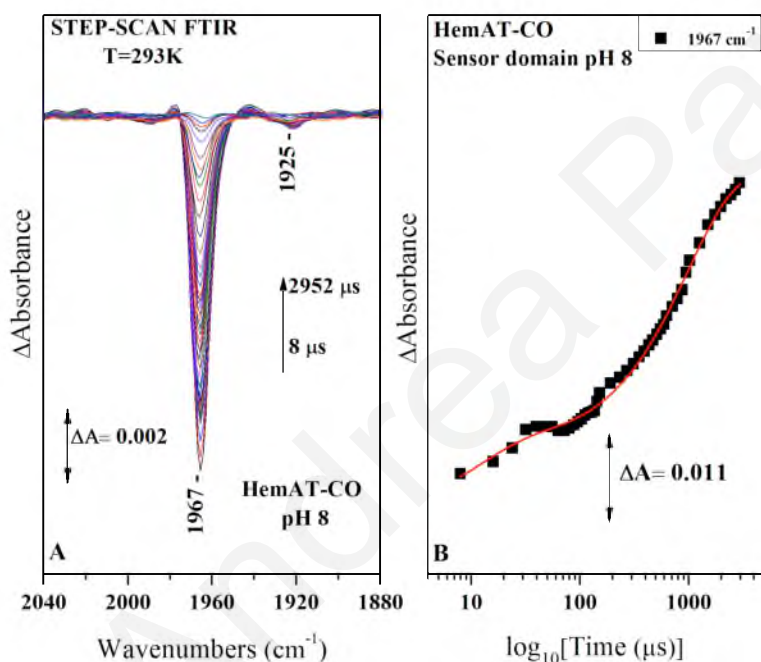


Figure 5.4 (A) Time-resolved step-scan FTIR difference spectra of the wild type truncated Sensor domain HemAT-CO adduct at pH 8 from 0.008 to 2.952 ms subsequent to CO photolysis. (B) Plot of the ΔA of the 1967 cm^{-1} mode versus time on a logarithmic scale subsequent to CO photolysis. The red line corresponds to the exponential fit of the experimental data.

Similar results have been obtained for the Fe(II) form of the wild type truncated sensor domain HemAT-CO adduct at pH 8, (Figure 5.5 (A)) with the two C-O modes at 1967 and 1925 cm^{-1} observed, thus remaining unchanged after $\text{H}_2\text{O}/\text{D}_2\text{O}$ exchange. We have however, observed minor differences in the time evolution of CO rebinding to heme-Fe(II). Specifically, CO rebinding demonstrates a slower rate at pH 8, with the transient phase being resolved by $\sim 48 \mu\text{s}$, and CO being fully rebound to heme Fe^{2+} by 3.4 ms. We attribute the observed slower rebinding in D_2O buffer to the solvent isotope effect; proteins tend to be more stable in D_2O compared to H_2O . Their kinetic parameters are compared as follow. The

ΔA of the 1967 cm^{-1} Fe^{2+} - CO mode has been measured as a function of time, to determine the rate of recombination of CO to heme iron at pD 8 and pH 8 at 293K. The difference in CO rebinding rate is depicted by the calculated Fe^{2+} -CO rebinding constants, $t_1=22\text{ }\mu\text{s}$ / $k_1 = 32\times 10^3\text{ s}^{-1}$ (fast phase), $t_2= 680\text{ }\mu\text{s}$ / $k_2 = 1018\text{ s}^{-1}$ (slow phase) at pH 8, and $t_1=29\text{ }\mu\text{s}$ / $k_1 = 24\times 10^3\text{ s}^{-1}$ (fast phase) and $t_2= 722\text{ }\mu\text{s}$ / $k_2 = 960\text{ s}^{-1}$ (slow phase) at pD 8 (**Table 5.1**).

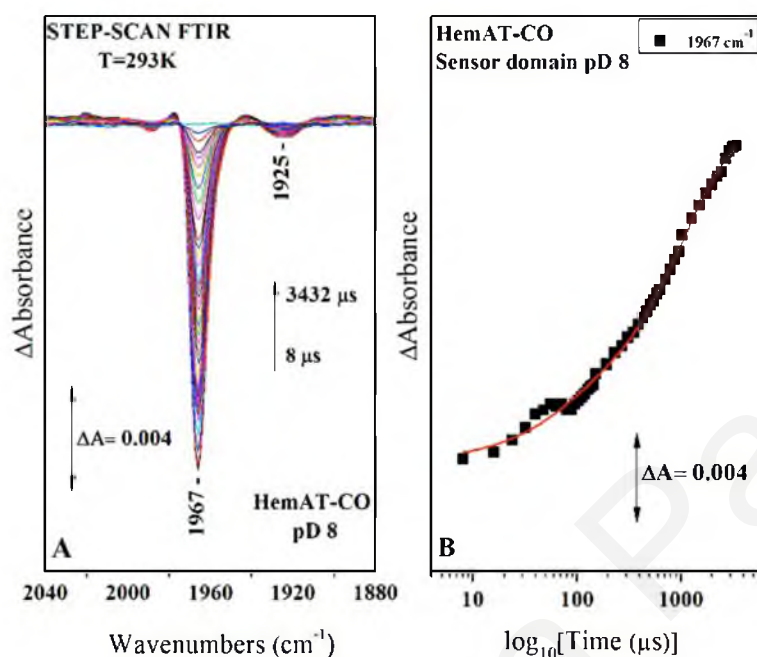


Figure 5.5 (A) Time-resolved step-scan FTIR difference spectra of the wild type truncated Sensor domain HemAT-CO adduct at pD 8 from 0.008 to 3.432 ms subsequent to CO photolysis. (B) Plot of the ΔA of the 1967 cm^{-1} mode versus time on a logarithmic scale subsequent to CO photolysis. The red line corresponds to the exponential fit of the experimental data.

Figure 5.6(A) illustrates the TRS2-FTIR difference spectra of the wild type sensor domain HemAT-CO at pD 8 in the $1700\text{-}1500\text{ cm}^{-1}$ frequency range; the strong H-O-D bending modes greatly mask the $1300\text{-}1500\text{ cm}^{-1}$ spectral region. To supplement the vibrational modes observed in the $1700\text{-}1600\text{ cm}^{-1}$ frequency range of the spectrum of the wild type truncated sensor domain HemAT-CO adduct pD 8 $t_d = 250\text{ ns-}4\text{ }\mu\text{s}$, the peaks at $1572(-)/1560(+)/1543(-)\text{ cm}^{-1}$ as depicted in **Figure 5.6 (A)** are tentatively attributed to $\nu(\text{COO}^-)^{\text{asym}}$ of the deprotonated heme propionates with possible contribution of $\nu(\text{COO}^-)^{\text{asym}}$ of Asp/Glu residues.¹²⁻¹⁵ The detection of vibrations attributed to both the protonated and deprotonated forms of heme propionates indicates the presence of both conformations. The kinetic evolution of the protein vibrations found in the amide I region at $1638(+)\text{ cm}^{-1}$ and $1654(-)\text{ cm}^{-1}$ is depicted in **Figures 5.6 (B)** and **(C)** respectively. The protein vibrations follow the same kinetic trend as the $\nu(\text{C-O})$ vibrations, indicating that the protein becomes fully relaxed before the onset of CO rebinding. The rebinding constants have been calculated as $t_1=25\text{ }\mu\text{s}$ / $k_1 = 27\times 10^3\text{ s}^{-1}$ (fast phase), $t_2= 694\text{ }\mu\text{s}$ / $k_2 = 999\text{ s}^{-1}$ (slow phase) for the mode at 1638 cm^{-1} , and $t_1=24\text{ }\mu\text{s}$ / $k_1 = 29\times 10^3\text{ s}^{-1}$ (fast phase), $t_2= 637\text{ }\mu\text{s}$ / $k_2 = 1088\text{ s}^{-1}$ (slow phase) for the mode at 1654 cm^{-1} .

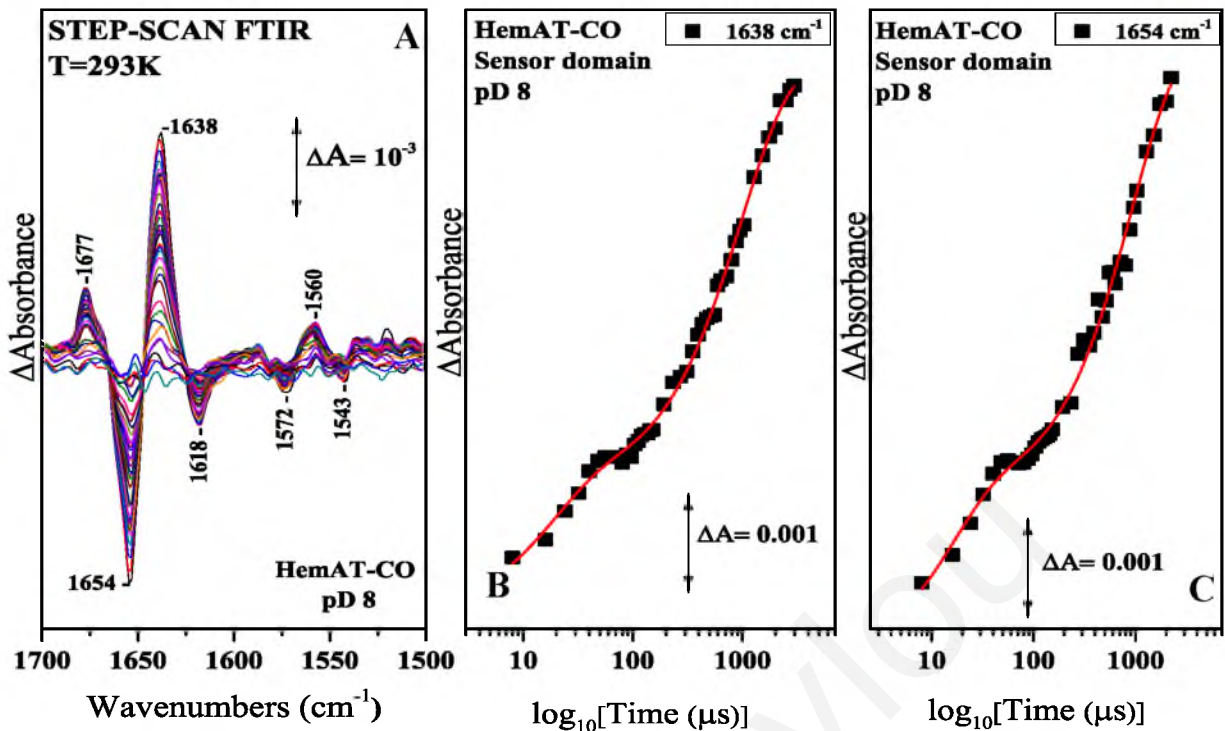


Figure 5.6 (A) Time-resolved step-scan FTIR difference spectra of the wild type truncated sensor domain HemAT-CO adduct at pD 8 in the range of 1700-1500 cm^{-1} and $t_d = 8 - 3400 \mu\text{s}$. Plot of the ΔA of (B) 1638 cm^{-1} , and (C) 1654 cm^{-1} , protein vibration modes of the truncated sensor domain HemAT-CO adduct at pD 8 versus time on a logarithmic scale subsequent to CO photolysis. The red lines correspond to the exponential fitting of the experimental data.

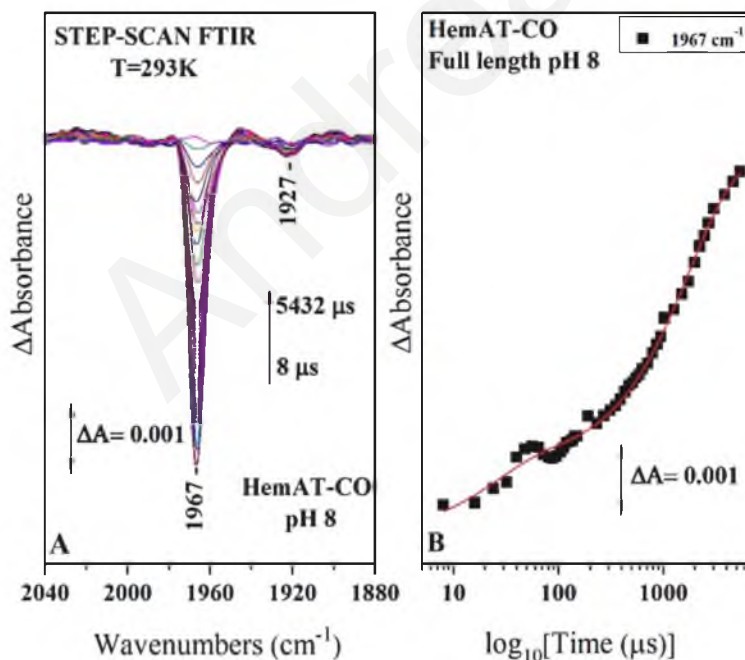


Figure 5.7 (A) Time-resolved step-scan FTIR difference spectra of the wild type full length HemAT-CO adduct at pH 8 from 0.008 to 5.432 ms subsequent to CO photolysis. (B) Plot of the ΔA of the 1967 cm^{-1} mode versus time on a logarithmic scale subsequent to CO photolysis. The red line corresponds to the exponential fit of the experimental data.

The F(II) form of the wild type full length HemAT-CO adduct at pH and pD 8 produced similar results with the truncated sensor domain HemAT-CO, depicted in **Figures**

5.7 & 5.8 respectively. The two C-O modes at 1967 and 1925 cm^{-1} have been observed as negative indicating the photodissociation of CO, and remained unchanged after $\text{H}_2\text{O}/\text{D}_2\text{O}$ exchange (**Figures 5.7 (A) & 5.8 (A)**). For both wild type full length HemAT-CO at pH 8 and at pD 8 we have observed biphasic kinetics (**Figures 5.7 (B) & 5.8 (B)**) with faster CO-rebinding at pH 8. The difference in CO rebinding rate is depicted by the calculated Fe^{2+} -CO rebinding constants, $t_1=32 \mu\text{s} / k_1 = 22 \times 10^3 \text{s}^{-1}$ (fast phase), $t_2= 1232 \mu\text{s} / k_2 = 562 \text{s}^{-1}$ (slow phase) for pH 8, and $t_1=32 \mu\text{s} / k_1 = 22 \times 10^3 \text{s}^{-1}$ (fast phase) and $t_2= 1327 \mu\text{s} / k_2 = 522 \text{s}^{-1}$ (slow phase) for pD 8 (**Table 5.1**). Comparing the rebinding constants between the wild type truncated sensor domain HemAT-CO and the wild type full length HemAT-CO, faster CO rebinding for the wild type truncated sensor domain form of the protein was observed.

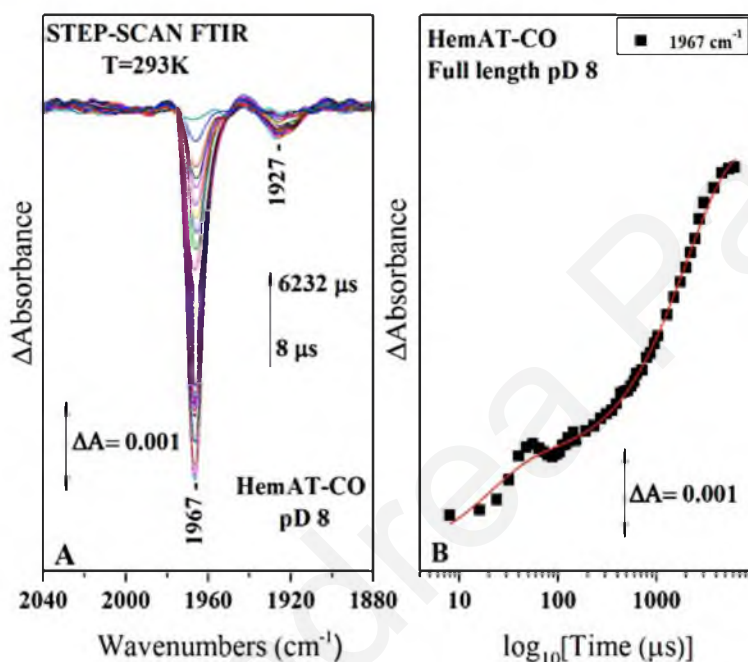


Figure 5.8 (A) Time-resolved step-scan FTIR difference spectra of the wild type full length HemAT-CO adduct at pD 8 from 0.008 to 6.232 ms subsequent to CO photolysis. **(B)** Plot of the ΔA of the 1967 cm^{-1} mode versus time on a logarithmic scale subsequent to CO photolysis. The red line corresponds to the exponential fit of the experimental data.

Figure 5.9 (A) illustrates the -FTIR difference spectra of WT full length HemAT-CO at pD 8 in the 1500-1700 cm^{-1} frequency range. As described previously for the HemAT sensor domain protein, the positive peak at 1677 cm^{-1} is attributed to $\nu(\text{C}=\text{O})$ of the protonated heme propionates that are perturbed upon CO photolysis, while the distinct split trough-peak modes at 1661(-)/1652(-)/1638(+) cm^{-1} are attributed to α -helix. The split of the 1654 cm^{-1} into two distinct peaks at 1661 and 1652 cm^{-1} observed when comparing the spectrum of the full length HemAT-Bs with that of the truncated sensor domain protein, provides evidence for possible movement/reorientation of an additional α -helix. Finally, the peaks at 1576(-)/1561(+)/1547(-)/1534(+) cm^{-1} are tentatively assigned to the $\nu(\text{COO}^-)^{\text{asym}}$ of the deprotonated heme propionates with possible contribution of $\nu(\text{COO}^-)^{\text{asym}}$ from Asp/Glu.¹²⁻¹⁵ The kinetic

evolution of the protein vibration at $1638(+)$ cm^{-1} located in the amide I region is illustrated in **Figures 5.9 (B)**. Interestingly and in contrast to the kinetic evolution of the protein vibrations of the photodissociated wild type truncated sensor domain HemAT-CO adduct, the corresponding protein vibration of the wild type full length HemAT-CO complex did not follow the same trend as the $\nu(\text{CO})$ vibration at 1967 cm^{-1} . Rather, we have observed monophasic pattern indicating distinctly different protein relaxation process compared to CO rebinding to heme-Fe(II). (**Figure 5.10**). The constants for the protein vibration at $1638(+)$ cm^{-1} have been calculated as $t_1=1253$ μs / $k_1= 553$ s^{-1} (**Table 5.1**).

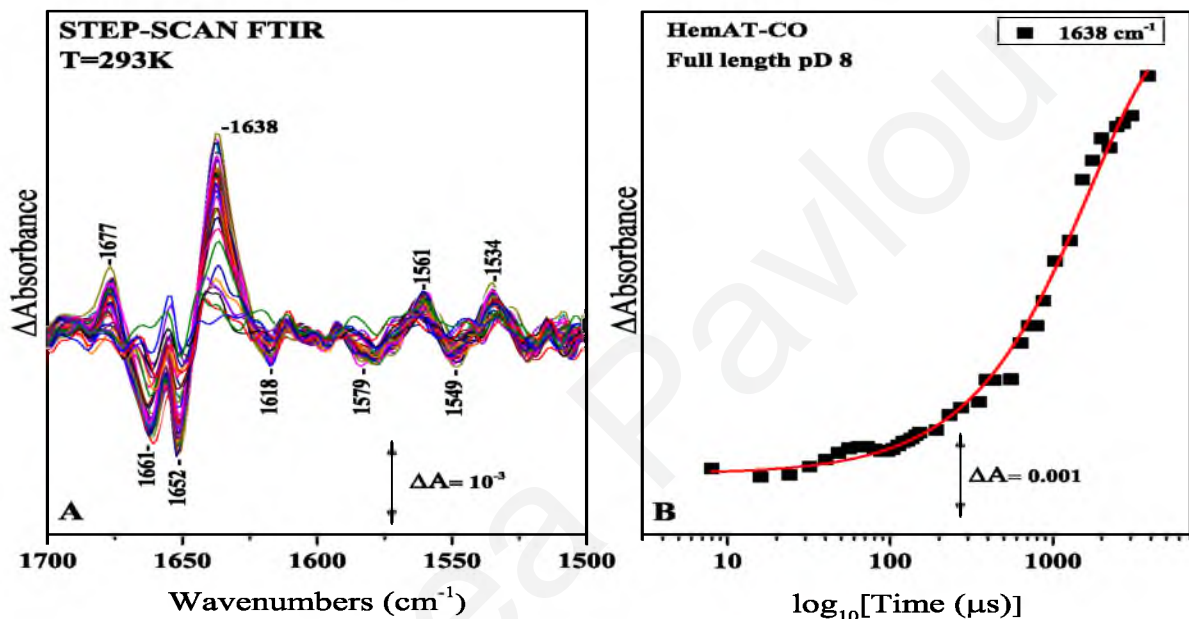


Figure 5.9 (A) Time-resolved step-scan FTIR difference spectra of the wild type full length HemAT-CO adduct at pD 8 in the range of $1700\text{-}1500$ cm^{-1} and $t_d = 8 - 6232$ μs . Plot of the ΔA of the **(B)** 1638 cm^{-1} protein vibration mode of the full length HemAT-CO adduct at pD 8 versus time on a logarithmic scale subsequent to CO photolysis. The red lines correspond to the exponential fitting of the experimental data.

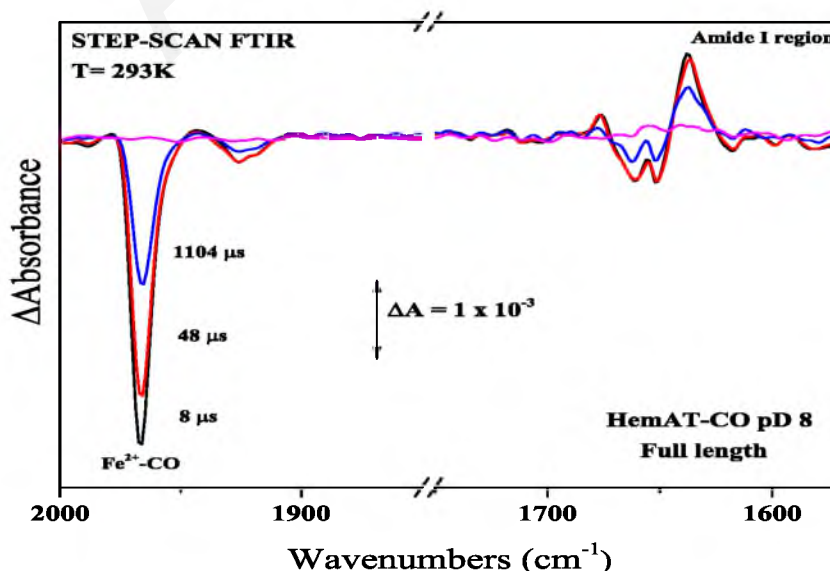


Figure 5.10 Time-resolved step-scan FTIR difference spectra of the wild type full length HemAT-CO adduct at pD 8 in the range of $2000\text{-}1850$ cm^{-1} / $1750\text{-}1560$ cm^{-1} and $t_d = 8 - 1104$ μs .

We have performed TRS²-FTIR experiments on the Y70F, L92A, and T95A HemAT mutants which are located in the distal site of the heme, as well as of the proximal site mutant Y133F since they have been “pinpointed” by the static FTIR spectra as the amino acids potentially playing a crucial role in the ligand recognition and discrimination mechanism as well in intramolecular signal transduction processes. The time courses of CO rebinding for sensor domain HemAT-*Bs* mutants Y70F, L92A, T95A and Y133F at pD 8 have been monitored and the observations are reported below.

Monitoring the kinetic evolution of CO rebinding in L92A HemAT-CO (**Figure 5.11 (B)**) revealed faster rebinding compared to the wild type forms and the other mutant forms of the protein. The amplitudes of the two phases change considerably for L92A compared to the wild type HemAT. We have calculated higher amplitude for the transient fast phase at 30%, leaving the slow phase with an amplitude of 70%. The Fe²⁺-CO rebinding constants have been calculated as $t_1=26 \mu\text{s} / k_1 = 26 \times 10^3 \text{ s}^{-1}$ (fast phase) and $t_2= 243 \mu\text{s} / k_2 = 2850 \text{ s}^{-1}$ (slow phase). The mutant T95A gave similar results to those of WT HemAT-*Bs* (**Figure 5.12 (A)**). We have only noted that CO-rebinding in T95A resolves by $\sim 7 \text{ ms}$ compared to $\sim 3 \text{ ms}$ for the WT protein. The Fe²⁺-CO rebinding constants for T95A have been calculated as $t_1=18 \mu\text{s} / k_1 = 37 \times 10^3 \text{ s}^{-1}$ (fast phase), $t_2= 854 \mu\text{s} / k_2 = 811 \text{ s}^{-1}$ (slow phase) (**Figure 5.12 (B)**). Although mutation of Tyr70 significantly influences the conformations of the heme-bound CO, it does not appear to influence the time evolution of CO rebinding. In terms of CO rebinding, the results are similar to the WT protein with the Fe²⁺-CO rebinding constants calculated as $t_1=19 \mu\text{s} / k_1 = 36 \times 10^3 \text{ s}^{-1}$ (fast phase), $t_2= 904 \mu\text{s} / k_2 = 767 \text{ s}^{-1}$ (slow phase).

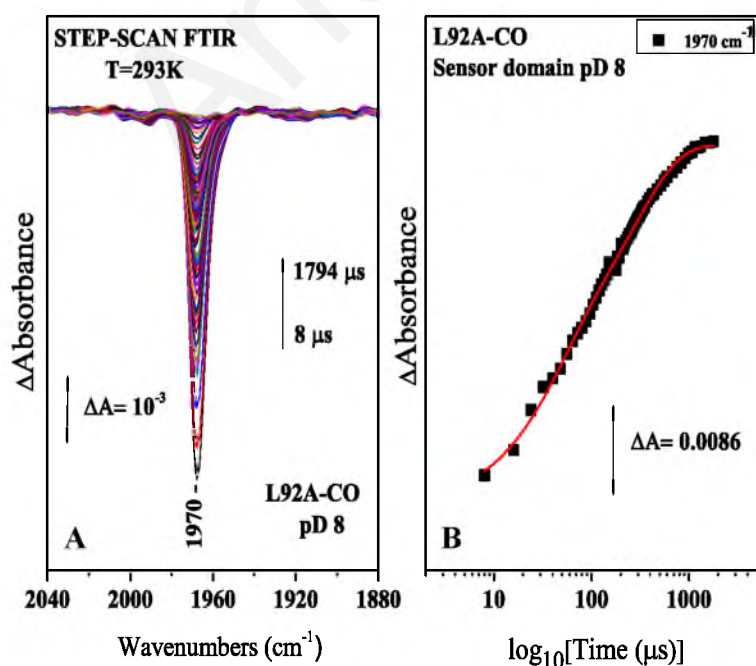


Figure 5.11 (A) Time-resolved step-scan FTIR difference spectra of the sensor domain L92A HemAT-CO adduct at pD 8 from 0.008 to 1.794 ms subsequent to CO photolysis. **(B)** Plot of the ΔA of the 1970 cm^{-1} mode versus time on a logarithmic scale subsequent to CO photolysis. The red line corresponds to the exponential fit of the experimental data.

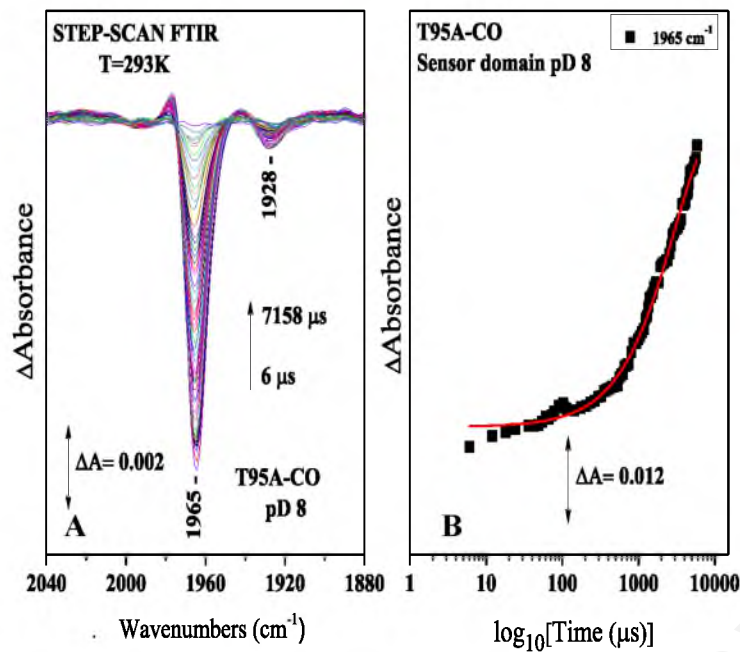


Figure 5.12 (A) Time-resolved step-scan FTIR difference spectra of the sensor domain T95A HemAT-CO adduct at pD 8 from 0.006 to 7.158 ms subsequent to CO photolysis. (B) Plot of the ΔA of the 1965 cm⁻¹ mode versus time on a logarithmic scale subsequent to CO photolysis. The red line corresponds to the exponential fit of the experimental data.

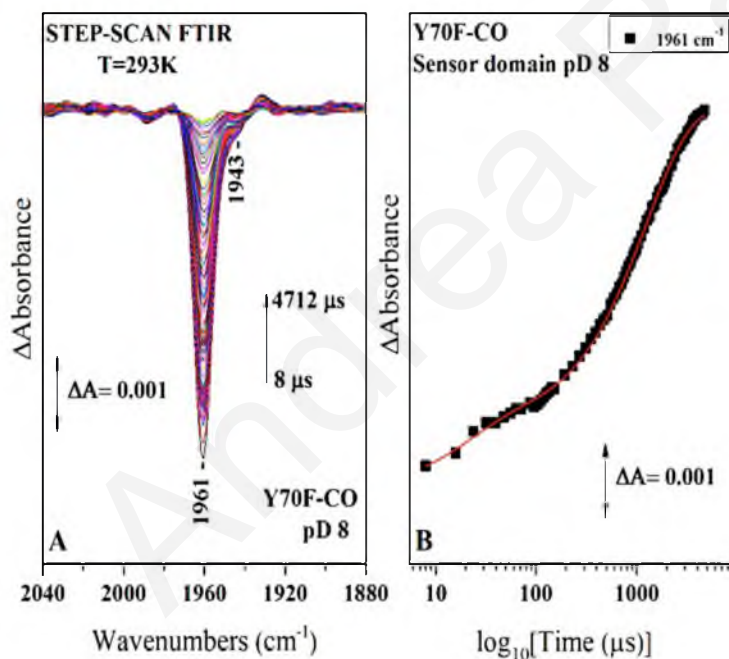


Figure 5.13 (A) Time-resolved step-scan FTIR difference spectra of the sensor domain Y70F HemAT-CO adduct at pD 8 from 0.008 to 4.712 ms subsequent to CO photolysis. (B) Plot of the ΔA of the 1961 cm⁻¹ mode versus time on a logarithmic scale subsequent to CO photolysis. The red line corresponds to the exponential fit of the experimental data.

However, a distinct difference in the kinetic evolution of CO-rebinding for Y133F was observed, compared to both the wild type and the other mutant forms of HemAT. The Fe²⁺-CO rebinding in Y133F demonstrated a monophasic pattern with calculated Fe²⁺-CO rebinding constants $t_1=1028 \mu\text{s} / k_1 = 674 \text{s}^{-1}$ (**Figure 5.14 (B)**), compared to biphasic for all the other mutants under study as well as the wild type protein.

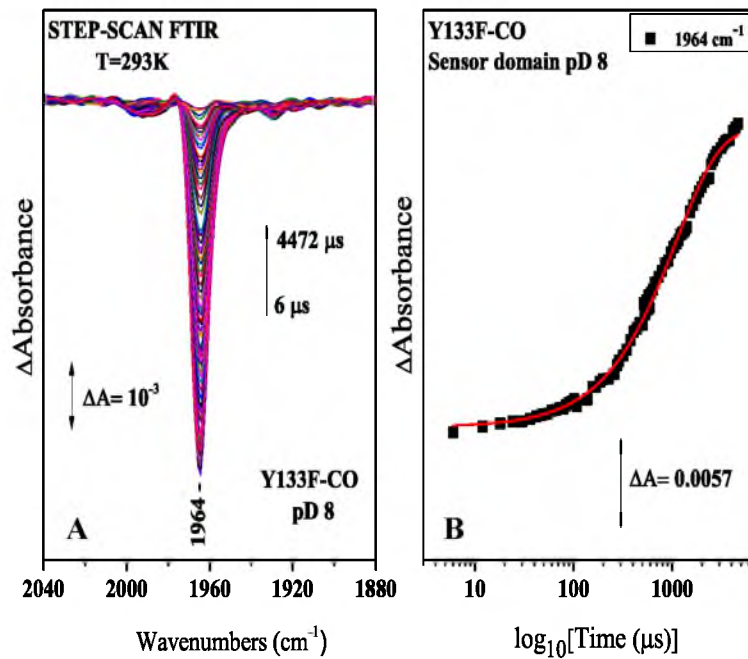


Figure 5.14 (A) Time-resolved step-scan FTIR difference spectra of the sensor domain Y133F HemAT-CO adduct at pD 8 from 0.006 to 4.472 ms subsequent to CO photolysis. (B) Plot of the ΔA of the 1965 cm^{-1} mode versus time on a logarithmic scale subsequent to CO photolysis. The red line corresponds to the exponential fit of the experimental data.

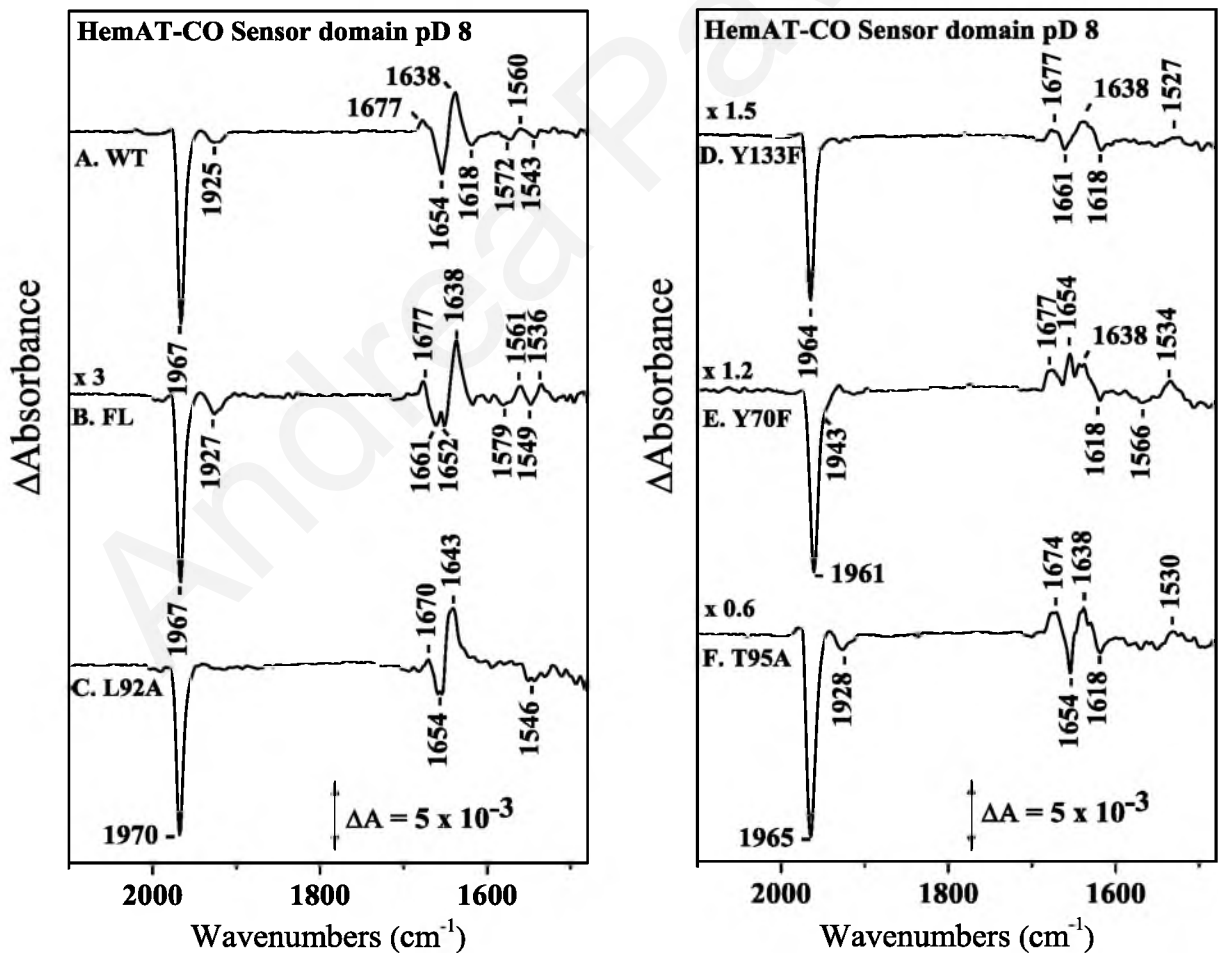


Figure 5.15 Time-resolved step-scan FTIR difference spectra of HemAT-CO adducts at pD 8, at $t_d = 8 \mu\text{s}$ WT truncated Sensor domain (trace A), WT Full length (trace B), L92A (trace C), Y70F (trace E), and at $t_d = 6 \mu\text{s}$, Y133F (trace D), and T95A (trace F).

Comparing the TRS²-FTIR difference spectrum of L92A and T95A (**Figure 5.15, traces C & F**) at $t_d = 8 \mu\text{s}$ subsequent to CO-photodissociation with that of the wild type protein (**Figure 5.15, trace A**), in the protein vibrations region (1700-1500 cm^{-1} frequency range), no significant changes have been observed. Yet, distinct differences have been observed when comparing the spectrum of Y70F with that of WT protein at 8 μs in the amide I region (**Figure 5.15, trace E**). Specifically, upon mutation of Tyr70 to Phe, the large peak to trough at 1656/1638 cm^{-1} disappeared and only positive peaks were observed at 1654 cm^{-1} and 1638 cm^{-1} . Hence, absence of Tyr70 possibly influences the movement of an α -helix presumably B-helix where Tyr70 is located in. In addition, we have also observed broadening of the α -helix vibrations in the amide I region of the spectrum of Y133F (**Figure 5.15, trace E**) compared to the wild type protein. The latter provides a possible indication that absence of Tyr133 impacts the movement/orientation of the G-helix where Tyr133 is located in.

1967 cm^{-1}	t_1 (μs)	k_1 (s^{-1})	t_2 (μs)	k_2 (s^{-1})	% photoproduct yield at 8/6 μs	% 1 st phase	% 2 nd phase
WT Sensor pD 8	29 ± 11	24x10 ³	722 ± 33	960	95	18	82
WT Sensor pH 8	22 ± 5	32x10 ³	680 ± 35	1018	95	18	82
WT FL pD 8	32 ± 13	22x10 ³	1327 ± 56	522	92	18	82
WT FL pH 8	32 ± 16	22x10 ³	1232 ± 63	562	92	18	82
L92A Sensor pD 8	26 ± 12	26x10 ³	243 ± 2	2850	72	30	70
T95A Sensor pD 8	18 ± 7	37x10 ³	854 ± 121	811	92	15	85
Y70F Sensor pD 8	19 ± 8	36x10 ³	904 ± 18	767	92	17	83
Y133F Sensor pD 8	1028 ± 23	674	-	-	92	100	-
amide I Sensor pD 8	t_1 (μs)	k_1 (s^{-1})	t_2 (μs)	k_2 (s^{-1})	-	% 1 st phase	% 2 nd phase
1638 cm^{-1}	25 ± 6	27x10 ³	694 ± 34	999	-	18	82
1654 cm^{-1}	24 ± 8	29x10 ³	637 ± 32	1088	-	18	82
amide I Full length pD 8	t_1 (μs)	k_1 (s^{-1})	t_2 (μs)	k_2 (s^{-1})	-	% 1 st phase	% 2 nd phase
1638 cm^{-1}	1253 ± 119	553	-	-	-	100	-

Table 5.1 Summary of estimated % photoproduct yield at $t_d = 6 \mu\text{s}$, as well as calculated constants and amplitude for each of the CO-rebinding phases for the wild type and mutant HemAT-CO adducts.

5.3 Discussion

The static FTIR spectra of the CO-bound wild type truncated sensor domain HemAT-*Bs* revealed two conformations of the heme-bound CO at 1967 and 1928 cm^{-1} that we attributed to the “open” and “closed” CO conformations of the heme-bound CO and are in agreement with previous studies.⁸ The $\nu(\text{CO})$ modes of the wild type full length HemAT-*Bs* have been observed at frequencies similar to those of the truncated sensor domain suggesting that no difference exists in the way that CO binds to heme-Fe(II) between the full length and the truncated sensor domain forms of the protein. The FTIR spectra of L92A, Y133F, Y70F and T95A coincide with those previously reported.⁸ Absence of the 1928 cm^{-1} mode from the spectrum of L92A infers a critical role of L92 in maintaining the hydrogen bonding network between the heme-bound CO and the distal site of the protein. The 1928 cm^{-1} mode was also absent from the FTIR spectrum of Y133F, indicating a communication linkage between the heme proximal and distal active sites. Early studies by Ohta *et al.*¹ reported that the heme-bound CO does not interact with the distal site of the heme active site. Specifically, they had indicated Y70F RR spectral features similar to those of the wild type protein. However, the upshift of the “closed” conformer at 1943 cm^{-1} , along with 6 cm^{-1} downshift of the “open” conformer observed in the spectra of Y70F, suggest direct interaction of Y70 with CO in the HemAT-CO adduct. Furthermore, UVRR findings by El-Mashtoly *et al.*¹⁶ inferred that Tyr70 does not directly interact through hydrogen bonding with the heme-bound CO but rather a hydrophobicity change in the surrounding environment of Tyr70 influences CO-binding. It is plausible that Tyr70 might in part control the hydrophobicity of the environment surrounding the heme-bound CO and thus mutation to a more hydrophobic residue might have contributed to the changes seen in the spectrum of Y70F compared to the WT protein. However our FTIR spectra suggest that it is mainly the electrostatic interactions between the side chain of Tyr70 and Fe^{2+} -CO that are perturbed upon absence of Tyr70.

The sensor domain of HemAT-*Bs* has been depicted in the X-ray crystal structure as a homodimer characterized by an anti-parallel four-helical bundle formed by helices H and G of each subunit as a core and the rest of the helices closely surrounding the core. The H-helix precedes the effector domain of the protein and a B-helix is located near the G-helix. The heme binding pocket is effectively shielded by the E-helix that is joined to the C-helix forming an intermediate CE loop.¹⁷ Time-resolved step-scan FTIR spectroscopy $t_d = \text{ns} - \text{ms}$ has been proven to be a powerful technique to investigate such structural changes induced to

the protein moiety upon CO dissociation/rebinding. Although CO is not the physiological ligand, its high quantum yield, stability and oxygen mimicry rendered it an acceptable probe for the elucidation of the initial events of the intramolecular signal transduction mechanism of HemAT-*Bs*.

The TRS²-FTIR difference spectra at $t_d = 250$ ns of the wild type truncated sensor domain protein upon CO photodissociation, suggested that instantaneous protein structural relaxation back to the CO-bound form due to geminate recombination does not occur in HemAT-*Bs*, rather the ligand escapes into the solvent away from the distal heme site assisted by protein conformational changes that transiently open exit channels. The lack of significant intensity variations and the observation of protein vibrations in the transient difference spectra ($t_d = 250$ ns – 4 μ s) led to the conclusion that CO-rebinding begins after 4 μ s.

The wild type truncated sensor domain HemAT-*Bs* revealed microsecond to millisecond kinetic events initiated by CO dissociation from heme-Fe(II) that characterize dynamic structural changes in the environment surrounding the heme active site, while the ligand is escaping away into the solvent and back to heme-Fe(II). Our TRS²-FTIR CO-photodissociation experiments $t_d = \mu$ s – ms revealed a two phase CO-rebinding process with a high photolysis yield of 95% confirming that no immediate structural relaxation back to the CO-bound form exists. The biphasic pseudo first-order kinetics demonstrate two distinct structural components within the homodimer; one component is characterized by the initial fast phase I with a small amplitude that resolves by 48 μ s and the other component is characterized by the second slower CO-rebinding phase II with a much larger amplitude that completes by 3.4 ms when CO is fully rebound to heme-Fe(II). El-Mashtoly *et al.*⁶ constructed a mathematical model of the CO photocycle from A (starting CO-adduct) \rightarrow D \rightarrow A in HemAT-*Bs*. The latter model was used to set a timeframe for the conformational changes observed in the corresponding TR-UVRR spectra of aromatic residues. Specifically, they proposed two intermediate species in the photocycle of CO in the 100 ns – 17 ms timescale recognized as C and D, which correspond to individual displacement events of B- and G-helices occurring before the onset of CO-rebinding. For the truncated sensor domain the first B- and G-helices displacement events occur at 0.20 μ s (0.45 μ s for the full length protein) while the second occur at 45 μ s (same for full length protein). The measured 48 μ s of the current study as the threshold for the transition from CO-rebinding phase I \rightarrow II, agrees with the proposed scheme by El-Mashtoly *et al.*⁶ that sets the transition from C intermediate \rightarrow D intermediate for both the truncated sensor domain and full length protein at 45 μ s. We, however, observe complete rebinding and protein relaxation back to CO-bound form at 3.4

ms, while this process (D-intermediate \rightarrow A) is set to ~ 17 ms.

It has been established from the X-ray crystal structure that subunit A has a Tyr70 residue with its hydroxyl side chain turned towards the heme binding pocket.¹⁷ If we assign the slow phase to the protein in an open conformation with a more hydrophilic heme pocket environment, while the fast phase to the protein in a closed conformation with a more hydrophobic environment, then it is acceptable that the fast rebinding process refers to CO binding first to subunit A that undergoes only minimal structural rearrangement to accommodate the hydrogen bonding interaction between the distal site and the heme-bound CO. Upon achievement of CO-binding to subunit A by a time scale of ~ 48 μ s, these conformational changes are transmitted to subunit B which undergoes substantial reorientation in the vicinity of B-helix (Tyr70) and G-helix (Tyr133) at a much slower time scale, to successfully bind CO and stabilize the Fe²⁺-CO complex. Therefore we propose that the observed biphasic CO-rebinding pattern is a result of cooperativity between the two subunits of the sensor domain HemAT-*Bs* homodimer to facilitate effective CO-binding. Interestingly, all previous kinetic studies CO-dissociation/rebinding defined this process as monophasic^{5,7,18} which oppose our findings. Rather, they only establish biphasic kinetics for O₂ binding to HemAT-*Bs*.

Furthermore, monitoring the process of CO-rebinding in wild type HemAT-*Bs* also revealed differences between the full length and truncated sensor domain forms of the protein. The latter indicates possible differences between the two forms in the cavities the ligand is accommodated while escaping away from the distal site of the protein. In addition, while the protein relaxation in the truncated sensor domain HemAT-*Bs* seem to follow the same trend with CO-rebinding, the protein vibrations in the wild type full length protein demonstrate a different pattern of protein relaxation. We propose that this is an indication of the influence of the presence of the effector domain on the structural relaxation of the protein back to the CO-bound. It should be mentioned that the process of CO rebinding appears slightly faster in H₂O buffer for both the wild type full length and the wild type truncated sensor domain HemAT-*Bs*, phenomenon, which we attributed to the solvent isotope effect. To elaborate, the increase of protein stability in D₂O can be explained by the observation that D₂O increases the rigidity of the native structure, since the frequency of exchange of the solvent molecules involved in the protein-solvent H-bonding formation is strongly reduced, leading to a stronger hydrophobic effect.¹⁹⁻²¹

The TRS²-FTIR difference spectrum of the wild type truncated sensor domain HemAT-*Bs* pD 8, subsequent to CO photodissociation at $t_d = 8$ μ s, exposed protein vibrations

associated with the global protein structure that is perturbed upon CO dissociation/rebinding. The identification of vibrations in the amide I region associated with solely α -helical structure are in agreement with the predominantly helical composition of the truncated sensor domain of HemAT-*Bs*, much like that of *S_wMb*.^{17,22} Hence, the strong peak/trough identified in the 1660-1640 cm^{-1} frequency range attributed to α -helix provides an indication of an overall structural rearrangement of the protein moiety upon CO photodissociation. The downshift of amide I vibrations demonstrates that upon CO-photodissociation, there is an increase in the solvent-accessible areas of the protein. Furthermore, the detection of vibrations attributed to both the protonated and deprotonated forms of heme propionates in the spectra indicates the presence of both conformations within the homodimer, thus we propose that the heme periphery is perturbed upon CO photodissociation. We cannot deduce from our spectra which of the two heme propionate groups is protonated and which is deprotonated or whether both states exist in both subunits. Comparing the X-ray crystal structures of the unliganded and CN-bound forms of the truncated sensor domain HemAT-*Bs*, we observe two protonation/deprotonation events of the heme-propionate groups in subunit B.¹⁷ It seems that upon ligand binding the hydrogen bond between Ser87 and heme-6-propionate is cleaved while a new hydrogen bond forms between heme-7-propionate and a water molecule. The protonation state of the heme propionate groups in subunit A is not altered upon ligand binding. Therefore, we speculate that the detected vibrations attributed to the deprotonated heme propionates might arise from the formation of the hydrogen bond between the heme-6-propionate and the distal residue Ser87 in subunit B upon dissociation of CO from the heme-Fe(II) although to confirm the latter speculation spectroscopic studies of mutant S87 would be necessary. It is rather interesting that Yoshimura *et al.*⁴ demonstrated that upon oxygen binding a hydrogen bond forms between His86 located adjacent to Ser87, which does not seem to form neither upon CO nor upon NO binding.

Comparison of the TRS²-FTIR difference spectrum of the wild type truncated sensor domain with that of the wild type full length HemAT-*Bs* at pD 8, subsequent to CO photodissociation at $t_d = 8 \mu\text{s}$, revealed a distinct split of the α -helix mode in the amide I region of the full length protein. The latter provides evidence for movement of an additional α -helix upon CO dissociation in wild type full length HemAT-*Bs*. In addition, the difference in the kinetic evolution of the protein vibrations observed between the wild type full length and truncated sensor domain HemAT-*Bs*, further supports the notion that the protein conformational motions upon ligand photodissociation in the full length form follow a different pattern compared to the truncated sensor domain form. Of course, lack of a resolved

X-ray crystal structure for the complete HemAT-*Bs* protein does not allow for definite assignment of the proposed additional α -helix movement to a specific helix. However, if we consider that the H-helix located adjacent the G-helix is the communication link between the sensor domain and the helical structure of the effector domain, a possible scenario could be that the distinct additional α -helix movement observed in the full length protein spectrum must be due to interactions between the sensor and effector domain upon CO dissociation communicated through structural reorientation of the H-helix. Obviously the above speculation requires further investigation, by performing mutations of residues that lie in the vicinity of the H-helix that could potentially give more information on the dynamic changes induced to the H-helix upon CO-dissociation and rebinding. It is important to comment that the present results challenge the suggestion by El-Mashtoly *et al.*⁶ that based on absence of the 1660 cm^{-1} amide I peak in the full length HemAT-CO TR-UVRR, otherwise present in the spectra of the sensor domain protein, conformational changes of the sensor domain are not propagated to the effector domain upon CO binding in HemAT-*Bs*.

Absence of the distal residue Thr95 to Ala was shown to affect neither the Fe^{2+} -CO conformations nor the kinetic evolution of CO-rebinding. The similarity between the spectrum of the wild type protein to that of T95A denotes little effect from the absence of Thr95 located near Leu92 in E-helix, on the environment surrounding the heme-bound CO. The latter suggest that Thr95 is not the distal site residue that directly interacts through hydrogen bonding with the heme-bound CO and signifies the specificity of the hydrogen bonding interaction of Thr95 with the heme-bound gaseous ligand solely upon O_2 binding, as previously reported.^{1,3,4,7}

Superpositioning the crystal structure of the unliganded truncated sensor domain HemAT-*Bs* over the CN-bound unveiled substantial structural reorientation of the B-helix, particularly in regards to subunit B. Relating the above with the perturbation of the CO conformations seen in the FTIR spectrum of Y70F and the evident change of α -helix movement observed in the TRS²-FTIR difference spectrum of Y70F at $8\ \mu\text{s}$ after CO-photodissociation, it is equitable to conclude that Tyr70 is the distal site residue involved in direct interactions with the heme-bound CO. Tyr70 is located in the B-helix and in contrast to the findings of Zhang *et al.*¹⁸ that suggest an “up” conformation pointed away from the heme pocket for both subunits of the HemAT-CO adduct, we propose that upon CO-binding the B-helix undergoes structural reorientation so as for Tyr70 to adopt a “down” conformation where its phenolic hydroxyl group can act as a hydrogen bond donor to the heme-bound CO (**Figure 5.16**). It is important to mention that the mutation of Tyr70 to Phe does not seem to

influence the time evolution of CO rebinding. Evidently, since both Tyr and Phe have similar size side chains that tend to orient towards the interior of the protein structure, the latter mutation does not cause steric effects near the heme binding pocket.

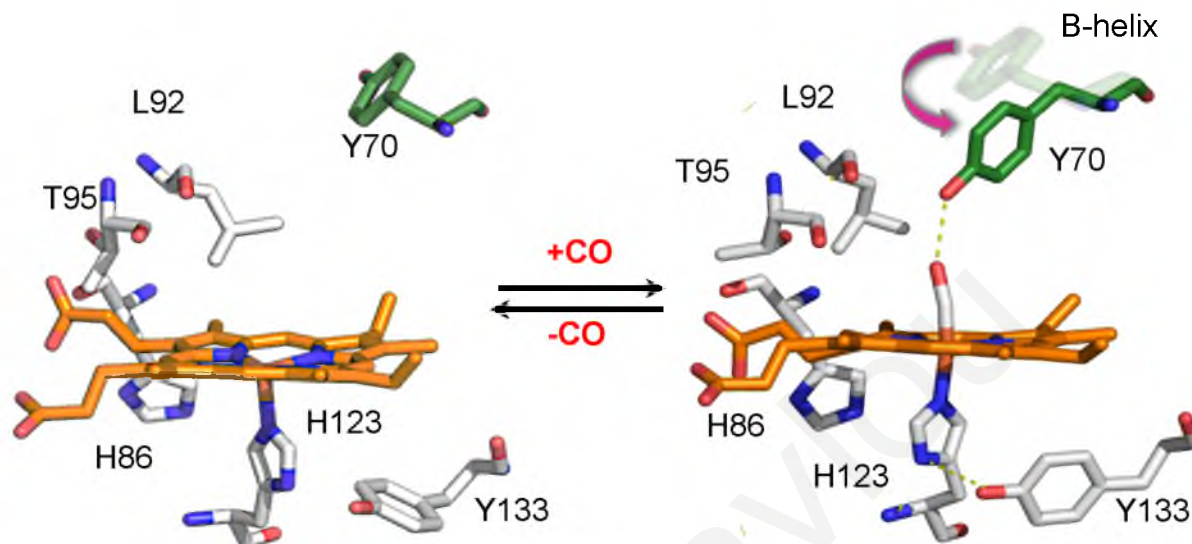


Figure 5.16 Schematic representation of the proposed structural reorientation of Tyr70 and its hydrogen bonding interaction with Fe^{2+} -CO upon CO-binding to the heme-iron (PDB IDs 1OR4 & 1OR6).

Yoshimura *et al.*⁴ proposed a reversible formation of a hydrogen bond between a proximal residue and His123 triggered upon CO binding, based on the absence of the 227 cm^{-1} $\nu_{\text{Fe-His}}$ peak noted in the time-resolved resonance Raman spectra, of the wild type HemAT-CO adduct upon CO photolysis. The *trans* axial ligand His123 is positioned near the proximal residue Tyr133 located on the G-helix.¹⁷ Indeed, the $\nu_{\text{Fe-His}}$ peak was attributed to a hydrogen bond between proximal residue Tyr133 and His123 after a 2 cm^{-1} downshift was observed in the TR³ spectrum of Y133F. The fact that this frequency downshift of the $\nu_{\text{Fe-His}}$ peak progressed independently from its intensity change established that it was predominantly due to a change of the hydrogen bond to His123 upon CO-photodissociation. The change in the width and intensity of the amide I (α -helix) vibration modes observed in our TRS²-FTIR difference spectrum of Y133F at $6\ \mu\text{s}$ after CO-photodissociation, suggests increased flexibility of protein secondary structure. In general, broadening of vibrational bands can provide information about the rigidity of the protein structure, with flexible structures giving broader bands than rigid structures. If we consider that H-bonding with the N_δH of His123 increases backbonding by facilitating the donation of Fe d_π electrons to the CO π^* orbitals,

therefore strengthening the Fe-CO bond and increasing the rigidity of the heme-CO complex²⁴⁻²⁶, then the formation of the hydrogen bond between proximal His123 and Tyr133 upon CO-binding as described by Yoshimura *et al.*³ is also consistent with our TRS²-FTIR data. Spectral changes in the amide (α -helix) region of Y133F also denote disruption of movement of an α -helix. The X-ray crystal structure of the unliganded truncated sensor domain HemAT-*Bs*, shows the phenolic hydroxyl group of proximal residue Tyr133 located at a distance that is not possible for it to form a hydrogen bond with the N δ H of His123.^{4,18,23} Therefore, upon CO-binding, reorientation of the G-helix allows the side chain of Tyr133 to be positioned at an optimal distance for its phenolic OH group to form a hydrogen bond with the N δ H of His123 (**Figure 5.17**). It is of particular interest that this bond seems to be a critical constituent of both the CO-bound and O₂- forms of HemAT-*Bs*.^{4,23} Yoshida *et al.* suggest that although both the oxy and carbonmonoxy HemAT-*Bs* presumably possess such hydrogen bond, the conformational motions caused by the formation of this H-bond must be different for each form.²³

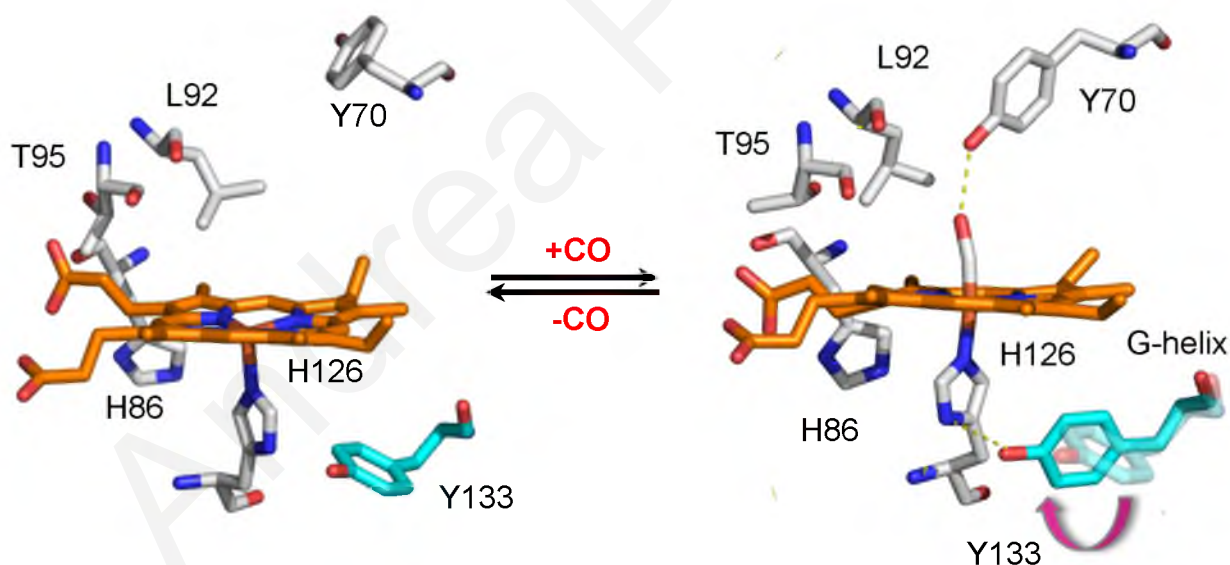


Figure 5.17 Schematic representation of the proposed structural reorientation of Tyr133 and its hydrogen bonding interaction with the N δ H of the trans axial His123 upon CO-binding to the heme-iron (PDB IDs 1OR4 & 1OR6).

Intriguingly, the truncated sensor domain Y133F was the only form of HemAT-*Bs* that demonstrated monophasic CO-rebinding kinetics. As mentioned earlier, biphasic CO-rebinding process denotes two distinct components within the homodimer. Assuming the validity of the above observation, we propose that the initial fast CO-rebinding phase involves

a component with the Tyr70 side chain at a “down” conformation and the following slow CO-rebinding phase involves a component with the Tyr70 side chain exposed to the solvent. If we suppose that conformational changes are cross-communicated between B- and G-helices upon CO-dissociation/rebinding, then mutation of Tyr133 to Phe would result in a global domino effect for the heme active site. Specifically, absence of Tyr133 means absence of a hydrogen bond between Tyr133 and His123 that should have formed upon CO-binding. Since no hydrogen bond is present between these two proximal residues, then the structural rearrangement of the G-helix upon CO-photodissociation is perturbed, possibly affecting the movement of B-helix, thus resulting in a monophasic CO-rebinding pattern. Hence, Tyr133 is a critical constituent of the CO-binding process, as its hydrogen bonding interactions with His123 facilitate the distinct conformational motion not only of G-helix but potentially of the adjacent B-helix upon CO-binding.

Mutation of Leu92 to Ala hardly affected the vibrations of the amide I region indicating that absence of Leu92 does not significantly influence the structural orientation of E-helix or the secondary structure surrounding the heme binding pocket. However, the latter mutation resulted in a transient CO-rebinding phase with a larger amplitude with a three-fold faster second CO-rebinding phase. In general, a faster CO-rebinding process indicates a distal pocket that is likely to be open and readily accessible to solvent. Therefore, we propose that Leu92 acts as the conformational gate in the migration pathway of the photodissociated CO (Figure 5.18). For more detailed analysis refer to Chapter 6.

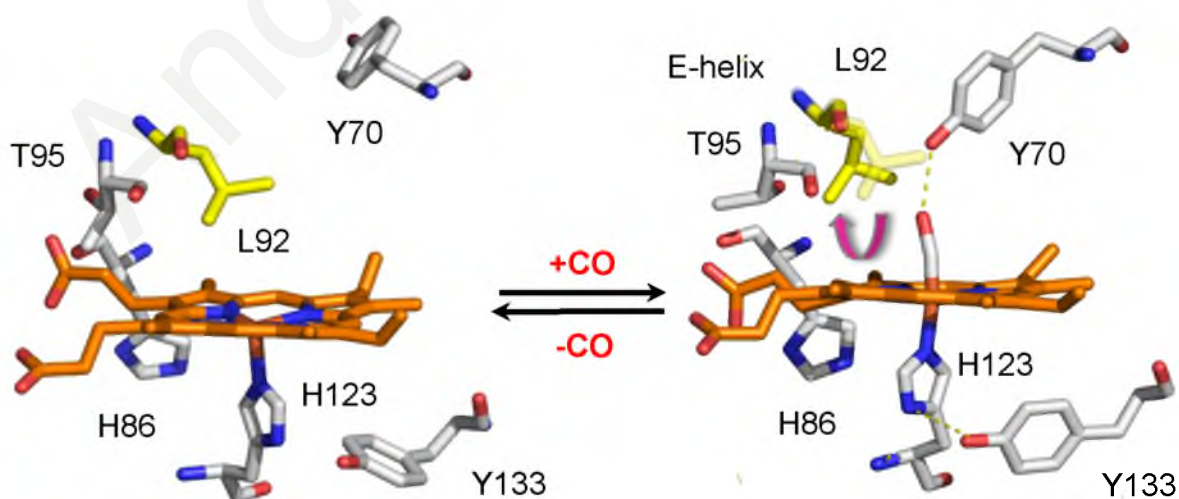


Figure 5.18 Schematic representation of the proposed lateral movement of Leu92 upon CO-binding that blocks water molecules from entering the distal site of the heme pocket (PDB IDs 1OR4 & 1OR6).

Henceforth, based on the findings from both the static FTIR and the time-resolved step-scan FTIR experiments of the present work we propose a model describing the conformational motions that take place upon CO binding to HemAT-Bs.

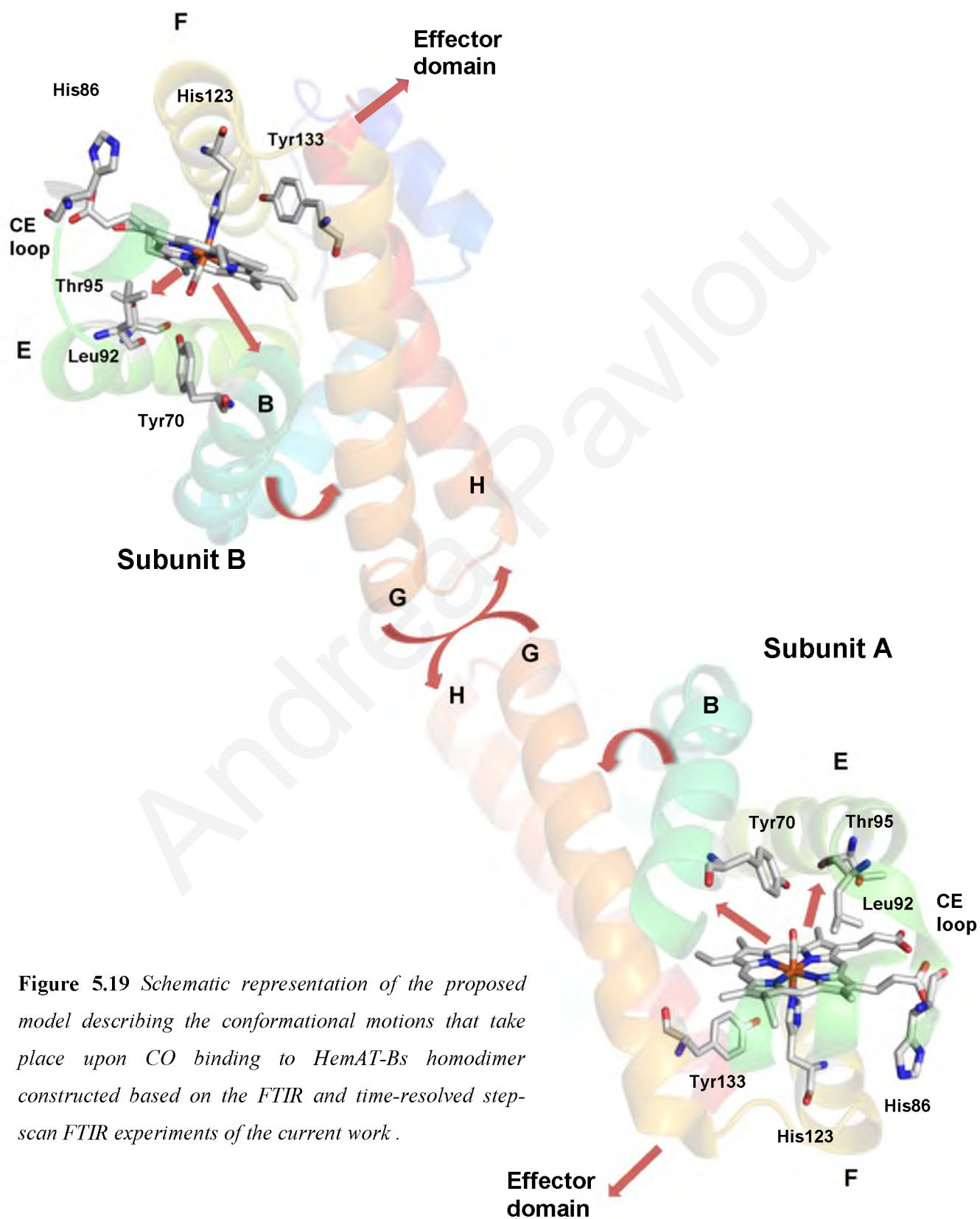


Figure 5.19 Schematic representation of the proposed model describing the conformational motions that take place upon CO binding to HemAT-Bs homodimer constructed based on the FTIR and time-resolved step-scan FTIR experiments of the current work .

To elaborate, as illustrated in **Figure 5.19**, upon CO binding, there is movement of the B-helix causing reorientation of the distal residue Tyr70 which adopts a position optimal for its phenolic hydroxyl side chain to act as a hydrogen bond donor to the heme-bound CO. The hydrogen bonding interaction between Tyr70 and Fe²⁺-CO communicates these conformational changes to the G-helix that undergoes structural reorientation to position Tyr133 at such distance that permits a hydrogen bond to form between the OH⁻ of Tyr133 and the N_δH of axial His123. The latter hydrogen bond strengthens the Fe-His bond and consequently the Fe²⁺-CO bond hence, stabilizing the complex. At the same time the hydrogen bond between Ser87 (C-helix) and the heme-6-propionate in subunit B is cleaved, shifting the propionate group downwards. These structural rearrangements are then propagated through the CE-loop to the E-helix, causing a lateral movement of the side chain of Leu92 that shields the heme-binding pocket thus, controlling the CO migration pathway.

Though previous studies suggested that changes in the sensor domain are not propagated to the effector domain upon CO-binding, the identification of additional α -helix movement in the full length protein, as well as the observed differences in the process of protein relaxation between the sensor domain and the full length HemAT-*Bs* in the present work, infer a possible interaction between the sensor and the effector domain in the CO-bound HemAT-*Bs*. Of course to establish the existence of such interaction it is necessary to perform site-specific spectroscopic studies involving the environment surrounding H-helix, proposed to be the connecting link between the helical structures of the sensor and the effector domains, and investigate the dynamic changes induced to H-helix upon ligand dissociation/rebinding.

5.4 Conclusions

In an attempt to gain insight into the initial events of the intramolecular signal transduction mechanism of HemAT-*Bs*, we have employed FTIR and time-resolved step-scan FTIR spectroscopies. The sensitivity of time-resolved step-scan FTIR spectroscopy to protein structural changes allowed us to monitor the dynamic changes induced to HemAT-*Bs* upon CO-dissociation/rebinding. Although not the physiological ligand, the excellent spectroscopic properties of CO, as well as its effective binding to HemAT-*Bs* and its high quantum yield rendered it a suitable probe to investigate the structure-function properties of the enzyme. The FTIR spectra of the HemAT-*Bs*-CO adducts of both the wild type full length and truncated

sensor domain forms of the protein reveal two conformations of the heme-bound CO that are attributed to (a) an “open” conformation where the heme-bound CO exhibits weak interactions with the distal site and to (b) a “closed” conformation where hydrogen bonding interactions of the heme-bound CO with the distal residues exist. The two modes appear negative upon CO-photodissociation with a high photoproduct yield excluding the possibility of geminate recombination. Monitoring the kinetic evolution of CO rebinding in the wild type HemAT-*Bs* uncovers biphasic kinetics in the microsecond to millisecond time scale with two distinct phases of conformational changes, a transient phase with small amplitude resolved by 48 μ s and a slow phase with a large amplitude persisting until 3 ms. We assume that it is the existence of cooperativity between the two structurally asymmetric components within the homodimer that gives rise to the two distinct CO-rebinding phases; binding of CO to one component results in conformational changes that affect CO binding to the other component. The CO-rebinding process appears slower for the wild type full length compared to the wild type sensor domain HemAT-*Bs* suggesting possible differences between the two forms in the cavities the ligand is accommodated while escaping away the distal site of the heme pocket. A clear split of the amide I peak as well as a different trend in the protein relaxation process for the wild type full length HemAT-*Bs* compared to the truncated sensor domain protein, allow us to suggest the possibility of signal transduction from the sensor to the effector domain of HemAT-*Bs* not only in the O₂-bound but in the CO-bound form as well.

The perturbation of the $\nu(\text{CO})$ conformations upon mutation of the distal residues Tyr70, Leu92 and the proximal residue Tyr133 suggests interaction of the latter residues with Fe²⁺-CO. Indeed, the presence of only positive peaks in the amide I region for Y70F (B-helix) and the loss of intensity and the broadening of the same peaks for Y133F (G-helix) observed in the TRS²-FTIR difference spectra subsequent to CO-photodissociation, denotes disruption of α -helix movement. We propose substantial structural reorientation for B- and G-helices upon CO binding, so as to position the phenolic hydroxyl side chains of Tyr70 and Tyr133 at such position that is possible to form hydrogen bonds with Fe²⁺-CO and axial His123 respectively. The monophasic CO-rebinding process for Y133F suggests that the conformational changes in the B- and G-helices are in some degree concomitant. Although Leu92 does not seem to interact directly with the heme-bound CO, we demonstrate for the first time its role as the conformational gate in the migration pathway of photodissociated CO.

5.5 References

1. T. Ohta, H. Yoshimura, S. Yoshioka, S. Aono, T. Kitagawa, *J. Am. Chem. Soc.* **2004**, *126*, 15000-15001.
2. T. Ohta, T. Kitagawa, *Inorg Chem.* **2005**, *44*, 758-69.
3. H. Yoshimura, S. Yoshioka, K. Kobayashi, T. Ohta, T. Uchida, M. Kubo, T. Kitagawa, S. Aono, *Biochemistry* **2006**, *45*, 8301-8307.
4. H. Yoshimura, S. Yoshioka, Y. Mizutani, S. Aono, *Biochem. Biophys. Res. Comm.* **2007**, *357*, 1053-1057.
5. A. Mokdad, M. Nissen, J. D. Satterlee, R. W. Larsen, *FEBS Lett.* **2007**, *581*, 4512-4518.
6. S. F. El-Mashtoly, M. Kubo, Y. Gu, H. Sawai, S. Nakashima, T. Ogura, S. Aono T. Kitagawa, *J. Biol. Chem.* **2012**, *287*, 19973-19984.
7. S. Aono, T. Kato, H. Nakajima, T. Ohta, T. Uchida, T. Kitagawa, *J. Biol. Chem.* **2002**, *277*, 13528-13538.
8. E. Pinakoulaki, H. Yoshimura, S. Yoshioka, S. Aono, C. Varotsis, *Biochemistry* **2006**, *45*, 7763-7766.
9. T. Li, M. Quillin, G. Phillips, J. Olson, *Biochemistry* **1994**, *33*, 1433-1446.
10. M. Unno, J. Christian, J. Olson, T. Sage, P. Champion, *J. Am. Chem. Soc.* **1998**, *120*, 2670-2671.
11. M. Schleegeer, C. Wagner, M. J. Vellekoop, B. Lendl, J. Heberle *Anal Bioanal Chem* **2009**, *394*, 1869-1877.

12. A. Barth, C. Zscherp, *Q. Rev. Biophys.* **2002**, *35*, 369–430.
13. A. Barth, *Prog. Biophys. Mol. Bio.* **2000**, *74*, 141–173.
14. P. Hellwig, T. Soulimane, G. Buse, W. Mantele, *Biochemistry* **1999**, *38*, 9648-9658.
15. A. Koutsoupakis, T. Soulimane, C. Varotsis, *Biophys. J.* **2004**, *86*, 2438- 2444.
16. S. F. El-Mashtoly, Y. Gu, H. Yoshimura, S. Yoshioka, S. Aono, T. Kitagawa, *J. Biol. Chem.* **2008**, *283*, 6942-6949.
17. W. Zhang, G. N. Jr. Phillips, *Structure* **2003**, *11*, 1097-1110.
18. W. Zhang, J. S. Olson, G. N. Jr. Phillips G.N.Jr.; *Biophys. J.* **2005**, *88*, 2801-2815.
19. M. Jasnin, M. Tehei, M. Moulin, M. Haertlein, G. Zaccai, *Eur Biophys J.* **2008**, *37*, 613-617.
20. P. Cioni, G. Strambini, *Biophys J.* **2002**, *82*, 3246–3253.
21. S. Sheu, E. Schlag, H. Selzle, D. Yang, *J. Phys. Chem. A* **2008**, *112*, 797-802.
22. H. C. Watson, *Prog. Stereochem.* **1969**, *4*, 299.
23. Y. Yoshida, H. Ishikawa, S. Aono, Y. Mizutani, *Biochim. Biophys. Act.* **2012**, *1824*, 866–872.
24. G. B. Ray, X. Y. Li, A. J. Ibers, J. L. Sessler, T. G. Spiro, *J. Am. Chem. Soc.* **1994**, *116*, 162-176.
25. T. G. Spiro, A. V. Soldatova, G. Balakrishnan *Coord. Chem. Rev.* **2013**, *257*, 511–527.
26. M. Zhang, M. Lis, J. H. Wang, H. J. Vogel, *J. Biol. Chem.* **1994**, *269*, 15546-15552.



CHAPTER 6

Ligand Docking Sites in HemAT-*Bs*

Andrea Pavlou

6.1 Introduction

The comprehending of the physiological significance of the molecular mechanism through which heme-based sensor proteins accomplish their biological role, becomes perplexed due to their diverse ligand recognition and discrimination properties. Comparison of different globin proteins, with Mb and Hb being the most extensively studied, established that ligand migration between distinct docking cavities is a common event in this group of proteins, and ultimately essential for the efficiency of their ligand binding properties to small diatomic gaseous molecules such as O₂, CO, and NO.¹⁻⁴ Kinetic and spectroscopic experiments recognized a series of temporary intermediate docking sites in proteins such as Mb, through which the photodissociated gaseous ligand migrates. These cavities usually located next to the heme binding pocket, serve as “reservoirs” that transiently host O₂, CO, or NO thus, mediating the gradual diffusion of ligands to and from the heme binding site. In addition, accommodation of a specific ligand within the protein matrix does not only assist ligand binding but can potentially multiply its effective concentration and influence its relative affinity compared to other competitive exogenous or internal ligands.^{4,6,7}

For the investigation of the existence of such cavities with FTIR spectroscopy, CO has been the preferred ligand of choice due to its strong stretching vibration given the high sensitivity of the CO dipole to the local structure and electric fields.^{7,8} It has been shown that in heme-proteins upon photodissociation from heme-iron, the photolyzed CO transiently hops between pre-existing cavities assisted by secondary structure reorientations before escaping the protein, without implying however that it sequentially hops through all cavities. Consequently, the photodissociated CO trapped inside of the protein matrix displays IR modes near 2130 cm⁻¹ that arise from the confinement of CO for a substantial amount of time in these distinctive internal docking sites. Due to the small absorbance intensities and wavenumber shifts of these modes, following the migration of CO trapped into the protein matrix requires particularly meticulous experiments.^{9,10}

In response to the latter statement, in this work we employ time-resolved step-scan FTIR spectroscopy in the nanosecond time scale ($t_d = 200$ ns) to structurally and kinetically investigate the transient events of protein relaxation and CO migration in full length HemAT-*Bs* pD 8 (wild type and mutant L92A). The TRS²-FTIR difference spectra $t_d = 200$ ns subsequent to CO photodissociation confirm the biphasic CO rebinding pattern for both the

wild type and L92A protein observed in the TRS²-FTIR difference spectra $t_d = 6 \mu\text{s}$, with L92A having a transient phase with much larger amplitude. In addition to the A_0 (1967 and 1970 cm^{-1} WT and L92A respectively) and A_2 (1927 cm^{-1} WT) $\nu(\text{CO})$ negative peaks, we observe positive peaks at 2149 and 2136 cm^{-1} for the wild type protein and at 2132 cm^{-1} for the L92A mutant. These peaks are attributed to the portion of the photolyzed CO that is trapped in a cavity in the protein matrix before escaping away. Accordingly, based on the bands of heme-bound CO in wild type Mb B_0 at 2149 cm^{-1} and B_1 at 2131 cm^{-1} , we attribute the positive peaks at 2149 and 2136 cm^{-1} for the wild type protein and at 2132 cm^{-1} for the L92A mutant to different photoproduct states B in which CO interchanges and docks between pre-existing internal cavities of HemAT-Bs.

6.2 Results and Discussion

To observe transient CO recombination and migration events as a function of time we have employed time-resolved step-scan FTIR spectroscopy. To impact the occupancy of potential CO docking sites, besides the wild type full length protein we chose to perform experiments on the L92A mutant as it was the sole distal residue mutation of HemAT-Bs that demonstrated lower photoproduct yield in the microsecond timescale TRS²-FTIR experiments; 70% compared to 92% for the wild type protein.

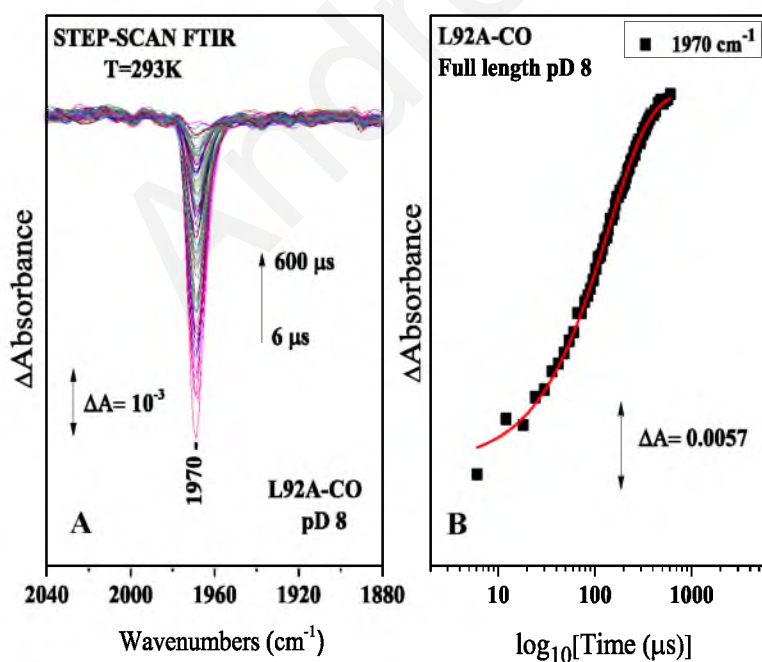


Figure 6.1 (A) Time-resolved step-scan FTIR difference spectra of the L92A full length HemAT-CO adduct at pD 8 from 0.006 to 600 μs subsequent to CO photolysis. (B) Plot of the ΔA of the 1970 cm^{-1} mode versus time on a logarithmic scale subsequent to CO photolysis. The red line corresponds to the exponential fit of the experimental data.

In addition, although the initial CO-rebinding phase for L92A was found to be \sim two-fold slower compared to the wild type protein (**Figure 5.6**) and other heme active site

mutants, a significantly faster second CO recombination phase resulted in an overall 10-fold faster CO rebinding rate to L92A (**Figure 6.1**).

Figure 6.2 depicts the TRS²-FTIR difference spectra of the wild type full length HemAT-CO adduct at pD 8 and $t_d = 300$ ns, 2.4 μ s and 6.4 μ s subsequent to CO photodissociation. Monitoring the existence of docking sites in real time has revealed two positive peaks of weak intensity at 2149 and 2136 cm^{-1} . We attribute these peaks to the 8% of photodissociated CO molecules trapped within the protein matrix.

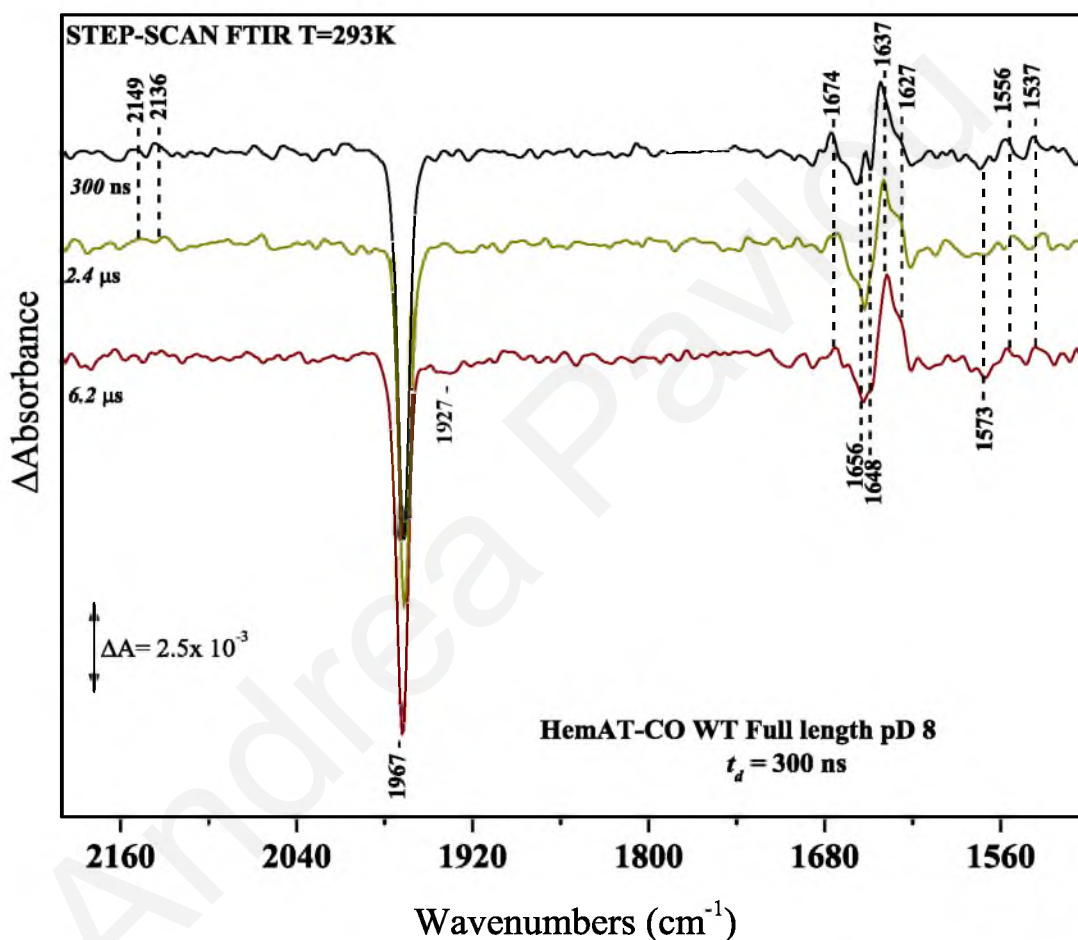


Figure 6.2 Time-resolved step-scan FTIR difference spectra of the wild type full length HemAT-CO adduct at pD 8 from 300 ns to 6 μ s subsequent to CO photolysis.

Proteins can adopt a vast number of somewhat distinctive structures, known as conformational substates. It has been proposed based on studies on the photodissociated Mb-CO complex that ligands interchange to an exclusive docking site *B* (*B* substates: $B_0 = 2149$ cm^{-1} and $B_1 = 2131$ cm^{-1}) in the distal heme pocket, which plays a critical role in establishment of the Fe^{2+} -ligand bond. When CO moves to the *B* docking site, it is parallel to the heme plane. The structural architecture of this pre-existing primary cavity allows for the ligand to be accommodated for long times at a timescale of nanoseconds without rebinding,

and this probability is further reduced with CO hopping from the primary docking cavity *B* to any other cavities that exist near the heme active site. The ligand (CO-) finally escapes from the protein assisted by conformational changes that take place in the nanosecond to microsecond timescales that transiently open exit channels for the migration of CO⁸ (**Figure 6.3**). Accordingly, based on the bands of heme-bound CO in wild type Mb B₀ at 2149 cm⁻¹ and B₁ at 2131 cm⁻¹, we attribute the positive peaks at 2149 and 2136 cm⁻¹ for the wild type protein to different photoproduct states *B* in which CO interchanges and docks between pre-existing internal cavities of HemAT-Bs. It is also probable that the difference in the rate of CO-rebinding observed between wild type full length and wild type truncated sensor domain HemAT-Bs is due to CO being accommodated into different docking sites along the migration pathway of the photodissociated CO. Monitoring the kinetic evolution of the B₀ and B₁ states of photodissociated CO, we have observed their disappearance by 6.5 μs indicating that CO has already escaped the protein matrix and its recombination back to heme-Fe²⁺ has begun.

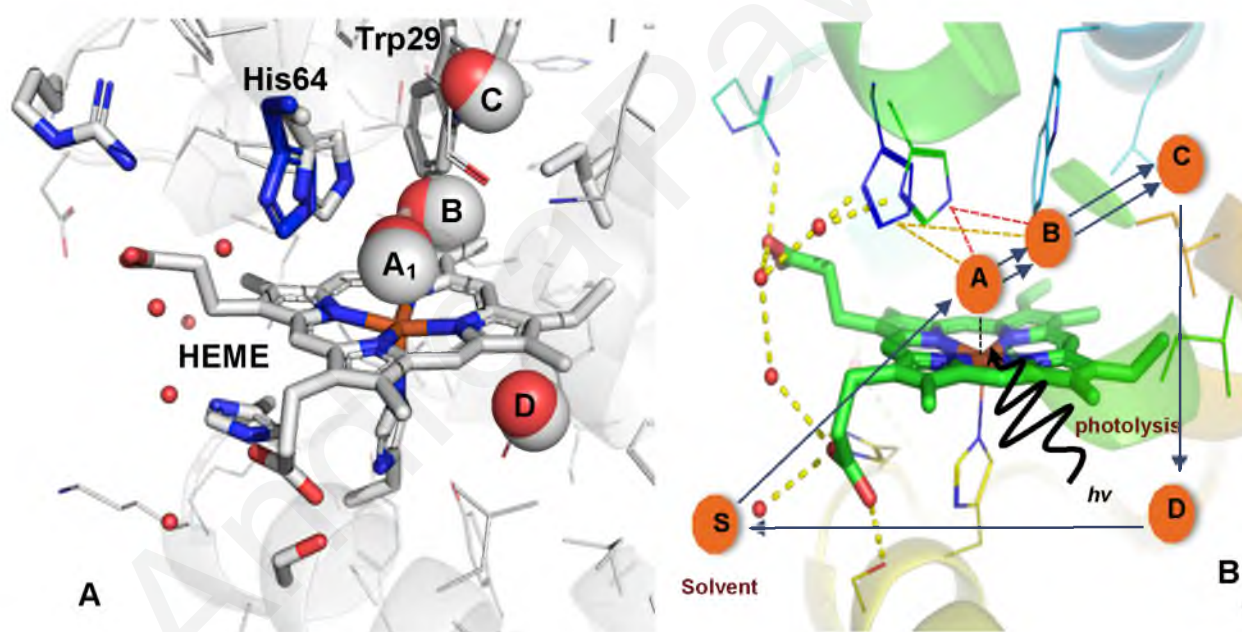


Figure 6.3 (A) & (B) Schematic representation of the photodissociation reaction of wild-type sperm whale MbCO depicting the movement of CO from the bound state *A* to the primary docking site *B*, and from there to the secondary docking sites *C*, and *D* until it is finally released into the solvent *S*. The position of these ligand docking substates are represented in (B) by the orange spheres. Figures adapted from Ref 11 & 12 respectively.

Observing the kinetic evolution of CO-rebinding as demonstrated through the TRS²-FTIR difference spectra of the wild type full length HemAT-CO adduct at pD 8 and $t_d = 6 \mu\text{s}$, revealed a transient initial CO-rebinding phase with a small amplitude that is completed by 50

μs (Figure 6.4). Plotting the continuous variability in intensity of the CO mode at 1967 cm^{-1} associated with heme- Fe^{2+} over a 1 - 50 μs time frame on a logarithmic scale confirmed both the existence of the initial transient rebinding phase and the rate of CO recombination. The latter results provided further evidence that support the speculation of two different components within the HemAT-Bs homodimer.

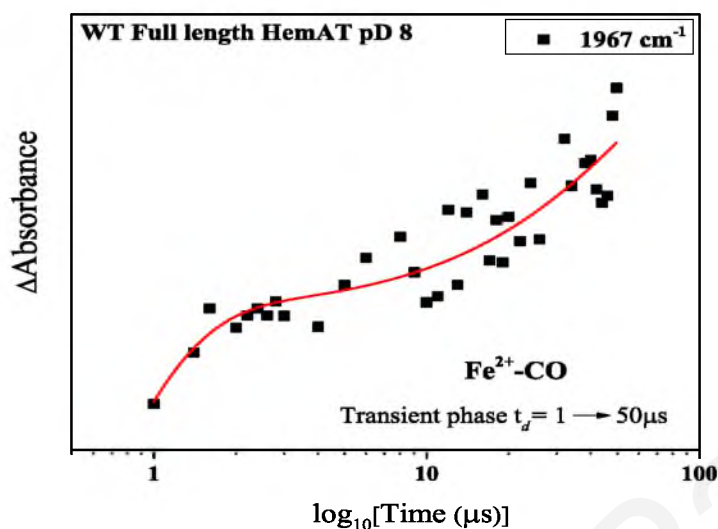


Figure 6.4 Plot of the ΔA of the 1967 cm^{-1} mode versus time on a logarithmic scale of the wild type full length HemAT-CO adduct subsequent to CO photolysis during the transient phase $t_d = 1 - 50\ \mu\text{s}$. The red line corresponds to the exponential fit of the experimental data.

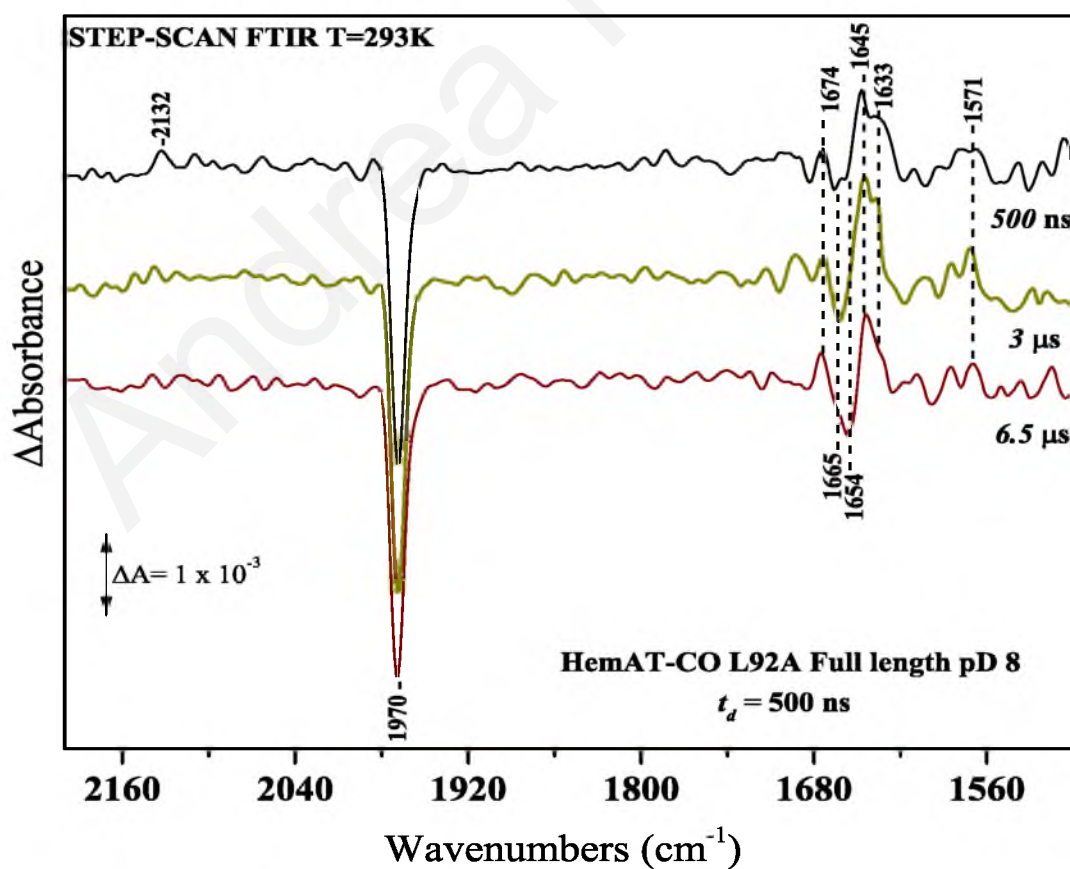


Figure 6.5 Time-resolved step-scan FTIR difference spectra of the L92A full length HemAT-CO adduct at pD 8 from 500 ns to 6 μs subsequent to CO photolysis.

Figure 6.5 illustrates the TRS²-FTIR difference spectra of the L92A full length HemAT-CO adduct at pD 8 and $t_d = 500$ ns, 2.5 μ s and 6.5 μ s subsequent to CO photodissociation. The difference in time resolution from the wild type protein is due to lower signal-to-noise ratio which in the case of L92A required averaging with more than one time slices. Monitoring the existence of docking sites in real time has revealed only one positive peak of weak intensity at 2132 cm^{-1} . We attribute this peak to the 30% of photodissociated CO molecules trapped within the protein matrix in state B₁ with no population visible in B₀.

The question that should follow is why does mutation of Leu92 to Ala affect the population of photodissociated CO trapped at primary docking state B. In general photodissociated ligands will initially dock in site B, which is in contact with the heme group. Leu92 is located very near the heme binding site, essentially capping the bound-CO. We presume that mutation of Leu92 brings upon such conformational changes to the protein that the migration pathway towards state B₀ is blocked and therefore only state B₁ accumulates any photodissociated CO population. Interestingly, IR studies of photodissociated crystal orthorhombic MbCO complex indicated that $\sim 90\%$ of B substates (2131 and 2149 cm^{-1}) adopted the 1927 cm^{-1} state upon rebinding¹¹, which could relate the absence of the $\nu(\text{CO})$ mode at 1927 cm^{-1} with the absence of the photodissociated CO mode at 2149 cm^{-1} in L92A. Undoubtedly however, our experiments and analysis are not in a position to provide quantitative information concerning the above speculation. Finally, as the protein fluctuates and relaxes towards CO-recombination initiation, the positive peak at 2132 cm^{-1} disappears.

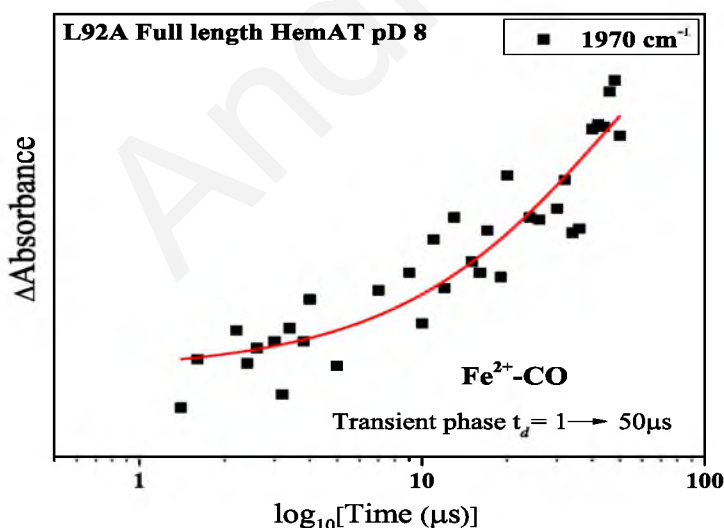


Figure 6.6 Plot of the ΔA of the 1970 cm^{-1} mode versus time on a logarithmic scale of full length L92A HemAT-CO adduct subsequent to CO photolysis during the transient phase $t_d = 1 - 50$ μ s. The red line corresponds to the exponential fit of the experimental data.

Similar to the wild type protein, we plotted the continuous variability in intensity of the CO mode at 1970 cm^{-1} associated with heme-Fe²⁺ over a 1 - 150 μ s time frame on a

logarithmic scale and observed a transient initial rebinding phase with trend and rate analogous to that observed in the TRS²-FTIR difference spectra of the L92A full length HemAT-CO adduct at pD 8 and $t_d = 6 \mu\text{s}$ with the transient initial phase of CO rebinding completed by 150 μs compared to 50 μs in the wild type protein (**Figure 6.6**).

6.3 Conclusions

Photodissociation TRS² – FTIR spectroscopy experiments coupled with kinetic analysis provided valuable insight into the transient protein–ligand interactions of HemAT-*Bs* with CO. We have reported the identification of a ligand (CO) docking site in HemAT-*Bs* that corresponds to *B* state in which CO is trapped in a cavity within the protein matrix. The observation of two *B* state bands suggests that protein fluctuations allow the transition of CO populations from one *B* state to another, prior to the ligand escaping away from the distal site and into the solvent. The absence of the 2149 cm^{-1} band from the spectra of the L92A demonstrates that mutation of Leu92 partially blocks the photodissociated CO from accessing specific pre-existing internal ligand cavities in HemAT-*Bs*.

6.4 References

1. M. Brunori, *Biophys. Chem.* **2000**, *86*, 221-230.
2. M. Brunori, B. Vallone, F. Cutruzzola, C. Travaglini-Allocatelli, J. Berendzen, K. Chu, R. M. Sweet, I. Schlichting, *Proc. Natl. Acad. Sci. U S A* **2000**, *97*, 2058- 2063.
3. M. Lim, T. A. Jackson, P. A. Anfinrud, *Science* **1995**, *269*, 962-966.
4. M. Lim, T. A. Jackson, P. A. Anfinrud, *Nat. Struct. Biol.* **1997**, *4*, 209-214.
5. A. Ostermann, R. Waschipky, F. G. Parak, G. U. Nienhaus, *Nature* **2000**, *404*, 205-208.
6. D. C. Lamb, K. Nienhaus, A. Arcovito, F. Draghi, A. E. Miele, M. Brunori, G. U.

- Nienhaus *J. Biol. Chem.* **2002**, *277*, 11636-11644.
7. K. Nienhaus, G. U. Nienhaus, *Biochim. Biophys Acta* **2011**, *1814*, 1030–1041.
 8. L. Mouawad, C. Tetreau, S. Abdel-Azeim, D. Perahia, D. Lavalette, *Protein Sci.* **2007**, *16*, 781–794.
 9. K. Chu, J. Vojtchovsky, B. H. McMahon, R. M. Sweet, J. Berendzen, I. Schlichting, *Nature* **2000**, *403*, 921-923.
 10. J. R. Mourant, D. P. Braunstein, K. Chu, H. Frauenfelder, G. U. Nienhaus, P. Ormos, R. D. Young, *Biophys. J.* **1993**, *65*, 1496-1507.
 11. K. Nienhaus, D. C. Lamb, P. Deng, G. U. Nienhaus, *Biophys. J.* **2002**, *82*, 1059–1067.
 12. K. Y. Oang, J. G. Kim, C. Yang, T. W. Kim, Y. Kim, K. H. Kim, J. Kim, H. Ihee, *J. Phys. Chem. Lett.*, **2014**, *5*, 804–808



CHAPTER 7

**Probing the Ligand Recognition and Discrimination
Environment of the Globin-coupled Oxygen Sensor
Protein YddV (or *EcDosC*) by FTIR and Time-
resolved step-scan FTIR (TRS²-FTIR) Spectroscopy**

7.1 Introduction

In the *Escherichia coli* genome, *yddV* and *dos* genes are organized as a bicistronic operon to regulate synthesis and degradation of 3',5'-cyclic diguanylic acid (c-di-GMP), respectively. Modulation of overall conversion from GTP to pGpG via c-di-GMP is catalysed by YddV (or *EcDosC*) and *EcDOS* (or *EcDosP*).¹⁻⁷ The *dos* gene product is the heme-based oxygen sensor protein *EcDOS* (*E. coli* direct oxygen sensor) and the *yddV* product from *Escherichia coli* (*Ec*) is a globin-coupled heme based oxygen sensor protein displaying diguanylate cyclase activity in response to oxygen availability.^{1,2} The globin-coupled oxygen sensor protein structures and signal transduction mechanisms are unique and differ from those of FixL^{8,9} and *EcDOS*^{10,11}, which contain the heme bound PAS fold domain. The sensor of the globin-coupled oxygen sensor family has a globin fold at the N-terminus and contains a heme that acts as the O₂-binding site but with limited amino acid homology to myoglobin (Mb) and hemoglobin (Hb) and the diguanylate cyclase (DGC) domain at the C-terminus. The globin fold lacks the D and half of the E-helices of Mb and Hb.¹ To date, seven heme-based oxygen sensor proteins with the globin fold have been identified; YddV, *AjGcHK*, *HemAT-Bs*, *HemDGC*, *BpeGReg*, *AvGReg*, and *GsGCS*.^{1,12-17} Because of the importance of c-di-GMP as messenger in bacteria and the increasing interest in understanding the connectivity between O₂ and the metabolism of c-di-GMP it is essential to elucidate the properties of the newly discovered globin-coupled oxygen sensor proteins. In addition, little is known about the dynamics of signal transduction and the role of the distal environment in regulating the binding of O₂ and CO. Determination of the structural dynamics of the protein moiety associated with the ligand binding/photodissociation from bound ligand(s) to the heme Fe(II) is of particular importance towards our interest in understanding the initial steps in the signaling mechanism.

Based on the catalytic activities in terms of the initial rate of product formation (c-di-GMP) similar turnover numbers (0.022 min⁻¹) were measured for O₂ and CO indication that YddV recognizes both O₂ and CO. In the absence of x-ray crystallographic data based on the comparative amino acid sequence study with well-known heme-based sensor it has been proposed that H98 is the proximal to the heme ligand.¹⁸ As isolated sensor domain form (YddV-heme), YddV-heme forms only five-coordinate high spin Fe(III) complex containing a proximal H98 as the fifth ligand. On the distal site it has been demonstrated that the conserved

residues L65 and Y43 are important for the binding and stabilization of the heme Fe(II)-O₂ complex. The absorption spectra of wild type YddV has a Soret band at 391 nm, a Q band at 509 nm and a charge-transfer band at 642 nm which are characteristic of a five-coordinated, high spin species.^{18,19} Extensive pH studies on L65 mutant proteins have revealed the presence of H₂O molecule as the sixth axial ligand, which is converted to OH⁻ at alkaline pH, and the formation of a six-coordinated low-spin species.¹⁹ Resonance Raman (RR) Soret excitation experiments of wild type and Y43F mutant protein, have been reported. The RR frequencies of the wild type protein of the oxy complex with $\nu(\text{Fe-O}_2) = 565 \text{ cm}^{-1}$ and CO complex with $\nu(\text{Fe-CO}) = 495 \text{ cm}^{-1}$ are distinctly different from those reported at $\nu(\text{Fe-O}_2) = 559 \text{ cm}^{-1}$ and $\nu(\text{Fe-CO}) = 505 \text{ cm}^{-1}$ for the Y43F mutant protein, suggesting that Y43 forms a H-bond with the bound to the heme iron, O₂ and CO ligands. Interestingly, the Y43A and Y43L mutant proteins exhibited very low O₂ affinities, and thus, the $\nu(\text{Fe-O}_2)$ was not observed. In addition, the $\nu(\text{CO})$ for the wild-type and Y43F mutant protein were reported at 1965 and 1959 cm⁻¹, respectively, indicating the formation of a single conformation.¹⁹

Fourier transform infrared (FTIR) spectroscopy has been extensively applied to monitor the distal to the heme environment of the bound to the heme CO ligand and time-resolved step-scan FTIR (TRS²-FTIR) spectroscopy has already proven to be very powerful technique in studying transient changes at the level of individual amino acids during protein action and conformational changes of the protein backbone. In the FTIR spectrum of the CO-bound YddV we detect two CO modes at 1962 and 1923 cm⁻¹ which we attribute to neutral (apolar) and strong H-bonded conformers, respectively. In the spectra of the L65M mutant a single vibration of the C-O is observed at 1953 cm⁻¹ indicating strong alteration in the distal structure upon the L65M mutation. The CO vibration in the L65T mutant, although produced a low yield of photoproduct (29%) was observed at the same frequency as the wild-type at 1962 cm⁻¹, suggesting that the L65T mutant makes no significant alterations in the interactions of the bound CO with the distal environment. Both the Y43A and Y43W mutants produced similar photoproduct yields as that observed in the wild type (>90%) and the C-O mode is observed at 1962 and 1953 cm⁻¹, respectively. The Y43F mutant produced low photoproduct yield and the C-O mode at 1955 cm⁻¹. The only pD sensitivity observed is the loss of the strong H-bonding conformer at 1923 cm⁻¹. The rest of the data for all proteins examines at pD 8 are similar to those observed at pH 8. The loss of the strong H-bonding conformer indicates that exchangeable residues are present in the distal site. The TRS²-FTIR difference spectra show that the heme propionates are in the protonated and deprotonated forms and the observed recombination constant $k_{\text{WT}} = 528 \text{ s}^{-1}$ at pD 8. The final spectrum demonstrates that there is no

irreversible light-induced effect on the heme and the photodissociated CO has recombined to the heme iron.

7.2 Experimental Procedures

YddV from *E.coli* K-12 was expressed and purified according to previously published procedures.^{1,18,19} The samples used for the FTIR measurements had an enzyme concentration of ~1.0 mM in 50 mM Tris for pH 8 and pD 8 after buffer exchange. The pD solutions prepared in D₂O buffers were measured by using a pH meter and assuming pD = pH (observed) + 0.4. Dithionite reduced samples were exposed to 1 atm of CO in an anaerobic cell to prepare the carbonmonoxy adduct and transferred to a tightly sealed FTIR cell with two CaF₂ windows, under anaerobic conditions (path length (l)= 6μm). CO gas was obtained from Linde. The static FTIR spectra were recorded with 4 cm⁻¹ spectral resolution on a Bruker Vertex 70 FTIR spectrometer equipped with a liquid nitrogen cooled mercury cadmium telluride (MCT) detector.

For the time-resolved step-scan FTIR measurements, the 532 nm pulses from a Continuum Minilite II Nd:YAG laser (5 ns width, 10 Hz) were used as a pump light (8 mJ/pulse) to photolyze the YddV- CO adducts. These measurements were performed on a Bruker Vertex 80 V spectrometer equipped with the step-scan option. A vacuum pump was used to evacuate the interferometer compartment to a final pressure of 3.2 mbar. The FTIR spectrometer was placed on a Newport VH optical vibration isolation table to ensure that vibrational background noise from environmental sources was avoided. For the time-resolved experiments, a TTL (transistor transistor logic) pulse provided by a digital delay pulse generator (Quantum Composers, 9524) triggered in order the flashlamps, the Q-switch, and the FTIR spectrometer. Pre-triggering the FTIR spectrometer to begin data collection before the laser fires allows fixed reference points to be collected at each mirror position, which are used as the reference spectrum in the calculation of the difference spectra. Changes in intensity were recorded with a photovoltaic MCT detector (Kolmar Technologies KV100-1B-7/190, response limit 850 cm⁻¹) and digitized with a 84-kHz, 24-bit, analog-to-digital converter (ADC). A broadband interference optical filter (LP-4200, Spectrogon) with a short wavelength cutoff at 4.2 μm was used to limit the free spectral range from 4.2 to 11.8 μm. This led to a spectral range of 2633 cm⁻¹, which was equal to an undersampling ratio of 6. Single-sided spectra were collected at 4 cm⁻¹ spectral resolution, 6 μs time resolution, and 10 coadditions per data point. The total accumulation time for each measurement was 25 min,

and 15 measurements were collected and averaged. Blackman-Harris three-term apodization with 32 cm^{-1} phase resolution and the Mertz phase correction algorithm were used. Difference spectra were calculated as $\Delta A = -\log(I_S / I_R)$.

Optical absorption spectra were recorded with a Shimadzu UV1700 UV-visible spectrometer. A $2\mu\text{l}$ sample of wild type YddV heme domain was diluted into $300\mu\text{l}$ of 50 mM Tris-HCl buffer pH 8 to achieve a final concentration of about $8\mu\text{M}$. The reduction of YddV was carried out under anaerobic conditions by adding a few grains of sodium dithionite into Tris buffer and then $\sim 3\mu\text{l}$ in the YddV sample. For the preparation of the carbonmonoxy adduct, dithionite-reduced sample was exposed to 1 atm of CO (1mM) in an anaerobic sealed quartz cuvette of path length 1 cm. Optical absorption spectra were also recorded before and after the FTIR measurements to ensure the formation and stability of the CO adducts.

7.2 Results and Discussion

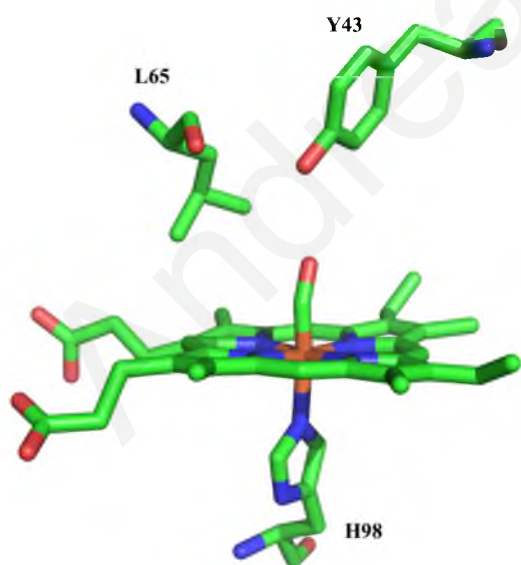


Figure 7.1 Schematic representation of the proposed structure of the CO-bound form of YddV (residues are numbered for YddV), based on the crystal structure of Fe(III)-CN adduct of HemAT-Bs (PDB 1OR4).

Figure 7.1 shows a schematic presentation of the heme site of CO-bound YddV. The optical absorption spectrum of Fe(III) form as isolated YddV heme domain (YddV-heme) shown in **Figure 7.2, trace A** displays Soret maxima at 394 nm and visible (Q-band) band at 506 nm which is typical of a five-coordinated, high spin Fe(III) form heme protein. The latter confirms the hitherto reported, distinctive structural architecture of Fe(III) form YddV as a 5-

coordinated high spin globin coupled sensor compared to other GCS which appear as 6-coordinated low or high spin in the Fe(III) form and provides evidence that there is no axial water or OH⁻ coordinated to the heme-Fe(III). In addition, a shoulder at 642 nm is observed which is typical of a porphyrin-to-ferric iron charge transfer (CT) transition characteristic of ferric high spin heme *b* (**Figure 7.2, trace A**). The dithionite reduced YddV-heme protein, shown in **Figure 7.2, trace B**, displays Soret maxima at 432 nm and a visible band at 560 nm, indicating the formation of a 5-coordinated high-spin complex. Upon exposure of the reduced protein to 1 atm of CO gas, a spectrum shown in Fig. 2C with a Soret maximum at 421 nm and visible bands at 540 and 566 nm was obtained. The spectrum of the Fe(II)-CO complex indicates the formation of a six-coordinated low-spin species, as shown, previously.¹⁸

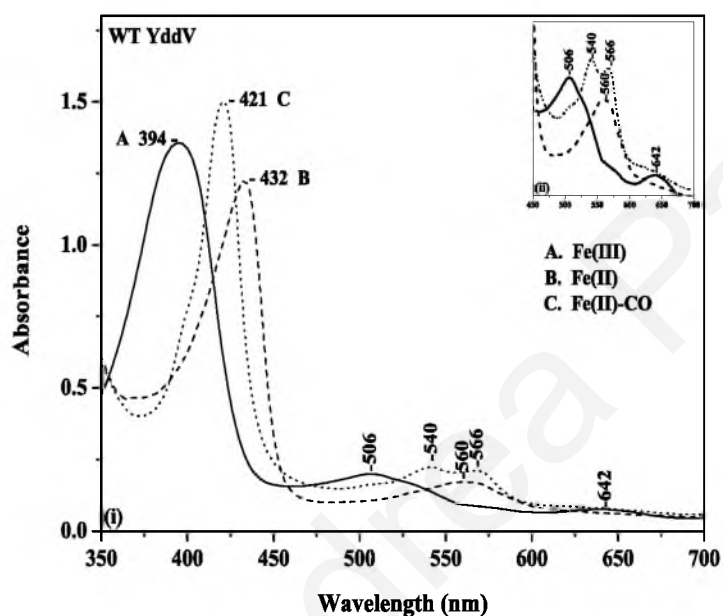


Figure 7.2 Optical absorption spectra of YddV-heme at pH 8. Trace A (solid line) is the Fe(III), trace B (dashed line) is the Fe(II) form, and trace C (dotted line) is the Fe(II)-CO form. The enzyme concentration was 8 μM , and the path length was 1 cm.

We detect two modes in the FTIR spectrum of the CO-bound YddV-heme (**Figure 7.3A trace a**). We assigned the $\nu(\text{CO})$ of YddV based on the $\nu(\text{CO})$ of Mb observed at 1910-1930 cm^{-1} as a result of a strong H-bonding interaction, 1940-1950 cm^{-1} corresponding to a moderate H-bonding interaction and 1960-1970 cm^{-1} as neutral.^{20,21} Therefore, we assign the major band in the FTIR spectrum of the CO-bound YddV-heme at 1962 cm^{-1} (neutral) and the minor band (strong H-bonding interaction) at 1923 cm^{-1} to the C-O modes of the heme Fe(II)-CO complex. The detection of the major band has been reported in the RR spectra ($\nu_{\text{CO}}=1965 \text{ cm}^{-1}$) in the past,¹⁸ but the strong H-bonding conformer is reported for the first time. The interactions of the heme Fe-CO complex with water molecules in the distal cavity should stabilize partial charged resonance forms causing the increase and decrease in the frequency of CO. In the presence of solvent water molecules next to the bound CO in the interior of the

pocket, the solvent water will act as a proton donor affecting the frequency of CO. The observed peak at 1962 cm^{-1} indicates an apolar environment and little or no hydrogen bonding between L65 and Y43. The polar interaction and/or steric hindrance was investigated by mutation of L65 and Y43 which are directly adjacent to heme Fe-CO. In the spectra of the L65M mutant (**Figure 7.3A trace b**) the C-O modes are observed at 1953 cm^{-1} which is 9 cm^{-1} lower than that observed in the wild type indicating strong alteration in the distal structure upon the L65M mutation. On the other hand, in the L65T mutant (**Figure 7.3A trace c**) was observed at the same frequency as the wild type at 1962 cm^{-1} , suggesting that the L65T mutant makes no significant alterations in the interactions of the bound CO with the distal environment and that similar polar and steric interactions occur between the heme Fe-CO and the tryptophan residue. In the Y43A mutant (**Figure 7.3A trace d**) the C-O mode is observed at the same frequency as the wild type but in the Y43F (**Figure 7.3A trace e**) and Y43W mutants (**Figure 7.3A trace f**) the C-O mode is observed at 1955 and 1953 cm^{-1} , respectively. Noticeably, in none of the mutant proteins examined the strong H-bonding conformer observed in the wild type at 1923 cm^{-1} was detected. In the absence of large side chains at the positions of L65 and Y43, distal pocket water molecules can act as proton donors and bases resulting in the broadening of the C-O bands.

Based on FTIR studies, it has been shown that in general protein functional groups, including carboxyl groups of amino acid residues are difficult to deuterate.²² Therefore, we have investigated the CO-bound YddV-heme complex at pD 8, aiming to finalize the pH/pD sensitivity of the distal site of the YddV-heme CO complex. The observed pD sensitivity, includes the loss of the strong H-bonding conformer at 1923 cm^{-1} and broadening of the CO peak in the Y43W mutant which indicates the involvement of multiple protein-ligand conformations differencing in the polarity of electrostatic interactions. In addition, a moderate hydrogen bonded conformer was observed at 1942 cm^{-1} in the Y43F mutant. The rest of the data in D_2O for all protein complexes examined are similar to those observed at pH. The loss of the strong H-bonding conformer indicates that exchangeable residues are present in the distal site and the $\text{H}_2\text{O}/\text{D}_2\text{O}$ exchanges results in structural rearrangements causing the loss of the 1923 cm^{-1} conformer. The results from the CO-bound YddV-heme experiments indicate that the CO-bound ligand does not retain the H-bonded conformations because all frequencies of the CO modes in the wild-type sensor protein are not independent of $\text{H}_2\text{O}/\text{D}_2\text{O}$ exchange. The absence of the strong H-bonding conformer in the L65 and Y43 mutant proteins indicates that both residues significantly perturb its formation. The insensitivity of the CO modes in L65M and Y43A mutant proteins, indicates in contrast to those for L65M, Y43W and Y43F,

that these specific mutations are not directly involved in controlling the strength of the C-O bond.

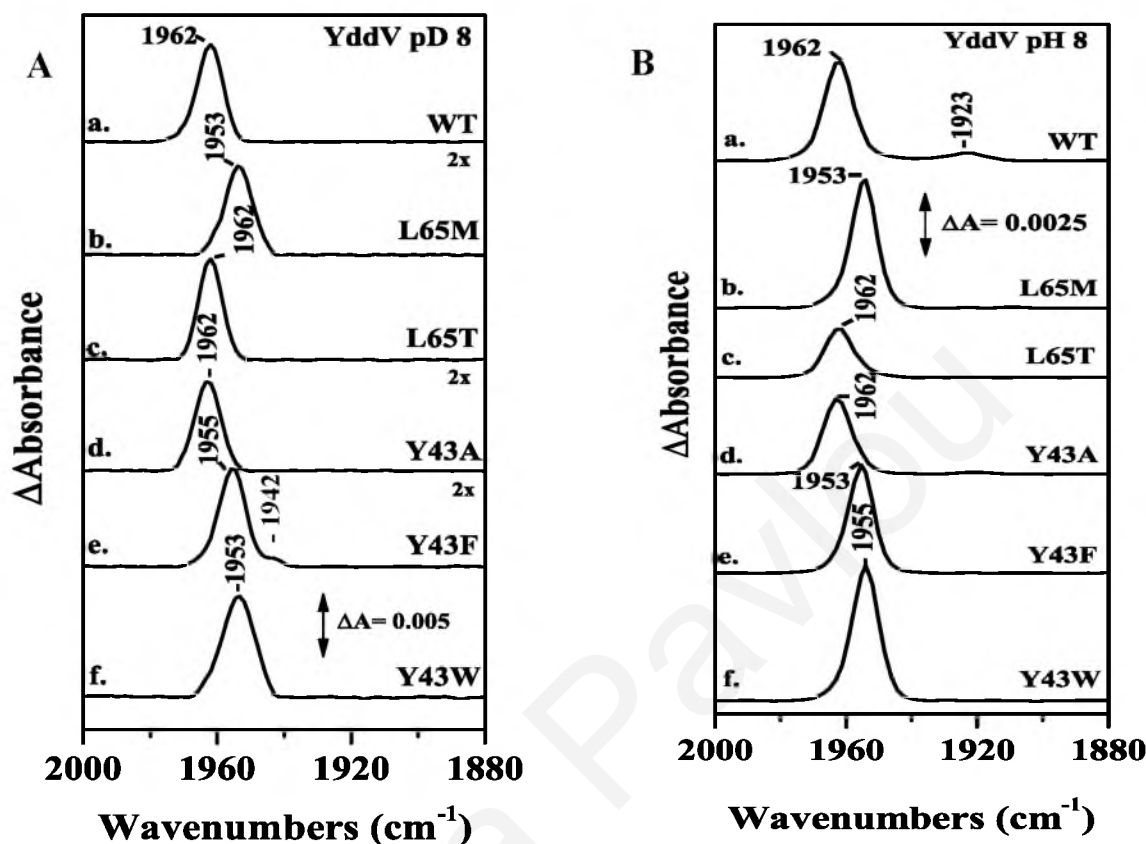


Figure 7.3 FTIR spectra of the heme domain YddV-CO adducts at (A) pH 8 and (B) pD 8 representing wild type YddV (trace a), and L65M (trace b), L65T (trace c), Y43A (trace d), Y43F (trace e), and Y43W (trace f) YddV mutants. The pathlength was 12 μm and the spectral resolution was 4 cm^{-1} .

Figures 7.4(A) and 7.5(A) show the TRS²-FTIR difference spectra ($t_d = 6 \text{ ms} - 7.4 \text{ ms}$, 4 cm^{-1} spectral resolution) of fully heme iron reduced YddV-heme at pD 8 subsequent to CO photolysis by a 532 nm nanosecond laser at 10 Hz in different wavenumbers ranges. The final spectrum at 7.4 ms demonstrates that there is no irreversible light-induced effect on the heme iron. The continuous variability in the intensity of the CO mode associated with heme iron over a 6 $\mu\text{s} - 7.4 \text{ ms}$ time scale is the most quantified aspect of ligand rebinding to heme iron, and is depicted in **Figure 7.4(A)**. The intensity of Fe(II)-CO band at 1962 cm^{-1} was measured as a function of time to determine the rate of recombination of CO to heme iron ($k = 528 \text{ s}^{-1}$) at room temperature (**Figure 7.4(B)**). The curve is a three parameter fit to the experimental data according to pseudo first-order kinetics. The presence of a trough/peak patterns in FTIR difference spectra of heme proteins (oxidized *minus* reduced form) has been interpreted as an environmental change induced by the change in the redox state of the metal center.

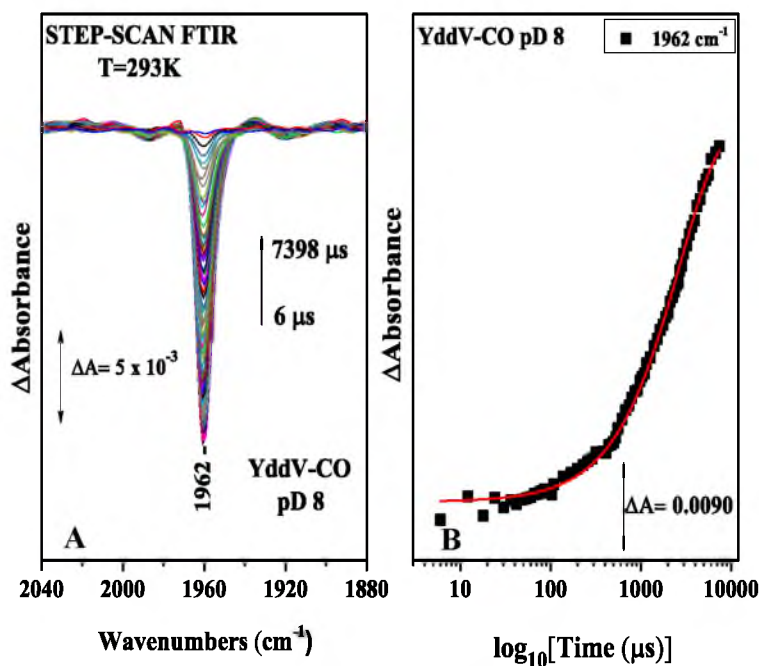


Figure 7.4 (A) Time-resolved step-scan FTIR difference spectra of the wild type heme domain YddV-CO adduct at pD 8 from 0.006 to 7.398 ms subsequent to CO photolysis. **(B)** Plot of the ΔA of the 1962 cm^{-1} mode versus time on a logarithmic scale subsequent to CO photolysis. The red line corresponds to the exponential fit of the experimental data.

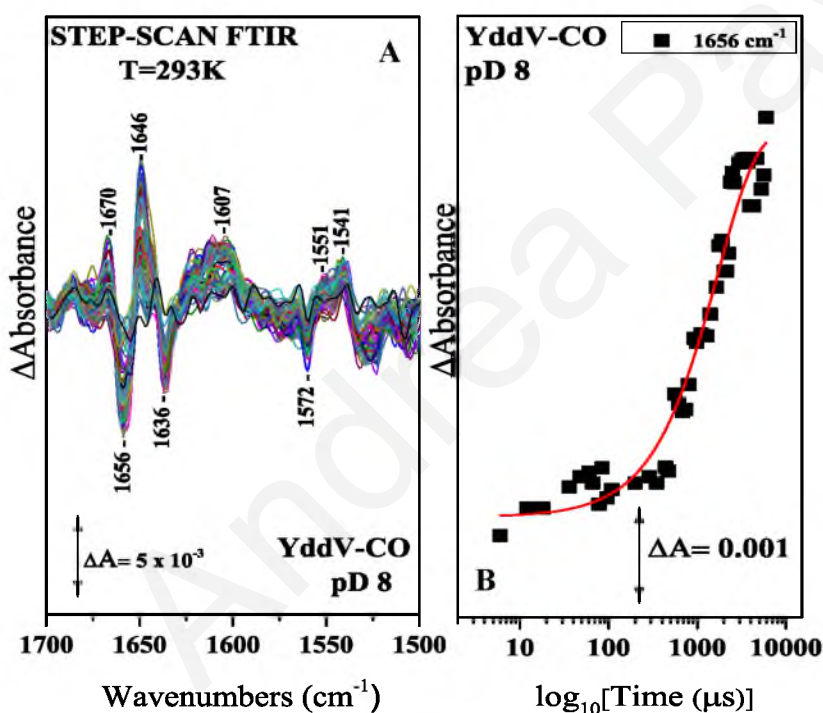


Figure 7.5 (A) Time-resolved step-scan FTIR difference spectra of the wild type heme domain YddV-CO adduct at pD 8 in the range of 1700-1300 cm^{-1} and $t_d = 6 - 7398 \mu\text{s}$. Plot of the ΔA of **(B)** 1656 cm^{-1} protein vibration mode of the heme domain YddV-CO adduct at pD 8 versus time on a logarithmic scale subsequent to CO photolysis. The red lines correspond to the exponential fitting of the experimental data.

In the FTIR difference spectra obtained upon CO-photolysis from the heme iron, the appearance of signals in the amide I region (1620- 1690 cm^{-1}) can be attributed to changes of the C=O modes caused by perturbation in the polypeptide backbone. Coupled CN stretching and NH bending modes and, the asymmetric COO^- modes from deprotonated heme propionates and Glu and Asp side chains are expected in the 1530-1590 cm^{-1} region. The presence of the positive peak at 1670 cm^{-1} in the time-resolved step-scan FTIR spectra of the YddV-heme-CO adduct subsequent to CO photodissociation (**Figure 7.5(A)**) can be

tentatively assigned to the protonated form of the heme propionates indicating that the propionates are perturbed upon CO photodissociation. We attribute the peaks/troughs at 1646/1656 cm^{-1} to amide I absorbance and the 1541/1572 cm^{-1} pair tentatively to the $\nu(\text{COO}^-)^{\text{asym}}$ of propionate(s). The intensity of the amide I mode at 1656 cm^{-1} was measured as a function of time ($k=480 \text{ s}^{-1}$) as shown in **Figure 5(B)**. Thus, the amide I mode follows the same kinetics with CO rebinding as has been described above. Intensity changes and/or frequency shifts at 1636 cm^{-1} could be attributed to the deprotonated forms of Gln or Asn observed in the TRS²-FTIR spectra.²³⁻²⁶

In an effort to elucidate the environment sensed by the bound CO, we have investigated the TRS²-FTIR of the CO-adducts of L65M (**Figure 7.6(A)**) and L65T (**Figure 7.7(A)**) as well as, Y43A (**Figure 7.8(A)**), Y43F (**Figure 7.9(A)**) and Y43W (**Figure 7.10(A)**) YddV mutants, subsequent to CO photolysis. The intensity of Fe(II)CO bands has been measured as a function of time to determine the rate of recombination of CO to heme iron in each mutant (**Figures 7.6(B) & 7.7(B)** for L65M and L65T; **Figures 7.8(B), 7.9(B) & 7.10(B)** for Y43A, Y43F and Y43W respectively). The rate of recombination of CO to heme iron in the wild type YddV and mutant proteins, as well as the yield of photoproduct formation, are summarized in **Table 1**. A close inspection of the data shows the large effect of the L65M and L65T mutants of YddV-heme protein on the recombination of CO and the lack of correlation between the recombination rate (k_1) and the frequency of CO. Both the ligand association rate constant and the ligand rebinding rate constant reflect the environment of the ligand access to the binding site. The fast recombination rates in both mutants imply significant role of L65 in controlling the ligand dynamics.

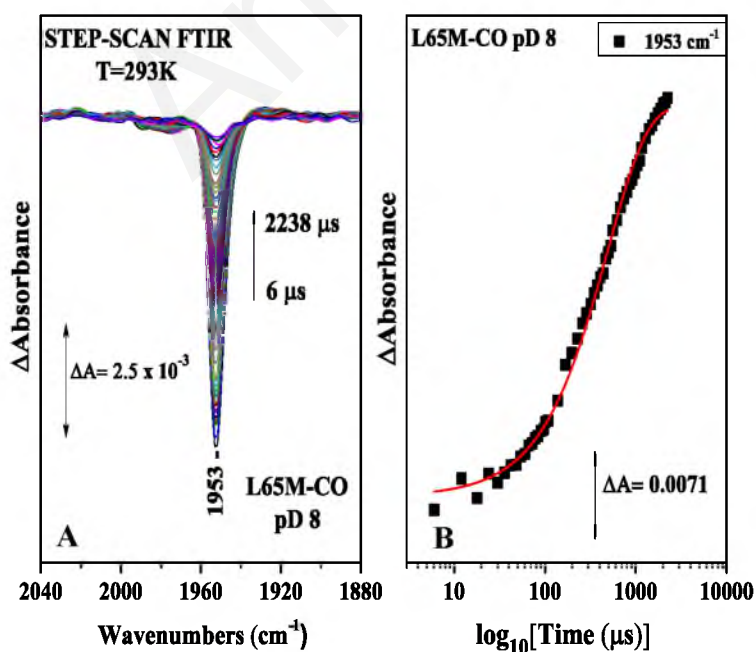


Figure 7.6 (A) Time-resolved step-scan FTIR difference spectra of the heme domain L65M CO adduct at pD 8 from 0.006 to 2.238 ms subsequent to CO photolysis. **(B)** Plot of the ΔA of the 1953 cm^{-1} mode versus time on a logarithmic scale subsequent to CO photolysis. The red line corresponds to the exponential fit of the experimental data.

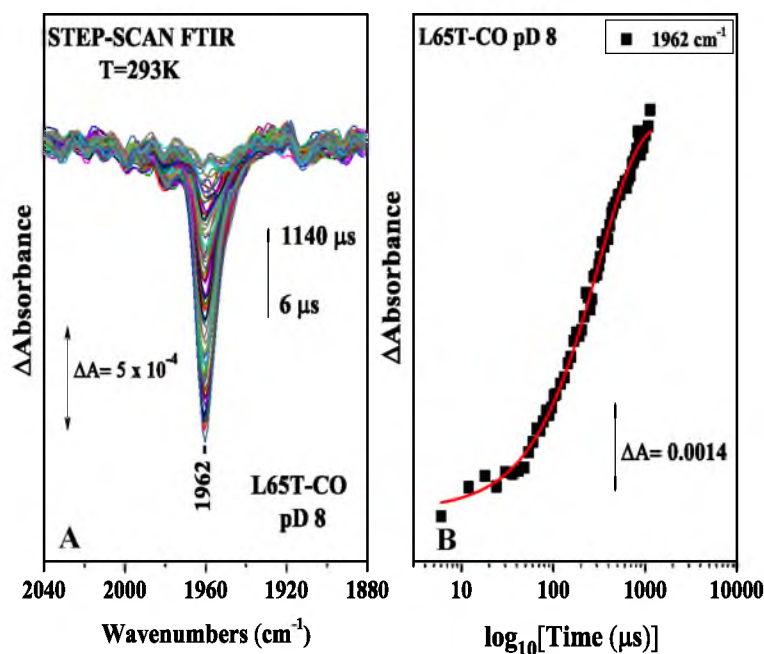


Figure 7.7 (A) Time-resolved step-scan FTIR difference spectra of the heme domain L65T-CO adduct at pD 8 from 0.006 to 1.140 ms subsequent to CO photolysis. **(B)** Plot of the ΔA of the 1962 cm^{-1} mode versus time on a logarithmic scale subsequent to CO photolysis. The red line corresponds to the exponential fit of the experimental data.

The data on the Y43 mutants demonstrate that the rate of recombination k_1 ($285\ \text{s}^{-1}$ - $820\ \text{s}^{-1}$) is mutant dependent and obviously a high barrier to recombination is formed in the case of the Y43A mutant. The binding of CO to the heme iron or the dissociation/rebinding induces a conformational change to L65 and Y43, the heme propionates, as well as structural changes in the polypeptide skeleton. The Y43A mutant proteins exhibited very low O_2 affinity and the Fe(II)- O_2 complex was not detected in the RR spectrum but in the case of the CO binding exhibited behaviour in terms of the frequency of CO, the photodissociation yield, and the rebinding constant similar to that of the wild type. On the other hand the Y43W mutant exhibited very high ($>150\ \text{s}^{-1}$) O_2 dissociation rate constant but the Fe(II)- O_2 complex was not detected.⁵ In the case of the bound CO in the Y43W mutant, the CO frequency was $9\ \text{cm}^{-1}$ lower than the wild type, exhibits high photoproduct yield but the recombination rate is double than that observed in the wild type. In the Y43F mutant, both the Fe-CO and Fe- O_2 frequencies were different from those of the wild type indicating that Y43 makes an H-bond with both the O_2 and CO ligands,¹⁸ and in this study, by the detection of the CO vibration, the H-bonded interaction is confirmed. In the case of the L65M mutant, both the k_{obs} ($1764\ \text{s}^{-1}$) and the yield of photoproducts formation (92%) are very high and the CO vibration is $9\ \text{cm}^{-1}$ lower than that observed in the wild type indicating an H-bonding interaction with L65. A close inspection of the recombination rates for the mutant proteins which reflect ligand association to the binding site, suggests strong coupling of the L65 and Y43 residues to the properties of the bound CO to the heme iron. The comparison of the O_2 and CO data

demonstrate that L65 and Y43 are crucial for ligand recognition and discrimination, and thus for specific sensing of gases and for controlling the conformational changes induced upon CO binding.^{18,19}

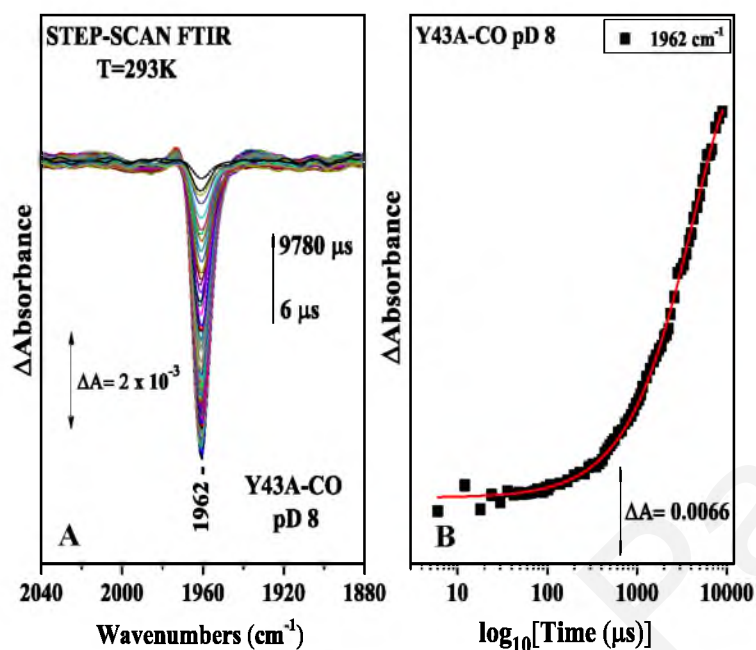


Figure 7.8 (A) Time-resolved step-scan FTIR difference spectra of the heme domain Y43A-CO adduct at pD 8 from 0.006 to 9.780 ms subsequent to CO photolysis. (B) Plot of the ΔA of the 1962 cm^{-1} mode versus time on a logarithmic scale subsequent to CO photolysis. The red line corresponds to the exponential fit of the experimental data.

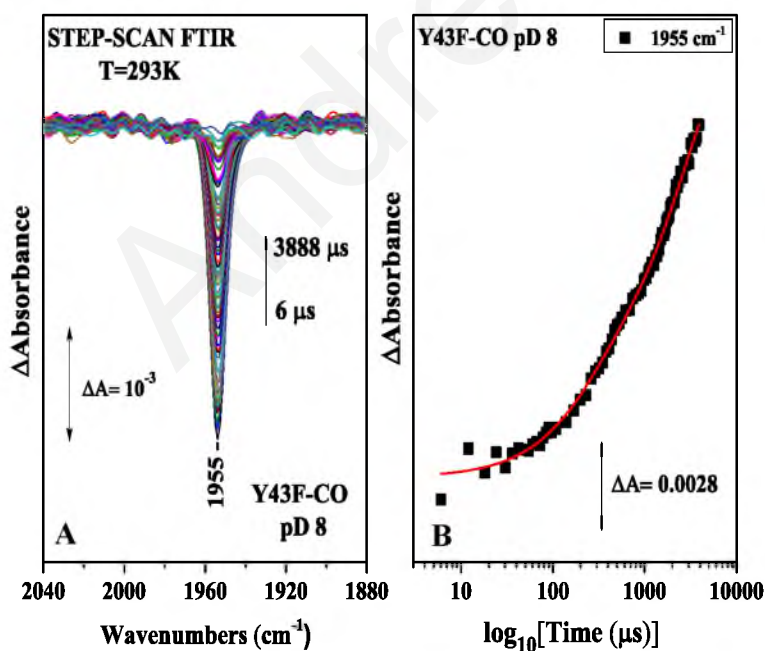


Figure 7.9 (A) Time-resolved step-scan FTIR difference spectra of the heme domain Y43F-CO adduct at pD 8 from 0.006 to 3.888 ms subsequent to CO photolysis. (B) Plot of the ΔA of the 1955 cm^{-1} mode versus time on a logarithmic scale subsequent to CO photolysis. The red line corresponds to the exponential fit of the experimental data.

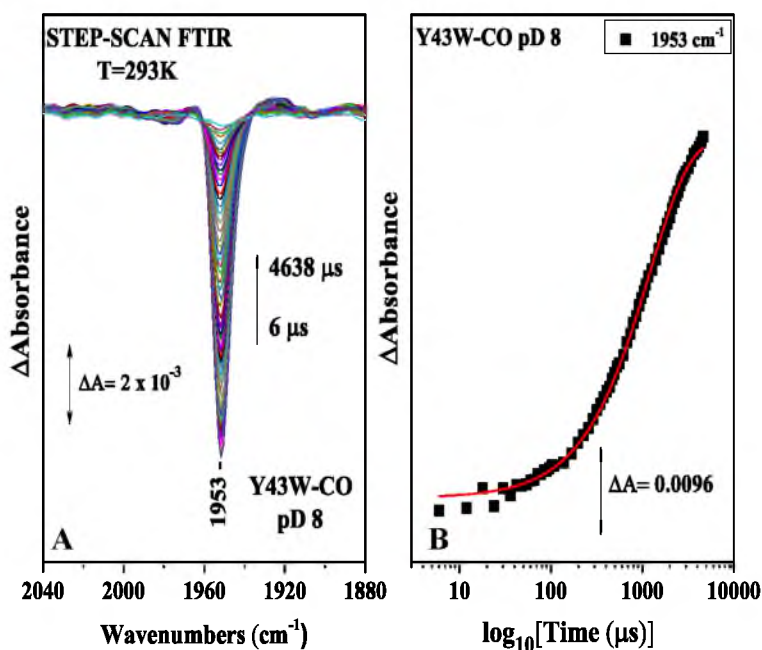


Figure 7.10 (A) Time-resolved step-scan FTIR difference spectra of the heme domain Y43W-CO adduct at pD 8 from 0.006 to 4.638 ms subsequent to CO photolysis. (B) Plot of the ΔA of the 1953 cm^{-1} mode versus time on a logarithmic scale subsequent to CO photolysis. The red line corresponds to the exponential fit of the experimental data.

1962 cm^{-1}	t_1 (μs)	k_1 (s^{-1})	% Photoproduct yield at 6 μs
WT pD 8	1312 ± 73	528	92
L65M pD 8	393 ± 13	1764	91
L65T pD 8	237 ± 8	2929	29
Y43A pD 8	2424 ± 92	508	92
Y43F pD 8	1363 ± 32	285	34
Y43W pD 8	845 ± 22	820	92
Amide I WT			
1656 cm^{-1} pD 8	1443 ± 179	480	-
1646 cm^{-1} pD 8	1130 ± 103	613	-

Table 7.1 Summary of the calculated CO rebinding constants as well as % photolysis for the wild type and mutant YddV-CO adducts.

The following discussion for the behavior of the distal residues Y43, L65, the ring propionates and amide vibrations observed in YddV-heme as compared to those observed in HemAT-*Bs*, is based partially on our tentative assignments. In a comprehensive study, the unique specificity and tuning of the distal amino acid residues of HemAT-*Bs* in constructing the necessary conformational changes towards ligand recognition was demonstrated. The behavior of T95 and Y70 upon binding of O₂, CO, and NO to the heme iron produced distinct conformations for HemAT-*Bs*, indicating that these residues are the major contributors

towards ligand recognition and discrimination.²⁷ In addition, L92 induced the necessary structural changes to T95 and Y70 to maintain the H-bonded conformer.^{27,28} Such specific recognition and discrimination of iron bound gaseous ligands by the distal protein environment is crucial to the intramolecular signal transduction by HemAT-*Bs*. For the signal transduction mechanism in HemAT-*Bs*, the G, H and B- helices undergo significant displacement upon CN binding which has been suggested to trigger conformational changes from the sensor domain to the function domain.¹⁵ In YddV, the crucial residues in the recognition of the O₂- and CO-bound to the heme iron are L65 and Y43 which both form H-bonded conformers.^{18,19} Therefore, the overall distal moiety dynamics of the heme in YddV is quite distinct from that of HemAT-*Bs*. In HemAT-*Bs*, the sensor domain displayed the amide vibration in hundreds of nanoseconds subsequent to CO photolysis and recovery in 50 μs indicating that the isolated sensor domain undergoes conformational changes of the protein backbone upon CO photolysis.²⁹ In addition, in Chapter 5 of the current doctoral thesis, we have shown the amide relaxation of isolated sensor domain HemAT-*Bs* following biphasic kinetics with rebinding constants calculated as $k_1 = 27 \times 10^3 \text{ s}^{-1}$ $k_2 = 999 \text{ s}^{-1}$ for the mode at 1638 cm⁻¹, and $k_1 = 29 \times 10^3 \text{ s}^{-1}$ $k_2 = 1088 \text{ s}^{-1}$ for the mode at 1654 cm⁻¹. In YddV the relaxation of the amide vibration is completed with $k = 480 \text{ s}^{-1}$ which is similar with the rebinding of CO ($k = 528 \text{ s}^{-1}$) indicating a much slower process for conformational relaxation of the protein compared to HemAT-*Bs*. Such protein dynamics in HemAT-*Bs* has been proposed to play a crucial role in the signaling process. In HemAT-*Bs* it has been shown that ligand binding to the heme induces a conformational change to the heme propionate that is communicated to the CE loop.³⁰ We observe similar conformational changes of the heme propionates of YddV.

7.3 Conclusions

Tyr43 and Leu65 have been pinpointed as the well conserved distal residues that cooperate in creating a heme active site appropriate for ligand binding in YddV. In this work we have demonstrated the importance of these residues in ligand binding by using CO as a probe. Our results taken together with those previously reported, suggest that there are distinct differences in the interaction of YddV with CO and O₂ as compared to HemAT-*Bs*. Of

particular interest is the behavior of the environment of the heme propionates in both YddV and HemAT-*Bs*; it behaves in a similar way in both proteins upon ligand binding or dissociation. In HemAT-*Bs* the hydrogen bonds between His86 and 6-propionate is part of the protein dynamics which are important for transduction of the conformational changes from the sensor to the signaling domain. Further experiments on the YddV-O₂ adduct will be attempted for elaborate investigation of the role of the heme propionates in signal transduction in YddV.

7.4 References

1. J. R. Tuckerman, G. Gonzalez, E. H. S. Sousa, X. Wan, J. A. Saito, M. Alam, M. A. Gilles Gonzalez, *Biochemistry* **2009**, *48*, 9764–9774.
2. L. Tagliabue, D. Antoniani, A. Maciag, P. Bocci, N. Raffaelli, P. Landini, *Microbiology*, **2010**, *156*, 2901–2911.
3. R. Hengge, *Nat. Rev. Microbiol.* **2009**, *7*, 263–273.
4. R. Simm, M. Morr, A. Kader, M. Nimtz, U. Römling, *Molec. Microbiol.* **2004**, *53*, 1123–1134.
5. D. A. Ryjenkov, M. Tarutina, O. V. Moskvina, M. Gomelsky *J. Bacteriol.* **2005**, *187*, 1792–1801.
6. A. D'Argenio, S. I. Miller, *Microbiology*, **2004**, *150*, 2497–2502.
7. U. Jenal, *Curr. Opin. Microbiol.* **2004**, *7*, 185–191.
8. W. Gong, B. Hao, M. K. Chan, *Biochemistry* **2000**, *39*, 3955–3962.
9. A. Hao, C. Isaza, J. Amdt, M. Soltis, M. K. Chan, *Biochemistry* **2002**, *41*, 12952–12958.

10. H. Kurokawa, D. S. Lee, M. Watanabe, I. Sagami, B. Mikami, C. S. Raman, T. Shimizu, *J. Biol. Chem.* **2004**, *279*, 20186-20193.
11. H. Park, C. Suquet, M. I. Savenkova, J. D. Satterlee, C. Kang, *Acta Cryst.* **2002**, *58*, 1504–1506.
12. L. Thijs, E. Vinck, A. Bolli, F. Trandafir, X. Wan, D. Hoogewijs, M. Coletta, A. Fago, R. E. Weber, S. Van Doorslaer, P. Ascenzi, M. Alam, L. Moens, S. Dewilde, *J. Biol. Chem.* **2007**, *282*, 37325-37340.
13. X. Wan, J. R. Tuckerman, J. A. Saito, T. A. K. Freitas, J. S. Newhouse, J. R. Denery, M. Y. Galperin, G. Gonzalez, M. A. Gillws-Gonzalez, M. Alam, *J. Mol. Biol.* **2009**, *388*, 262-270.
14. K. Kitanishi, K. Kobayashi, T. Uchida, K. Ishimori, J. Igarashi, T. Shimizu, *J. Biol. Chem.* **2011**, *286*, 35522-35534.
15. W. Zhang, G. N. Jr. Phillips, *Structure* **2003**, *11*, 1097-1110.
16. H. Sawai, S. Yoshioka, T. Uchida, M. Hyodo, Y. Hayakawa, K. Ishimori, S. Aono, *Biochim. Biophys. Acta* **2010**, *1804*, 166- 172.
17. A. Pesce, L. Thijs, M. Nardini, F. Desmet, L. Sisinni, L. Gourlay, A. Bolli, M. Coletta, S. Van Doorslaer, X. Wan, M. Alam, P. Ascenzi, L. Moens, M. Bolognesi, S. Dewilde, *J. Mol. Biol.* **2009**, *386*, 246-260.
18. K. Kitanishi, K. Kobayashi, Y. Kawamura, I. Ishigami, T. Ogura, K. Nakajima, J. Igarashi, A. Tanaka, T. Shimizu, *Biochemistry* **2010**, *49*, 10381–10393.
19. K. Nakajima, K. Kitanishi, K. Kobayashi, N. Kobayashi, J. Igarashi, T. Shimizu, *J. Inorg. Biochem.* **2012**, *108*, 163–170.
20. T. Li, M. Quillin, G. Phillips, J. Olson, *Biochemistry* **1994**, *33*, 1433-1446.
21. M. Unno, J. Christian, J. Olson, T. Sage, P. Champion, *J. Am. Chem. Soc* **1998**, *120*,

- 2670-2671.
22. D. Okuno, T. Iwase, K. Shinzawa-Itoh, S. Yoshikawa, T. Kitagawa, *J. Am. Chem. Soc.* **2003**, *125*, 7209–7218.
23. A. Barth, C. Zscherp, *Q. Rev. Biophys.* **2002**, *35*, 369–430.
24. A. Barth, *Prog. Biophys. Mol. Bio.* **2000**, *74*, 141–173
25. P. Hellwig, T. Soulimane, G. Buse, W. Mantele, *Biochemistry* **1999**, *38*, 9648-9658.
26. A. Koutsoupakis, T. Soulimane, C. Varotsis, *Biophys. J.* **2004**, *86*, 2438- 2444.
27. E. Pinakoulaki, H. Yoshimura, S. Yoshioka, S. Aono, C. Varotsis, *Biochemistry* **2006**, *45*, 7763-7766.
28. E. Pinakoulaki, H. Yoshimura, V. Daskalakis, S. Yoshioka, S. Aono, C. Varotsis, *Proc. Natl. Acad. Sci. U. S. A.* **2006**, *103*, 14796- 14801.
29. S. F. El-Mashtoly, M. Kubo, Y. Gu, H. Sawai, S. Nakashima, T. Ogura, S. Aono, T. Kitagawa, *J. Biol. Chem.* **2012**, *287*, 19973-19984.
30. H. Yoshimura, S. Yoshioka, K. Kobayashi, T. Ohta, T. Uchida, M. Kubo, T. Kitagawa, S. Aono, *Biochemistry* **2006**, *45*, 8301-8307.



CHAPTER 8

Structural Properties and Dynamics of *Ec*DOSH Probed by FTIR and Time-resolved Step-Scan FTIR Spectroscopy

Andrea Pavlou

8.1 Introduction

The heme-containing PAS-A domain of *Ec*DOSH acts as the sensor domain for the recognition and discrimination of small diatomic gas molecules. X-ray crystal structure of the enzyme's PAS domain suggests that the redox-dependent ligand interchange process between heme-Fe³⁺/Fe²⁺ is influenced by conformational changes in the vicinity of peripheral residue Met95. In the Fe(III) form, heme-Fe³⁺ retains a water molecule and His77 as the axial ligands in both subunits. Upon reduction of heme-Fe³⁺ to Fe²⁺, the water molecule is displaced by Met95 to form 6-coordinate structures.^{1,2} Resonance Raman spectra confirmed a 6-coordinate, low-spin state for *Ec*DOSH Fe(III) and Fe(II) heme complexes, with the distal site axial ligand Met95 in Fe(II) forming a hydrogen bond with the heme-7-propionate.^{3,4}

Although termed a direct oxygen sensor, *Ec*DOSH appears to be less selective compared to other heme-based oxygen sensor proteins; its PDE activity displays increase upon binding of other exogenous gas ligands such as CO and NO.^{5,6} In general, it has been observed that upon binding of either O₂, CO or NO, axial ligand Met95 is replaced and that global conformational changes in the surrounding environment of Met95 caused by exogenous ligand binding might be responsible for switching “on” the protein catalytic activity^{1,2,7,8}. Furthermore, several other residues have been identified to be involved in structural changes upon O₂, CO, and NO binding and, therefore, in signal transduction. The residues are Trp53, Asn84, Arg97, Phe113, and Tyr126,^{6,9,10,11} but their specific roles have been studied extensively merely in the *Ec*DOSH-O₂ complex. **Figure 8.1** illustrates the exact position of the latter residues in the heme periphery of *Ec*DOSH Fe(II) form.

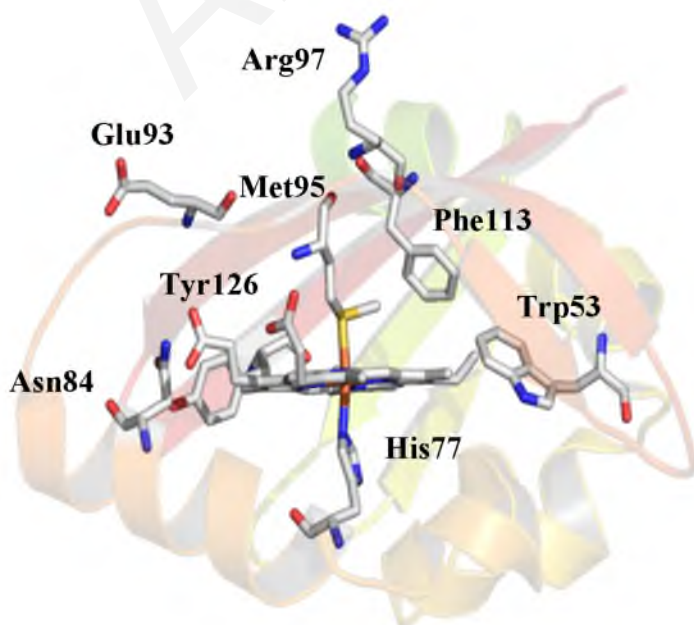


Figure 8.1 Structural representation of the Fe(II) form of the *Ec*DOSH heme active site (PDB ID 1V9Z).

Resonance Raman experiments have demonstrated that upon replacement of Met95 by O₂, a hydrogen bonding network forms between heme-7-propionate, the bound O₂, Arg97 and Phe113 rather than Met95. Based on the latter results, it has been suggested that the role of the electrostatic interactions of Arg97 with the heme-7-propionate, and the steric interactions of Phe113 with the bound O₂ is fundamental in modulating the competitive binding and displacement mechanism between Met95 and O₂ to heme-Fe(II).^{1,2,9} In addition, the environment surrounding Trp53 located near the 2-vinyl group has been shown via UVRR spectra to undergo hydrophobicity change to more hydrophobic upon O₂ binding, resulting presumably from substantial changes in the communication linkage between the 2-vinyl group with the surrounding residues.^{9,12} However, spectroscopic studies of the Fe(II)-CO form of *Ec*DOSH aimed at assessing the dynamic changes induced to the protein upon binding of CO, have been to a great extent limited to the time-resolved RR and UVRR studies by El-Mashtoly *et al.*^{10,13,14} Static resonance Raman spectra suggested Arg97 to be the distal site residue that interacts through hydrogen bonding with heme-bound CO in the hydrogen-bonded conformation, while steric interactions of the Phe113 residue to be crucial for regulating the competitive binding of Met95 to heme-Fe(II) before CO rebinding.⁹ In terms of protein dynamics subsequent to CO-dissociation/rebinding, Sato *et al.* have proposed, based on their time-resolved resonance Raman (TR³) experiments, that the heme propionates play a fundamental role in communicating the structural changes from the heme to the protein moiety upon binding of CO to heme-Fe(II).³ In addition, time-resolved UVRR (TR-UVRR) experiments revealed that heme structural changes prompted by CO-dissociation/rebinding trigger a structural rearrangement of the protein matrix that takes place at a nanosecond to microsecond time scale.¹²

To provide a better understanding of the structure-function relationship of the CO-bound form of *Ec*DOSH, we have used FTIR and time-resolved step-scan FTIR spectroscopies, as well as site-directed mutagenesis to investigate the conformational changes induced to the protein moiety upon CO-photodissociation in a microsecond to millisecond time scale. Our FTIR results indicate the presence of two conformations of the *Ec*DOSH-CO complex, a “closed” and an “open” at 1923 and 1970 cm⁻¹ respectively. The two conformations are largely perturbed upon mutation of distal residues Arg97 (upshift to 1972 cm⁻¹, absence of 1923 cm⁻¹) and Phe113 (downshift to 1965 cm⁻¹ and 1920 cm⁻¹), suggesting that Arg97 directly interacts through hydrogen bonding with the heme-bound CO while Phe113 largely controls the hydrogen bonding network near the heme-bound CO. The TRS²-FTIR difference spectra of wild type *Ec*DOSH upon CO photodissociation at $t_d = 6 \mu\text{s}$,

demonstrate a 55% photoproduct yield suggesting 45% CO geminate recombination occurring in nanosecond time scale. Monitoring the kinetic evolution of CO-rebinding for the remaining 55% reveals biphasic kinetics, where upon CO dissociation we observe the first phase to proceed at a fast rate ($t_1 = 95 \mu\text{s}$), while structural reorientation of the heme active site allows rebinding of CO at a slower rate ($t_2 = 3716 \mu\text{s}$) upon displacement of Met95 from the heme binding pocket.

8.2 Experimental Procedures

The expression of the direct oxygen sensor protein *Ec*DOS in *E. coli* BL21 (DE3) and the purification processes were performed according to previously published procedures.¹⁵ The samples used for the FTIR measurements had an enzyme concentration of $\sim 1.5 \text{ mM}$ for the isolated *Ec*DOSH in 50 mM Tris for pH 7.5 and pD 7.5 after buffer exchange. The pD solutions prepared in D₂O buffers were measured by using a pH meter and assuming pD = pH (observed) + 0.4. Sodium dithionite reduced Fe(II) form protein samples were exposed to 1 atm of CO in an anaerobic cell to prepare the carbonmonoxy adduct and transferred to a tightly sealed FTIR cell with two CaF₂ windows, under anaerobic conditions (path length (l) = 6 μm). CO gas was obtained from Linde. The static FTIR spectra were recorded with 4 cm^{-1} spectral resolution on a Bruker Vertex 70 FTIR spectrometer equipped with a liquid nitrogen cooled mercury cadmium telluride (MCT) detector.

For the time-resolved step-scan FTIR measurements, the 532 nm pulses from a Continuum Minilite II Nd:YAG laser (5 ns width, 10 Hz) were used as a pump light (8 mJ/pulse) to photolyze the YddV- CO adducts. These measurements were performed on a Bruker Vertex 80 V spectrometer equipped with the step-scan option. A vacuum pump was used to evacuate the interferometer compartment to a final pressure of 3.2 mbar. The FTIR spectrometer was placed on a Newport VH optical vibration isolation table to ensure that vibrational background noise from environmental sources was avoided. For the time-resolved experiments, a TTL (transistor transistor logic) pulse provided by a digital delay pulse generator (Quantum Composers, 9524) triggered in order the flashlamps, the Q-switch, and the FTIR spectrometer. Pretriggering the FTIR spectrometer to begin data collection before the laser fires allows fixed reference points to be collected at each mirror position, which are used as the reference spectrum in the calculation of the difference spectra. Changes in intensity were recorded with a photovoltaic MCT detector (Kolmar Technologies KV100-1B-

7/190, response limit 850 cm^{-1}) and digitized with a 180-kHz, 24-bit, analog-to-digital converter (ADC) for measurements in the μs to ms time scale. A broadband interference optical filter (LP-4200, Spectrogon) with a short wavelength cutoff at $4.2\ \mu\text{m}$ was used to limit the free spectral range from 4.2 to $11.8\ \mu\text{m}$. This led to a spectral range of 2633 cm^{-1} , which was equal to an undersampling ratio of 6.

For the $\mu\text{s} \rightarrow \text{ms}$ time scale measurements, single-sided spectra were collected at 4 cm^{-1} spectral resolution, $6\ \mu\text{s}$ time resolution and 10 coadditions per data point for noise reduction. The total accumulation time for each measurement was 25 min and 15 to 20 measurements were collected and averaged. The Blackman-Harris 3-Term apodization with 32 cm^{-1} phase resolution and the Mertz phase correction algorithm was used. Pre-triggering of the FTIR spectrometer was achieved so as to begin data collection before the firing of the laser thus, allowing for fixed reference points to be collected at each mirror position. Difference spectra were calculated as $\Delta A = -\log(I_S/I_R)$. Optical absorption spectra were also recorded with a Shimadzu UV1700 UV-visible spectrometer before and after the FTIR measurements to ensure the formation and stability of the *Ec*DOSH-CO adducts.

8.3 Results

For the investigation of CO binding to the Fe(II) form of the *Ec*DOSH proteins, we have employed FTIR spectroscopy. In the static FTIR spectrum of the wild type *Ec*DOSH-CO adduct in pH 7.5 (**Figure 8.2, trace B**) we have observed two vibrations at 1970 cm^{-1} and 1923 cm^{-1} , which we attribute to the $\nu(\text{CO})$ stretching vibrations of the two conformations of the Fe-CO complex of *Ec*DOSH. Based on the interaction of the heme-bound CO with the distal site of the protein, the conformer at 1970 cm^{-1} has been defined as the “open” conformation where the conformer at 1923 cm^{-1} the “closed” conformation.^{16,17} Both vibrations demonstrate sensitivity to isotopic substitution with the two modes being shifted to 1880 and 1925 cm^{-1} respectively in the spectrum of *Ec*DOSH- ^{13}C O (**Appendix of Supplementary data**). The two $\nu(\text{CO})$ vibrations retained the same frequencies at pH 6, pH 9 (**Appendix of Supplementary data**) and pD 7.5 (**Figure 8.2, trace A**). Therefore, binding of CO to *Ec*DOSH heme-Fe(II) is unaffected by $\text{H}_2\text{O}/\text{D}_2\text{O}$ buffer exchange, thus maintaining both the H-bonded and non-H-bonded conformations in the wild-type sensor protein and no protonation/deprotonation phenomena of residues near the binuclear center exist that significantly affect the heme-bound CO. Similar frequencies for the “open” conformation

with minor shifts have been observed for most of the mutated forms of *Ec*DOSH. However, when Phe is mutated to Thr (Figure 8.1, trace F) the 1970 cm^{-1} mode is downshifted by 5 cm^{-1} to 1965 cm^{-1} , while the two mutations of Arg97 to Ala and Ileu appear upshifted at 1972 cm^{-1} (Figure 8.2, traces C & F). Comparing the frequencies and intensities of the conformer at 1923 cm^{-1} (strong hydrogen bonding interactions of the distal pocket with the heme-bound CO) between the mutant and the wild type forms of *Ec*DOSH, significant variations have been observed. In terms of frequency, the majority of the mutated forms retain the $\nu(\text{CO})$ at 1923 cm^{-1} , except for E93I and F113T (Figure 8.2, traces D & F) where it appears shifted to 1920 cm^{-1} with substantially decreased intensity.

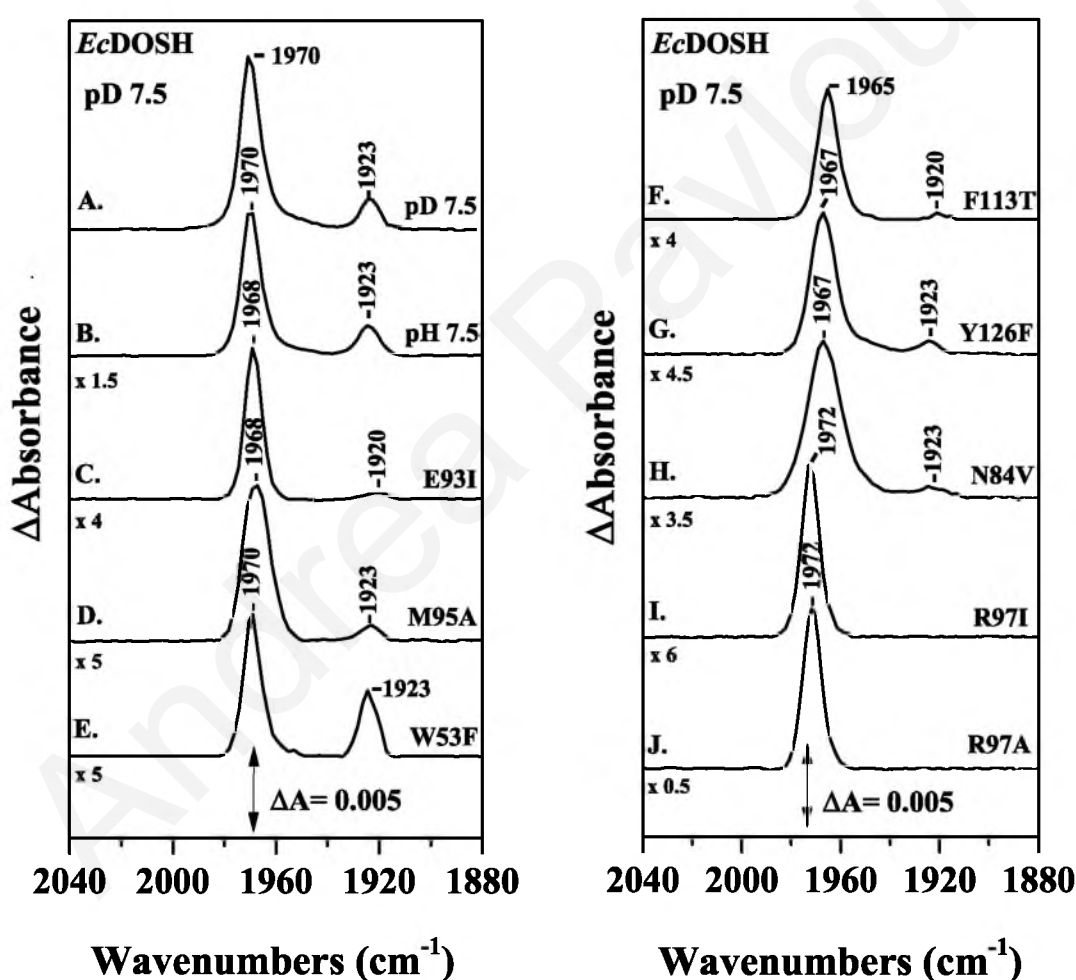


Figure 8.2 FTIR spectra of the *Ec*DOSH-CO adducts WT pD 7.5 (trace A), WT pH 7.5 (trace B), and of the mutants at pD 7.5, E93I (trace C), M95A (trace D), W53F (trace E), F113T (trace F), Y126F (trace G), N84V (trace H), R97I (trace I) and R97A (trace J). The pathlength was $6\text{ }\mu\text{m}$ and the spectral resolution was 4 cm^{-1} .

Intensity variations of the minor conformer have been also observed in the spectra of M95A, Y126F, N84V – decreased and W53F – increased (Figure 8.2, traces D, G, H & I).

The latter results suggest that these residues are in different degrees affected by the binding of CO to heme-Fe(II). Interestingly, the $\nu(\text{CO})$ at 1923 cm^{-1} is completely absent upon mutation of Arg97 to Ileu and Ala, providing a first indication that R97 is the distal site residue that directly interacts with the heme-bound CO through strong hydrogen bonding.

The dynamic changes induced to the protein matrix upon CO photodissociation / rebinding have been investigated with the use of time-resolved step-scan FTIR spectroscopy. **Figure 8.3 (A)** depicts the time-resolved step-scan FTIR difference spectra ($t_d = 6\ \mu\text{s} - 7.8\text{ ms}$) of the Fe(II) form, wild type *Ec*DOSH-CO at pH 7.5 subsequent to CO photolysis. The negative peaks at 1970 cm^{-1} and 1923 cm^{-1} arise from the photolyzed heme Fe-CO complex, indicating that both conformers are photolabile. The low photoproduct yield (58%) calculated for the wild type *Ec*DOSH protein suggests that the dissociated CO displays geminate rebinding in the nanosecond time scale with a very high yield (42%). This is in agreement with earlier ps - ns timescale optical absorption spectroscopy experimental findings.¹⁸ The latter phenomenon provides an indication that a large portion of the dissociated CO is presumably trapped in the heme cavity. Monitoring the kinetic evolution of CO rebinding for the wild type *Ec*DOSH, we have observed biphasic kinetics for the $\mu\text{s} - \text{ms}$ timescale. The first phase ($t_d = 6\ \mu\text{s} - 1\text{ ms}$) is governed by a rapidly decreasing intensity for the 1970 cm^{-1} mode denoting fast CO rebinding with an amplitude of $\sim 64\%$ where the second phase is much slower ($t_d = 1.006\text{ ms} - 7.8\text{ ms}$) with an amplitude of $\sim 36\%$, and continues until CO is fully rebound to heme-Fe(II). The existence of two distinct phases possibly signifies two distinct conformations for the two components of the Fe(II)-CO form of the protein, where heme-Fe(II) in one component is bound to CO and the other has Met95 as the *trans* axial ligand. The ΔA of the $1970\text{ cm}^{-1}\text{ Fe}^{2+} - \text{CO}$ mode has been measured and plotted as a function of time on a logarithmic scale, to determine the rate of recombination of CO to heme-Fe(II) at pD 7.5 and calculate the rebinding constants for each phase **Figure 8.3 (B)**. Accordingly, the CO rebinding constants for the wild type *Ec*DOSH protein at pD 7.5 have been calculated as $t_1=96\ \mu\text{s} / k_1 = 7220\text{ s}^{-1}$ (fast phase), $t_2=1927\ \mu\text{s} / k_2 = 360\text{ s}^{-1}$ (slow phase) (**Table 8.1**).

The results obtained for the wild type *Ec*DOSH protein at pD 7.5 are analogous to those of wild type *Ec*DOSH protein at pH 7.5 described above, with the frequencies of the two $\nu(\text{CO})$ modes at 1970 and 1923 cm^{-1} remaining unchanged upon $\text{H}_2\text{O}/\text{D}_2\text{O}$ exchange (**Figure 8.4 (A)**). In terms of the kinetic evolution of CO rebinding, we have observed an overall slower rebinding to heme-Fe(II) in D_2O . Although the transient phase has demonstrated comparable rate of CO rebinding, the subsequent slow phase had a markedly slower CO rebinding rate (three-fold slower). The slower CO rebinding rate for the wild type

*Ec*DOSH protein at pD 7.5 is confirmed by the calculated rebinding constants as follow: $t_1=95 \mu\text{s} / k_1 = 7267 \text{ s}^{-1}$ (fast phase), $t_2=3716 \mu\text{s} / k_2 = 186 \text{ s}^{-1}$ (slow phase) (**Figure 8.4 (B)**). This difference in the time evolution of CO rebinding to heme-Fe(II) observed between the protein in pD and pH 7.5 is attributed to the solvent isotope effect.

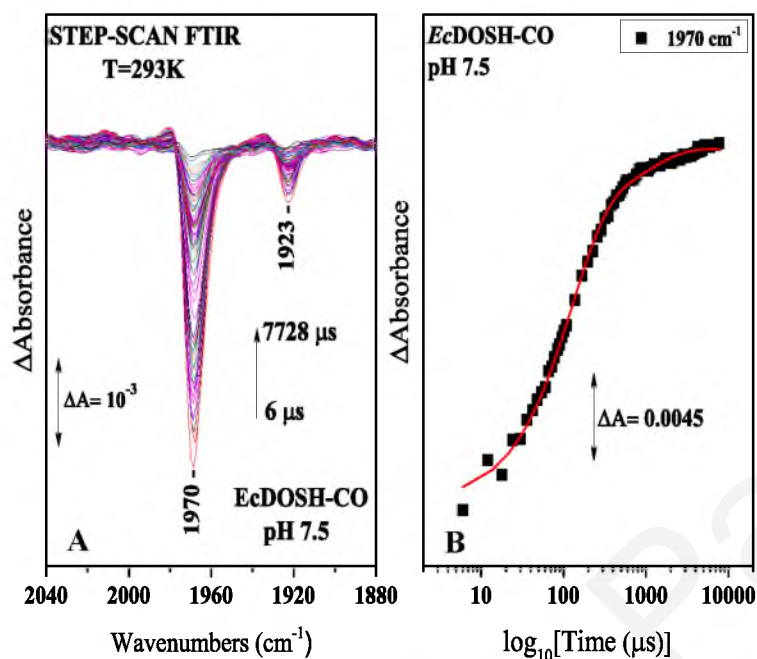


Figure 8.3 (A) Time-resolved step-scan FTIR difference spectra of the wild type *Ec*DOSH-CO adduct at pH 7.5 from 0.006 to 7.728 ms subsequent to CO photolysis. **(B)** Plot of the ΔA of the 1970 cm^{-1} mode versus time on a logarithmic scale subsequent to CO photolysis. The red line corresponds to the exponential fit of the experimental data.

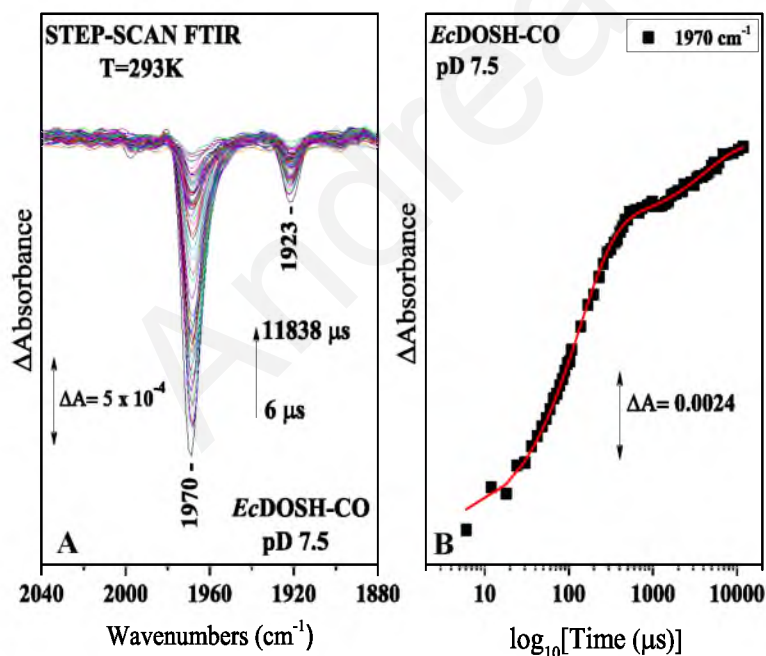


Figure 8.4 (A) Time-resolved step-scan FTIR difference spectra of the wild type *Ec*DOSH-CO adduct at pD 7.5 from 0.006 to 11.838 ms subsequent to CO photolysis. **(B)** Plot of the ΔA of the 1970 cm^{-1} mode versus time on a logarithmic scale subsequent to CO photolysis. The red line corresponds to the exponential fit of the experimental data.

Figure 8.5 depicts the TRS²-FTIR difference spectra of the wild type *Ec*DOSH protein upon CO photodissociation $t_d = 6, 24, 60, 108, 198, 288, 1000, 3100$ and $12000 \mu\text{s}$ with the identified protein vibrations in the $1700\text{-}1500 \text{ cm}^{-1}$ frequency range.

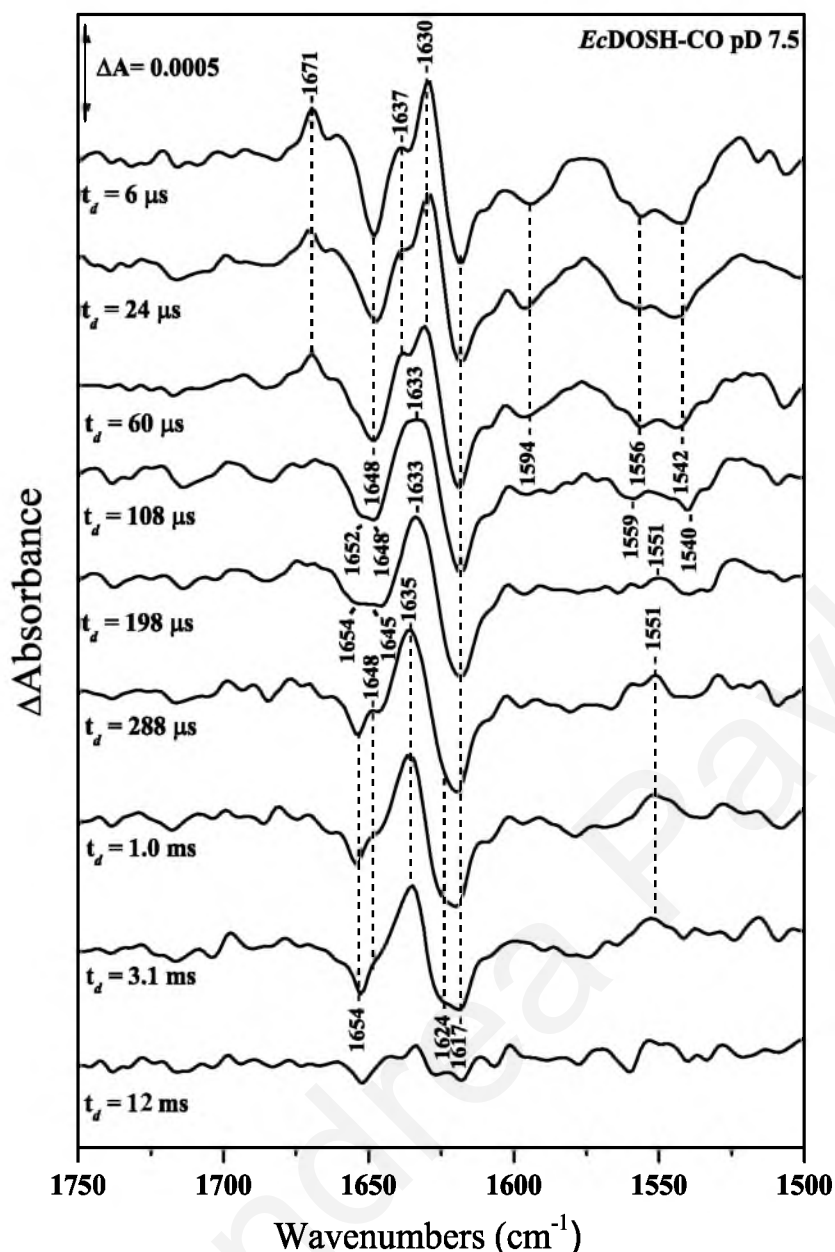


Figure 8.5 Time-resolved step-scan FTIR difference spectra of the wild *Ec*DOSH-CO adduct at pD 7.5 in the range of 1700–1500 cm^{-1} and $t_d = 6, 24, 60, 108, 198, 288, 1000, 3100$ and $1200 \mu\text{s}$.

From the spectrum at $t_d = 6 \mu\text{s}$ we have identified the following vibrational modes: the positive peak at 1671 cm^{-1} is tentatively assigned to the $\nu(\text{C}=\text{O})$ of the protonated heme propionates perturbed upon CO photolysis. In the amide I range, the modes at $1648(-)/1637(+)$ cm^{-1} are assigned to amide I (α -helix), while the modes at $1630(+)/1617(-)$ cm^{-1} are attributed to amide I (β -sheet) contribution. The negative peak at 1594 cm^{-1} indicates possible contribution from the $\nu(\text{CN}_3\text{H}_5^+)^{\text{asym}}$ of the protonation of the side chain of an Arg residue or the $\nu(\text{COO}^-)^{\text{asym}}$ of an Asp residue. In the amide II region, anti-symmetric stretching vibrations of the carboxyl group of deprotonated heme propionates can be observed, which are also overlapping with the side chain contribution of deprotonated acidic residues Asp/Glu. Therefore, the two negative signals at 1556 and 1542 cm^{-1} are assigned to the $\nu(\text{COO}^-)^{\text{asym}}$ of

both, heme propionates and the side chain of a Glu residue, without excluding possible contribution from $\nu(\text{CN}_3\text{H}_5^+)^{\text{sym}}$ of the redox-linked protonation of the side chain of an Arg residue.¹⁹⁻²²

To investigate the protein structure's reaction to CO photodissociation and rebinding we have monitored the kinetic evolution of the protein vibrations in the 1700-1500 cm^{-1} frequency range as depicted in **Figure 8.5**. The TRS²-FTIR spectra have suggested the presence of three different events in a time range of 6 - 200 μs following CO-photodissociation^{12,23}: (a) the 1671 cm^{-1} peak attributed to the $\nu(\text{C}=\text{O})$ of the protonated heme propionates perturbed upon CO photolysis as well as the negative peak at 1594 cm^{-1} attributed to possible contribution from the $\nu(\text{CN}_3\text{H}_5^+)^{\text{asym}}$ of the protonation of the side chain of an Arg residue disappear between 60 and 100 μs ; (b) the two negative signals at 1556 and 1542 cm^{-1} assigned to the $\nu(\text{COO}^-)^{\text{asym}}$ of deprotonated heme propionates disappear by $\sim 100 \mu\text{s}$ and a new positive peak at 1551 cm^{-1} appears and finally (c) a gradual upshifting and splitting/merging of the amide I modes takes place between 6 μs and 1 ms with an intermediate state existing around 200 μs . Specifically, the large positive split peak at 1637/1630 cm^{-1} merges into a single peak at 1633 cm^{-1} at $\sim 200 \mu\text{s}$ and then splits again into two distinct peaks at 1648 cm^{-1} and 1635 cm^{-1} . In parallel, the trough at 1648 cm^{-1} has been observed splitting around 100 μs and merging again into one distinct trough at 1654 cm^{-1} around 300 μs . At the same time, the negative peak at 1617 cm^{-1} has been observed to gradually split into two negative peaks at 1624 /1617 cm^{-1} , beginning at around 200 μs . We shouldn't omit the observation that the time scale of protein relaxation is slower than the time scale of CO-rebinding at room temperature, with the protein acquiring only a partially relaxed orientation after the onset of CO rebinding.

We have employed TRS²-FTIR spectroscopy and site-directed mutagenesis to investigate the role of individual residues of the distal and proximal *Ec*DOSH heme active site in CO dissociation and rebinding. Specifically we have examined the *Ec*DOSH mutations F113T, E93I, R97A, W53F, Y126F, M95A, R97I and N84V which have been stipulated by previous studies to be playing a crucial role in the ligand recognition and discrimination mechanism as well in intramolecular signal transduction processes. The eight mutant forms of *Ec*DOSH-CO adducts under study, demonstrated negative corresponding $\nu(\text{CO})$ modes indicating the photodissociation of CO. We have also monitored the time course of CO rebinding for these mutants at pD 7.5. We note that for the mutants we will refer to the first and second rebinding phase in the μs – ms timescale we have examined. However, all mutants also undergo geminate recombination as it is evident from their % photolysis yields

that are included in **Table 8.1**.

The crystal structure of *Ec*DOSH revealed that Met95 is heme-coordinated in the Fe(II) form, thus defining Met95 as the principal binding antagonist to heme-Fe(II) for the exogenous ligand.^{1,2} The latter phenomenon has been clearly depicted in our TRS²-FTIR difference spectra of the mutant M95A subsequent to CO photodissociation. We have observed a single phase between 6 μ s – 500 ms and significantly faster kinetics compared to the wild type *Ec*DOSH protein, with the CO being fully rebound to heme-Fe(II) by 438 μ s (**Figure 8.6 (A) & (B)**). The single phase kinetics at the 6 μ s – 500 ms timescale pattern denotes that absence of Met95 allows for solely CO rebinding since Met95, its principal antagonist for the heme-Fe(II) binding site, is replaced by Ala. The CO-rebinding constants for M95A were calculated as $t_1 = 81 \mu\text{s} / k_1 = 8857 \text{ s}^{-1}$.

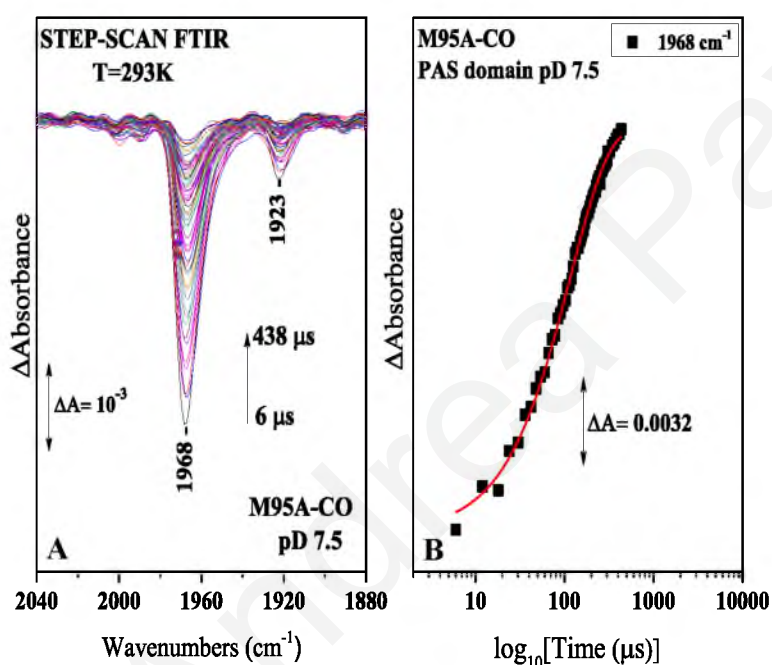


Figure 8.6 (A) Time-resolved step-scan FTIR difference spectra of the PAS domain M95A-CO adduct at pD 7.5 from 0.006 to 438 ms subsequent to CO photolysis. **(B)** Plot of the ΔA of the 1968 cm^{-1} mode versus time on a logarithmic scale subsequent to CO photolysis. The red line corresponds to the exponential fit of the experimental data.

Figure 8.7 (A) & (B) depict the time-resolved step-scan FTIR difference spectra of R97A and the kinetic evolution of CO rebinding respectively. The rapidly decreasing intensity of the $\nu(\text{CO})$ mode at 1972 cm^{-1} suggests a very fast initial CO rebinding phase in a biphasic process for R97A. The transient phase is followed by a significantly slower phase which persists until CO rebinding is complete (~ 10 ms). The CO-rebinding constants for the two phases in R97A have been calculated as $t_1 = 19 \mu\text{s} / k_1 = 37 \times 10^3 \text{ s}^{-1}$ (fast phase), $t_2 = 6086 \mu\text{s} / k_2 = 114 \text{ s}^{-1}$ (slow phase). Mutation of Arg97 to Ileu, has influenced the kinetic evolution of CO-rebinding to an even greater extent, bringing upon single phase rebinding kinetics at the 6 μ s - ms timescale (**Figure 8.8 (A) & (B)**). The CO-rebinding constants for R97I have been calculated as $t_1 = 17 \mu\text{s} / k_1 = 41 \times 10^3 \text{ s}^{-1}$. This phenomenon suggests that Arg-97 is a

critical residue and its mutation significantly perturbs the movement of Met95 in *Ec*DOSH. Hence, the electrostatic interactions of the side chain of Arg97 might be crucial for regulating the competitive recombination between Met95 and CO to the heme-Fe(II).

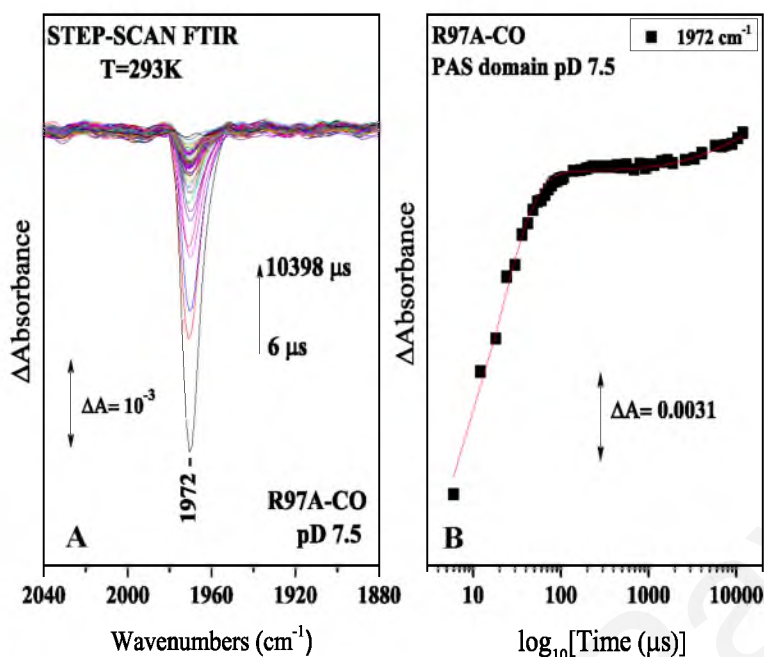


Figure 8.7 (A) Time-resolved step-scan FTIR difference spectra of the PAS domain R97A-CO adduct at pD 7.5 from 0.006 to 10.398 ms subsequent to CO photolysis. (B) Plot of the ΔA of the 1972 cm^{-1} mode versus time on a logarithmic scale subsequent to CO photolysis. The red line corresponds to the exponential fit of the experimental data.

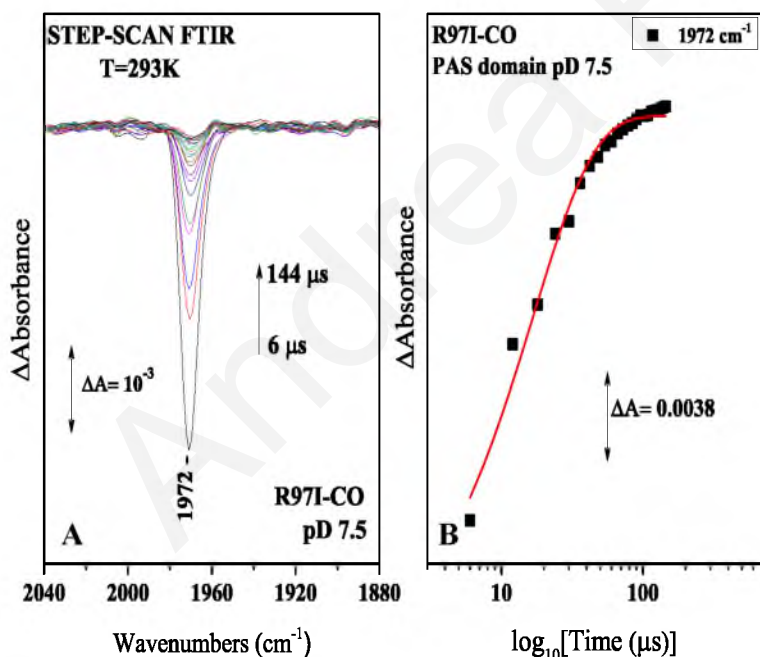


Figure 8.8 (A) Time-resolved step-scan FTIR difference spectra of the PAS domain R97I-CO adduct at pD 7.5 from 0.006 to 114 ms subsequent to CO photolysis. (B) Plot of the ΔA of the 1972 cm^{-1} mode versus time on a logarithmic scale subsequent to CO photolysis. The red line corresponds to the exponential fit of the experimental data.

It is important to mention that when Arg97 is mutated to Ileu, the overall CO-rebinding is evidently much faster compared to R97A, with the CO fully rebound to heme-Fe(II) by 144 μs . The latter could be explained on the basis of the bulkier side chain of isoleucine, which potentially acts as a barrier to the ligand exit channels restraining CO near the heme-binding site, therefore preventing Met95 from binding to heme-Fe(II) and allowing faster CO rebinding. The much smaller side chain of Ala allows ligand migration away from the heme

distal site and hence slows down CO rebinding. In terms of photoproduct yield, both R97A and R97I have demonstrated geminate recombination with 40 and 70% photoproduct yield at 6 μs respectively.

Although mutation of Phe113 to Thr has been specified by the static and TRS²-FTIR spectra to affect the hydrogen-bonding interactions near the heme binding pocket, it does not seem to affect the kinetic evolution of CO rebinding. The rate of CO rebinding to heme-Fe(II) for F113T was close to that of the wild type *Ec*DOSH and the rebinding constants were calculated as $t_1 = 117 \mu\text{s} / k_1 = 4107 \text{ s}^{-1}$ (fast phase), $t_2 = 5926 \mu\text{s} / k_2 = 169 \text{ s}^{-1}$ (slow phase)

Figure 8.9 (B).

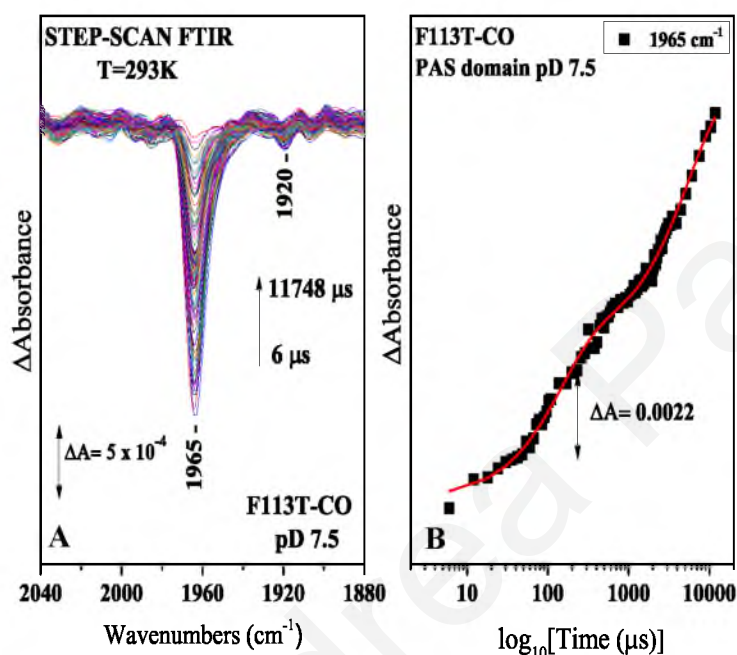


Figure 8.9 (A) Time-resolved step-scan FTIR difference spectra of the PAS domain F113T-CO adduct at pD 7.5 from 0.006 to 11.748 ms subsequent to CO photolysis. (B) Plot of the ΔA of the 1965 cm^{-1} mode versus time on a logarithmic scale subsequent to CO photolysis. The red line corresponds to the exponential fit of the experimental data.

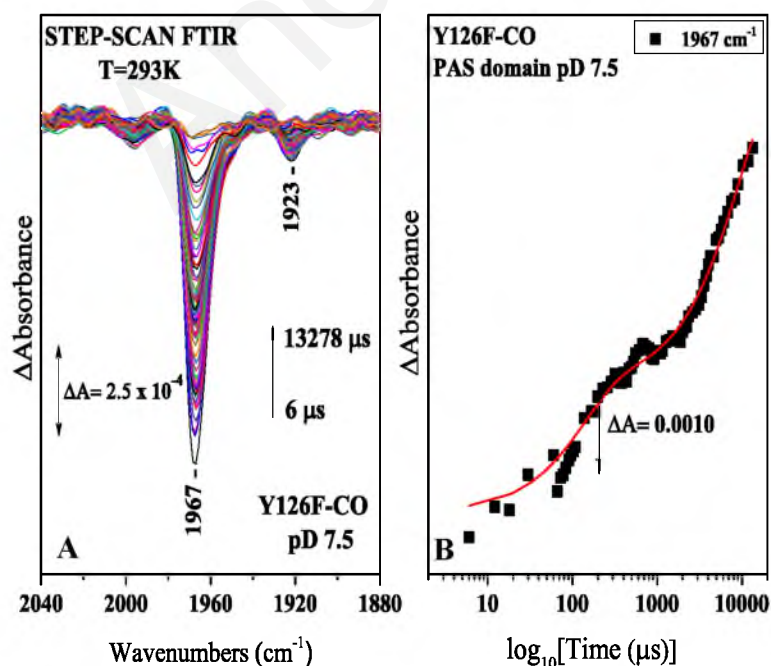


Figure 8.10 (A) Time-resolved step-scan FTIR difference spectra of the PAS domain Y126F-CO adduct at pD 7.5 from 0.006 to 13.278 ms subsequent to CO photolysis. (B) Plot of the ΔA of the 1967 cm^{-1} mode versus time on a logarithmic scale subsequent to CO photolysis. The red line corresponds to the exponential fit of the experimental data.

Figure 8.10 (A) illustrates the TRS²-FTIR difference spectra of the mutant Y126F subsequent to CO photodissociation, which undergoes major spectral changes upon CO-dissociation/rebinding. Firstly, we report a low photoproduct yield of ~10% for Y126F, substantially lower than both the wild type and the other mutant forms of *Ec*DOSH. Secondly, in terms of kinetic evolution of CO rebinding to heme-Fe(II) the rebinding rate for Y126F is comparable to that of the wild type protein with rebinding constants calculated as $t_1 = 173 \mu\text{s} / k_1 = 4015 \text{ s}^{-1}$ (fast phase), $t_2 = 3704 \mu\text{s} / k_2 = 187 \text{ s}^{-1}$ (slow phase) **Figure 8.10 (B)**.

The crystal structure of the O₂-bound form shows the heme 6-propionate establishing a H-bond network with Asn84 and Tyr126. To explore the possible existence of such H-bond network in the *Ec*DOSH form we have performed TRS²-FTIR experiments with N84V. In **Figure 8.11 (A)** we report the TRS²-FTIR difference spectra of N84V at pD 7.5. Monitoring the kinetic evolution of CO-rebinding for the N84V mutant revealed biphasic kinetics, with a transient initial phase with a small amplitude (~38%). The transient phase appeared two-fold faster compared to the wild type protein and was followed by a slower phase of a much larger amplitude (~62%) that persisted until the rebinding process was completed at 6.4 ms. The CO-rebinding constants were calculated as $t_1 = 55 \mu\text{s} / k_1 = 12637 \text{ s}^{-1}$ (fast phase), $t_2 = 782 \mu\text{s} / k_2 = 886 \text{ s}^{-1}$ (slow phase) **Figure 8.11 (B)**.

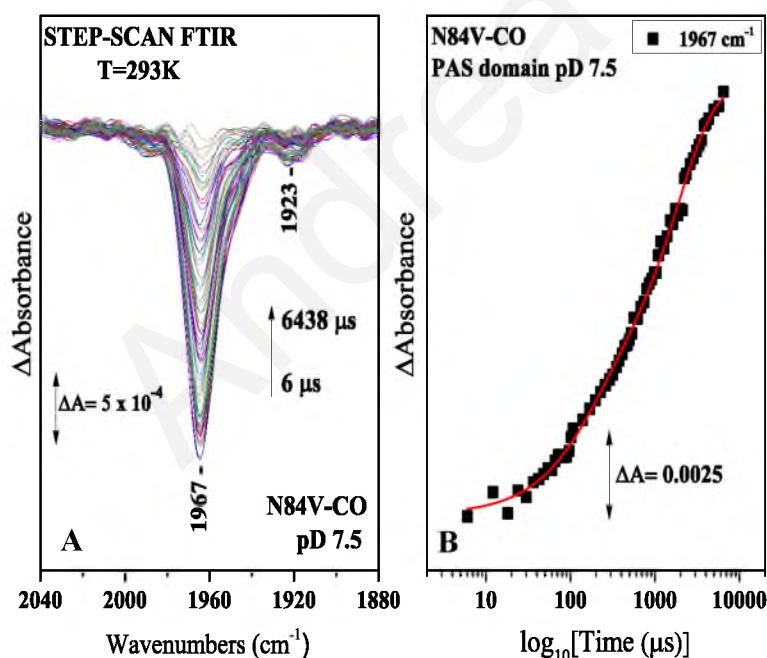


Figure 8.11 (A) Time-resolved step-scan FTIR difference spectra of the PAS domain N84V-CO adduct at pD 7.5 from 0.006 to 6.438 ms subsequent to CO photolysis. **(B)** Plot of the ΔA of the 1967 cm^{-1} mode versus time on a logarithmic scale subsequent to CO photolysis. The red line corresponds to the exponential fit of the experimental data.

The location of Trp53 in the C-helix near the heme 2-vinyl group established it as a possible candidate for playing an important role in ligand binding.^{1,2} Mutation of Trp53 to Phe drastically influenced the fast phase rate of CO-rebinding. Substitution of Trp53 with a

significantly more hydrophobic residue like Phe resulted in a three-fold slower initial CO-rebinding phase with rebinding constants calculated as $t_1 = 233 \mu\text{s} / k_1 = 2975 \text{ s}^{-1}$. The second phase of CO-rebinding exhibited similar rate with the WT protein with calculated rebinding constants equal to $t_2 = 4713 \mu\text{s} / k_2 = 147 \text{ s}^{-1}$ **Figure 8.12 (B)**.

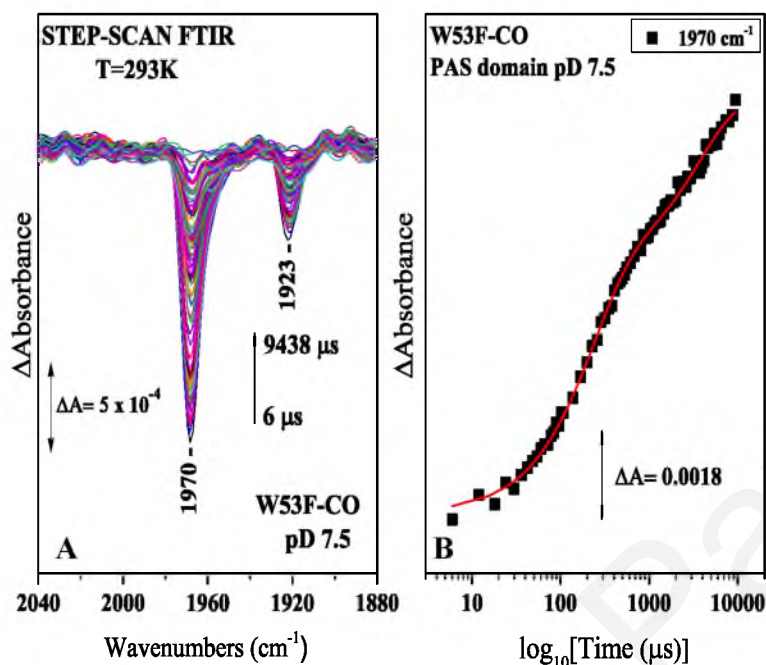


Figure 8.12 (A) Time-resolved step-scan FTIR difference spectra of the PAS domain W53F-CO adduct at pD 7.5 from 0.006 to 9.438 ms subsequent to CO photolysis. **(B)** Plot of the ΔA of the 1967 cm⁻¹ mode versus time on a logarithmic scale subsequent to CO photolysis. The red line corresponds to the exponential fit of the experimental data.

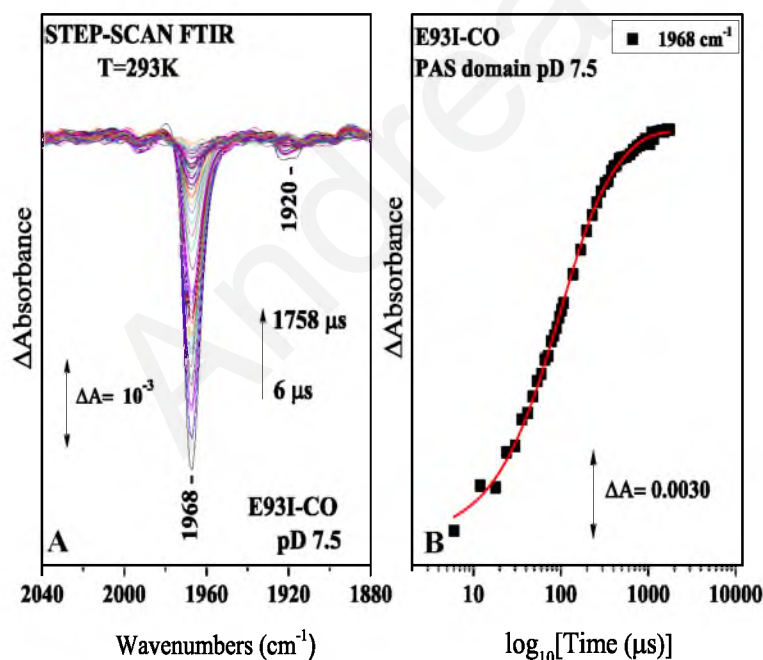


Figure 8.13 (A) Time-resolved step-scan FTIR difference spectra of the PAS domain W53F-CO adduct at pD 7.5 from 0.006 to 9.438 ms subsequent to CO photolysis. **(B)** Plot of the ΔA of the 1967 cm⁻¹ mode versus time on a logarithmic scale subsequent to CO photolysis. The red line corresponds to the exponential fit of the experimental data.

Finally, the markedly faster rate of CO-rebinding observed for E93I compared to the wild type *Ec*DOSH characterized by a single phase pattern in the 6 μs – ms timescale, could be due to Glue93 being located near Met95 in the FG loop^{1,2} and mutation to Ileu leads to such conformational orientation of the loop that hinders access of Met95 to the Fe²⁺ binding

site thus allowing sole and faster CO- rebinding **Figures 8.13 (A) & (B)**. The CO-rebinding constants were calculated as $t_1 = 97 \mu\text{s} / k_1 = 7154 \text{ s}^{-1}$ and are summarized along the wild type and other mutant forms of *Ec*DOSH pD 7.5 in **Table 8.1**.

1970 cm^{-1} (DOSH)	t_1 (μs)	k_1 (s^{-1})	t_2 (μs)	k_2 (s^{-1})	% photoproduct yield at 6 μs	% 1 st phase	% 2 nd phase
wild type pH 7.5	96 \pm 5	7220	1927 \pm 187	360	58	64	36
wild type pD 7.5	95 \pm 4	7267	3716 \pm 342	186	55	64	36
E93I	97 \pm 3	7153	-	-	65	100	-
F113T	117 \pm 12	4107	5926 \pm 356	169	35	55	45
M95A	81 \pm 2	8857	-	-	55	100	-
N84V	55 \pm 25	12 $\times 10^3$	782 \pm 42	886	70	38	62
R97A	19 \pm 1	37 $\times 10^3$	6086 \pm 928	114	40	89	11
R97I	17 \pm 1	41 $\times 10^3$	-	-	70	100	-
W53F	233 \pm 10	2975	4713 \pm 670	147	52	78	22
Y126F	173 \pm 12	4015	3704 \pm 519	187	9	54	46

Table 8.1 Summary of % photoproduct yield at $t_d = 6 \mu\text{s}$ as well as calculated constants and amplitude for each of the CO-rebinding phases for the wild type and mutant *Ec*DOSH-CO adducts.

Interesting results were drawn when comparing the TRS²-FTIR difference spectrum of the wild type protein with those of the mutated forms of *Ec*DOSH in the protein vibrations region (1500-1700 cm^{-1}), at $t_d = 6 \mu\text{s}$ subsequent to CO photodissociation. Comparing the spectrum of M95A with that of the wild type protein at 6 μs , we observe loss of the large trough/peak/trough pattern in the amide I region (1660-1620 cm^{-1}) and the presence of only positive peaks. Met95 is located on the G β -strand at the distal site of the protein.^{1,2} Upon ligand binding the secondary structure surrounding the heme active site (F-helix, G and H β -strands) undergoes a change in orientation so as to render the displacement of Met95 by the exogenous ligand possible. Therefore, the changes in the vibrations of amide I region observed in the spectrum of M95A possibly reflect the loss of this specific structural movement in the distal site of the protein. The spectra of R97I and R97A at 6 μs showed the

same deviation from the spectrum of the wild type protein in the amide I region (1690-1620 cm^{-1}) (Figure 8.14, traces *H* & *I*). Specifically, upon mutation of Arg97 the large negative split at 1648/1641 cm^{-1} (amide I α -helix) disappeared, suggesting that absence of Arg97 results in rearrangement of the secondary structure orientation of the protein. In addition, absence of the positive peak at 1671 cm^{-1} assigned to the $\nu(\text{C}=\text{O})$ of the protonated heme propionates provides evidence that Arg97 is potentially involved in a hydrogen bonding network with the heme-propionates. We also noted the absence of the negative peak at 1594 cm^{-1} which has been attributed to the $\nu(\text{CN}_3\text{H}_5^+)^{\text{asym}}$ of the protonation of the side chain of an Arg residue.¹⁹⁻²²

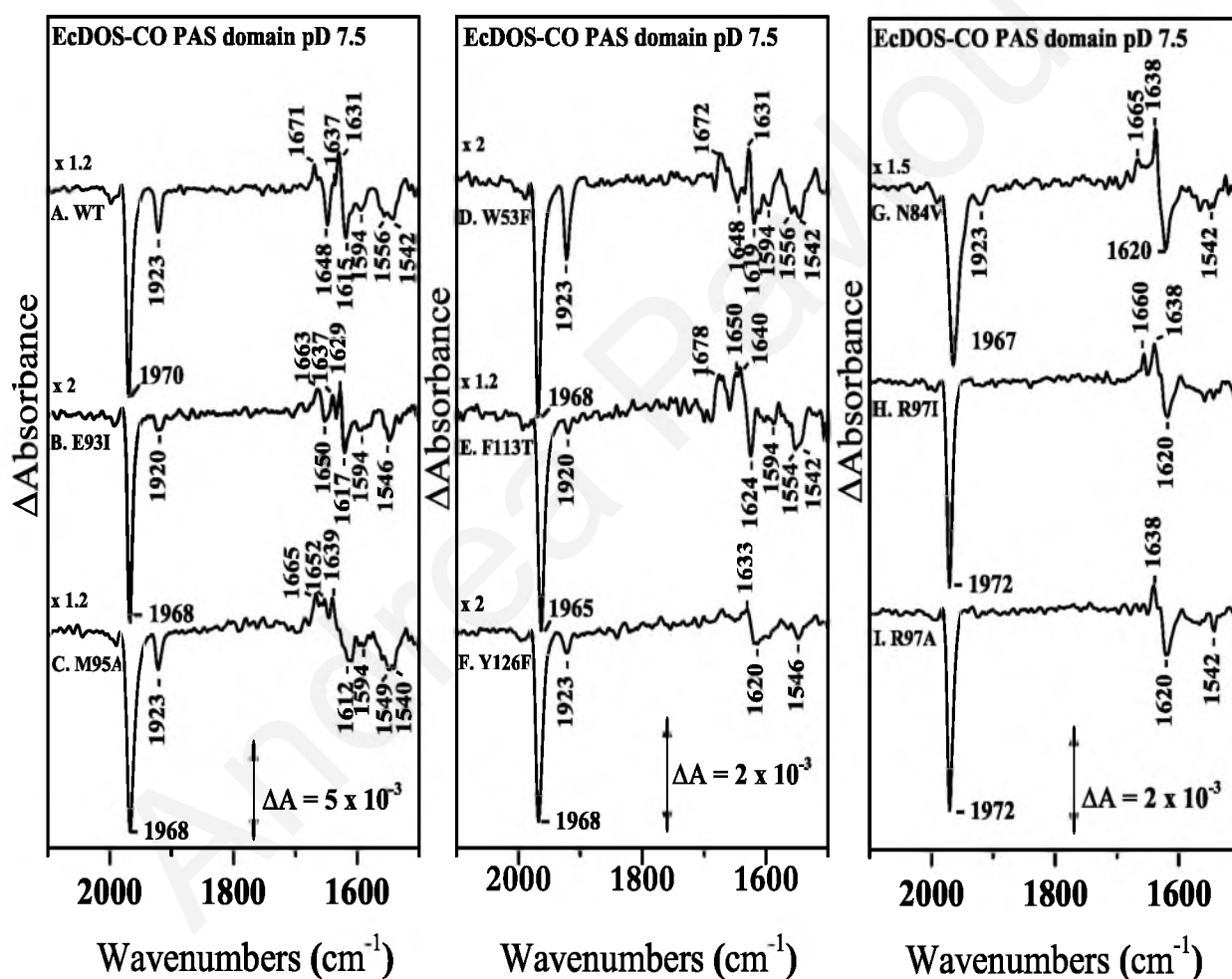


Figure 8.14 TRS² - FTIR difference spectra subsequent to CO-photodissociation at $t_d = 6 \mu\text{s}$ and pD 7.5, of *EcDOSH* WT (trace *A*), E93I (trace *B*), M95A (trace *C*), W53F (trace *D*), F113T (trace *E*), Y126F (trace *F*), N84V (trace *G*), R97I (trace *H*) and R97A (trace *I*). The pathlength was $6 \mu\text{m}$ and the spectral resolution was 4cm^{-1} .

We also report distinct differences when comparing the spectrum of the wild type protein with that of the mutant F113T in the protein vibrations region at $6 \mu\text{s}$. In general, the

protein vibrational modes appeared upshifted by $\sim 10\text{ cm}^{-1}$. In the amide I region ($1690\text{--}1620\text{ cm}^{-1}$) the two positive peak splits at $1678 / 1670$ and $1648 / 1641\text{ cm}^{-1}$ have gained in intensity and the large trough split at $1648 / 1641\text{ cm}^{-1}$ evident in the spectrum of the wild type *Ec*DOSH pD 7.5 is lost in F113T (**Figure 8.14, trace E**).¹⁷⁻²⁰ Moreover, in the spectrum of Y126F in the $1690\text{--}1620\text{ cm}^{-1}$ range at $6\text{ }\mu\text{s}$ the positive peaks disappeared or became weaker mainly due to the very low photoproduct yield of 9%. In the spectrum of N84V in the $1690\text{--}1620\text{ cm}^{-1}$ frequency range at $6\text{ }\mu\text{s}$ upon CO-photodissociation, we report a positive peak at 1667 cm^{-1} , a large peak-to-trough at $1638\text{ cm}^{-1} / 1621\text{ cm}^{-1}$ but lack of the amide I (alpha-helix) negative peak at 1648 cm^{-1} (**Figure 8.14, trace G**).¹⁷⁻²⁰ These spectral changes indicate that absence of Asn84 brings upon conformational changes to the F-helix, in which the residue is located and therefore possibly hampering the formation of a hydrogen bond with Tyr126 located on the adjacent I β -sheet, through the heme 6-propionate hydrogen-bonding network. On the other hand, mutation of Trp53 to Phe resulted in TRS²-FTIR difference spectra similar to the wild type protein indicating that absence of the residue does not induce structural changes to the protein moiety (**Figure 8.14, trace D**), nor does Trp53 influence the conformations of the heme-bound CO (**Figure 8.13 (A)**). Finally, the TRS²-FTIR difference spectra of E93I showed no significant variations from the wild type protein. Therefore, Glu93 has little or no effect on the environment surrounding the conformations of the heme-bound CO.

8.4 Discussion

In the present study, we aimed in characterizing the interactions of the heme-bound CO to the Fe(II) form of *Ec*DOSH with residues located in the surrounding environment of the heme active site by observing the changes induced to the FTIR and TRS²-FTIR spectra of *Ec*DOSH-CO adducts upon mutation of these specific residues. (R97A, R97I, M95A, F113T, Y126F, N84V, W53F and E93I). FTIR and time-resolved step-scan FTIR difference spectroscopy has been proven a valuable method in this work as it allowed for direct probing of structural changes and functional state of *Ec*DOSH in its various forms at the level of individual residues.

The static FTIR spectra revealed two conformations of the bound to heme-Fe(II) CO, a non hydrogen-bonded and a strong hydrogen bonded at 1970 and 1923 cm^{-1} that correspond to an “open” and a “closed” CO conformation respectively.^{16,17} The CO stretching modes

observed for *Ec*DOSH were similar to those of heme domains of other heme-based sensor proteins such as *Bj*FixL (1967 cm^{-1})⁴, HemAT-*Bs* (1967 cm^{-1}) and *CooA* (1969 cm^{-1})¹⁶. These conformations were present in the WT, E93I, M95A, Y126F, F113T, W53F and N84V. However the alterations in frequency and/or intensity of the $\nu(\text{CO})$ modes observed for all 6 of these mutants suggest that these residues affect CO-binding to the heme-Fe(II). The significant perturbation of both $\nu(\text{CO})$ modes noted in the spectrum of F113T infers a critical role of Phe113 in CO-binding. The bulky phenyl side chain of Phe113 physically dismisses the possibility of direct hydrogen bonding interactions with the bound CO, therefore it is more probable that the residue participates in a hydrogen bonding network that influences the surrounding environment of the bound ligand. Although previous RR studies⁹ noted that Glu93 is not affected by CO binding, the downshifting by 3 cm^{-1} of the 1923 cm^{-1} mode detected in our FTIR spectra upon mutation to Ileu contradicts their observation and suggests the possible existence of a communication pathway between Glu93 and the heme-bound CO presumably through the FG loop. The X-ray structure of the *Ec*DOSH-O₂ protein reveals a hydrogen-bond network between Tyr126, Asn84 and heme-6-propionate which potentially acts as a communication link between the heme periphery and the surrounding residues.^{1,2} From the individual static FTIR spectra of mutated Tyr126 and Asn84 we reported the major $\nu(\text{CO})$ modes downshifted by 3 cm^{-1} and the minor $\nu(\text{CO})$ modes with decreased intensity. It is possible that the hydrogen bonding network observed above could be forming upon CO binding.¹³ Mutations of Arg97 to Ala and Ileu brought upon the most significant changes to the two conformations of the bound CO. Specifically, the major conformer was upshifted by 2 cm^{-1} while the minor conformer was absent in both mutations. Consequently, we propose that Arg97 controls the hydrogen bonding interactions in the environment surrounding the heme-bound CO. Our findings agree with those previously reported by El-Mashtoly *et al.*⁹ It is notable to mention what was observed via optical absorption spectroscopy by Tanaka *et al.*,⁷ who reported that Arg97 is not important for stabilizing the Fe(II)-CO complex. Finally, the decrease in intensity of the minor conformer observed in the spectra of M95A also indicates perturbation of the hydrogen-binding network in the distal site upon mutation of Met95.¹⁷

*Ec*DOSH demonstrated sub-nanosecond to nanosecond kinetic events triggered by ligand dissociation from heme-Fe(II) representing changes in the heme active site prior to the ligand escaping away from the distal site.^{12,18, 24, 25} Our TRS²-FTIR photolysis experiments $t_d = \mu\text{s} - \text{ms}$ demonstrated the existence of a submicrosecond phase immediately following CO dissociation, and two distinct CO-rebinding phases in the microsecond to millisecond time scale, which we monitored in detail. To elaborate, monitoring the kinetic evolution of CO-

rebinding to the wild type *Ec*DOSH revealed biphasic single-exponential kinetics²⁴ with a photoproduct yield of ~55%. Therefore, we suggest that proximately after CO dissociation, 45% of CO molecules are trapped in the heme cavity inducing immediate protein structural relaxation back to the CO-bound form due to geminate recombination.²⁶⁻²⁸ Partial geminate rebinding of CO (60%) to heme-Fe(II) was previously reported at time scale of 1.5 ns after CO dissociation.^{12,24} Taguchi *et al.* have similarly proposed a three phase CO-rebinding process with an initial picosecond order phase that is independent of CO concentration followed by a CO-dependent transient phase and completed via CO-dependent slow phase.¹⁸

The biphasic rebinding denotes an antagonistic “binding and replacement” process between Met95 and CO. Specifically, after the migration of CO away from the heme pocket, Met95 competitively rebinds to heme-Fe(II) instigating a fast rebinding phase that takes place in the microsecond time scale. Our spectra have revealed that the fast rebinding phase is completed at a time-scale of approximately 1 ms. The re-association of CO to heme-Fe(II) after the protein reaches the equilibrium Met-bound form appears to be a much more time consuming process, as it involves important reorganization of the heme moiety in order for Met95 to be displaced. The above phenomenon gives rise to the observed slow rebinding phase with CO completely rebound to heme-Fe(II) in the wild type *Ec*DOSH at around 12 ms. Similar dynamic ligand exchange and cooperativity has been well documented in the CO-activated heme-containing protein (CooA), where CO displaces the axial residue Pro2 in order to bind to the heme iron.²⁹ Modeling of the coupling of protein relaxation to CO dissociation and rebinding in Mb, demonstrated that the slowing-down of ligand rebinding is due to both protein relaxation and ligand migration, with protein relaxation being more effective in slowing down the rebinding than ligand escape.³⁰ Interestingly, monitoring the protein structural relaxation through the kinetic evolution of the protein vibrations in *Ec*DOSH upon CO-dissociation, has revealed distinct phases in protein conformational motion after the onset of CO-rebinding. It is notable to mention that these observations concern *Ec*DOSH at pD 7.5 and due to the solvent isotope effect and the increased rigidity of the protein in the deuterated solvent, kinetic events take place at an overall slower rate.³¹⁻³³ We reported that for the wild type *Ec*DOSH protein at pH 7.5, CO-recombination to heme-Fe(II) takes place at ~8 ms which is in agreement with previously published results.²⁵

The role of Met95 as a heme axial ligand and principal binding antagonist for exogenous ligands was clearly defined by our CO-dissociation / rebinding kinetic studies. Mutation of Met95 to Ala, did not affect the initial phase immediately upon CO-dissociation, as we reported 45% geminate recombination alike the wild type protein. The latter denotes

that conformational changes induced to Met95 upon CO-dissociation are not responsible for the geminate rebinding of CO. However, the kinetics of CO rebinding to heme in M95A revealed a single CO-rebinding phase on the 6 μ s – 500 ms timescale, with a rate similar to that of the fast CO rebinding phase of the wild type protein. Therefore, absence of Met95 allows the protein to adopt a 5-coordinated structure after CO-dissociation compared to a 6-coordinated in the presence of Met95, markedly decreasing CO rebinding time since CO binds to heme without competition from an internal ligand.^{7,12,18,24}

Mutation of distal residue Arg97 to Ala resulted in very fast initial CO-rebinding process, still demonstrating biphasic CO-rebinding pattern in the 6 μ s – ms timescale with the transient phase completed by \sim 100 μ s. On the other hand mutation of Arg97 to Ileu markedly changed the kinetic evolution of CO-rebinding, demonstrating single phase kinetics in the 6 μ s - ms timescale compared to biphasic for R97A and the wild type protein. From the X-ray crystal structure of the O₂-bound *Ec*DOSH, we know that the side chain of Arg97 interacts through hydrogen bonding with the heme-7-propionate.^{1,2} It is plausible that mutation of Arg97 to a residue with different side chain hinders the electrostatic interactions at position 97 with the heme periphery, perturbing the movement of the FG loop inwards⁹, ultimately influencing the formation of the H-bond between Met95 and heme-7-propionate that helps anchoring Met95 to heme-Fe(II). By opening the ligand access channels toward heme-Fe(II) to CO, its rebinding is promoted instead of Met95. Therefore the electrostatic interactions of the side chain of Arg97 are crucial for regulating the competitive recombination between Met95 and CO to heme. The single phase kinetics of CO rebinding at the μ s – ms timescale for the R97I mutant compared to R97A, is suggested to be due to its bulkier side chain, hindering Met95 from binding hence allowing exclusive and faster rebinding for CO.

The kinetic evolution of CO-rebinding was monitored in several other mutations of residues of the heme distal site (Y126F, F113T, W53F and N84V) in order to better understand the heme structural changes upon CO photodissociation and rebinding. For all four mutants the evolution of CO-rebinding follows biphasic kinetics. The calculated constants of CO-rebinding for the F113T protein, indicated that absence of Phe113 results in slightly slower CO rebinding rate compared to the wild type protein. The latter confirms the role of Phe in regulating the competitive binding between Met95 and CO to heme-Fe(II).

Mutation of Trp53 to a highly more hydrophobic residue such as Phe, resulted in a substantially slower initial CO-rebinding phase. The three-fold slower initial rebinding phase observed in W53F suggests that in a hydrophobic environment binding of Met95 over CO is favored. Trp53 is located near the heme 2-vinyl group, which undergoes structural changes in

the initial events of CO-dissociation.^{10,12,13} Therefore, if we assume that upon CO-photodissociation alterations in the interactions of the heme 2-vinyl group with nearby residues such as Trp53 would change the surrounding environment to more hydrophobic to accommodate the binding of Met95, then we suggest that for CO to bind to heme-Fe(II) a hydrophilic environment must be sustained. The latter renders Trp53 important in controlling hydrophobicity around the heme binding pocket. Intriguingly, the environment surrounding Trp53 was suggested to be changing to more hydrophobic upon O₂-binding, a structural change that might be crucial in *Ec*DOSH ultimately discriminating and favoring O₂ for controlling its catalytic activity despite binding to both gaseous molecules with high affinity.^{10,12,13}

The kinetic evolution of CO rebinding in Y126F showed a first phase roughly two-fold slower compared to that of the wild type protein, while the second phase had a rate identical to that of the wild type protein. The fact that mutation of Tyr126 to a residue of which the side chain is unable to form hydrogen bonds affects the initial fast phase in which Met95 rebinds to heme-Fe(II), provides further evidence that Tyr126 is important in regulating competitive rebinding between Met95 and CO to the heme binding pocket. Surprisingly, the photoproduct yield reported from the TRS²-FTIR difference spectra of the Y126F *Ec*DOSH, was only 9%, suggesting the formation of a closed conformation in the initial events of CO-dissociation that traps the majority of CO into the heme pocket. We presume that conformational changes in the environment surrounding Tyr126, impact CO-binding sterically as well. On the other hand, mutation of nearby residue Asn84 resulted in almost two-fold faster initial CO-rebinding phase and approximately four-fold faster second phase. The changes observed in the kinetic evolution of CO-rebinding for N84V suggest that absence of Asn84 disrupts the hydrogen bonding network between Asn84 and heme-6-propionate that facilitates Met95 binding to heme, allowing CO to rebind at a faster rate. Consequently, the Asn84-heme-6-propionate hydrogen bonding network is crucial in the regulation of competitive binding between Met95 and CO. El-Mashtoly *et al.*, proposed that at 1 μ s after CO-dissociation from heme-Fe(II), the Asn84-heme-6-propionate complex undergoes structural rearrangement and the side chain of the heme-6-propionate is reoriented towards the heme binding pocket. These conformational changes are communicated to the FG loop via the formation of a hydrogen bond between the heme-6-propionate and Gly94 located adjacent to Met95 facilitating binding of Met95 to heme.^{10,12,13}

We have proposed earlier that despite previous reports that Glu93 does not influence CO-binding,¹³ the 3 cm⁻¹ downshift of the $\nu(\text{CO})$ of the hydrogen bonded conformation

observed in the static FTIR spectrum of E93I suggests otherwise. The observed kinetic evolution of CO rebinding supports the above speculation. We have reported single phase kinetics of CO rebinding at the 6 μ s - ms timescale upon mutation of Glu93 to Ileu, with a rebinding rate as fast as the transient first phase for the wild type protein. Glu93 is located on the FG loop near Met95.^{1,2} If absence of Glu93 blocks Met95 rebinding, thus allowing CO to rebind faster to heme-Fe(II), then we propose that Glu93 contributes in the regulation of the Met95 binding to the heme upon photodissociation of CO.

Structurally, each subunit of the *Ec*DOSH dimer is comprised of five α -helices and a five-stranded antiparallel β sheet. The heme group is located between the F helix and the G and H β -strands with the FG loop playing an important role in redox state change and consequently ligand binding.^{1,2,15,34,35} Mutations of critical amino acids surrounding the heme active site resulted in structural changes that potentially influence CO binding in *Ec*DOSH. The TRS²-FTIR difference spectra of the wild type *Ec*DOSH subsequent to CO photodissociation and $t_d = 6 \mu$ s revealed protein vibrations associated with the protein's secondary structure and the heme periphery that are perturbed upon CO dissociation/rebinding.

Superimposed structures of the unliganded and oxygen-bound forms of *Ec*DOSH signified three areas of the heme active site being affected by ligand binding; the FG loop (aa 88-93), the start of the G β strand (aa 94-97) and the HI loop (aa 121-122)(**Figure 8.15**).^{1,2}

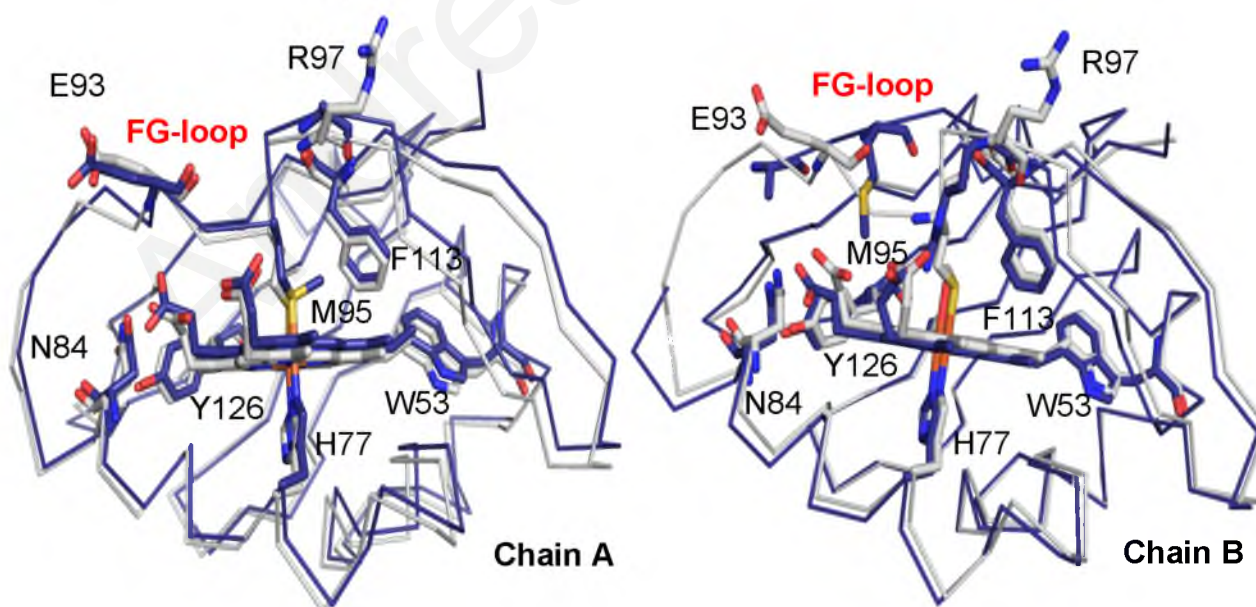


Figure 8.15 Superposition of chain A and B of Fe(II) *Ec*DOSH heme active site (grey) over chain A and B Fe(II)-O₂ *Ec*DOSH heme active site (blue) signifying the changes induced to the protein moiety upon ligand binding as depicted by the X-ray crystal structure of the protein (PDB IDS 1V9Z & 1VB6).

Indeed, the identification of vibrations attributed to both α -helix and β -sheet confirms that CO dissociation induces global structural changes to the heme active site. In addition, the observation of vibrations attributed to both the protonated and deprotonated heme propionates indicates the existence of both conformations within the dimer. It is not possible to decipher merely from our spectra which of the heme propionates is deprotonated or protonated and whether both conformations exist within the same subunit.

The crystal structure of *Ec*DOSH-O₂ clearly depicts a hydrogen bonding network between Arg97 and the heme-7-propionate as well as a hydrogen bond between the side-chain of Asn84 and heme-6-propionates. Based on UVR experiments¹² it has been demonstrated that upon dissociation of CO the Arg97-heme-7-propionate hydrogen bond is cleaved and by $t_d = 6 \mu\text{s}$ the hydrogen-bonding network between Asn84 and heme-6-propionate is formed, therefore the two heme propionate conformations reported in our TRS²-FTIR difference spectra possibly arise from the protonated heme-7-propionate and the deprotonated heme-6-propionate. Time resolved UVR experiments by El-Mashtoly *et al.*,¹² have set the cleavage of this Arg97-heme-7-propionate hydrogen bond within $t_d = 20 \text{ ns}$ of CO photodissociation and by $t_d = 1.0 \mu\text{s}$ a hydrogen bond between the side-chain of Asn84 and heme-6-propionates was evident.¹² An interesting observation was the identification of a vibration at 1594 cm^{-1} attributed to $\nu(\text{CN}_3\text{H}_5^+)^{\text{asym}}$ of protonation of the side chain of an Arg residue indicating the cleavage of the previously proven hydrogen bond formed between the side chain of Arg97 and the heme-bound CO, upon CO photodissociation.^{19,20} The disappearance of the latter peak by $100 \mu\text{s}$ suggests that binding of Met95 to heme-Fe(II) occurs at that time frame with the Met-bound form transiently adopting a structural architecture similar to that of the CO-bound form. It is evident from the spectral changes over time of the amide I modes that binding of Met95 brings upon significant structural reorientation of the heme active site. This structural reorientation is completed by $\sim 1 \text{ ms}$ where the second phase of CO-rebinding begins with CO replacing Met95 as the heme-Fe(II) bound ligand.

Met95 is located on the FG-loop and successful binding of this endogenous ligand has been associated with the rigidity/flexibility of the loop.^{6,7,36-39} In the Fe(II) form, the FG-loop is rigid enough to anchor Met95 to heme, while in the Fe(II)-O₂ structural conformations of the FG-loop increase its flexibility allowing the dissociation of Met95 and the binding of oxygen.^{1,2} Indeed our results demonstrated significant differences in the protein vibrations amide I region of the M95A spectrum, when compared to the wild type protein. The loss of the large trough-peak-trough that signifies movement of α -helix/ β -sheet, presumably attributed to movement of the FG-loop (F-helix / G β -strand), indicates that absence of Met95

hinders the structural rearrangement of the loop back to a more rigid conformation as no endogenous ligand exists to bind to heme-Fe(II) after CO dissociation. Therefore, we propose that in the absence of Met95, *Ec*DOSH adopts a conformation similar to that of the gas-bound protein rendering the displacement of Met95 from the ligand binding site critical for regulating the catalytic activity; previous studies demonstrated that mutations of Met95 exhibited enhanced catalytic activity similar to that of the O₂-bound protein.⁴⁰

Mutations of Arg97 to Ala and Ileu resulted in loss of the negative peak at 1594 cm⁻¹ providing evidence that support the above assignment. However, the most notable changes to the spectra of R97A and R97I compared to the wild type protein were observed in the amide I region. Specifically, the spectrum of R97A showed complete loss of the amide I (α -helix) modes (1660-1641 cm⁻¹) with only modes attributed to amide I (β -sheet) evident. Arg97 is the last constituent of the FG loop, located at the start of the G β strand adjacent to the end of the F helix and it has been associated with the control of the FG loop rigidity that allows Met95 to competitively bind to the heme-Fe(II).^{1,2,8,9,23} Absence of Arg97 apparently hinders the movement of the nearby F-helix. Superpositioning the crystal structure of Fe(II) chain B over O₂-bound chain B clearly demonstrates Arg97 undergoing substantial reorientation upon ligand binding (**Figure 8.15**).^{1,2} Therefore, we propose that when CO binds to heme-Fe(II), displacement of Met95 away from the heme pocket causes conformational changes to the FG loop that are communicated to the G β strand, which in turn reorients so that Arg97 turns towards the heme pocket allowing the formation of a hydrogen bonding network between heme-7-propionate and the heme-bound CO that is critical for Fe²⁺-CO stabilization and possibly signal transduction since Arg97 is situated on the protein surface.

The X-ray crystal structure of the *Ec*DOSH-O₂ protein indicates that upon O₂ binding, the distal residue Tyr126 directly interacts through hydrogen bonding with residue Asn84, which is further connected to the heme-6-propionate through another hydrogen bond. The hydrogen bond between Asn84 and Tyr126 does not exist in the Fe(II) form of the protein, therefore it is inferred that upon ligand dissociation this bond is cleaved.^{1,2,9,13} The major loss of intensity for the strong peaks at 1638-1620 cm⁻¹ as well as the disappearance of the strong trough split at 1648-1641 cm⁻¹ reported in the TRS²-FTIR difference spectrum at $t_d = 6 \mu\text{s}$ of Y126F compared to the wild type protein suggest that absence of Tyr126 induces structural reorientation of a β -sheet that largely affects the conformation of a nearby α -helix. Tyr126 is located in the I β strand near the F-helix. We assume that mutation of Tyr126 to Phe and therefore loss of the hydroxyl side chain, hinders the formation of the hydrogen bond with the nearby residue Asn84 located on the F-helix ultimately resulting in loss of movement of F-

helix that would otherwise reorient to allow the side chains of Tyr126 and Asn84 to interact. We, however, should not neglect to consider that the low intensity of the protein vibration modes in the 1700-1500 cm^{-1} frequency range, observed in the Y126F spectrum at $t_d = 6 \mu\text{s}$, is also a result of the very low photoproduct yield ($\sim 9\%$). In addition, the TRS²-FTIR difference spectrum at $t_d = 6$ demonstrated that mutation of Asn84 located in the F-helix resulted in loss of the strong trough split at 1648-1641 cm^{-1} attributed to α -helix but no change was noted in frequency and intensity for the strong peaks at 1620 cm^{-1} (β -sheet). This consists an indication that although the structural orientation of F-helix is influenced by structural changes in the nearby I_β -strand, the reverse does not apply. Conclusively, we propose that upon CO binding conformational changes induced to the I_β -strand by a rotation of the hydroxyl side chain of Tyr126, result in reorientation of the F-helix so as for the side chain of Asn84 to be able to communicate with Tyr126 through the formation of a hydrogen bond. Such large environmental changes were also evident in the UVRR spectra of Tyr126 by El-Mashtoly *et al.*, indicating an alteration of the orientation of the I_β strand upon CO binding.^{9,13,40} Furthermore, the positive peak at 1665 cm^{-1} reported in the spectrum of N84V at $t_d = 6 \mu\text{s}$ attributed to the $\nu(\text{C}=\text{O})$ of the protonated heme propionates indicates that absence of Asn84 results in cleavage of the bond proposed to be forming between heme-6-propionates and Asn84, which is unperturbed by CO-photodissociation.^{13,40}

Our TRS²-FTIR difference spectra at $t_d = 6$ subsequent to CO photodissociation, showed interesting variations in the vibration modes of the 1700-1500 frequency range when Phe113 was mutated to Thr. The strong intensity changes and frequency upshifts observed in the amide I region denote that absence of Phe113 influences the orientation of the surrounding secondary structure. Comparing the X-ray crystal structure of the Met95-bound Fe(II) with that of O₂-bound *Ec*DOSH we observe that Phe113 located on the H β sheet participates in a hydrogen bonding network with Gly94 located on the FG loop through its adjacent residue Leu115 and their intermediate water molecule (**Figure 8.16**).^{1,2,40} It seems probable that this hydrogen bonding network serves as the means of creating a rigid FG loop that allows Met95 to bind and be stabilized to heme-Fe(II). However, upon oxygen binding, Phe113 is seen breaking away from the hydrogen bonding network. Therefore, we propose that upon CO binding the displacement of Met95 from heme-Fe(II) results in structural reorientation of the FG loop due to increased flexibility. These conformational changes are then communicated to the H β sheet through the Gly94-Leu115 hydrogen bond which induces structural reorientation of the H β sheet. Such rotation places the main chain oxygen of Phe113 at such distance that it is impossible to form a hydrogen bond with the nitrogen of Leu115. Conclusively, Phe113

contributes essentially in ensuring binding of CO to heme-Fe(II). Our findings agree with the previously reported work by El-Mashtoly *et al.*, which consisted the only detailed spectroscopic report until now about the role of Phe113 in ligand binding to *Ec*DOSH.⁹ Specifically, El-Mashtoly *et al.* have proposed that steric interactions of Phe113 are critical in regulating the competitive binding between the endogenous ligand Met95 and CO to heme-Fe(II).⁹

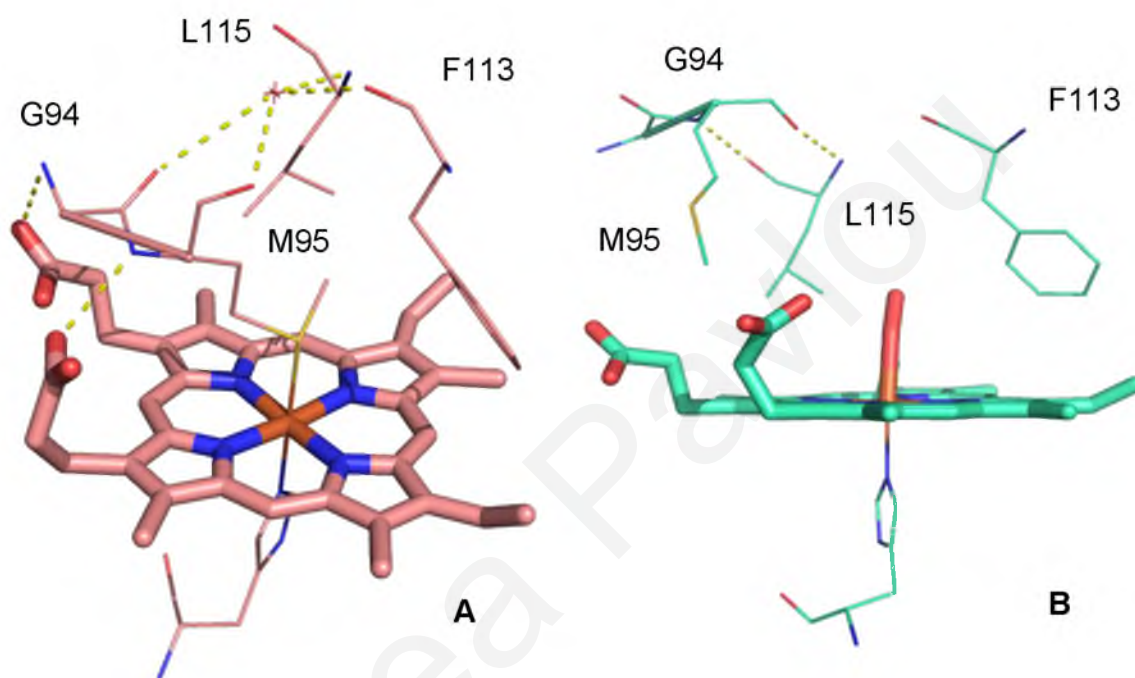


Figure 8.16 Schematic representation of the hydrogen bonding network between F113 located on the H_{β} sheet and G94 located on the rigid FG loop through a water molecule and L115, formed in the Fe(II) *Ec*DOSH (A) and its cleavage upon oxygen binding (B) (PDB IDS 1V9Z & 1VB6).

Trp53 is located near the well-conserved Glu59-Lys104 salt bridge located at the surface of the heme PAS sensor domain of *Ec*DOSH and proposed to be a key structural element in signal transduction.^{1,2} Consequently, it has been suggested that conformational changes of residue Trp53 are of critical importance due to its proximity to the salt bridge. The TRS²-FTIR difference spectrum of W53F at $t_d = 6 \mu\text{s}$ however, was similar to that of the wild type protein. As absence of Trp53 does seem not influence the conformation of the heme active site in the microsecond to millisecond time scale, we suggest that structural changes in the environment of Trp53 take place at the ps – ns timescale of CO dissociation/rebinding. According to recently published time-resolved UVRR studies by El-Mashtoly *et al.*, Trp53 residue undergoes structural changes on the subnanosecond time scale due to its interaction with the trapped in the heme cavity CO, therefore, if the above observation is valid, it was not

possible for us to observe any conformational changes of the Trp53 surrounding environment in the microsecond time scale.^{2,9,12}

8.5 Conclusions

We have initially employed FTIR spectroscopy to investigate the interactions of specific residues of the heme active site with the heme-bound CO of the Fe(II) form of *Ec*DOSH. The FTIR results demonstrated that Arg97 directly interacts through hydrogen bonding with the heme-bound CO while Phe113 largely controls the hydrogen bonding network near the heme-bound CO. To deduce the dynamic changes induced to the protein moiety upon CO-photodissociation / rebinding we have applied time-resolved step-scan FTIR spectroscopy $t_d = 6 \mu\text{s}$ on both the wild type and specific mutated forms (R97A, R97I, M95A, F113T, Y126F, W53F, N84V and E93I) of *Ec*DOSH. The low photoproduct yield observed suggested that a portion of CO molecules remain trapped in the heme cavity inducing immediate protein structural relaxation back to the CO-bound form due to geminate recombination. We have observed biphasic kinetics for the wild type protein, compared to single phase kinetics at the $6 \mu\text{s} - 500 \text{ms}$ timescale for M95A, indicating a “binding and replacement” competitive rebinding process between Met95 and CO; dissociation of CO leads to structural reorganization of the heme active site that promotes fast binding of endogenous ligand Met95. In order for CO to rebind to heme-Fe(II), the protein is subjected to a slower process of structural rearrangement that displaces Met95 and allows for the Fe^{2+} -CO complex to form. The latter structural rearrangements are instigated by steric and electrostatic interactions of the distal site residues with the heme periphery. We have shown that Asn84, Arg97 and Phe113 maintain three different hydrogen bonding networks in the heme active site that are critical in regulating competitive binding between Met95 and CO. Specifically, our results, in agreement with previous reports indicate that upon CO dissociation, the hydrogen bonds between heme-7-propionate and the side chain of Arg97, heme-6-propionate and the side chain Asn84, as well as between the side chains of Phe113, Leu115 and a nearby water molecule are altered inducing protein conformational changes that are communicated to the FG loop ultimately regulating Met95 binding to heme-Fe(II) prior to CO recombination.⁹ Finally, our results established that the environment surrounding Trp53 residue located near the heme 2-vinyl group is hydrophilic in the CO-bound form as opposed to hydrophobic in the O₂-bound form indicating that different conformational changes in the heme 2-vinyl group might be a key in discriminating O₂ from CO.

8.6 References

1. H. Kurokawa, D.S Lee, M. Watanabe, I. Sagami, B. Mikami, C.S. Raman, T. Shimizu, *J Biol Chem.* **2004**, *279*, 20186-20193.
2. H. Park, C. Suquet, J. D. Satterlee, C. Kang, *Biochemistry* **2004**, *43*, 2738-2746.
3. Sato, Y. Sasakura, S. Sugiyama, I. Sagami, T. Shimizu, Y. Mizutani, T. Kitagawa, *J. Biol. Chem.* **2002**, *277*, 32650–32658.
4. T. Tomita, G. Gonzalez, A.L. Chang, M. Ikeda-Saito, M.A. Gilles-Gonzalez, *Biochemistry* **2002**, *41*, 4819–4826.
5. T. Yoshimura, I. Sagami, Y. Sasakura, T. Shimizu *J. Biol. Chem.* **2003**, *278*, 53105-53111.
6. A. Tanaka, T. Shimizu, *Biochemistry* **2008**, *47*, 13438–13446.
7. A. Tanaka, H. Takahashi, T. Shimizu, *J. Biol. Chem.* **2007**, *282*, 21301-21307.
8. Y. Ishitsuka, Y. Araki, A. Tanaka, J. Igarashi, O. Ito, T. Shimizu, *Biochemistry* **2008**, *47*, 8874–8884.
9. S. F. El-Mashtoly, S. Nakashima, A. Tanaka, T. Shimizu, T. Kitagawa *J. Biol. Chem.* **2012**, *283*, 19000-19010.
10. S. F. El-Mashtoly, H. Takahashi, H. Kurokawa, A. Sato, T. Shimizu, T. Kitagawa, *J. Raman Spectrosc.* **2008**, *39*, 1614–1626.
11. S. Ito, Y. Araki, A. Tanaka, J. Igarashi, T. Wada, T. Shimizu, *J. Inorg. Biochem.* **2009**, *103*, 989–996.

12. S. F. El-Mashtoly, M. Kubo, S. Nakashima, T. Shimizu, T. Kitagawa, *J. Phys. Chem. Lett.* **2011**, *2*, 2212–2217.
13. S. F. El-Mashtoly, H. Takahashi, T. Shimizu, T. Kitagawa, *J. Am. Chem. Soc.* **2007**, *129*, 3556–3563.
14. S. F. El-Mashtoly, T. Kitagawa, *Pure Appl. Chem.* **2008**, *80*, 2667–2678
15. Y. Sasakura, S. Hirata, S. Sugiyama, S. Suzuki, S. Taguchi, M. Watanabe, T. Matsui, I. Sagami, Toru Shimizu, *J. Biol. Chem.* **2002**, *277*, 23821–23827.
16. T. Li, M. Quillin, G. Phillips, J. Olson, *Biochemistry* **1994**, *33*, 1433–1446.
17. M. Unno, J. Christian, J. Olson, T. Sage, P. Champion, *J. Am. Chem. Soc.* **1998**, *120*, 2670–2671.
18. S. Taguchi, T. Matsui, J. Igarashi, Y. Sasakura, Y. Araki, O. Ito, S. Sugiyama, I. Sagami, T. Shimizu, *J. Biol. Chem.* **2004**, *279*, 3340–3347.
19. A. Barth, C. Zscherp, *Q. Rev. Biophys.* **2002**, *35*, 369–430.
20. A. Barth, *Prog. Biophys. Mol. Bio.* **2000**, *74*, 141–173
21. P. Hellwig, T. Soulimane, G. Buse, W. Mantele, *Biochemistry* **1999**, *38*, 9648–9658.
22. A. Koutsoupakis, T. Soulimane, C. Varotsis, *Biophys. J.* **2004**, *86*, 2438–2444.
23. M. Schleeper, C. Wagner, M. J. Vellekoop, B. Lendl, J. Heberle *Anal Bioanal Chem* **2009**, *394*, 1869–1877
24. C. Lechauve, L. Bouzahir-Sima, T. Yamashita, M.C. Marden, M.H. Vos, U. Liebl, L. Kiger, *J Biol Chem.* **2009**, *284*, 36146–36159.

25. U. Liebl, L. Bouzahir-Sima, L. Kiger, M.C. Marden, J.-C. Lambry, M. Négrerie, M.H. Vos, *Biochemistry* **2003**, *42*, 6527–6535.
26. T. Uchida, H. Ishikawa, S. Takahashi, K. Ishimori, I. Morishima, K. Ohkubo, H. Nakajima, S. Aono, *J. Biol. Chem.* **1998**, *273*, 19988-19992.
27. A. Benabbas, V. Karunakaran, H. Youn, T. L. Poulos, P. M. Champion, *J. Biol. Chem.* **2012**, *287*, 21729–21740.
28. E.R. Henry *et al.*, *J. Mol. Biol.* **1983**, *166*, 443-451.
29. M. Coyle, M. Puranik, H. Youn, S. B. Nielsen, R. D. Williams, R. L. Kerby, G. P. Roberts, T. G. Spiro, *J. Biol. Chem.* **2003**, *278*, 35384-35393.
30. N. Agmon, *Biophys. J.* **2004**, *87*, 1537–1543.
31. M. Jasnin, M. Tehei, M. Moulin, M. Haertlein, G. Zaccai, *Eur Biophys J.* **2008**, *37*, 613-617.
32. P. Cioni, G. Strambini, *Biophys J.* **2002**, *82*, 3246–3253.
33. S. Sheu, E. Schlag, H. Selzle, D. Yang, *J. Phys. Chem. A* **2008**, *112*, 797-802.
34. J. Green, J. C. Crack, A. J. Thomson, N. E. LeBrun, *Curr. Opin Microbiol.* **2009**, *12*, 145–151.
35. J. Green, M. S. Paget, *Nat. Rev. Microbiol.* **2004**, *2*, 954–966.
36. Y. Sasakura, T. Yoshimura-Suzuki, H. Kurokawa, T. Shimizu, *Acc. Chem. Res.* **2006**, *39*, 37–43.
37. Sato, Y. Sasakura, S. Sugiyama, I. Sagami, T. Shimizu, Y. Mizutani, et al. *J. Biol. Chem.* **2002**, *277*, 32650–32658.

38. S. Hirata, T. Matsui, Y. Sasakura, S. Sugiyama, T. Yoshimura, I. Sagami, T. Shimizu, *Eur. J. Biochem.* **2003**, *270*, 4771–4779
39. M. Watanabe, T. Matsui, Y. Sasakura, I. Sagami, T. Shimizu, *Biochem. Biophys. Res. Commun.* **2002**, *299*, 169–172.
40. S. Ito, J. Igarashi, T. Shimizu, *J. Inorg. Biochem.* **2009**, *103*, 1380–1385.

Andrea Pavlou



CHAPTER 9

Conclusion

Andrea Pavlou

9.1 Conclusions

In an attempt to gain insight into the initial events of the intramolecular signal transduction mechanisms of heme-based gas sensor proteins HemAT-*Bs*, YddV and *Ec*DOSH we have employed FTIR and time-resolved step-scan FTIR spectroscopy and investigated the structure-function properties of the proteins. The sensitivity of time-resolved step-scan FTIR spectroscopy to protein structural changes allowed us to monitor the dynamic changes induced to the protein matrix upon CO-dissociation/rebinding. Here we present a summary of the conclusions drawn from the current doctoral thesis project:

HemAT-*Bs*

- The FTIR spectra of the HemAT-*Bs*-CO adducts of both the wild type full length and truncated sensor domain forms of the protein reveal two conformations of the heme-bound CO that are attributed to (a) an “open” conformation where the heme-bound CO exhibits weak interactions with the distal site and to (b) a “closed” conformation where hydrogen bonding interactions of the heme-bound CO with the distal residues exist.
- The two modes appear negative upon CO-photodissociation with a high photoproduct yield excluding the possibility of geminate recombination. The kinetic evolution of CO rebinding in the wild type HemAT-*Bs* uncovers biphasic kinetics in the microsecond to millisecond time scale with two distinct phases of conformational changes, a transient phase and a slow phase. We propose that it is the existence of cooperativity between the two structurally asymmetric components within the homodimer that gives rise to the two distinct CO-rebinding phases.
- The perturbation of the $\nu(\text{CO})$ conformations upon mutation of the distal residues Tyr70, Leu92 and the proximal residue Tyr133 suggests distinctly different interaction of each of these residues with the heme-bound CO. Specifically, Tyr70 directly interacts with the heme-bound CO, Leu92 is deemed necessary for maintaining the hydrogen bonding network between the distal site of the protein and the heme-bound CO, while Tyr133 appears as the communication linkage between the heme distal and

proximal sites.

- The comparison between the wild type and Y70F HemAT-*Bs* TRS²-FTIR difference spectra, subsequent to CO-photodissociation at 8 μ s in the Amide I region, shows that Tyr70 contributes to the control of B-helix movement. Similarly, the comparison between the wild type and Y133F TRS²-FTIR difference spectra subsequent to CO-photodissociation at 8 and 6 μ s respectively in the Amide I region, indicates that the conformation of Tyr133 affects the movement of G-helix.
- Although Leu92 does not seem to interact directly with the heme-bound CO, we demonstrate for the first time its role as the conformational gate in the migration pathway of photodissociated CO.
- The identification of the ligand (CO) docking site in HemAT-*Bs* corresponds to *B* state in which CO is trapped in a cavity within the protein matrix.
- The observation of two *B* (B_0 at 2149 cm^{-1} , B_1 at 2136 cm^{-1}) state bands suggests that protein fluctuations allow the transition of CO populations from one *B* state to another, prior to the ligand escaping away from the distal site and into the solvent.
- The absence of the B_0 band from the spectra of the L92A demonstrates that mutation of Leu92 partially blocks the photodissociated CO from accessing specific pre-existing internal ligand cavities in HemAT-*Bs*.

YddV heme domain

- Two conformation of the YddV –CO adduct are detected in the FTIR spectra of the wild type YddV protein and are attributed to neutral (open) and strong H-bonded conformers (closed), respectively.
- The environment of the heme propionates behaves similarly in both YddV and HemAT-*Bs*; it behaves in a similar way in both proteins upon ligand binding or dissociation.

- The fast recombination rates for both L65M and L65T mutants imply significant role of Leu65 in controlling the ligand dynamics.
- The rate of recombination for Tyr43 is mutant-dependent and a high barrier to recombination is formed upon mutation to Ala.

*Ec*DOSH

- The FTIR spectra indicate the presence of two conformations of the *Ec*DOSH-CO complex attributed to a “closed” and “open” CO conformation respectively. The two conformations are largely perturbed upon mutation of distal residues Arg97 and Phe113 suggesting that Arg97 directly interacts through hydrogen bonding with the heme-bound CO while Phe113 largely controls the hydrogen bonding network near the heme-bound CO.
- The low photoproduct yield observed in the TRS²-FTIR difference spectra suggest that a portion of CO molecules remain trapped in the heme cavity inducing immediate protein structural relaxation back to the CO-bound form due to geminate recombination.
- The comparison between the wild type and M95A *Ec*DOSH TRS²-FTIR spectra, indicates a “binding and replacement” competitive rebinding process between Met95 and CO; dissociation of CO leads to structural reorganization of the heme active site that promotes fast binding of endogenous ligand Met95. In order for CO to rebind to heme-Fe²⁺ the protein is subjected to a slower process of structural rearrangement that displaces Met95 and allows for the Fe²⁺-CO complex to form. The latter structural rearrangements are instigated by steric and electrostatic interactions of the distal site residues with the heme periphery.
- The residues Asn84, Arg97 and Phe113 maintain three different hydrogen bonding networks in the heme active site that are critical in regulating competitive binding between Met95 and CO.

- In agreement with previous reports the current investigation suggests that upon CO dissociation, the hydrogen bonds between heme-7-propionate and the side chain of Arg97, heme-6-propionate and the side chain Asn84, as well as between the side chains of Phe113, Leu115 and a nearby water molecule are altered inducing protein conformational changes that are communicated to the FG loop ultimately regulating Met95 binding to heme-Fe(II) prior to CO recombination.
- The kinetic evolution of CO rebinding in W53F mutant verifies that the environment surrounding Trp53 residue located near the heme 2-vinyl group is hydrophilic in the CO-bound form, as opposed to previously reported hydrophobic in the O₂-bound form, indicating that different conformational changes in the heme 2-vinyl group might be a key in discriminating O₂ from CO.

Overview

Although both the structural architecture and the catalytic activity of the effector domains of the globin coupled oxygen sensors, HemAT-*Bs* and YddV, differ significantly, their sensor domains seem to retain common structural features that have been shown through our FTIR and TRS²-FTIR studies to play important roles in the initial events of intramolecular signal transduction from the sensor to the effector domain. To elaborate, our results have shown conformational changes of the heme propionates for HemAT-*Bs* and YddV, concluding that the heme propionate groups are involved in the transmission of the signal from the heme to the protein. Analogous observations have been made for the heme propionate groups in *EcDOS*, suggesting that the heme propionates are critical constituents of the intramolecular signal transduction process not just in globin coupled sensors, but also for PAS containing proteins. The influences of ancillary bonding interactions of the distal site of the heme with the bound ligand vary considerably between the various heme-based sensor proteins. It has been established that GCS and PAS containing heme-based oxygen sensors contain conserved Tyr or Arg residues, respectively, adjacent to the heme Fe.¹ Our data demonstrate that these residues are important for direct interactions with the heme-bound ligand; in *EcDOS* Arg97 is hydrogen bonded to the heme bound CO and O₂,² while in GCS HemAT-*Bs* and YddV tyrosine residues (Y70 and Y43, respectively) display hydrogen bonding interactions with the heme bound CO. Interestingly, none of the studied bacterial heme-based sensor proteins

possess a distal histidine adjacent the heme – binding pocket, which appears more important to mammalian heme-based proteins such as myoglobin.³

Globins possess highly diverse sequences, yet maintain a common fold. Aside from the sequence differentiation, there are highly-conserved residues at several sites.⁴ In addition to distal Tyr, GCS HemAT-*Bs* and YddV have a conserved leucine residue (Leu92 and Leu65 respectively) also in the vicinity of the heme Fe. Our proposition that Leu92 in HemAT-*Bs* serves as the conformational gate to the migration pathway of photodissociated CO, as well as the suggested significant role of Leu65 in YddV in controlling ligand dynamics, lead us to the conclusion that distal Leu residues are apparently critical constituents of the ligand binding process in globin coupled sensors of prokaryotic cells. Similar role has been proposed for the conserved residue Leu29 of human Mb (eukaryotic cells), where CO binding to the heme iron of Mb was shown to be regulated by Leu29, by affecting the structural of the environment surrounding the heme binding pocket.⁵

Eukaryotic and prokaryotic PAS domains do not vary considerably in their structure and length, but they differ in their signal transduction-controlled catalytic functions as histidine protein kinase domains and cyclic dinucleotide phosphodiesterase domains are found only in prokaryotic cells, while they function as bHLH DNA-binding domains in eukaryotic cells.³ Our TRS²-FTIR spectra and kinetic evolution of CO-rebinding in *EcDOSH*, in agreement with previous studies, lead to the conclusion that the PDE activity of the catalytic domain of the protein is controlled by an antagonistic “binding and replacement” process between endogenous Met95 and CO.⁶⁻⁹ Although heme-PAS protein NPAS2, the first to be discovered in eukaryotes, apparently demonstrates different catalytic function than *EcDOS* (control gene expression by directly regulating DNA binding), it still exhibits displaceable coordination on the distal side of the heme iron. Optical absorption spectroscopy of deoxy-NPAS2 and its independent heme-binding domains has revealed features that suggest a hexacoordinate structure of the heme iron and existence of a displaceable residue.³ The observation of displaceable residues in both prokaryotic and eukaryotic heme-based PAS-containing oxygen sensors, proposes a possible role in regulating ligand affinity for these structural elements.

9.2 References

1. M. Martinkova, K. Kitanishi, T. Shimizu, *J. Biol. Chem.* **2013**, *288*, 27702-27711.
2. Y. Ishitsuka, Y. Araki, A. Tanaka, J. Igarashi, O. Ito, T. Shimizu, *Biochemistry* **2008**, *47*, 8874-8884.
3. M.A Gilles-Gonzalez, G. Gonzalez, *J. Appl. Physiol.* **2004**, *96*, 774-783.
4. M. Ota, Y. Isogai, K. Nishikawa, *FEBS Lett.* **1997**, *417*, 129-133.
5. A.N. Sunohara, K. Ishimori, I. Maorishima, *J. Biol. Chem.* **1992**, *267*, 12614-12621.
6. A. Tanaka, H. Takahashi and T. Shimizu, *J. Biol. Chem.* **2007**, *282*, 21301-21307.
7. S. F. El-Mashtoly, M. Kubo, S. Nakashima, T. Shimizu and T. Kitagawa, *J. Phys. Chem. Lett.* **2011**, *2*, 2212-2217.
8. S. Taguchi, T. Matsui, J. Igarashi, Y. Sasakura, Y. Araki, O. Ito, S. Sugiyama, I. Sagami and T. Shimizu, *J. Biol. Chem.* **2004**, *279*, 3340-3347.
9. C. Lechauve, L. Bouzhir-Sima, T. Yamashita, M. C. Marden, M. H. Vos, U. Liebl, L. Kiger, *J. Biol. Chem.* **2009**, *284*, 36146-36159.



CHAPTER 10

Future Work

Andrea Pavlou

Suggestions for future work

A number of unresolved questions still remain to be addressed to allow a complete understanding of how the structures of heme-based gas sensor proteins relate to their function. These questions open possible research directions that could be pursued in the future and further develop the conclusions of the current PhD project. Henceforth we suggest as prospective experimental work:

- Site-directed mutagenesis of critical residues of HemAT-*Bs* that lie in the vicinity of the H-helix followed by CO-dissociation/rebinding studies using time-resolved step-scan FTIR, to further investigate the observation that intramolecular signal transduction in HemAT-*Bs* possibly occurs upon CO binding.
- Identification and site-directed mutagenesis of other residues of the YddV heme periphery apart from Leu65 and Tyr43 that might play a critical role in the molecular mechanisms of signal transduction processes. Spectroscopic investigation of the mutations of such residues to elucidate their role.
- Time-resolved step-scan FTIR experiments on the wild type and mutant full length *EcDOS*-CO adducts, to investigate and compare the dynamic changes induced to the structure of the full length protein upon CO-dissociation / rebinding with the dynamic changes induced to the truncated heme domain form of *EcDOS*.



CHAPTER 11

Appendix

Andrea Pavlou

Appendix index		Page
11.1 Supplementary figures		
11.1.1 HemAT-Bs		162
Figure 11.1.1a	TRS ² -FTIR difference spectra of full length Y70F HemAT-CO pD 8	
Figure 11.1.1b	TRS ² -FTIR difference spectra of full length Y133F HemAT-CO pD 8	
Figure 11.1.1c	TRS ² -FTIR difference spectra of full length T95A HemAT-CO pD 8	
11.1.2 YddV		163
Figure 11.1.2a	TRS ² -FTIR difference spectra of heme domain wild type YddV-CO adducts at 6 μ s and pD 8	
Figure 11.1.2b	TRS ² -FTIR difference spectra of heme domain L65M YddV-CO adducts pH 8	
Figure 11.1.2c	TRS ² -FTIR difference spectra of heme domain L65T YddV-CO adducts pH 8	
Figure 11.1.2d	TRS ² -FTIR difference spectra of heme domain Y43A YddV-CO adducts pH 8	
Figure 11.1.2e	TRS ² -FTIR difference spectra of heme domain Y43F YddV-CO adducts pH 8	
Figure 11.1.2f	TRS ² -FTIR difference spectra of heme domain Y43W YddV-CO adducts pH 8	
Figure 11.1.2g	TRS ² -FTIR difference spectra of heme domain wild type YddV-CO adducts at 6 μ s and pD 8	

11.1.3 *Ec*DOSH

167

Figure 11.1.3a Static FTIR spectra of wild type *Ec*DOSH-CO at pH 7.5, 6, 9 and pD 7.5. Static FTIR spectrum of wild type *Ec*DOSH-CO¹³ at pH 7.5.

11.2 Supplementary tables

HemAT-*Bs* 168

Table 11.2.1 Spectral time resolutions of full length HemAT-CO adducts

Table 11.2.2 Spectral time resolutions of sensor domain HemAT-CO adducts

YddV 172

Table 11.2.3 Spectral time resolutions of heme domain YddV-CO adducts pH 8

Table 11.2.4 Spectral time resolutions of heme domain YddV-CO adducts pD 8

***Ec*DOSH** 176

Table 11.2.5 Spectral time resolutions of heme domain *Ec*DOSH-CO adducts pD 8

Table 11.2.6 Spectral time resolutions of heme domain *Ec*DOSH -CO adducts pD 8

11.1 Supplementary figures

11.1.1 HemAT-Bs: Time-resolved step-scan FTIR difference spectra of the full length mutant HemAT-CO adducts pD 8

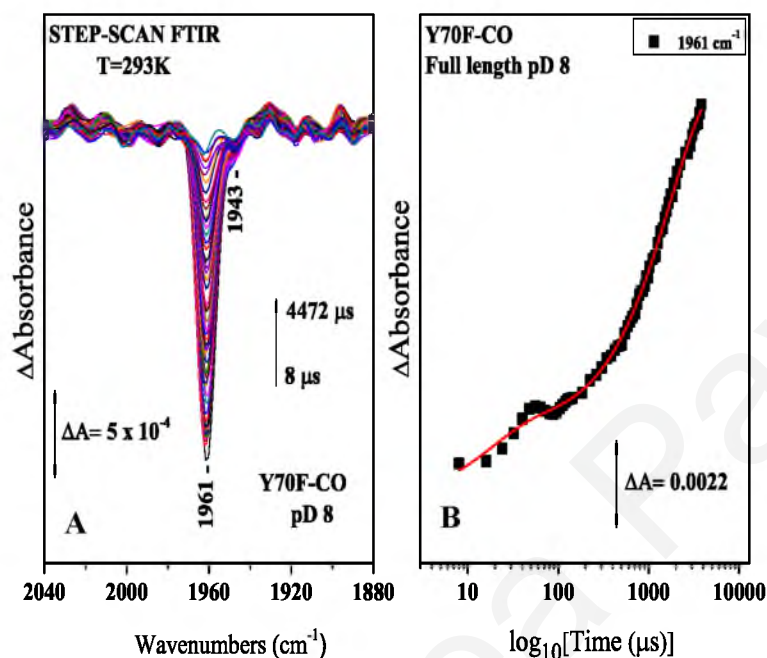


Figure 11.1.1a (A) Time-resolved step-scan FTIR difference spectra of the Y70F full length HemAT-CO adduct at pD 8 from 0.008 to 4.472 ms subsequent to CO photolysis. **(B)** Plot of the ΔA of the 1961 cm^{-1} mode versus time on a logarithmic scale subsequent to CO photolysis. The red line corresponds to the exponential fit of the experimental data.

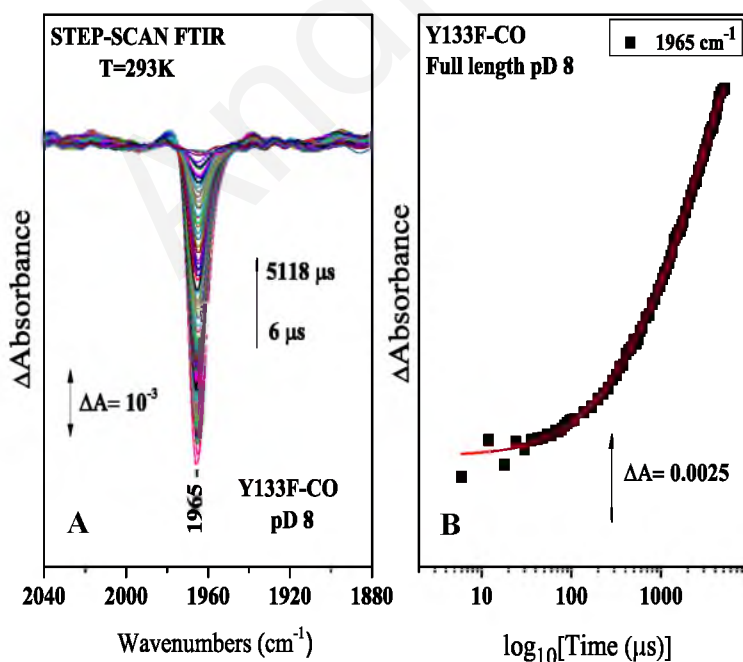


Figure 11.1.1b (A) Time-resolved step-scan FTIR difference spectra of the Y133F full length HemAT-CO adduct at pD 8 from 0.006 to 5.118 ms subsequent to CO photolysis. **(B)** Plot of the ΔA of the 1965 cm^{-1} mode versus time on a logarithmic scale subsequent to CO photolysis. The red line corresponds to the exponential fit of the experimental data.

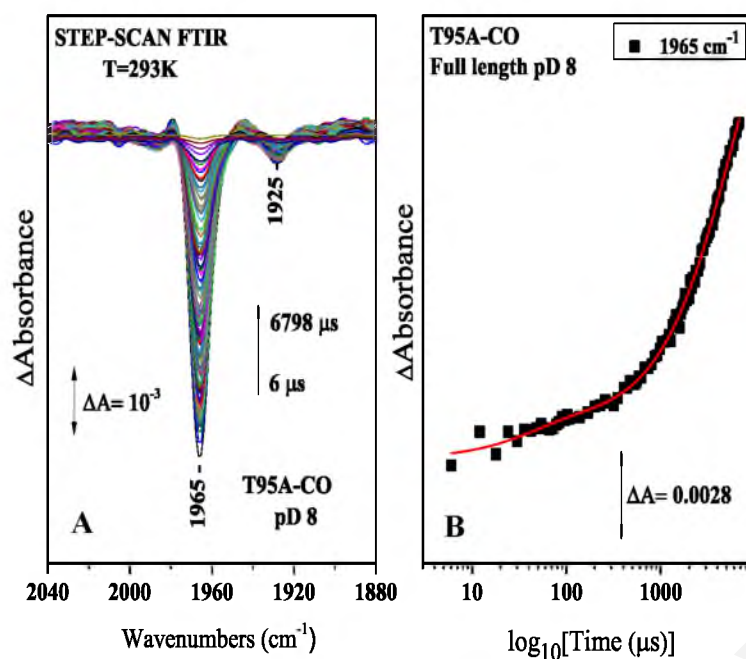


Figure 11.1.1c (A) Time-resolved step-scan FTIR difference spectra of the T95A full length HemAT-CO adduct at pH 8 from 0.008 to 6.798 ms subsequent to CO photolysis. **(B)** Plot of the ΔA of the 1965 cm⁻¹ mode versus time on a logarithmic scale subsequent to CO photolysis. The red line corresponds to the exponential fit of the experimental data.

11.1.2 YddV: Time-resolved step-scan FTIR difference spectra of the heme domain mutant YddV-CO adducts pH 8.

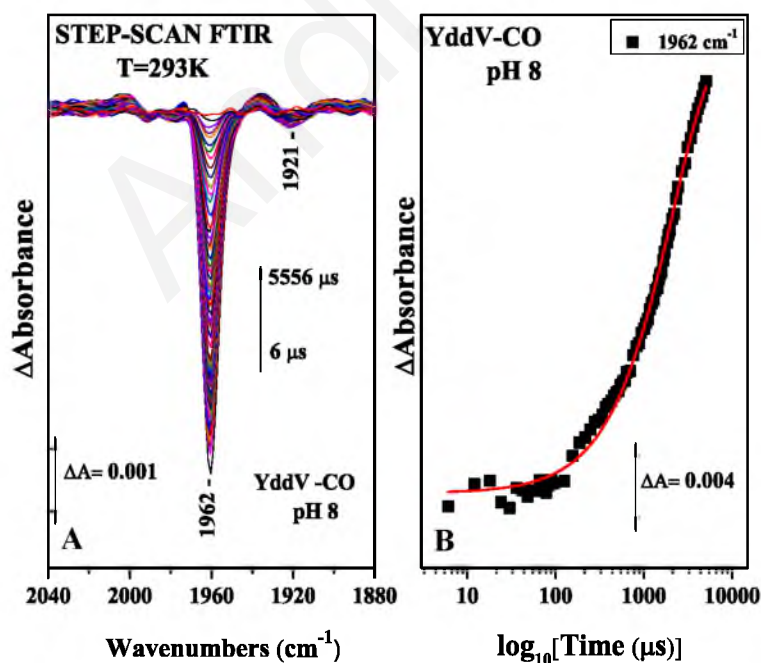
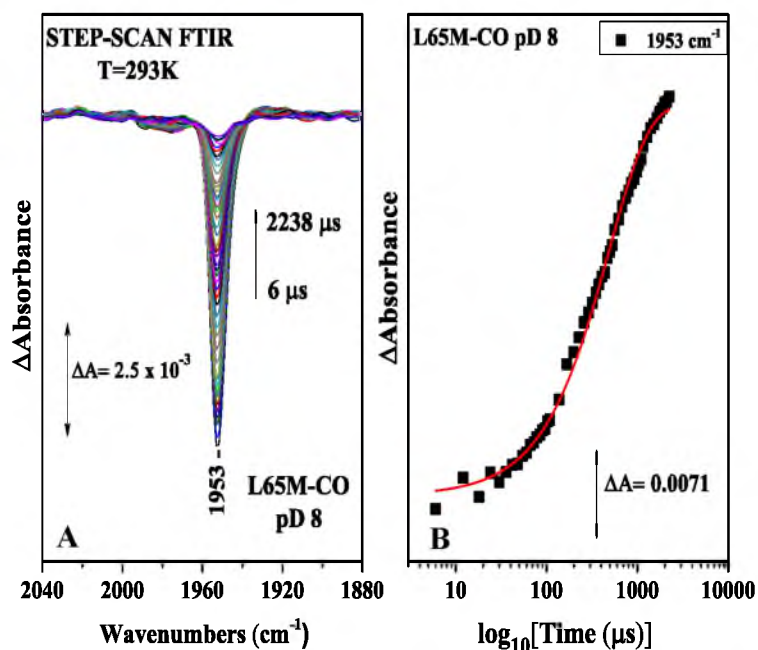


Figure 11.1.2a (A) Time-resolved step-scan FTIR difference spectra of the wild type heme domain YddV-CO adduct at pH 8 from 0.006 to 5.556 ms subsequent to CO photolysis. **(B)** Plot of the ΔA of the 1962 cm⁻¹ mode versus time on a logarithmic scale subsequent to CO photolysis. The red line corresponds to the exponential fit of the experimental data.



11.1.2b (A) Time-resolved step-scan FTIR difference spectra of the heme domain L65M YddV-CO adduct at pD 8 from 0.006 to 2.238 ms subsequent to CO photolysis. (B) Plot of the ΔA of the 1953 cm^{-1} mode versus time on a logarithmic scale subsequent to CO photolysis. The red line corresponds to the exponential fit of the experimental data.

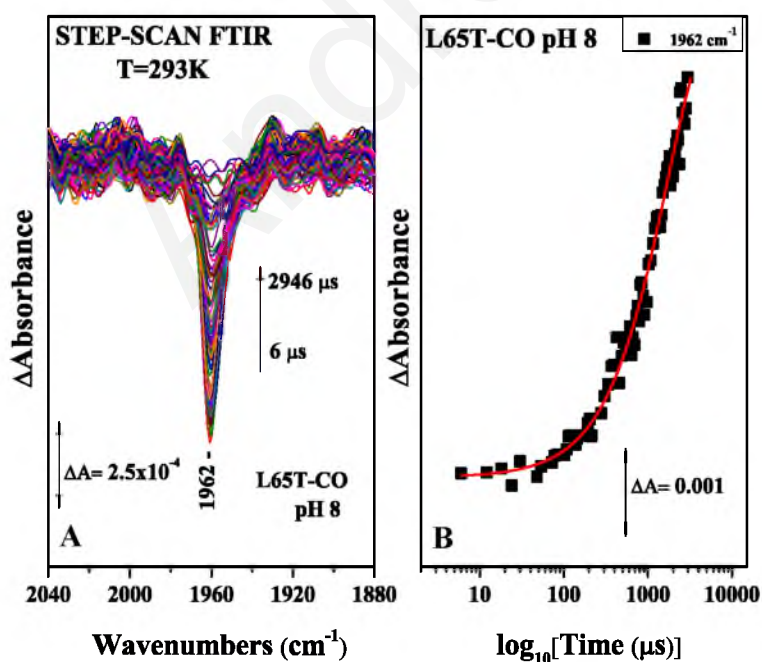


Figure 11.1.2c (A) Time-resolved step-scan FTIR difference spectra of the L65T heme domain YddV-CO adduct from 0.006 to 2.946 ms subsequent to CO photolysis. (B) Plot of the ΔA of the 1962 cm^{-1} mode versus time on a logarithmic scale subsequent to CO photolysis. The red line corresponds to the exponential fit of the experimental data.

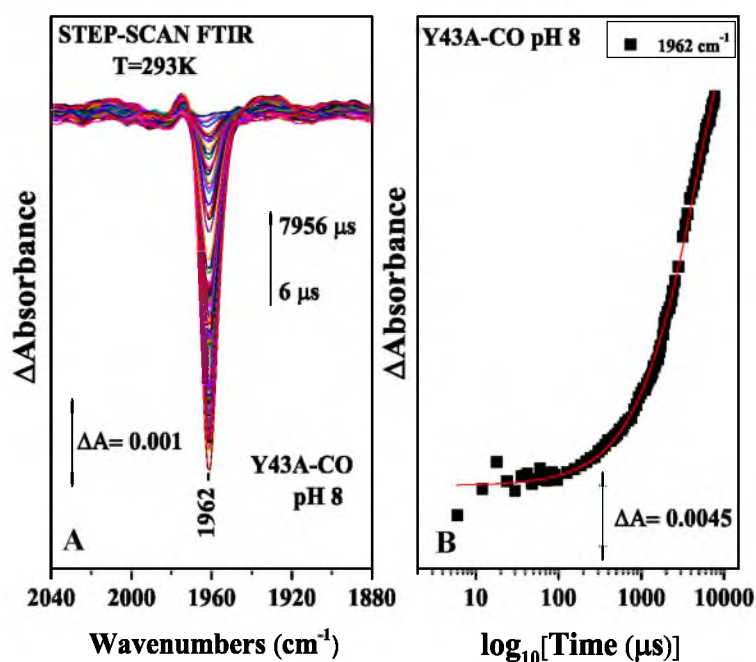


Figure 11.1.2d (A) Time-resolved step-scan FTIR difference spectra of the Y43A heme domain YddV-CO adduct at pD 8 from 0.006 to 7.956 ms subsequent to CO photolysis. (B) Plot of the ΔA of the 1962 cm^{-1} mode versus time on a logarithmic scale subsequent to CO photolysis. The red line corresponds to the exponential fit of the experimental data.

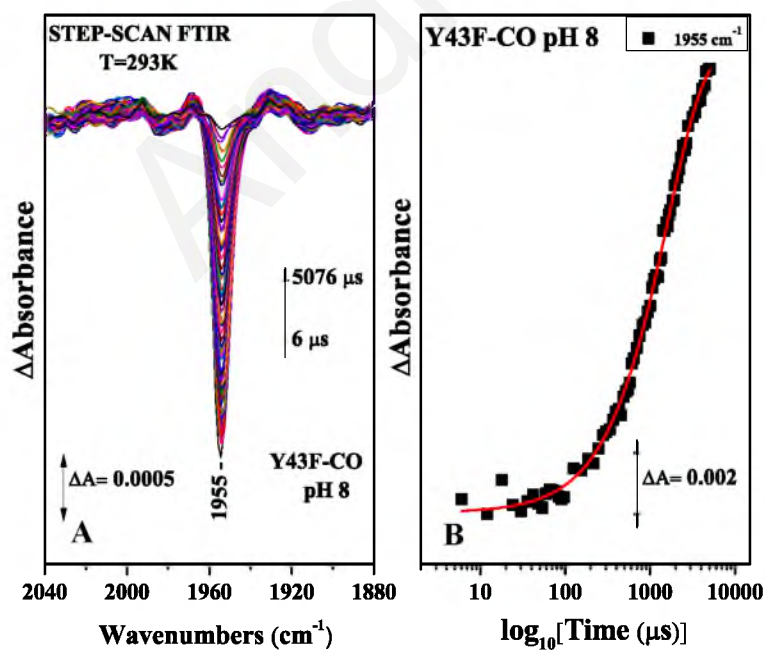


Figure 11.1.2e (A) Time-resolved step-scan FTIR difference spectra of the Y43F heme domain YddV-CO adduct at pD 8 from 0.006 to 5.076 ms subsequent to CO photolysis. (B) Plot of the ΔA of the 1955 cm^{-1} mode versus time on a logarithmic scale subsequent to CO photolysis. The red line corresponds to the exponential fit of the experimental data.

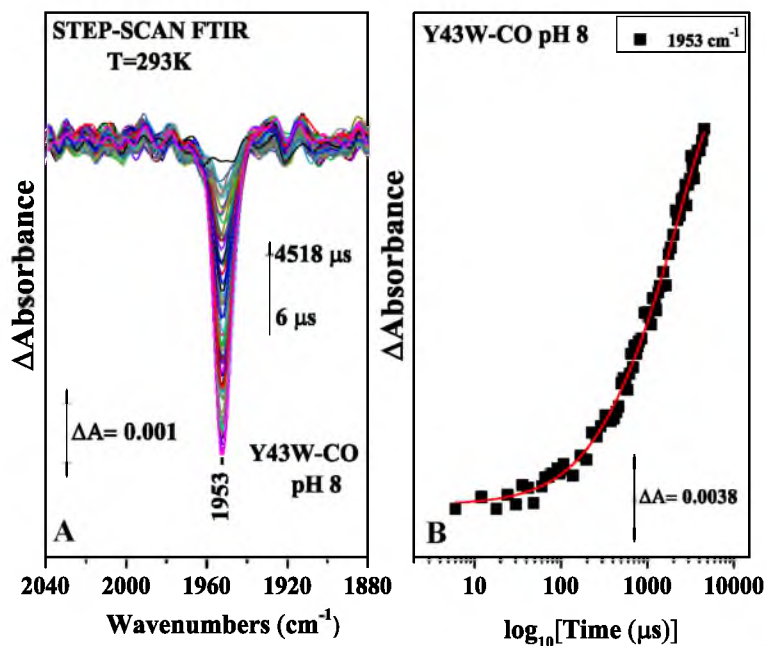


Figure 11.1.2f (A) Time-resolved step-scan FTIR difference spectra of the Y43W heme domain YddV-CO adduct at pH 8 from 0.006 to 4.518 ms subsequent to CO photolysis. (B) Plot of the ΔA of the 1953 cm^{-1} mode versus time on a logarithmic scale subsequent to CO photolysis. The red line corresponds to the exponential fit of the experimental data.

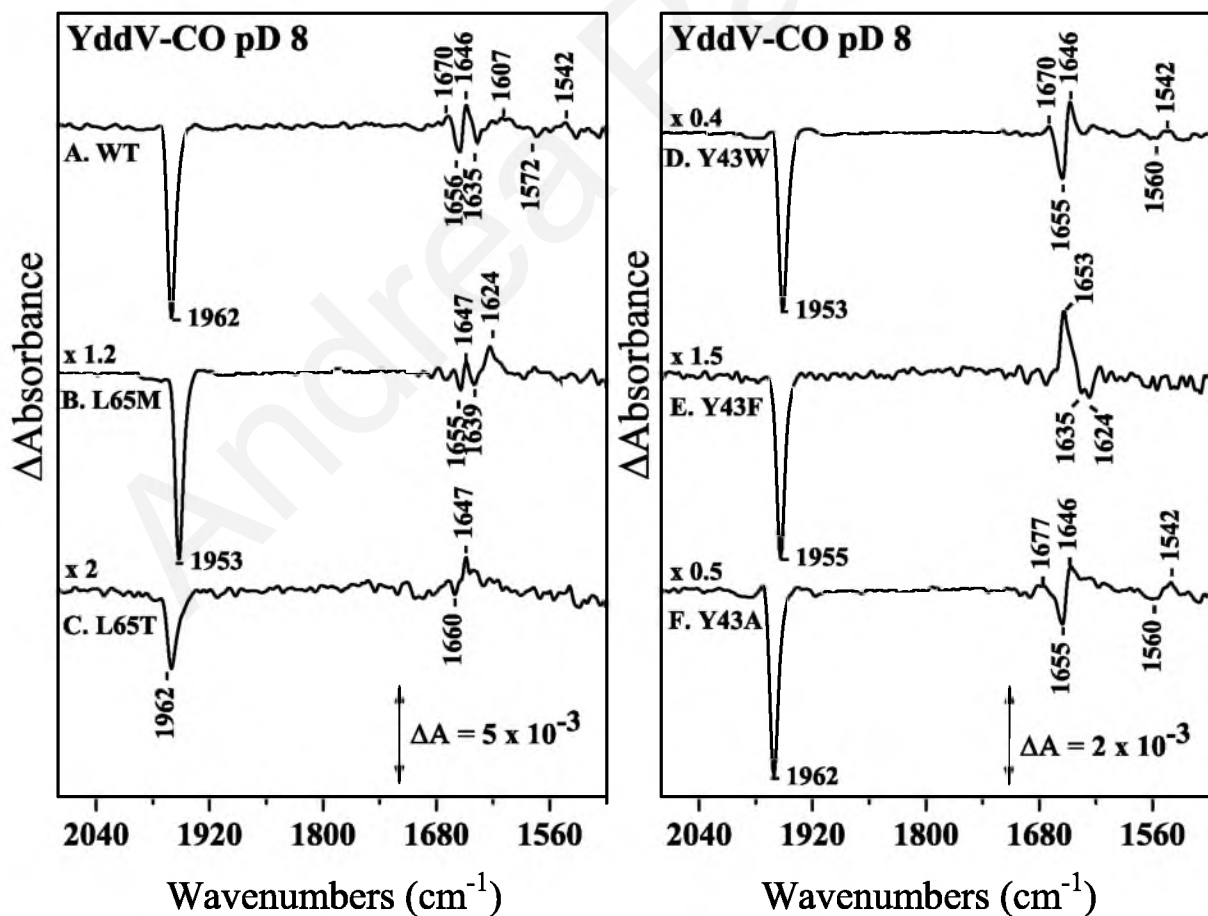


Figure 11.1.2g TRS² - FTIR difference spectra of heme domain YddV-CO adducts at pH 8, at $t_d = 6\ \mu\text{s}$, wild type (trace A), L65M (trace B), L65T (trace C), Y43W (trace E), Y43F (trace D), and Y43A (trace F)

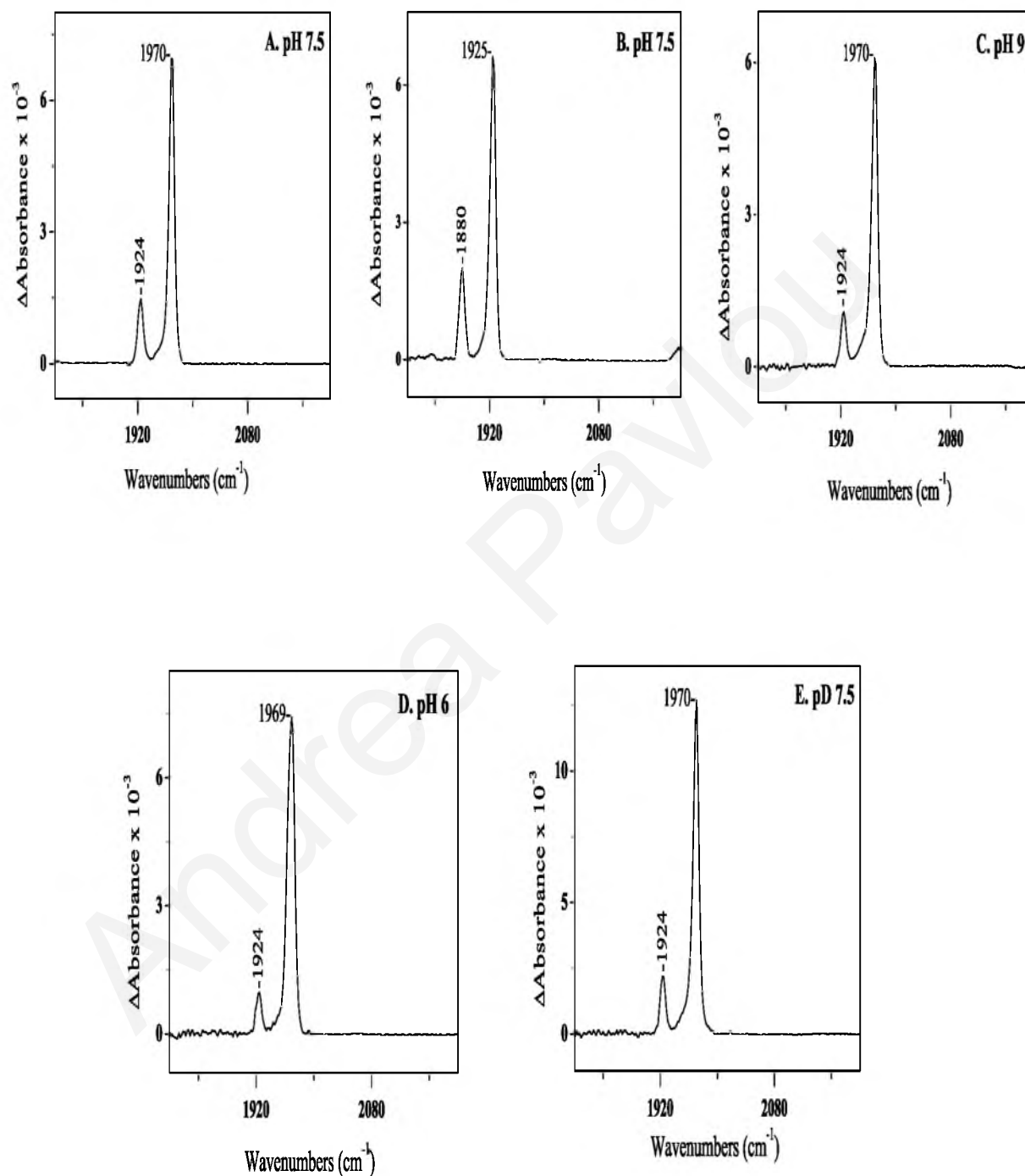
11.1.3 *Ec*DOSH: Static FTIR spectra of *Ec*DOSH-CO adducts.

Figure 11.1.3a FTIR spectra of the wild type *Ec*DOSH-CO adducts at pH 7.5 (trace A), *Ec*DOSH- ^{13}C O pH 7.5 (trace B), pH 9 (trace C), pH 6 (trace D), and pD 7.5 (trace E). The pathlength was 6 μm and the spectral resolution was 4 cm^{-1} .

11.2 Supplementary tables

Table 11.2.1: Spectral time resolutions of full length HemAT-CO adducts

L92A	T95A	Y133F	Y70F	WT H ₂ O	WT D ₂ O
6	6	6	8	8	8
12	12	12	16	16	16
18	18	18	24	24	24
24	24	24	32	32	32
30	30	30	40	40	40
36	36	36	48	48	48
42	42	42	56	56	56
48	48	48	64	64	64
54	54	54	72	72	72
60	60	60	80	80	80
66	66	66	88	88	88
72	72	72	96	96	96
78	78	78	104	104	104
84	84	84	112	112	112
90	90	90	120	120	120
96	96	96	128	128	128
102	102	102	136	136	136
108	108	108	144	144	144
114	138	138	184	152	152
120	168	168	224	192	192
126	198	198	264	232	232
132	228	228	304	272	272
138	258	258	344	312	312
144	288	288	384	352	352
150	318	318	424	392	392
156	348	348	464	432	432
162	378	378	504	472	472
168	408	408	544	512	512
174	438	438	584	552	552
180	468	468	624	592	592
186	498	498	664	632	632
192	528	528	704	712	712
198	558	558	744	792	792
204	588	588	784	872	872
210	618	618	824	952	952
216	678	678	864	1032	1032
222	738	738	904	1272	1272
228	798	798	944	1512	1512
234	858	858	984	1752	1752
240	918	918	1024	1992	1992
246	978	978	1104	2232	2232

252	1038	1038	1184	2472	2472
258	1098	1098	1264	2712	2712
264	1158	1158	1344	3032	3032
270	1218	1218	1424	3832	3832
276	1278	1278	1504	4632	4632
282	1338	1338	1584	5432	5432
288	1398	1398	1664		6232
294	1458	1458	1744		
300	1518	1518	1824		
306	1578	1578	1904		
312	1638	1638	1984		
318	1698	1698	2064		
324	1758	1758	2224		
330	1818	1878	2544		
336	1878	1998	2704		
342	1938	2118	2864		
348	1998	2238	3024		
354	2058	2358	3184		
360	2118	2478	3344		
366	2178	2598	3504		
372	2238	2718	3664		
378	2298	2838	3824		
384	2358	2958			
402	2478	3078			
420	2598	3198			
450	2718	3318			
480	2838	3438			
510	2958	3558			
540	3078	3678			
570	3198	3798			
600	3318	3918			
	3438	4038			
	3558	4158			
	3678	4278			
	3798	4398			
	3918	4638			
	4038	4878			
	4158	5118			
	4398				
	4638				
	4878				
	5118				
	5358				
	5598				
	5838				
	6078				
	6318				
	6558				
	6798				

Table 11.2.2: Spectral time resolutions of sensor domain HemAT-CO adducts

L92A	T95A	Y133F	Y70F	WT H ₂ O	WT D ₂ O
8	6	6	8	8	8
16	12	12	16	16	16
24	18	18	24	24	24
32	24	24	32	32	32
40	36	30	40	40	40
48	42	36	48	48	48
56	48	42	56	56	56
64	54	48	64	64	64
72	60	54	72	72	72
80	66	60	88	80	80
88	72	66	96	88	88
96	78	72	104	96	96
104	90	78	112	104	104
112	96	84	120	112	112
120	102	90	128	120	120
128	108	96	136	128	128
136	114	102	144	136	136
144	144	108	152	144	144
152	174	138	192	152	152
178	204	156	232	192	192
186	234	168	272	232	232
194	264	186	312	272	272
202	294	198	352	312	312
210	324	228	392	352	352
218	354	258	432	392	392
226	384	276	472	432	432
234	414	288	512	472	472
242	444	318	552	512	512
250	474	348	592	552	552
258	504	378	632	592	592
266	534	408	672	632	632
274	564	438	712	712	712
282	594	468	752	792	792
290	624	498	792	872	872
298	654	528	832	952	952
306	684	558	872	1032	1032
314	714	588	912	1272	1272
322	744	518	952	1512	1512
330	804	548	992	1752	1752
338	864	578	1032	1992	1992
346	924	608	1112	2232	2232
354	984	638	1192	2472	2472
378	1044	668	1272	2712	2712
394	1104	728	1352	2952	2952

418	1164	788	1432	3192
434	1224	848	1512	3432
474	1284	908	1592	
514	1344	968	1672	
554	1404	1028	1752	
594	1464	1038	1832	
674	1524	1098	1912	
754	1584	1158	1992	
834	1704	1218	2072	
914	1824	1278	2232	
994	1944	1338	2392	
1074	2064	1398	2552	
1154	2184	1518	2712	
1234	2304	1638	2872	
1314	2424	1758	3032	
1474	2544	1878	3192	
1634	2664	1998	3352	
1794	2784	2118	3512	
	2904	2238	3672	
	3024	2358	3832	
	3144	2478	3992	
	3264	2598	4232	
	3384	2718	4472	
	3504	2838	4712	
	3624	3118		
	3744	3298		
	3864	3478		
	3984	3658		
	4104	3838		
	4224	4118		
	4344	4358		
	4464	4658		
	4584			
	4704			
	4944			
	5184			
	5424			
	5664			
	5832			

Table 11.2.3: Spectral time resolutions of heme domain YddV-CO adducts pH 8

L65M	L65T	Y43A	Y43F	Y43W	WT
6	6	6	6	6	6
12	12	12	12	12	12
18	18	18	18	18	18
24	24	24	24	24	24
30	30	30	30	30	30
36	36	36	36	36	36
42	42	42	42	42	42
48	48	48	48	48	48
54	54	54	54	60	54
60	60	60	60	66	60
66	66	66	66	72	66
72	72	72	72	78	72
78	78	78	78	90	78
84	84	84	84	96	84
90	90	90	90	102	90
96	96	96	96	108	96
102	102	126	126	138	126
108	108	156	156	168	156
114	114	186	186	198	186
120	120	216	216	228	216
126	126	246	246	258	246
132	132	276	276	288	276
138	138	306	306	324	306
144	144	336	336	348	336
150	150	366	366	378	366
156	156	396	396	408	396
162	162	426	426	438	426
168	168	456	456	468	456
174	174	486	486	498	486
180	180	516	516	528	516
186	186	546	546	558	546
192	192	576	576	588	576
198	198	606	606	618	606
204	204	636	636	648	636
210	210	696	696	678	696
216	216	756	756	708	756
228	276	816	816	744	816
240	306	876	876	768	876
252	336	936	936	798	936
264	366	996	996	858	996
276	396	1056	1056	918	1056
288	426	1116	1116	984	1116
300	456	1176	1176	1038	1176
312	486	1236	1236	1098	1236
324	516	1296	1296	1158	1296
336	546	1356	1356	1218	1356
348	576	1416	1416	1278	1416
360	606	1476	1476	1338	1476

372	636	1536	1536	1398	1536
384	666	1596	1596	1458	1596
396	696	1656	1656	1518	1656
408	726	1716	1716	1638	1716
420	756	1836	1836	1758	1836
432	786	1896	1896	1878	1896
444	816	1956	1956	1998	1956
456	846	2076	2076	2118	2076
468	876	2196	2196	2238	2196
480	906	2316	2316	2358	2316
492	966	2396	2436	2478	2436
504	1026	2546	2556	2598	2676
534	1086	2796	2676	2718	2916
564	1146	3166	2796	2838	3156
594	1206	3396	3156	2958	3396
624	1266	3636	3396	3078	3636
654	1326	3876	3636	3198	3876
684	1386	4116	3876	3318	4116
714	1446	4356	4116	3438	4356
744	1506	4596	4356	3558	4596
774	1566	4836	4596	3798	4836
804	1626	5076	4836	4038	5076
834	1686	5316	5076	4278	
864	1746	5556		4518	
894	1806	5796			
924	1866	6036			
954	1926	6276			
984	1986	6516			
1014	2046	6756			
1074	2106	6996			
1134	2166	7236			
1194	2226	7476			
1254	2286	7716			
1314	2346				
1374	2406				
1434	2466				
1494	2586				
1554	2706				
1614	2826				
1734	2946				
1854					
1974					
2094					
2214					
2334					
2454					
2574					
2694					
2814					
2934					
3054					

Table 11.2.4: Spectral time resolutions of heme domain YddV-CO adducts pD 8

L65M	L65T	WT	Y43W	Y43A	Y43F
6	6	6	6	6	6
12	12	12	12	12	12
18	18	18	18	18	18
24	24	24	24	24	24
30	30	30	30	30	30
36	36	36	36	36	36
42	42	42	42	42	42
48	48	48	48	48	48
54	54	54	54	54	54
60	60	60	60	60	60
66	66	66	66	66	66
72	72	72	72	72	72
78	78	78	78	78	78
84	84	84	84	84	84
90	90	90	90	90	90
96	96	96	96	96	96
102	102	102	102	102	102
108	108	108	108	108	108
138	120	138	138	138	138
168	132	168	168	168	168
198	144	198	198	198	198
228	156	228	228	228	228
258	168	258	258	258	258
288	180	288	288	288	288
318	192	318	318	318	318
348	204	348	348	348	348
378	216	378	378	378	378
408	228	408	408	408	408
438	240	438	438	438	438
468	252	468	468	468	468
498	264	498	498	498	498
528	276	528	528	528	528
558	288	558	558	558	558
618	300	618	618	618	618
678	312	678	678	678	678
738	324	738	738	738	738

798	342	798	798	798	798
858	360	858	858	858	858
918	378	918	918	918	918
978	396	978	978	978	978
1038	414	1038	1038	1038	1038
1098	432	1098	1098	1098	1098
1158	450	1158	1158	1158	1128
1278	480	1278	1278	1278	1188
1398	510	1398	1398	1398	1248
1518	540	1518	1518	1518	1308
1638	570	1638	1638	1638	1368
1758	600	1758	1758	1758	1428
1878	630	1878	1878	1878	1488
1998	660	1998	1998	1998	1548
2118	690	2118	2118	2118	1608
2238	720	2238	2238	2238	1668
	750	2358	2358	2358	1728
	780	2478	2478	2598	1788
	810	2598	2598	2838	1848
	840	2718	2718	3078	1908
	870	2838	2838	3318	1968
	900	2958	2958	3558	2028
	960	3198	3198	3798	2088
	1020	3438	3438	4038	2148
	1080	3678	3678	4278	2208
	1140	3918	3918	4638	2268
		4158	4158	4998	2328
		4518	4398	5358	2448
		4878	4638	5718	2568
		5238		6078	2688
		5598		6438	2808
		5958		6798	2928
		6678		7518	3048
		7398		8238	3168
				8958	3288
					3408
					3528
					3648
					3768
					3888

Table 11.2.5: Spectral time resolutions of heme domain *Ec*DOS-CO adducts pD 8

WT H ₂ O	WT D ₂ O	E93I	M95A	W53F
6	6	6	6	6
12	12	12	12	12
18	18	18	18	18
24	24	24	24	24
30	30	30	30	30
36	36	36	36	36
42	42	42	42	42
48	48	48	48	48
54	54	54	54	54
60	60	60	60	60
66	66	66	66	66
72	72	72	72	72
78	78	78	78	78
84	84	84	84	84
90	90	90	90	90
96	96	96	96	96
102	102	102	102	102
108	108	108	108	108
138	138	138	114	138
168	168	168	120	168
198	198	198	126	198
228	228	228	132	228
258	258	258	138	258
288	288	288	144	288
318	318	318	150	318
348	348	348	156	348
378	378	378	162	378
408	408	408	168	408
438	438	438	174	438
468	468	468	180	468
498	498	498	186	498
528	528	558	192	528
558	558	618	198	558
588	618	678	204	618
648	678	738	210	678
708	738	798	216	738
768	858	858	222	798
828	918	918	228	858
888	978	978	234	918
948	1038	1038	240	978

1008	1098	1098	246	1038
1068	1158	1158	252	1098
1128	1278	1278	258	1158
1248	1398	1398	264	1218
1368	1518	1518	270	1278
1488	1638	1638	276	1338
1608	1758	1758	282	1398
1728	1878		288	1458
1848	1998		294	1518
1968	2118		300	1578
2088	2238		306	1638
2208	2358		324	1698
2328	2598		342	1758
2568	2838		360	1878
2808	3078		378	1998
3048	3318		396	2118
3288	3558		414	2238
3528	3918		432	2358
3768	4278			2478
4008	4638			2598
4248	4998			2718
4488	5358			2838
4848	5718			2958
5208	6078			3198
5568	6798			3438
5928	7518			3678
6288	8958			3918
7008	10398			4158
7728	11838			4398
				4638
				5118
				5478
				5838
				6198
				6558
				7278
				7998
				8718
				9438

Table 11.2.6: Spectral time resolutions of heme domain *Ec*DOS-CO adducts pD 8

Y126F	F113T	N84V	R97A	R97I
6	6	6	6	6
12	12	12	12	12
18	18	18	18	18
24	24	24	24	24
30	30	30	30	30
36	36	36	36	36
42	42	42	42	42
48	48	48	48	48
54	54	54	54	54
60	60	60	60	60
66	66	66	66	66
72	72	72	72	72
78	78	78	78	78
84	84	84	84	84
90	90	90	90	90
96	96	96	96	96
102	102	102	102	102
108	108	108	108	108
138	138	138	138	114
168	168	168	168	120
198	198	198	198	126
228	228	228	228	132
258	258	258	258	138
288	288	288	288	144
318	318	318	318	
348	348	348	348	
378	378	378	378	
408	408	408	408	
438	438	438	438	
468	468	468	468	
498	498	498	498	
528	528	528	528	
558	558	558	558	
618	588	618	678	
678	618	678	798	
738	678	738	918	
798	738	798	1038	
858	798	858	1158	
918	858	918	1398	
978	918	978	1638	
1038	978	1038	1878	

1098	1038	1098	2598
1158	1098	1158	3318
1278	1158	1278	4038
1398	1218	1398	4998
1518	1278	1518	5718
1638	1338	1638	6798
1758	1398	1758	7518
1878	1458	1878	8958
1998	1518	1998	10398
2118	1578	2118	11838
2238	1638	2238	
2358	1698	2358	
2598	1758	2598	
2838	1818	2838	
3078	1878	3078	
3318	1938	3318	
3558	1998	3558	
3798	2058	3798	
4038	2118	4038	
4278	2178	4278	
4638	2238	4998	
4998	2298	5718	
5358	2358	6438	
5718	2478		
6078	2598		
6798	2718		
7518	2838		
8238	2958		
8958	3078		
10398	3198		
11838	3318		
13278	3438		
	3558		
	3918		
	4398		
	5118		
	6078		
	7518		
	8958		
	10398		
	11748		
